WINTER 2025

GEMS & GEMOLOGY

VOLUME LXI

Montana Sapphire from French Bar Sill

Emerald from Shaanxi, China

Mona Lisa Turquoise from Arkansas

2025 Converge Report

THE QUARTERLY JOURNAL OF THE GEMOLOGICAL INSTITUTE OF AMERICA

GEMS & GEMOLOGY®
Winter 2025
VOLUME 61, No. 4


p. 333


p. 357

EDITORIAL

FEATURE ARTICLES


p. 396

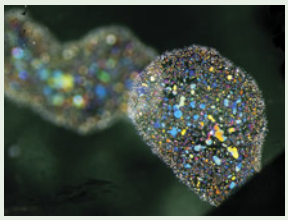
p. 401


p. 409

REGULAR FEATURES

GEMS & GEMOLOGY®

gia.edu/gems-gemology

Customer Service
(760) 603-4200
gandg@gia.edu

Subscriptions
Copies of the current issue may be purchased for $35.95 plus shipping. Subscriptions are $95.99 for one year (4 issues) in the U.S. and $119.99 elsewhere. Canadian subscribers should add GST. Discounts are available for renewals, group subscriptions, GIA alumni, and current GIA students. To purchase print subscriptions, visit store.gia.edu or contact Customer Service. For institutional rates, contact Customer Service.

Database Coverage
Gems & Gemology's impact factor is 2.6, according to the 2024 Journal Citation Reports by Clarivate Analytics (issued June 2025). *G&G* is abstracted in Thomson Reuters products (Current Contents: Physical, Chemical & Earth Sciences and Science Citation Index—Expanded, including the Web of Knowledge) and other databases. For a complete list of sources abstracting *G&G*, go to gia.edu/gems-gemology, and click on "Publication Information."

Manuscript Submissions
Gems & Gemology, a peer-reviewed journal, welcomes the submission of articles on all aspects of the field. Please see the Author Guidelines at gia.edu/gems-gemology or contact the editors (gandgeditorial@gia.edu). Letters on articles published in *G&G* are also welcome. Please note that Field Reports, Lab Notes, Gem News International, Micro-World, Colored Stones Unearthed, Diamond Reflections, Charts, and In the Spotlight are not peer-reviewed sections but do undergo technical and editorial review.

Gems & Gemology is published quarterly by the Gemological Institute of America, a nonprofit educational organization for the gem and jewelry industry.

Postmaster: Return undeliverable copies of *Gems & Gemology* to GIA, The Robert Mouawad Campus, 5345 Armada Drive, Carlsbad, CA 92008.

Our Canadian goods and service registration number is 126142892RT.

About the Cover

This vibrant green gecko is carved from maw sit-sit, an ornamental stone found only in northern Myanmar. Sitting atop a smoky quartz base, the Patrick Dreher carving (measuring 18 × 13.5 × 9 inches) is part of the GIA Museum's Temples and Treasures of Southeast Asia exhibit, which is featured in this issue's In the Spotlight *column. Photos by Robert Weldon; courtesy of the Larson family.*

Printing is by L+L Printers, Carlsbad, CA.

GIA World Headquarters The Robert Mouawad Campus 5345 Armada Drive Carlsbad, CA 92008 USA

ISSN 0016-626X

Intriguing Sapphire from Montana, a New Source of Emerald in Central China, and Arkansas Turquoise

Fittingly for our Winter issue, which comes out at the 2026 AGTA GemFair in Tucson, colored stones step into the spotlight! Our feature articles focus on sapphires from the French Bar sill in Montana, emeralds from Shaanxi, China, and turquoise from Arkansas's Mona Lisa mine.

"...colored stones step into the spotlight!"

In our lead paper, a team of gemologists headed by independent researcher Robert Kane detail the primary sapphire occurrence at the French Bar sill along Montana's Missouri River. Other than Yogo Gulch, this is the state's only other known source of gem-quality *in situ* sapphire. For this study, the authors examined sapphires in matrix, as well as rough, partially polished, and faceted samples. The authors show that the inclusions and trace element chemistry of samples from this primary deposit overlap with sapphires from secondary sources elsewhere in the state.

Emeralds from Zhen'an County, Shaanxi Province, China, are a very recent discovery, first turning up in drill cores in 2017, and again in association with beryllium mining in 2025. In our second article, a team of Chinese researchers led by Yi Guo provide a comprehensive study of the gemological and spectroscopic characteristics and trace element chemistry of these new emeralds using traditional and advanced gemological methods.

Many historic turquoise sources—especially those across the American Southwest—are depleted, so when turquoise from the Mona Lisa mine in Arkansas reentered gem markets in 2018, a renewed interest followed. The mine's unique geology provoked questions about the identity of the material. Our final paper, authored by GIA's Alexander Goodsuhm, uses careful fieldwork backed by gemological evaluation, X-ray diffraction, Raman spectroscopy, and chemistry to investigate the mine's geologic setting and confirm the nature of the material as turquoise.

Our regular columns offer a rich variety of content! The *Lab Notes* section, which features reports from GIA's global laboratories, includes polished specimens of the rare minerals armenite and friedelite, the largest cuprite ever submitted to GIA, fracture-filled diamonds mounted in jewelry, and an extraordinary cat's-eye boulder opal.

Micro-World dives into the remarkable interiors of gems. This issue's entries present a "bamboo forest" and a colorful "artist's palette" in emerald, nacre platelets resembling a human fingerprint in pearl, elongated wormlike inclusions in opal, and more.

Be sure to check out the summaries of presentations from Converge in our *Gem News International* section. This recent conference, which took place in Carlsbad, California, covered the most important gemological topics challenging the industry. Also in the *GNI* section, we highlight new red garnet production from northern Vietnam, an interesting new jadeite imitation, and deceptive reconstructed rough gem-on-matrix specimens from Pakistan.

Colored Stones Unearthed celebrates the diversity of gemstone deposits, exploring where specific gem minerals are found together and the conditions that produce each distinct geological setting.

In the Spotlight surveys the GIA Museum's current Temples and Treasures of Southeast Asia exhibit, which showcases the extraordinary crystals and gems central to the cultures of the area. The exhibit is on display at the Institute's Carlsbad campus until April 2026.

Welcome to our Winter issue!

Duncan Pay | Editor-in-Chief | dpay@gia.edu

The Primary Sapphire Occurrence at French Bar Sill Along the Missouri River, Near Helena, Montana

Robert E. Kane, Kory L. Pettman, Aaron C. Palke, Rachelle B. Turnier, Richard B. Berg, Nathan D. Renfro, and Christopher P. Smith

Sapphires have been mined in Montana since being discovered at Eldorado Bar, along the Missouri River, in 1865. The most valuable gold deposit in the area was mined near the top of the French Bar complex from 1867 to 1869. On portions of the Virginia terrace and the Center terrace, the French Bar sill, which sparsely contained sapphires in a host rock—identified here as a basaltic trachyandesite, but described elsewhere as a minette—was reported by Kunz in 1891. Other than Yogo Gulch, where the sapphires are in a lamprophyre dike, the French Bar sill is Montana's only other source of gem-quality *in situ* sapphire. New ownership of the property in 2020 has resulted in the largest production to date, although it is still sparse. In this study, the authors examined 80 French Bar sill sapphires in matrix; 16 sapphires removed from the matrix, ranging from very small to 17.99 ct; 4 faceted stones; and 5 partly polished crystals. Trace element chemistry and inclusions were consistent with—and generally indistinguishable from—faceted Montana sapphires from the secondary deposits of the Missouri River, Rock Creek, and Dry Cottonwood Creek. This indicates that while the magmatic material (Eocene volcanism) that transported the sapphires from deep within the earth was different in certain cases, such as with French Bar sill, the genesis of the sapphires may be the same or similar. Many of the surface resorption features are similar, but one important distinction exists. Around 25% of Missouri River alluvial sapphires have encrustations of spinel, likely a result of reaction during transport by a mafic magma. Primary French Bar sill sapphires always have an encrustation of biotite (phlogopite) mica, but never spinel. The French Bar sill itself is certainly too small in extent to have supplied all the alluvial sapphires found at the Missouri River.

In the gemological literature, Yogo Gulch is the only well-documented primary occurrence of gem-quality sapphire in Montana, although French Bar—the only other *in situ* deposit of gem-quality sapphire, also in igneous rock (figure 1)—has been occasionally mentioned throughout the decades, beginning with Kunz in 1891. However, three *in situ* deposits of non-gemmy (opaque) corundum in the Precambrian metamorphic rocks of southwestern Montana have been described by Clabaugh (1952): Elk Creek, Bozeman, and Bear Trap. All three are located southwest of Bozeman.

Figure 1. A gem-quality in situ *French Bar sill primary sapphire (9 mm long) partially embedded in basaltic trachyandesite rock (sample RK-FBS 001). Photo by Jeff Mason.*

See end of article for About the Authors and Acknowledgments.
Gems & Gemology, Vol. 61, No. 4, pp. 332–353,
http://dx.doi.org/10.5741/GEMS.61.4.332

Figure 2. This 3.49 ct sapphire (sample RK-FBS 030) measuring 13.23 mm long was faceted from an 11.15 ct rough crystal in basaltic trachyandesite matrix recovered from the French Bar sill. A combination of diffused daylight-equivalent (6500 K) LED monolights from the front and a narrow beam of light from behind accentuate both the Rose channel inclusions and the body-color. Photo by Jeff Mason.

A recent rediscovery in 2020 and expanded excavation at the French Bar sill shed new light on this lesser-known deposit. Significant direct excavation of the sill began to produce an increased number of larger sapphire-in-matrix specimens. It has been 135 years since the discovery of the French Bar sill, and with many larger *in situ* sapphires recently recovered, there has been an opportunity to extensively research this material. Many of those results are presented in this article.

In 2020, Kale and Sharlene Wetherell purchased 107 acres of property containing the French Bar sill. In late 2023, Kale Wetherell provided author KP, an expert gem cutter specializing in Montana sapphire who has had the privilege of working with some of the world's rarest and most exceptional sapphires, with several photographs of sapphires in matrix from the French Bar sill locality. One of these specimens contained an 11.15 ct sapphire crystal, which was later faceted by author KP into a 3.49 ct sapphire (figure 2). Though specimens of such remarkable size and quality have been recovered, French Bar has remained a secret among gem enthusiasts. As more sapphires in matrix were recovered and documented from this location, author KP shared the find with the coauthors of this paper. This discovery has significant implications for the understanding of sapphire deposits in Montana and warrants further research and documentation.

HISTORY

Kunz (1891, 1893, and 1897) was the first gem and mineral expert to describe the primary (*in situ*) occurrence of Montana sapphire in an andesite dike. In 1891, a Helena newspaper also reported sapphire in matrix at French Bar (*Daily Independent*, 1891). Today we recognize the French Bar sapphire occurrence as a sill. Dikes and sills form similarly; dikes cut vertically through rock layers, and sills are tabular (horizontal) intrusions. Kunz (1890) initially described the host rock as "trachyte rock" and then as an "andesite" in subsequent publications. Today

In Brief

- Beyond Yogo Gulch, French Bar sill is the only other documented primary occurrence of gem-quality sapphire in Montana.
- Characteristics of French Bar sill sapphires—inclusions, UV-Vis-NIR and FTIR spectra, trace element chemistry, and oxygen isotope analysis—largely overlap other secondary sapphire deposits at the Missouri River, Rock Creek, and Dry Cottonwood Creek.
- French Bar sill sapphire crystals are encrusted with biotite (phlogopite) mica, but unlike around 25% of Missouri River alluvial rough sapphire, a spinel encrustation has not been observed.

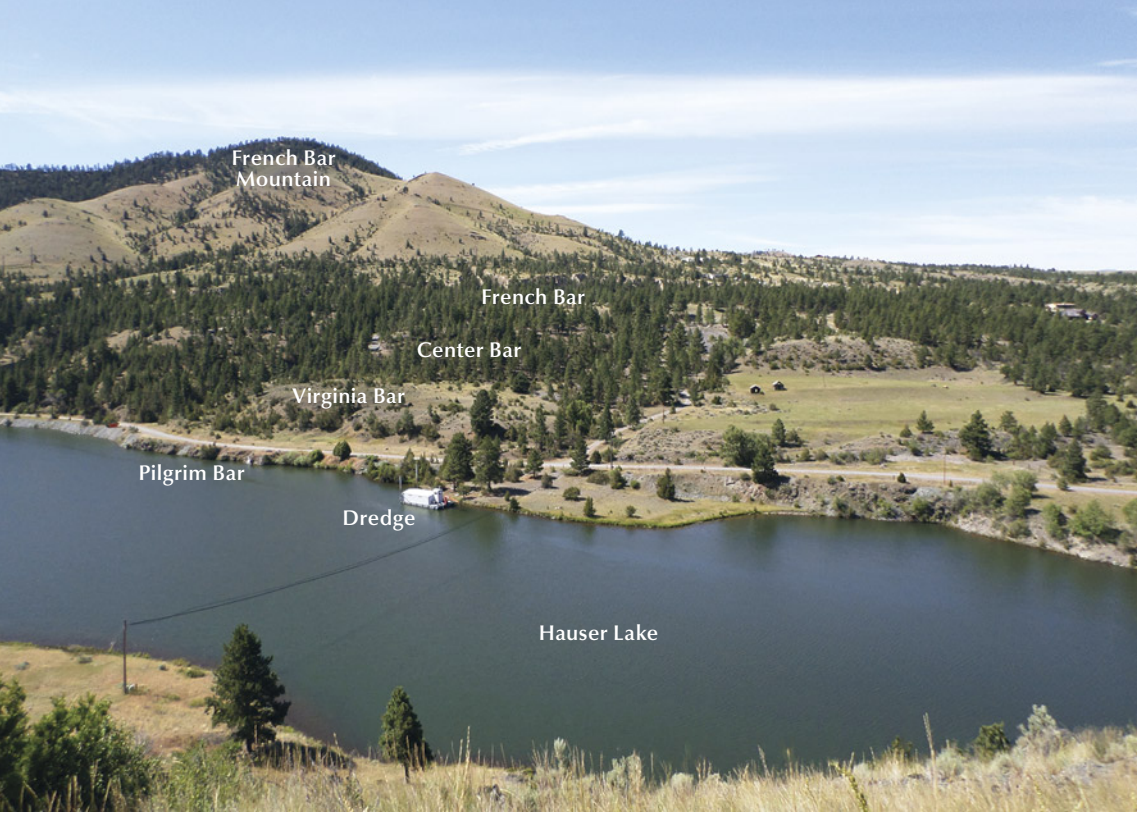

Figure 3. The view southwest across Hauser Lake from Riverside Campground. The French Bar complex starts underwater in Hauser Lake and continues steeply uphill southwest to the historic 1867–1869 hydraulic gold mining area, known as French Bar. The sapphire-bearing French Bar sill is poorly exposed and lies partially on Virginia Bar and Center Bar. Photo by Richard B. Berg; courtesy of the Montana Bureau of Mines and Geology.

we recognize it as a basaltic trachyandesite (Berg and Palke, 2016; Berg, 2018), which is a rock with a composition between trachyte and andesite.

In 1906, Pratt offered a very good description of the French Bar sill based upon his own visit to the Montana deposit as well as Kunz's work. Pratt described two occurrences of corundum-bearing dikes of andesite (the one he visited at French Bar and the one Kunz described as a sapphire-in-andesite occurrence, known as "Ruby Bar"). He concluded that "it is possible that the bar described by Kunz is the same one known as French Bar." Clabaugh (1952) agreed with these sentiments.

Over the last 135 years, the literature has included conflicting reports about the number of different locations of sapphire-bearing dikes along the Missouri River. Many writers identified two different ones, and Mertie et al. (1951) mentioned three localities. The current authors' exploration of the area, as well as Berg and Landry's (2018) historical analysis, suggest that there is likely only one sapphire-bearing area of the sill on the southern side of the Missouri River.

Among miners and geologists and in the literature, this area is often referred to collectively as French Bar. However, Raymond (1870) noted that at the lower portion of French Bar Mountain are four terraces or plateaus (today's vernacular calls them "bars" because they are gravel bars, or more precisely "strath terraces"), one adjacent to another. Pilgrim Bar begins at the river (today it is partially submerged under Hauser Lake) and continues uphill through Virginia Bar, followed by Center Bar, and then the largest area, French Bar, at the top (figure 3). The approximate elevations are: Pilgrim Bar at 1,121 m; Virginia Bar at 1,122 m; Center Bar at 1,144 m; and French Bar at 1,168 m.

According to Pardee and Schrader (1933), the strath terrace known as "French Bar" was the richest and most extensively mined of the river terraces among the various gold fields of the Missouri River near Helena during the 1860s (figure 4). The French Bar hydraulic mining pits were collectively more than 1.60 km in length and ranged from 15 to 123 m wide, totaling around 125 square meters (150,000 square yards). They were estimated to have yielded $10 of gold per yard, for a total of $1.5 million (Lyden, 1948)—a considerable sum of money for 1933.

Pardee and Schrader (1933), as well as the various subsequent authors writing about French Bar (e.g., Kunz, 1897; Pratt, 1906; and Clabaugh, 1952) did not mention sapphires being found among the extensive dredging of French Bar from 1867 to 1869. It is possible that the French Bar hydraulic gold miners did recover small amounts of secondary sapphires and, like other gold miners along the Missouri River, discarded them due to lack of interest.

Kunz (1893) reported "…no doubt that all of the sapphire along these bars of the Missouri is derived from the breaking down, by glacial action, of a rock similar to this. The outcrop at the Ruby Bar cannot, however, account for the deposit of sapphires at Eldorado Bar, 6 miles to the north; and it will be necessary

Figure 4. Hydraulic mining of gold from 1867 to 1869 at French Bar proved it the richest and most extensively mined of the river terraces among the Missouri River's gold fields near Helena in the 1860s. Courtesy of the Photographic Archives of the Montana Historical Society, Helena, Montana.

to await further discoveries before attempting to determine the exact source of these gems."

The Spratt brothers obtained an option in late 1889 to purchase Ruby Bar, located on the eastern end of French Bar. In 1890, the Sapphire and Ruby Company of Montana Limited, an English syndicate company partly owned by well-known gem dealer, author, and jeweler Edwin Streeter, entered into a contract to purchase the Ruby Bar (known today as French Bar) and Eldorado Bar properties (Streeter, 1892) (figure 5). The purchased property included nearly all 7,000 acres of the sapphire-bearing property,

Figure 5. Left: A stock certificate of the Sapphire and Ruby Company of Montana Limited. In 1890, Edwin Streeter's English syndicate company purchased nearly all of the 7,000 acres of sapphire-bearing property but never commercially mined it for gold or sapphire. Right: This hand-painted illustration shows Montana sapphire crystals from Streeter's fifth edition of his 1892 book Precious Stones and Gems. *Courtesy of Robert E. Kane.*

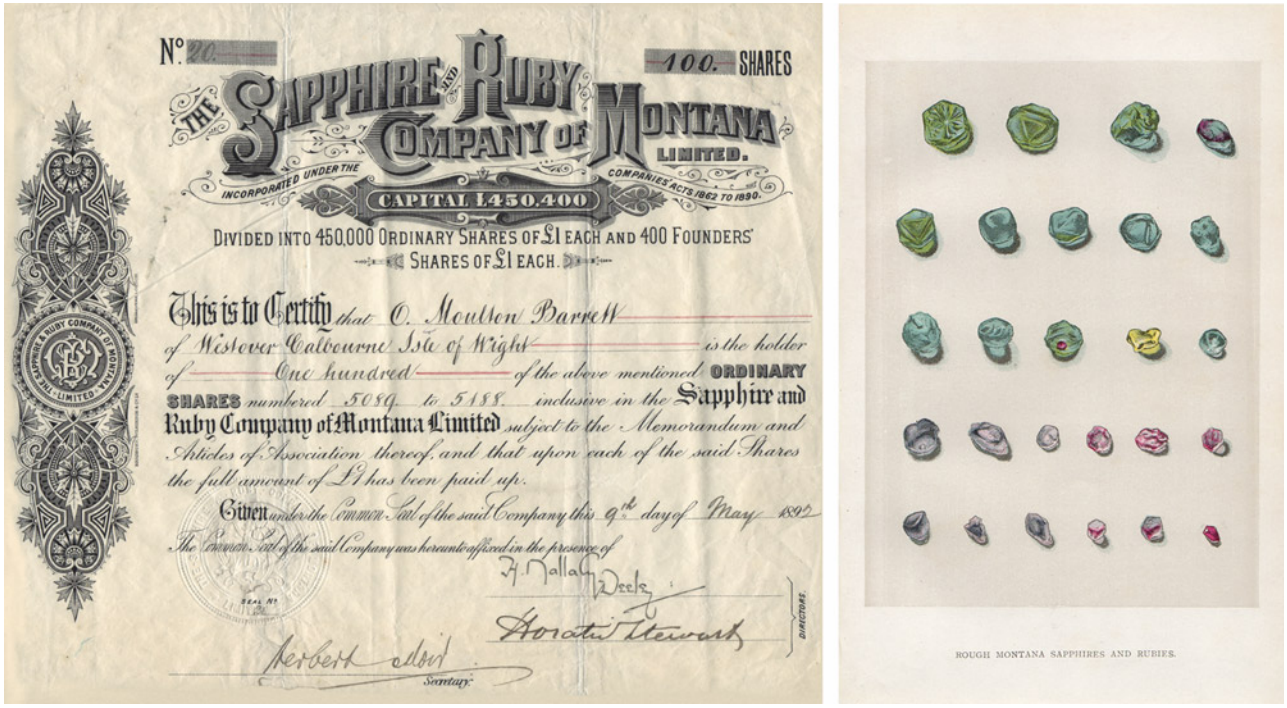

extending along the Missouri River for approximately 24 km. Streeter's company owned French Bar for a short time but never commercially mined it for gold or sapphire. The 1897 ownership liquidation of the properties went back to Augustus N. Spratt and was reorganized as the Montana Gold and Gem Company.

Mertie et al. (1951) stated that Streeter's company "drove several tunnels wherein one or more sapphire-bearing dikes were discovered. These tunnels are now submerged by the water of Hauser Dam, but in one of these dikes, visible at the surface, crystals of sapphire occur sparingly."

In 2025, Crystel Thompson discovered what appears to be a new extension of the French Bar sill across a reservoir portion of the Missouri River (Hauser Lake), located 0.12 km from the shore near the campground in a north-northeast direction. This new area is also across the river and north-northeast of the abovementioned "sapphire-bearing dikes" (now underwater) discovered in the 1890s (Mertie et al., 1951), and approximately 0.5 km from the 1891 sill described in this article. This newly discovered sill contains primary sapphires in matrix. Numerous sapphire crystals have been recovered thus far, including one larger than 11 ct that was faceted into a 4.01 ct gem, which exhibits a strong color change from medium blue to blue-violet. In this new area, sapphires in matrix have adhering biotite (phlogopite). Not only do the rocks containing these sapphires visually match the appearance of the basaltic trachyandesite from the other side of the river, but data from the whole rock chemical analyses plotted in a total alkali silica (TAS) diagram (to be published separately) confirm this. Mapping and further research will be necessary to establish whether this is an extension of the sill first mentioned by Kunz in 1891 and discussed throughout this article.

LOCATION AND ACCESS

The primary French Bar sill is located in Lewis and Clark County, 21 km northeast of the Helena airport. It is situated at the eastern end of the seven historical secondary sapphire-bearing gravel bars, which are spread out among the approximately 22 km length between Canyon Ferry Dam and Hauser Dam (figures 6 and 7).

The French Bar complex contains four named bars, or strath terraces: Pilgrim, Virginia, Center, and French, which is the largest and highest. Pilgrim is 0.61 km from Canyon Ferry Dam, beginning underwater in Hauser Lake and continuing steeply uphill southwest to the historic 1867–1869 hydraulic gold mining area named French Bar (again, see figure 3). The sapphire-bearing French Bar sill is currently poorly exposed and lies partially on Center terrace and Virginia terrace. The area is accessible from Helena by car, or by boat directly across the lake from the Riverside Campground and boat launch.

Figure 6. Gem-quality sapphires are recovered from four major areas in Montana. Yogo Gulch is Montana's only primary sapphire deposit other than French Bar, which is located in the small rectangle and shown in detail in figure 7. The other three areas—Missouri River, Dry Cottonwood Creek, and Rock Creek—are all secondary deposits.

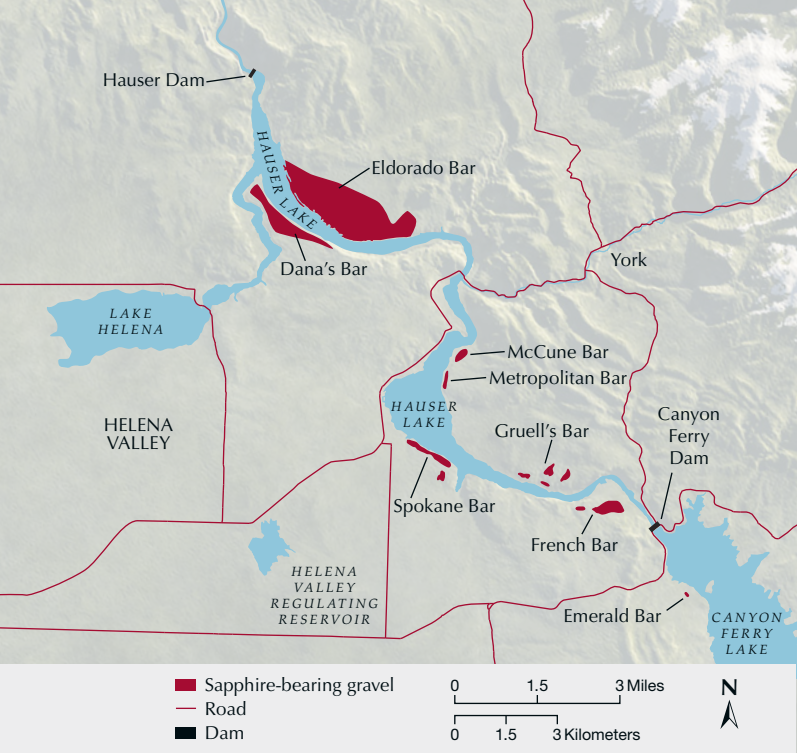

Figure 7. A map of sapphire-bearing gravel bars along Hauser Lake. Much of the sapphire-bearing gravel is on strath terraces along the Missouri River, as well as in the riverbed itself. The primary French Bar sill is at the southeastern end of the seven historical secondary sapphire-bearing gravel bars, which are spread out among the approximately 22 km length between Canyon Ferry Dam and Hauser Dam. Modified by Robert E. Kane from Berg (2015); courtesy of the Montana Bureau of Mines and Geology.

DESCRIPTION OF FRENCH BAR SILL AND SAPPHIRES FOUND *IN SITU*

General Description of the French Bar Sill. The sapphire-bearing French Bar sill (figure 8) is poorly exposed between French Bar and Hauser Lake (partially on Center Bar and Virginia Bar) for a length of less than 98 m and is 1–2 m thick, as reported by Berg and Dahy (2002) and Berg and Landry (2018). Pratt (1906) noted that the compass bearing of a horizontal line within the dike's plane is N 5° to 10° E, and it dips 45° E. This exposure is around 53 m south of the lake's shore.

Sapphires in a primary (hard rock) deposit are more difficult to recover, and fewer are present per cubic meter of earth than in secondary mining. As a result, at this time the deposit is more of a curiosity and lacks the potential to become a profitable and productive sapphire mine. Although the French Bar sill mine could become an important source of Montana sapphire-in-matrix mineral specimens, its greatest value is from a scientific point of view because it provides clues to understanding the genesis of Montana's sapphires.

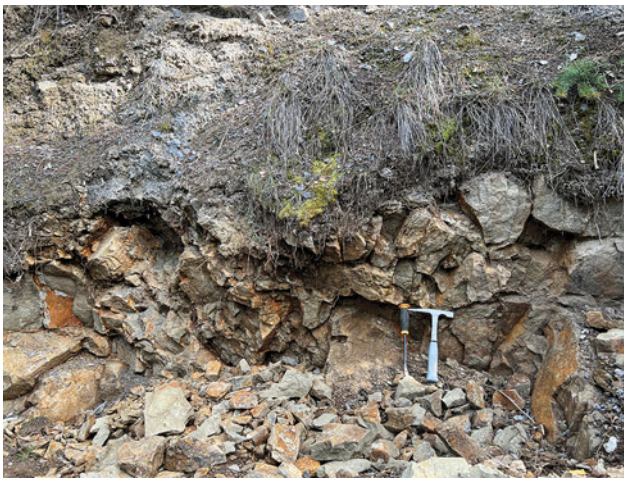

Figure 8. The French Bar sill composed of basaltic trachyandesite, occasionally containing sapphires, is poorly exposed partially on Center Bar and Virginia Bar, for a length of less than 98 m and a thickness of 1–2 m. Only a small portion is visible here. Photo by Robert E. Kane.

General Description of the French Bar Sill Rock. The French Bar sill is composed of sparse biotite (phlogopite)[1] and augite phenocrysts set in a partly altered groundmass of plagioclase microlites and biotite (phlogopite) autoliths as well as apparent volcanic glass (Berg and Palke, 2016). Berg and Dahy (2002) and Berg and Palke (2016) also described xenocrysts of garnet, quartz, and corundum as well as xenoliths composed of calcic plagioclase, amphibole, garnet, margarite, and spinel, occasionally containing corundum. When found, corundum xenocrysts have a rind of biotite (phlogopite) mica and a thin inner layer of clay (Berg and Palke, 2016) (see Mining Techniques section, as well as discussion below).

Previous authors have described the French Bar sill rock as either a basaltic trachyandesite (Berg and Palke, 2016) using the TAS diagram of LeBas et al. (1986) or as an evolved minette, a type of lamprophyre (Irving and Hearn, 2003; Prelević et al., 2004). The distinction between these two classification schemes is that one is based on a petrogenetic classification that estimates the abundance of constituent minerals in the rock (minette), while the other is

[1]As described later in this manuscript, previous works used the name *biotite* for the dark mica found in the French Bar sill and adhering to its sapphires. Using chemical analysis, this work has determined the dark mica to be phlogopite, the magnesium-dominant end member of the biotite group. However, acknowledging the ubiquitous use of *biotite* in related works, the name is used here as well in addition to its proper mineral name, *phlogopite*.

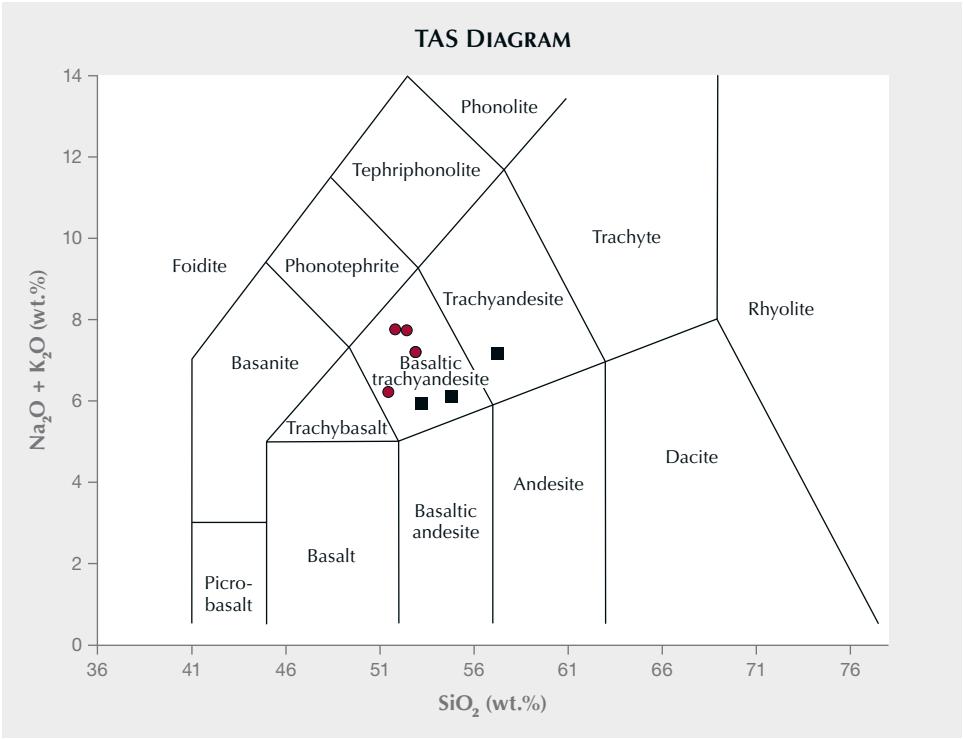

Figure 9. Plot of chemical analyses of volcanic rocks on a total alkali silica (TAS) diagram after LeBas et al. (1986). The dots indicate chemical analyses of four specimens from the French Bar sill (FBS1 through FBS4), which classify the rock as a basaltic trachyandesite. The squares indicate the whole rock geochemistry of sapphire-in-matrix specimens from Serbia, which Prelević et al. (2004) described as a minette (a type of lamprophyre), yet also classified on a TAS diagram as basaltic trachyandesite and trachyandesite.

based on chemical classification (basaltic trachyandesite). In fine-grained rocks in which the abundance of constituent minerals cannot be estimated, a chemical classification based on the TAS compositions is a more suitable naming scheme. Given that the French Bar sill rocks consist of fine-grained mineral textures showing predominantly glass and few phenocrysts, these rocks are better described using the TAS diagram for volcanic rocks, suggesting the appropriate term is *basaltic trachyandesite* (figure 9 and table 1).

Table 1 shows the major element composition of these rocks (a description of the data collection is in the Methods section). The loss on ignition (LOI), which represents the water taken up in the rock or in hydrous minerals, was from 9.29 to 14.75 wt.%. This relatively high LOI indicates that the overall composition may have been altered to some extent

TABLE 1. Major element chemistry (in wt.%) from ICP-OES and ICP-MS of the French Bar sill volcanic rock.

Sample no.	SiO_2	Al_2O_3	Fe_2O_3(T)[a]	MnO	MgO	CaO	Na_2O	K_2O	TiO_2	P_2O_5
FBS1	52.4	17.4	3.9	0.1	3.1	13.8	2.8	4.9	1.0	0.5
FBS2	51.9	17.3	3.9	0.1	3.2	14.2	2.8	5.0	1.0	0.5
FBS3	51.5	17.4	5.6	0.1	4.0	13.5	1.8	4.4	1.1	0.6
FBS4	52.9	16.6	6.5	0.1	4.1	11.1	2.5	4.7	0.9	0.5
Detection limit (wt.%)	0.01	0.01	0.01	0.005	0.01	0.01	0.01	0.01	0.001	0.01

[a]*Total iron oxide as FeO + Fe_2O_3.*

Figure 10. Left: This French Bar sill sapphire-in-matrix specimen was removed using simple hand tools. Right: When hammered, the matrix often breaks along the sapphire edge, with the crystal protruding out of the broken matrix (left, CRK-FBS 045), while the other portion has a concave impression covered in a layer of biotite (phlogopite) over a very thin layer of clay (right, CRK-FBS 046). The sapphire crystal is 9 mm in length. Photos by Jeff Mason.

by weathering at the surface, which is also consistent with the relatively high calcium oxide content, suggesting the possible presence of secondary carbonate minerals. Berg and Palke (2016) came to a similar conclusion.

However, with everything taken into consideration, this discussion becomes somewhat academic. For instance, Prelević et al. (2004) plotted the whole rock geochemistry of a rock classified as a minette on a TAS diagram where it plotted in the basaltic trachyandesite and trachyandesite fields (again, see figure 9). The possible similarity in chemistry between these two rock types indicates that they likely have a similar genetic origin even if they have differences in petrographic textures. Also, Rock (1991) has pointed out that classification of lamprophyres is exceedingly difficult, using the example of the Arrow Peak dike in Montana, wherein the ultramafic rock was classified as five different rock types by five different authors.

MINING TECHNIQUES

Sapphire-in-matrix specimens are collected using simple hand tools, such as rock hammers, pry bars, and chisels. Occasionally a small excavator has been used to remove overburden to widen the exposure of the basaltic trachyandesite hard rock sill. Only a few loose sapphires have been found in the soil surrounding an area where the sill is weathering (breaking apart).

Once a smaller piece of rock has been removed from the sill, liberating the sapphires is done by further breaking down the basaltic trachyandesite matrix with a hammer and chisel. If a sapphire is present in the piece being hammered, the rock often breaks along the sapphire's edge, with the sapphire protruding out in one piece of the broken matrix, leaving the other portion with a concave impression covered in a thicker layer of biotite (phlogopite) crystals over a very thin layer of clay (figure 10). If the piece containing a sapphire will be preserved as a mineral specimen, dental tools and/or a small abrasive air gun are used to neatly remove some of the matrix surrounding the sapphire to create an attractive appearance (figure 11).

Figure 11. A sapphire (8 mm in length) in French Bar sill matrix rock showing a thin biotite (phlogopite) coating (RK-FBS 003). To be preserved as an attractive mineral specimen, enough matrix surrounding the sapphire is removed. Photo by Jeff Mason.

Traditionally used for medical imaging, X-ray computed microtomography is now widely used on geological and gemological material, for example, identifying some natural and cultured pearls. Korbin and Peterson (2018) used an X-ray computed tomography (CT) scan to reveal previously hidden Yogo Gulch sapphires entirely within the lamprophyre rock matrix. Similarly, in this study, CT was used experimentally on several French Bar sill matrix samples to identify the presence of sapphire crystals inside the rock.

All of the remaining pieces of basaltic trachyandesite matrix without visible sapphires at the surface undergo a tumbling process in which they are put into a cement mixer with a small amount of water. After a few days, the matrix is nearly all broken down, leaving a surprising number of sapphires.

THE PRIMARY FRENCH BAR SILL AND POSSIBLE BEDROCK SOURCES FOR THE SECONDARY MISSOURI RIVER DEPOSITS

As mentioned above, some early reports described the French Bar intrusive body as a dike, but it is more accurately described as a sill that was emplaced in near-horizontal metasedimentary beds of the Mesoproterozoic Belt Supergroup. The earliest published reference to this sapphire occurrence was by Kunz in 1890. The sill is 1–2 m thick and exposed for a length of 98 m when examined in a shallow excavation made more than 50 years ago. More recent excavation has exposed a greater length of the sill.

Sapphires have been found in only one bedrock occurrence in this area, a small sill at French Bar along Hauser Lake. As mentioned above, however, another area has sapphires *in situ* in rock outcrops. These rocks were recently identified as basaltic trachyandesite. It appears to be a continuation of the French Bar sill across the river, but future research and mapping are necessary. The French Bar sapphire-bearing sill has a low concentration of corundum and is clearly not the source of most of the sapphires in the Hauser Lake deposits. This unique occurrence could provide insight into other bedrock sources of sapphires in the area.

Magma forming the French Bar sill intruded metasedimentary rocks of the Precambrian Belt Supergroup during the Eocene as determined by an argon-argon plateau age of 49.5 ± 0.1 Ma (Irving and Hearn, 2003), which is very close to the age of the Yogo sapphire-bearing dike in central Montana. The sill is poorly exposed near the south shore of Hauser Lake between Virginia Bar and Center Bar, two of the four strath terraces identified at this locality. Although several dikes are exposed on the west slope of French Bar Mountain, sapphires have not been found in any besides the one in this study.

The most direct method of determining the bedrock source for an alluvial sapphire deposit is to identify sapphire in bedrock. Because of sapphire's durability and density, it can be concentrated in alluvium where there is no apparent bedrock source. This is the case for sapphires at the Missouri River, Rock Creek, and Dry Cottonwood Creek deposits, where all of the original volcanic transport rock (i.e., the matrix) has been completely weathered away.

Berg and Landry (2018) stated that the following considerations aid in limiting the possible bedrock sources of sapphires mined along the Missouri River in this area:

1. The majority of the Missouri River sapphires—from Canyon Ferry Dam to Hauser Lake Dam—do not show significant evidence of abrasion, suggesting relatively short river transport.
2. Sapphire occurrences such as McCune Bar, Metropolitan Bar, and Gruell's Bar occur at significantly higher elevations and are restricted to the east side of Hauser Lake.
3. The previous hypothesis that Missouri River sapphires might have formed where intrusive igneous rocks had metamorphosed local aluminous sedimentary rocks is unlikely due to a lack of sapphire occurrences in the Spokane Hills on the east side of Canyon Ferry Lake.
4. The surfaces of approximately 25% of the sapphires from the Missouri River deposits are partially coated with spinel. This implies that the magma that transported these sapphires contained significant magnesium and that the surface-coating spinel formed as a result of the magnesium reacting with the sapphires.

Occasionally sapphire crystals with rounded and smooth surfaces have been found, which is visibly different from the irregular surfaces of typical sapphires from these bars. This may indicate that these sapphires were abraded as they were transported over a long period along the river. This could indicate a possibility that some sapphires in the Missouri River bars came from distant upriver sources. However, the absence of significant sapphire deposits in more distant locales suggests a more local source for the Missouri River sapphires.

MATERIALS AND METHODS

Samples. For this study, 80 matrix specimens, 16 loose sapphire crystals (removed from the matrix), 4 faceted stones, and 5 partly polished loose sapphire crystals were examined. All samples were from the primary French Bar sill. To locate sapphire phenocrysts, 40 kg of French Bar sill rock was sawn (slabbed) and turned into more than 150 glass-backed "thick sections" approximately 100 μm thick. (Thin sections are typically ground and polished to only 30 μm thick.) These petrographic thick sections were used by author RB in his research on the sill and then donated to GIA for inclusion in their research collection. All samples exhibited natural colors and were not heat treated. On a few samples, remnants of adhering dike rock, including biotite (phlogopite), were removed by placing the specimens in hydrofluoric acid for several days. Unless stated otherwise, all instrumental analyses described here were performed at the GIA laboratory in Carlsbad, California. The bulk of the samples were collected by Kale Wetherell during the last four years. Some of the samples were recovered by the authors during on-site exploration at the mine in June 2024. Additional samples came from the collections of authors RK, RB, and RT, as well as Crystel Thompson. All materials studied were given sample identifiers including initials and a number.

Standard Gemological Examination. Routine gemological testing was performed using standard techniques and equipment in Helena, Montana, and at the Montana Bureau of Mines and Geology at Montana Tech of the University of Montana. These included standard gemological instruments used to measure refractive index, birefringence, specific gravity, and pleochroism. Microscopic observation was performed using a GIA/Leica gemological binocular digital microscope, a Dolan-Jenner 150-watt Fiber-Lite, and a Leica M165C microscope.

Photomicrographs. Photomicrographs were taken at both GIA in Carlsbad and AGL. Either a Nikon Eclipse LV100 compound microscope or a Nikon SMZ1500 binocular microscope outfitted with a Nikon DS-Ri2 camera was used for recording images. Differential interference contrast (DIC) images were taken on the LV100. Also used was a Nikon SMZ25 stereo microscope equipped with dual fiber-optic illuminators, darkfield and brightfield illumination, polarizing filters, and a Nikon DS-Ri2 camera.

Whole Rock Geochemistry. Whole rock geochemistry analysis was carried out during this study at Actlabs in Ancaster, Ontario, Canada, using lithium metaborate/tetraborate fusion and inductively coupled plasma–optical emission spectrometry (ICP-OES) and inductively coupled plasma–mass spectrometry (ICP-MS) using 14 prepared USGS- and CANMET-certified reference materials. Details of this analysis can be found under the 4B and 4B2-STD sections: https://actlabs.com/geochemistry/lithogeochemistry-and-whole-rock-analysis/lithogeochemistry/. The processed data from this work is presented in table 1 and is plotted in a TAS diagram in figure 9.

Ultraviolet/Visible/Near-Infrared (UV-Vis-NIR) Spectroscopy. Non-polarized spectra were collected with a GIA UV-Vis-NIR spectrometer, constructed from an AvaSphere-50 integrating sphere, an AvaLight-DS deuterium light source, and a QE Pro high-performance spectrometer. Polarized UV-Vis-NIR spectra were collected at American Gemological Laboratories (AGL) in New York, with a Perkin-Elmer Lambda 950 spectrophotometer.

Fourier-Transform Infrared (FTIR) Spectroscopy. FTIR spectra were collected at GIA in Carlsbad and AGL using a Thermo Fisher Nicolet 6700 FTIR spectrometer equipped with an XT-KBr beam splitter and a mercury-cadmium-telluride (MCT) detector operating with a 4× beam condenser accessory. The resolution for this data collection was set at 4 cm^{-1} with 1.928 cm^{-1} data spacing.

Raman Spectroscopy. Inclusions were identified, when possible, using Raman spectroscopy at AGL with a Renishaw InVia RM1000 micro-Raman spectrometer equipped with 514 nm argon-ion laser excitation. In many cases, the confocal capabilities of the Raman system allowed inclusions beneath the surface to be analyzed.

Laser Ablation–Inductively Coupled Plasma–Mass Spectrometry (LA-ICP-MS). Trace element chemistry was collected by LA-ICP-MS using a Thermo Fisher iCAP Qc ICP-MS, coupled to an Elemental Scientific Lasers NWR 213 laser ablation system with a frequency-quintupled Nd:YAG laser (213 nm wavelength with 4 ns pulse width). Ablation was carried out with 55 μm spot sizes, with a fluence of 8–10 J/cm^2 and a repetition rate of 20 Hz. The isotope ^{27}Al was used as an internal standard at 529250 ppmw, and synthetic and natural corundum reference materials

were used as external standards (Stone-Sundberg et al., 2017). Detection limits ranged from 0.02 to 0.06 ppma for magnesium, 0.05 to 0.27 ppma for titanium, 0.005 to 0.006 ppma for vanadium, 0.09 to 0.34 ppma for chromium, 1.2 to 14 ppma for iron, and 0.003 to 0.004 ppma for gallium. Trace element values are reported here in parts per million on an atomic basis rather than the more typical parts per million by weight basis used for trace elements in many geochemical studies. Units of ppma are the standard used in GIA laboratories for corundum, as they allow a simpler analysis of crystal chemical properties and an understanding of the color mechanisms of sapphire and ruby. Conversion factors were determined by a simple formula that can be found in table 1 of Emmett et al. (2003).

Petrographic, Scanning Electron Microscopy (SEM), and Energy Dispersive Spectroscopy (EDS) Analyses. The prepared thick sections were studied with a binocular petrographic microscope by author RB at the Montana Bureau of Mines and Geology at Montana Tech of the University of Montana. Some SEM images were recorded using a JEOL 6100 scanning electron microscope in the Image and Chemical Analysis Laboratory in the Department of Physics at Montana State University. Most specimens were coated with gold-palladium and a few with iridium. Other SEM work including backscattered electron (BSE) imaging and chemical measurements by EDS were carried out with 15 kV accelerating voltage on a Zeiss EVO MA10 scanning electron microscope equipped with an Oxford X-Max^N EDS detector. BSE images were stitched together using the method described by Preibisch et al. (2009).

Photoluminescence (PL) Mapping. Photoluminescence maps of Cr^{3+} fluorescence of the sapphires were collected on a Thermo Scientific DXRxi Raman imaging microscope with a 633 nm laser excitation wavelength. Count times varied from 0.033 to 0.167 s exposure time and 0.1 to 1.5 mW power. The PL maps display changes in the area of the ~694 nm PL band to reveal growth zoning patterns related to differences in chromium concentrations throughout the table of each faceted sapphire's surface. This is displayed as a false-color image showing maximum peak areas in red and minimum in blue.

Oxygen Isotope Analysis. Oxygen isotope ratios were collected from sapphires on a CAMECA IMS 1280 secondary ion mass spectrometer (SIMS) in the WiscSIMS lab at the University of Wisconsin–Madison. The sapphires from which data are reported in this study were extracted from five French Bar sill matrix samples (collected on-site by authors RT and RB in 2019) by dissolution with hydrofluoric acid and were then mounted into an epoxy puck for analysis by SIMS. Only four of the five matrix samples contained sapphires. One rock contained four of the tested sapphire crystals (samples 19FB1-1-1, 19FB1-1-2, 19FB1-1-3, and 19FB1-1-4), and the other three rocks contained one crystal each (samples 19FB1-2-1, 19FB1-3-1, and 19FB1-5-1). All samples were mounted in epoxy. Details of oxygen isotope methodology are provided in Turnier et al. (2024).

GEMOLOGICAL CHARACTERISTICS OF FRENCH BAR SILL PRIMARY SAPPHIRE

Standard Gemological Properties. In general, all gem sapphires from different geological deposits share the same or overlapping values (depending upon color and trace element chemistry) for specific gravity, refractive index and birefringence, exposure to long-wave and short-wave ultraviolet radiation, and pleochroism, and thus do not have significant differences. The French Bar sill sapphires were verified to have measured values and reactions that were standard for sapphire. However, trace element chemistry and the full inclusion suite (including color zoning) can often distinguish secondary Montana sapphires—and French Bar sill sapphires—from those produced in other areas around the world. While groups (lots) of rough crystals from the three Montana secondary deposits can often be distinguished from one another based on their surface features, once they are faceted, they often cannot be reliably differentiated.

Based on examinations of the inclusions, spectra (UV-Vis-NIR and FTIR), trace element chemistry, and oxygen isotope analysis of French Bar sill sapphires—as discussed in the following sections—the characteristics of these sapphires overlap to a large extent with the secondary sapphires at the Missouri River, Rock Creek, and Dry Cottonwood Creek deposits. The main distinctions are the presence of biotite (phlogopite) rims around the French Bar sill sapphires in matrix and the absence of biotite (phlogopite) rims on alluvial Missouri River sapphires. Given that biotite (phlogopite) weathers easily in an alluvial setting, it is possible that any biotite (phlogopite) present was removed during weathering.

Inclusions/Microscopic Observation. Four of the French Bar sill sapphires were faceted, and five other pieces of rough were polished to add one large flat facet (window), allowing their inclusions to be observed. As with sapphire from many deposits around the world—including Montana's secondary sapphire deposits—rutile was the most common mineral inclusion in the French Bar sill sapphires. Small flakes and "dust" (minute particles) of exsolved rutile arranged in straight, angular, and hexagonal bands were seen under the microscope as a fiber-optic light tube was moved in various directions around the stationary stone. Occasionally, straight short needles were encountered. These epigenetic exsolutions of fine rutile formations extended in three directions following the three-fold symmetry of corundum, as well as in hexagonal banded patterns following the crystal habit of corundum (figure 12A). In addition, primary protogenetic orange-brown crystals of rutile were identified with micro-Raman spectra (figure 12B).

The second most common inclusion scenes observed in the French Bar sill sapphires were linear tubelike structures oriented in intersecting rhombohedral twin planes (or twin lamellae) following the positive rhombohedral crystal face *r* (1011) in three directions with angles of 90° (figure 12, C and D). They were often numerous and parallel to one another. These coarse tubelike inclusions are often referred to as "intersection tubules" or more recently "Rose channels" (e.g., Notari et al., 2018), named after Gustav Rose, who first discovered them in calcite in 1868 (Rose, 1868). Rose channels in ruby and sapphire have been referred to in the past as "boehmite needles" and are encountered in corundum from most sources around the world (Hughes et al., 2017). In different stones, whether from French Bar sill or other geographic locations, these coarse needlelike inclusions extended in one, two, or three directions, following the directions of twinning.

Thin film–type inclusions oriented along the basal growth planes were also a very common feature.

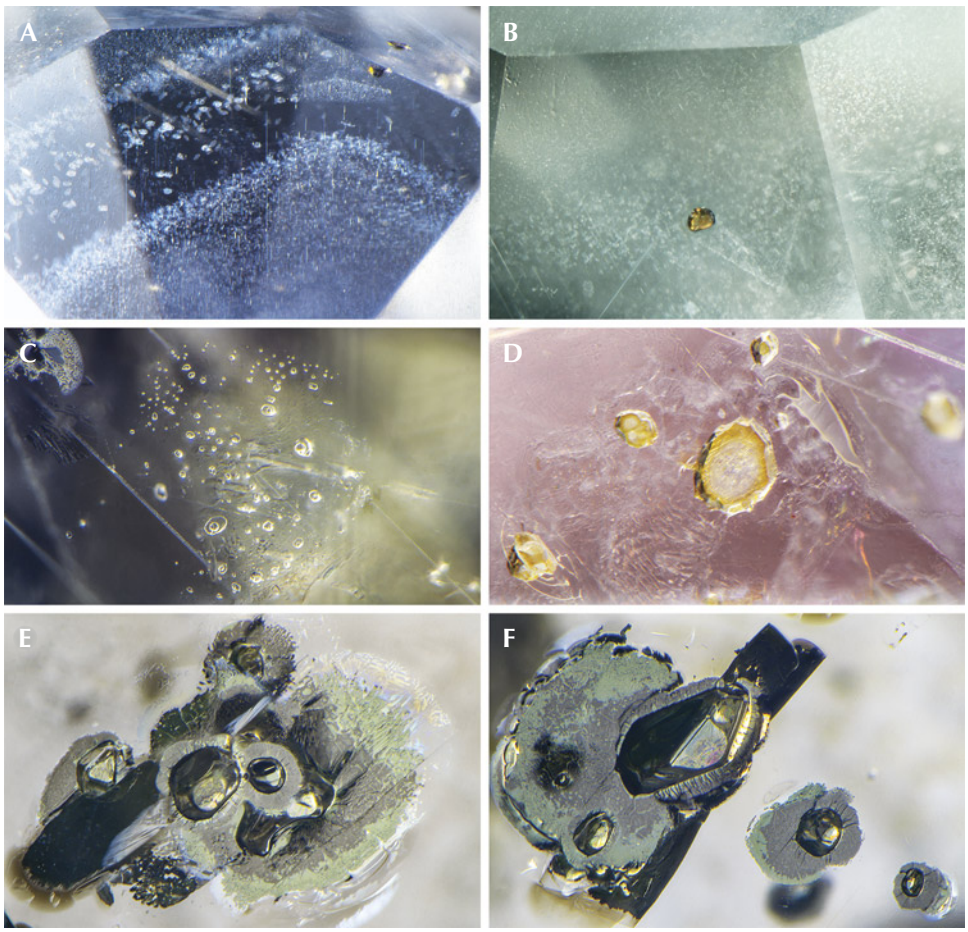

Figure 12. Inclusion scenes in French Bar sill sapphires. A: Angular to hexagonal bands of fine to elongate exsolved rutile silk and particulate platelets, as well as larger rutile crystals (RK-FBS 030). B: Primary protogenetic orange-brown rutile crystal (RK-FBS 051). C: Glassy silicate melt inclusions, natural melty fingerprints, and Rose channels (RK-FBS 030). D: Glassy silicate melt inclusions with partial decrepitation haloes (RK-FBS 030). E and F: Angular metallic included crystals with a black to gold appearance (depending upon lighting), which confocal micro-Raman spectra identified as pyrrhotite (RK-FBS 044). Photomicrographs by Nathan Renfro (A and C–F) and Christopher Smith (B); fields of view 2.07 mm (A), 1.21 mm (B), 1.23 mm (C), 1.31 mm (D), 2.13 mm (E), and 1.93 mm (F).

These were frequently associated with fine, tabular two-phase negative crystals containing a gas phase and amorphous melt (figure 12C). Such silicate melt inclusions were initially trapped as the corundum formed and were later quenched to a glassy state with a contraction bubble during the eruptive event that brought the stones to the surface with subsequent cooling (e.g., Gübelin and Koivula, 1986; Palke et al., 2017).

A 5.81 ct sapphire crystal was removed from a very large piece of French Bar sill basaltic trachyandesite matrix. After grinding and polishing a 14.5 mm long window on this sapphire, more than three dozen angular metallic included crystals with a black appearance were revealed (figure 12, E and F). This specimen was easily moved across a table with a strong 1-inch NdFeB, grade N52 rare earth element magnet. In addition, the characteristic highly metallic luster, hexagonal habit to irregular masses, and black color led GIA's analytical microscopist, John Koivula, to identify these inclusions as pyrrhotite, an iron sulfide mineral. Confocal micro-Raman spectra also identified pyrrhotite in these inclusions. However, Palke et al. (2023) identified multiple different sulfide minerals in these sulfide inclusions and interpreted them as sulfide melt inclusions rather than single sulfide mineral inclusions. These inclusions in other Montana sapphires, then, are similar to the glassy melt inclusions described above in that some sulfide melt must have been present when the sapphires were growing, which was trapped as a sulfide melt inclusion as the sapphire grew around the melt (also see Palke, 2022).

Other mineral inclusions identified by FTIR consisted of small translucent white to yellow calcite crystals, which were occasionally associated with the thin film–type features (figure 12D). Also frequently encountered were open fissures containing a yellowish epigenetic staining (typically kaolinite), as well as epigenetic mineralizations such as aluminum hydroxide or weathering minerals that filled cracks well after the sapphire crystals formed.

Spectroscopy. Non-polarized UV-Vis-NIR spectroscopy on the loose French Bar sill sapphire crystals showed absorption features typical of higher-iron-bearing metamorphic sapphires. These features were consistent with those seen in the secondary Montana sapphires (e.g., Palke et al., 2023). The spectra displayed prominent peaks in the ultraviolet region at 375 and 387 nm, as well as in the visible region with a dominant structure consisting of three bands, with

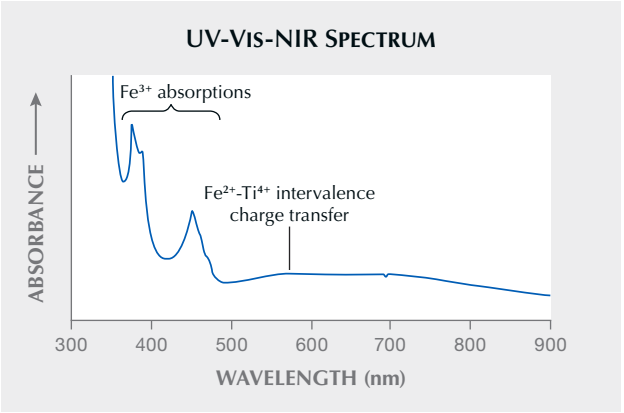

Figure 13. Representative non-polarized UV-Vis-NIR spectrum of a loose French Bar sill sapphire (RK-FBS 037). Dominant features include Fe^{3+}-related absorption bands at 378, 388, and 450 nm.

the maxima positioned at approximately 450 nm, accompanied by two side bands at approximately 460 and 470 nm, all of which are related to Fe^{3+} (figure 13). Additionally, the sapphires in this study exhibiting a subtle blue to green hue also revealed weaker, broader bands related to the Fe^{2+}-Ti^{4+} intervalence charge transfer. When a polarized spectrum was taken, these broader bands had maxima positioned at approximately 580 nm along the ordinary ray (o-ray) and 700 nm along the extraordinary ray (e-ray), while in non-polarized spectra, these two bands merged to form a larger, broader region of absorption. For those with a pink color component, Cr^{3+}-related bands were revealed consisting of a sharp peak at approximately 694 nm, as well as two broader bands centered at roughly 400 and 560 nm.

FTIR spectra of many of the rough sapphires showed mineral peaks related to calcite, gibbsite, and possibly other unidentified mineral phases, probably due to weathering. These minerals are likely only on the sapphires' surfaces and not representative of their inclusions. Therefore, the four faceted stones studied here (RK-FBS 030 and RK-FBS 051 through RK-FBS 053) are the most useful for characterizing the FTIR spectra that may be encountered in faceted stones from this locale, where there would be no chance of surface contamination. In these samples, a small, asymmetrical compound band structure was recorded consisting of at least three bands, with the maxima typically positioned at approximately 3220 cm^{-1}. The nature of this band structure is not fully understood; however, it is consistent with sapphires from other Montana sources (e.g., Palke et al.,

TABLE 2. LA-ICP-MS trace element chemistry analysis (in ppma) of French Bar sill sapphires studied.[a]

Sample no.	Color	Mg	Ti	V	Cr	Fe	Ga
APRT-FBS1	Greenish blue	27.90	3.4	1.21	4.8	1126	15.12
APRT-FBS4	Greenish yellow	24.33	6.2	1.56	6.4	1405	13.57
APRT-FBS5	Greenish yellow	26.01	7.1	1.57	5.8	1377	13.95
APRT-FBS7	Greenish blue	44.30	10.3	2.68	7.3	1249	12.93
RK-FBS 001	Green	26.46	17.5	3.91	0.7	2206	15.43
RK-FBS 005	Green-blue	22.54	15.8	3.31	9.0	1144	15.40
RK-FBS 006	Blue-green	15.05	9.5	3.56	1.0	1369	18.17
RK-FBS 007	Grayish blue	22.57	15.6	4.34	15.7	691	13.40
RK-FBS 008	Gray-green	17.37	13.3	2.03	12.5	811	12.74
RK-FBS 012	Greenish yellow	41.08	10.1	1.39	18.8	1727	13.62
RK-FBS 019	Grayish green	21.20	10.8	2.32	16.4	1409	12.34
RK-FBS 028	Brownish pink	14.71	10.9	0.54	59.3	791	10.14
RK-FBS 029	Brownish pink	23.35	17.3	0.59	52.6	819	10.56
RK-FBS 030	Bluish green to pinkish purple (color change)	17.12	15.8	3.36	49.8	1835	14.20
RK-FBS 031	Green-gray to purple-pink (color change)	42.51	39.9	4.07	57.9	2086	15.64
RK-FBS 034	Green-blue	25.56	21.6	2.37	4.8	1459	11.29
RK-FBS 035	Bluish green	24.58	16.6	4.04	26.4	2059	16.42
RK-FBS 036	Blue	40.78	38.9	8.10	26.0	2286	15.52
RK-FBS 037	Bluish green	22.74	17.7	3.70	3.1	2199	14.80
RK-FBS 038	Grayish green	11.24	6.5	1.30	5.0	847	11.23
RK-FBS 039	Green-gray to brownish pink (color change)	12.98	13.5	4.54	38.5	1308	12.24
RK-FBS 040	Greenish blue to bluish purple (color change)	19.21	18.3	6.14	15.9	1625	13.32
RK-FBS 041	Greenish blue	18.85	10.1	2.26	10.7	1467	15.03
RK-FBS 042	Greenish blue	37.59	34.5	4.20	1.9	1391	14.94
RK-FBS 043	Grayish green	19.67	15.3	2.19	18.8	1282	11.87
Detection limit (ppma)		0.02–0.06	0.05–0.27	0.005–0.006	0.09–0.34	1.2–14	0.003–0.004

[a]*Data from 25 French Bar sill sapphires with 1–3 spots per sample presented as averages, 66 spots total.*

2023). Inclusions of calcite were also identified with FTIR in one sample (RK-FBS 030), while phyllosilicate minerals such as various micas and clay minerals, including kaolinite, were also recorded in the FTIR spectra of the other three faceted stones.

LA-ICP-MS Trace Element Chemistry. The trace element chemistry of the French Bar sill sapphires is summarized in table 2. Sapphires partially embedded in matrix pieces that measured less than 10 × 10 cm wide and 4 cm thick fit into the sample compartment.

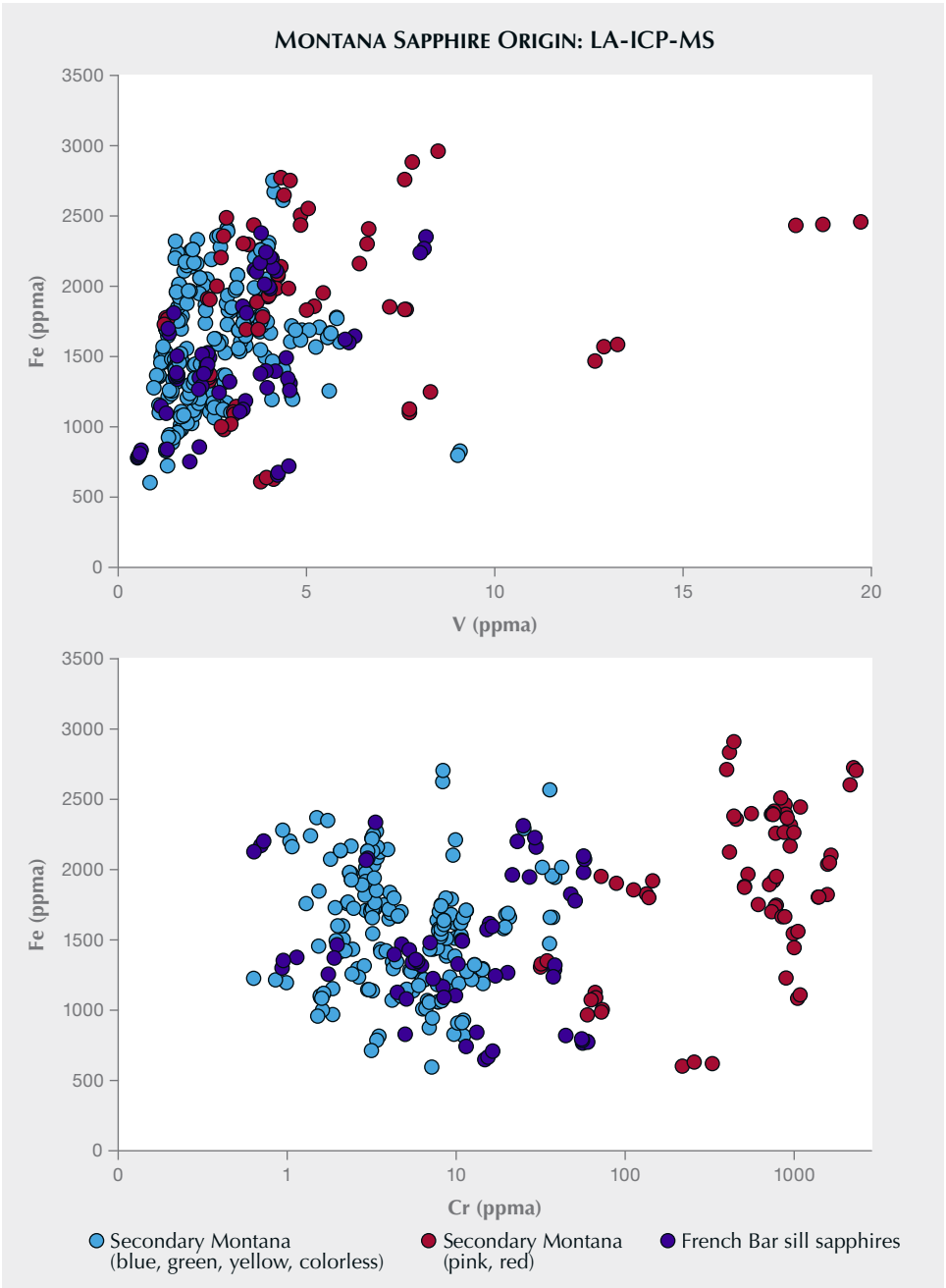

Figure 14. Plots of iron vs. vanadium and iron vs. chromium of primary French Bar sill sapphires compared to secondary Montana sapphires from Rock Creek, Dry Cottonwood Creek, and Missouri River. The LA-ICP-MS trace element chemistry generally overlaps.

LA-ICP-MS trace element chemistry was analyzed on 11 *in situ* sapphire crystals and on 14 sapphires removed from the French Bar sill basaltic trachyandesite (1 faceted and 13 rough crystals). Their trace element profiles were consistent overall with those reported for secondary Montana sapphires by Palke et al. (2023). This was confirmed by plotting the chemistry of the French Bar sill sapphires, such as the iron versus vanadium and the iron versus chromium plots shown in figure 14 displaying essentially complete overlap with the secondary Montana sapphires. Full results of the French Bar sill sapphire trace element chemistry are provided as supplementary material in table S1 (https://www.gia.edu/gems-gemology/winter-2025-sapphire-from-french-bar-sill).

Photoluminescence Mapping. Photoluminescence maps of Cr^{3+} in French Bar sill sapphires indicate some samples are zoned in their chromium and likely other trace element concentrations (figure 15, left). The general pattern is similar to that seen in many Missouri River alluvial sapphires with hexagonal

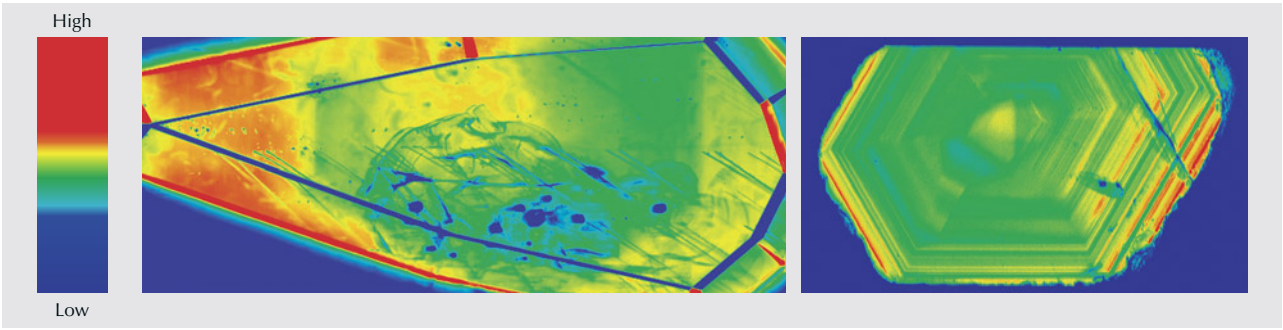

Figure 15. Photoluminescence (PL) false-color maps displaying changes in the area of the ~694 nm PL band revealed growth zoning patterns in sapphires related to differences in chromium concentrations with maximum peak areas in red and minimum in blue. Complex zoning in a faceted French Bar sill sapphire (RK-FBS 041, left) and a rough Missouri River sapphire (AC325, right) showing distribution of Cr^{3+} luminescence marking the hexagonal growth patterns.

growth patterns displayed in the Cr^{3+} luminescence intensities (figure 15, right).

Oxygen Isotope Analysis. The isotope geochemistry of French Bar sill sapphires ($\delta^{18}O$ = 4.0 to 6.7‰, avg. 4.9‰, 7 crystal samples with 14 analyses) overlaps with that of Missouri River sapphires ($\delta^{18}O$ = 1.7 to 8.1‰, avg. 5.4‰, 38 samples with 76 analyses), suggesting derivation from similar sources (Turnier et al., 2024). Overlapping trace element chemistry from sapphires at the French Bar sill compared to Missouri River, Rock Creek, and Dry Cottonwood Creek (again, see figure 14) supports the possibility of a shared source but differing magmatic transport rocks.

CRYSTAL MORPHOLOGY: BASIC CRYSTAL SHAPE AND SURFACE FEATURES

The general term *secondary deposit* is used to include sapphires recovered from colluvial and eluvial deposits both at Rock Creek and Dry Cottonwood Creek, as well as the alluvial deposits of the Missouri River. Among the three Montana secondary sapphire deposits, the crystals exhibit some similarities and differences in their morphology, falling into three distinct categories.

Sapphires Retaining the Original Crystal Shape. Some of the secondary sapphires exhibit their original growth features before transporting magma incorporation—this includes hexagonal tablets and partly preserved hexagonal crystals (Berg, 2022). A triangular pattern on the basal plane, which is perpendicular to the *c*-axis, is rarely encountered in crystals from all three secondary deposits, as well as those from the primary French Bar sill (figure 16).

Sapphires Exhibiting Resorption Surface Features. Features attributed to resorption found in some of these secondary sapphires are based upon two assumptions. First, no further sapphire growth

Figure 16. This 5.23 ct, 13.7 mm French Bar sill sapphire (RK-FBS 041) still shows the rarely occurring triangular pattern on the basal plane, among significant resorption that occurred during the magmatic transport to the surface (left). The other side of the same crystal shows much adhering biotite (phlogopite), as well as other mineralization (right). Photos by Jeff Mason.

occurred while they were transported by magma. A model presented by Levinson and Cook (1994), which has been universally accepted, relates the formation of gem corundum deposits to subduction zones at depths of about 25–50 km that are later brought to the surface by volcanic magmas. Sapphire (Al_2O_3) is not in chemical equilibrium with magma of these compositions and would be slowly dissolved. Berg and Landry (2018) and other researchers have reported that the source bedrock for the Missouri River sapphires is unknown, whereas French Bar sill sapphires are found in a basaltic trachyandesite matrix rock. Second, it is assumed that during magmatic transport, resorption occurred, resulting in the features observed on the sapphires. The conditions these sapphires were exposed to during their magmatic transport from the mantle, lithosphere, or lower crust are not well understood. Once these sapphire gems were at the surface, weathering released them from the solidified magma.

Berg (2022) speculated that while the magma was at a higher temperature, coarser etching rapidly formed, followed by a slower creation of smoother etching after the magma cooled and resorption proceeded more slowly.

Sapphires with Features Formed by Weathering and Alluvial Action. Small chips on ridges and projections on secondary sapphires are easily visible with low-to-medium gemological magnification but are perhaps best studied by SEM. Most of these tiny chips likely formed when the sapphire crystals were tumbled in the sediment load of the Missouri River rather than in the washing plant, because the crystals were subjected to fluvial action for exponentially longer than they were in the washing plant and jigs. Smooth rounding of the crystals, seen with the unaided eye, is attributed to abrasion during fluvial transport. Of the three secondary deposits, sapphire crystals from the Missouri River's various alluvial deposits are the only sapphires to display a smooth rounded appearance. Sapphires from Rock Creek and Dry Cottonwood Creek show rounding due to resorption.

COLOR AND MORPHOLOGY OF FRENCH BAR SILL SAPPHIRES

French Bar sill sapphires observed thus far by the authors are typically light to medium tones in hues of green, blue-green, blue, green-blue, pink, yellow, and colorless. Some specimens have displayed a color-change phenomenon, shifting from bluish green to pinkish purple (figure 17), while others have exhibited a strong color change from medium blue to blue-violet.

Because the French Bar sill sapphires are still in the volcanic rock that transported them to the surface, they only exhibit original crystal shape and resorption surface features—not features formed by weathering and fluvial transport.

The general appearance of the *in situ* sapphires from the French Bar sill matches those found in a

Figure 17. A strong color change—going from bluish green to pinkish purple—is observed in this 3.49 ct French Bar sill sapphire (RK-FBS 030; also shown in figure 2) with a change from fluorescent (5500 K, left) to incandescent light (2800 K, right). Photos by Jeff Mason.

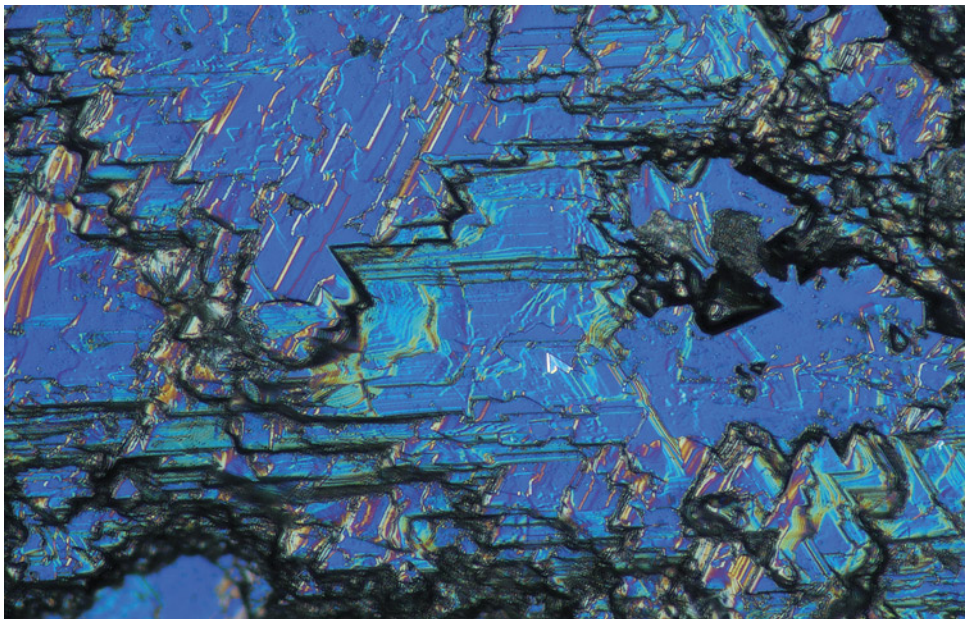

Figure 18. French Bar sill sapphires show a variety of different resorption features, also called etching or dissolution. In this sapphire (RK-FBS 041), differential interference contrast (DIC) photomicrography shows angular geometric patterns reflecting disequilibrium with the carrier magma during its volcanic transport to the surface. Photomicrograph by Aaron Palke; field of view 0.52 mm.

small-to-moderate percentage of sapphires in the alluvial deposits in the bars or strath terraces along the banks of the Missouri River, as well as some of the secondary deposits at Rock Creek and Dry Cottonwood Creek. Rough French Bar sill sapphires range in shape from flat, tabular hexagonal plates to more equant hexagonal prisms, sometimes apparently modified by rhombohedral faces. The French Bar sill sapphires have prominently rounded crystal edges due to resorption.

French Bar sill sapphires display a corroded and rounded appearance on all surfaces, which is particularly prominent on the crystal edges, reflecting disequilibrium with the carrier magma during their volcanic transport to the surface. The angular geometric patterns captured in the DIC photomicrograph in figure 18 suggest etching or dissolution of the sapphire in the host carrier magma. SEM images of the surface of a sapphire from the French Bar sill show this intricate and variable resorption (figure 19); the craters are attributed to resorption of the crystal in the magma that cooled from the sill.

COMPARING FRENCH BAR SILL SAPPHIRES TO SAPPHIRES FROM MONTANA'S SECONDARY DEPOSITS

The colors of the French Bar sill sapphires also occur in sapphires at other localities along the banks of the Missouri River, and at the other two Montana secondary deposits (Rock Creek and Dry Cottonwood Creek).

The sapphire crystals from Montana's secondary deposits, as well as from the French Bar sill, are generally tabular or blocky in shape and can also appear somewhat less commonly as hexagonal prisms. The rough stones from Rock Creek and Dry Cottonwood Creek, as well as the primary French Bar *in situ* crystals, often show a rounded appearance, which might

Figure 19. A: SEM image of sapphire sample S290-1. B and C: Deep resorption features showing flat-bottomed depressions (B) and resorption controlled by crystallography (C). Images by Nancy Equall.

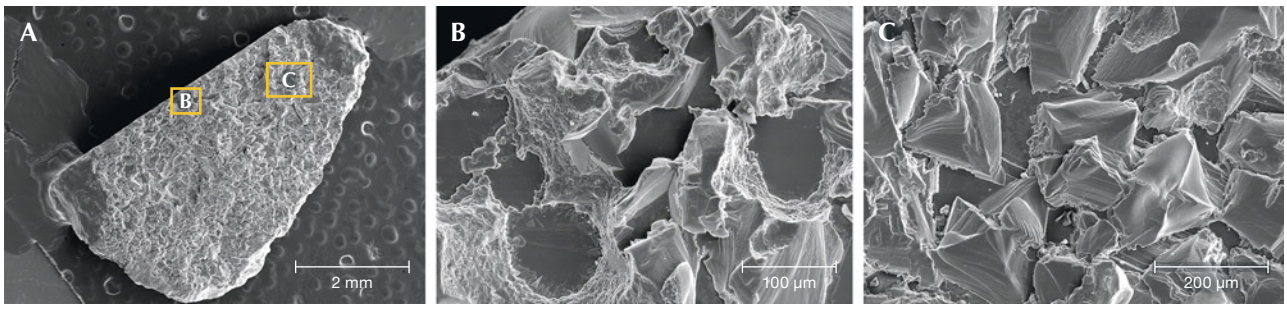

cause one to suspect they were subjected to rounding by abrasion from water transport. This is not the case—nearly all the surface features on secondary Rock Creek and Dry Cottonwood Creek sapphires, as well as primary French Bar sill sapphires, are entirely from resorption (Berg, 2022). Some Missouri River sapphires have rounding due to alluvial transport, but they also all show resorption features.

In fact, the sapphire morphology from the three deposits generally differs enough to allow identification of the origin of large parcels of rough sapphires from either Rock Creek, Dry Cottonwood Creek, and the Missouri River, even if most of the individual rough stones, or mixed parcels, cannot be traced back to their source (Palke et al., 2023). In most cases, a gemologist using only a microscope will *not* be able to distinguish between the various secondary faceted Montana sapphires (Kane, 2020), nor can a sophisticated laboratory using advanced gemological testing, including "chemical fingerprinting" with LA-ICP-MS on rough or cut Montana sapphires (Palke et al., 2023). Only sapphires from Yogo Gulch show a distinct difference in inclusion suites and trace element chemistry (Renfro et al., 2018). Because of the extreme differences in price, color, and chemistry, a few of the major independent laboratories following industry nomenclature norms will call all stones from Yogo Gulch "Yogo sapphires" and sapphires from any of the three secondary deposits simply "Montana sapphires." The inclusions in the French Bar sill sapphires examined thus far—and the trace element chemistry—overlap with those in Montana's secondary sapphires (Palke et al., 2024).

Spinel Coatings on Alluvial Missouri River Sapphires. Remnants of very dark green (almost black) spinel are preserved in depressions on the surfaces of Missouri River sapphires, where they were protected from abrasion during river transport. Spinel has not been found on the surfaces of sapphires from the other Montana secondary deposits (Berg, 2022). Because spinel has not been identified as a mineral inclusion in these sapphires (Berg and Landry, 2018), it is interpreted to have formed by reaction between the sapphire and iron and magnesium in a mafic magma. Spinel-variety hercynite adheres to some of the sapphires from the Yogo deposits (Clabaugh, 1952), where sapphires are mined from a lamprophyre dike. Also, sapphires from a basalt in the Siebengebirge Volcanic Field in Germany have spinel coronas (Baldwin and Ballhaus, 2018).

Spinel has not been identified on sapphires from the Rock Creek district or from Dry Cottonwood Creek, where the transporting magma was inferred to be of rhyolite or dacite composition (Berg, 2007, 2014). Similarly, spinel was not observed on the surfaces of sapphire xenocrysts in the French Bar sill exposed along Hauser Lake, which is a basaltic trachyandesite. However, spinel on sapphires from the Missouri River deposits suggests that these sapphires may have weathered from a mafic igneous bedrock source that has not been recognized.

Biotite (Phlogopite) Coatings on Primary French Bar Sill Sapphires. All of the *in situ* French Bar sill sapphires studied by the authors and others have a dark mineral coating composed mostly of biotite (phlogopite) mica (figures 20 and 21). The existence of this coating is different from that of many of the alluvial Missouri River sapphires, for which around 25% of them are characterized by the presence of a dark-colored spinel encrustation (Berg, 2022; Palke et al., 2024). Raman spectroscopy confirmed the presence of biotite mica in these coatings on the French Bar sill sapphire, and chemical analysis by LA-ICP-MS confirmed them as the magnesium-rich endmember in the biotite group (phlogopite). In the absence of chemical analysis of the mica, previous works described it as biotite. However, biotite is more of a field name for dark mica. When the chemical makeup of dark mica is known, it should be referred to as the dominant mineral species, as the name

Figure 20. Pink sapphires are occasionally seen in French Bar sill basaltic trachyandesite (CRK-FBS 047). This 10 mm long pink sapphire crystal is outlined in easily visible biotite (phlogopite). Photo by Jeff Mason.

Figure 21. This 6 mm long sapphire in French Bar sill basaltic trachyandesite (RK-FBS 061) displays a small amount of easily visible biotite (phlogopite). Photo by Jeff Mason.

biotite is not strictly correct. Nonetheless, in recognition of the use of the name *biotite* in previous works on the French Bar sill, the name has been used here alongside the correct mineral name *phlogopite*. The sapphire xenocrysts always have a rind of biotite (phlogopite) mica and a thin inner layer of clay (Berg and Dahy, 2002; Berg and Palke, 2016). However, careful SEM imaging and chemical mapping show the presence of a second, very iron-rich layer between the biotite (phlogopite) layer and the sapphire (figure 22). The identity of this inner layer is currently unknown, but future work to identify this phase could help explain the dynamics of magmatic sapphire transportation and how the magmas transporting the French Bar sill and alluvial Missouri River sapphires may (or may not be) related.

As Berg and Palke (2016)—and many researchers over the decades, starting with Kunz in 1893—pointed out, the French Bar sill itself is certainly too small in extent to have supplied all the alluvial sapphires found at the Missouri River. More research will be needed to characterize the mineral coatings of the *in situ* French Bar sill sapphires in order to understand the dynamics of magmatic transport of those stones compared to other possible magmatic sources of alluvial Missouri River sapphires.

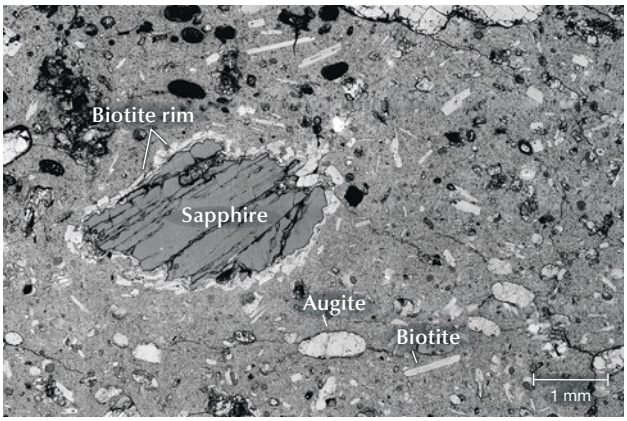

Figure 22. Backscattered electron (BSE) image of a thick section glass slide containing a French Bar sill rock showing a sapphire xenocryst surrounded by a layer of biotite (phlogopite), set in a fine-grained groundmass with sparse phenocrysts of biotite (phlogopite) and possibly augite (SS10A). Image by Henry Towbin.

CONCLUSION

Yogo Gulch is the only well-documented primary occurrence of gem-quality sapphire in Montana, although French Bar—the only other *in situ* deposit of gem-quality sapphire—has been very briefly mentioned in the gemological literature since 1891. Since the initial discovery of sapphires in Montana at Eldorado Bar along the Missouri River in 1865, the geologic source of Montana's secondary sapphires has remained a mystery.

The French Bar sill primary sapphire deposit is fascinating for the gemologist and mineral collector, as well as scientifically interesting for the geoscientist. This small sill at French Bar contains sparse sapphires and is clearly not the source of most of the sapphires in the deposits along Hauser Lake (frequently referred to as the Missouri River deposits). The French Bar sill sapphires studied here will continue to provide clues about possible bedrock sources for the Missouri River deposit.

Microscopic examination of the sapphires from this unique source, by scanning electron imaging and optical microscopy, shows some rare surface morphologies not seen in other Montana sapphires. However, inclusions and trace element chemistry overlap with Missouri River sapphires, as well as with those from Rock Creek and Dry Cottonwood Creek. The ability to obtain more primary sapphires from the French Bar sill has presented a rare opportunity to investigate this sapphire occurrence in greater detail. French Bar sill sapphires in matrix will continue to be of great interest to the gemologist, collector, and scientist.

ABOUT THE AUTHORS

Robert E. Kane is an independent researcher living in Helena, Montana, and is former manager of the GIA identification laboratory in Santa Monica, California, and former director of the Gübelin Gem Lab in Lucerne, Switzerland. Kory L. Pettman is an expert gem cutter in San Antonio, Texas, specializing in Montana sapphire. Dr. Aaron C. Palke is senior manager of colored stone research, Dr. Rachelle B. Turnier is museum manager, and Nathan D. Renfro is senior manager of colored stone identification, at GIA in Carlsbad, California. Dr. Richard Berg is a research geologist emeritus at the Montana Bureau of Mines and Geology at Montana Tech of the University of Montana in Butte. Christopher P. Smith is president and chief gemologist at American Gemological Laboratories (AGL) in New York.

ACKNOWLEDGMENTS

The authors express their gratitude and sincere thanks to Kale and Sharlene Wetherell for supplying the majority of the French Bar sill sapphire and matrix specimens for study, as well as detailed information. Tom Smith, geological engineer, assessed the property and details of the exposed extent of the sill. Crystel Thompson provided French Bar sill sapphire and matrix specimens collected before 2020. The authors are also grateful for thorough reviews by Gaston Giuliani and three anonymous reviewers.

REFERENCES

Baldwin L.C., Ballhaus C. (2018) Experimental investigation of the reaction between corundum xenocrysts and alkaline basalt host magma: Constraints on magma residence times of basalt-hosted sapphires. *Lithos*, Vol. 302-303, pp. 447–454, http://dx.doi.org/10.1016/j.lithos.2018.01.020

Berg R.B. (2007) Sapphires in the Butte-Deer Lodge area, Montana. *Montana Bureau of Mines and Geology Bulletin*, Vol. 134, 62 pp.

——— (2014) Sapphires in the southwestern part of the Rock Creek Sapphire District, Granite County, Montana. *Montana Bureau of Mines and Geology Bulletin*, Vol. 135, 86 pp.

——— (2015) Compilation of reported sapphire occurrences in Montana. *Montana Bureau of Mines and Geology, Report of Investigation 23*, 84 pp.

——— (2018) Magmatic fragmentation of sapphire xenocrysts in a basaltic trachyandesite sill near Helena, Montana. *Geological Society of America Abstracts with Programs*, GSA Annual Meeting, Vol. 50, No. 6, paper no. 110-4, http://dx.doi.org/10.1130/abs/2018AM-316110

——— (2022) Morphology of sapphires from secondary deposits, southwestern Montana. *Montana Bureau of Mines and Geology, Report of Investigation 34*, 45 pp., http://dx.doi.org/10.59691/NOAG5489

Berg R.B., Dahy J.P. (2002) Montana sapphires and speculation on their origin. In P.W. Scott and C.M. Bristow, Eds., *Industrial Minerals and Extractive Industry Geology*. Geological Society, London, pp. 199–204.

Berg R.B., Landry M.T. (2018) Sapphire deposits along the Missouri River near Helena, Montana. *Montana Bureau of Mines and Geology Bulletin*, Vol. 136.

Berg R.B., Palke A.C. (2016) Sapphires from an Eocene sill near Helena, Montana. *Geological Society of America Abstracts with Programs*, GSA Annual Meeting, Vol. 48, No. 7, paper no. 254-3, http://dx.doi.org/10.1130/abs/2016AM-278371

Clabaugh S.E. (1952) *Corundum Deposits of Montana*. U.S. Geological Survey Bulletin 983, Washington, DC.

Daily Independent (1891) Rich in precious stones. Helena, MT, February 6, p. 8.

Emmett J.L., Scarratt K., McClure S.F., Moses T., Douthit T.R., Hughes R., Novak S., Shigley J.E., Wang W., Bordelon O., Kane R.E. (2003) Beryllium diffusion of ruby and sapphire. *G&G*, Vol. 39, No. 2, pp. 84–135, http://dx.doi.org/10.5741/GEMS.39.2.84

Gübelin E.J., Koivula J.I. (1986) *Photoatlas of Inclusions in Gemstones, Volume 1*. ABC Edition, Zurich.

Hughes R., Manorotkul W., Hughes B. (2017) *Ruby & Sapphire: A Gemologist's Guide*. RWH Publishing/Lotus Publishing, Bangkok.

Irving A.J., Hearn B.C. Jr. (2003) Alkalic rocks of Montana: Kimberlites, lamproites, and related magmatic rocks. In B.A. Kjarsgaard, Ed., *Guidebook Prepared for the VIIIth International Kimberlite Conference, Montana Field Trip*, Geological Survey of Canada, Ottawa.

Kane R.E. (2020) America's royal gem: Montana and Yogo sapphires. *InColor*, Vol. 45, pp. 30–39.

Korbin J., Peterson D. (2018) How will X-ray computed tomography impact your future? *The Santa Fe Symposium on Jewelry Manufacturing Technology*, Albuquerque, pp. 309–326.

Kunz G.F. (1890) *Gems and Precious Stones of North America*. Scientific Publishing Company, New York.

——— (1892) The sapphire deposits of the northern Missouri River, near Helena, Montana. *Mineralogical Magazine*, Vol. 9, No. 44, pp. 394–396.

——— (1893) Precious stones (Sapphire). In D.T. Day, Ed., *Mineral Resources of the United States, Calendar Year 1892*, United States Geological Survey, Government Printing Office, Washington, DC, pp. 760–763.

——— (1897) On the sapphires from Montana, with special reference to those from Yogo Gulch in Fergus County. *American Journal of Science*, Vol. 4, pp. 417–420.

LeBas M.J., LeMaitre R.W., Streckeisen A.L., Zanettin B.A. (1986) A chemical classification of volcanic rocks based on the total alkali-silica diagram. *Journal of Petrology*, Vol. 27, No. 3, pp. 745–750, http://dx.doi.org/10.1093/petrology/27.3.745

Levinson A.A., Cook F.A. (1994) Gem corundum in alkali basalt: Origin and occurrence. *G&G*, Vol. 30, No. 4, pp. 253–262.

Lyden C.J. (1948) *The Gold Placers of Montana*. Montana Bureau of Mines and Geology, Memoir No. 26, Butte, Montana.

Mertie J.B., Fischer R.P., Hobbs S.W. (1951) *Geology of the Canyon Ferry Quadrangle, Montana*. Geological Survey Bulletin 972, United States Government Printing Office, Washington, DC.

Notari F., Fritsch E., Caplan C., Hainschwang T. (2018) "Boehmite needles" in corundum are Rose channels. *G&G*, Vol. 54, No. 3, p. 257.

Palke A.C. (2022) Origins of secondary Montana sapphires: Melts, melts, and more melts. GSA Annual Meeting, Denver. *Geological Society of America Abstracts with Programs*. Vol. 54, No. 5, paper no. 225-4, http://dx.doi.org/10.1130/abs/2022AM-383521

Palke A.C., Renfro N.D., Berg R.B. (2017) Melt inclusions in alluvial sapphires from Montana, USA: Formation of sapphires as a restitic component of lower crustal melting? *Lithos*, Vol. 278, pp. 43–53, http://dx.doi.org/10.1016/j.lithos.2017.01.026

Palke A.C., Renfro N.D., Hapeman J.R., Berg R.B. (2023)

Gemological characterization of Montana sapphire from the secondary deposits at Rock Creek, Missouri River, and Dry Cottonwood Creek. *G&G*, Vol. 59, No. 1, pp. 2–45, http://dx.doi.org/10.5741/GEMS.59.1.2
Palke A.C., Kane R.E., Turnier R.B., Berg R.B., Pettman K.L. (2024) Large, gem-quality primary sapphires from the French Bar sill, Montana: Implications for the origins of alluvial Missouri River sapphire. GSA Annual Meeting, Anaheim, California. *Geological Society of America Abstracts with Programs*, Vol. 56, No. 5, paper no. 164-6.
Pardee J.T., Schrader F.C. (1933) *Metalliferous Deposits of the Greater Helena Mining Region Montana*. U.S. Geological Survey Bulletin 842, Washington, DC.
Pratt J.H. (1906) *Corundum and Its Occurrence and Distribution in the United States*. U.S. Geological Survey Bulletin 180, Washington, DC.
Preibisch S., Saalfeld S., Tomancak P. (2009) Globally optimal stitching of tiled 3D microscopic image acquisitions. *Bioinformatics*, Vol. 25, No. 11, pp. 1463–1465, http://dx.doi.org/10.1093/bioinformatics/btp184
Prelević D., Foley S.F., Cvetković V., Romer R.L. (2004) Origin of minette by mixing of lamproite and dacite magmas in Veliki Majdan, Serbia. *Journal of Petrology*, Vol. 45, No. 4, pp. 759–792, http://dx.doi.org/10.1093/petrology/egg109
Raymond R.W. (1872) *Statistics of Mines and Mining in the States and Territories West of the Rocky Mountains*. Government Printing Office, Washington, DC.
Renfro N.D., Palke A.C., Berg R.B. (2018) Gemological characterization of sapphires from Yogo Gulch, Montana. *G&G*, Vol. 54, No. 2, pp. 184–201, http://dx.doi.org/10.5741/GEMS.54.2.184
Rock N.M.S. (1991) *Lamprophyres*. Springer New York NY, http://dx.doi.org/10.1007/978-1-4757-0929-2
Rose G. (1868) Über die im kalkspath vorkommenden hohlen canäle. In *Abhandlungen der Königlichen Akademie der Wissenschaften*, Berlin, pp. 55–82.
Stone-Sundberg J., Thomas T., Sun Z., Guan Y., Cole Z., Equall R., Emmett J.L. (2017) Accurate reporting of key trace elements in ruby and sapphire using matrix-matched standards. *G&G*, Vol. 53, No. 4, pp. 438–451, http://dx.doi.org/10.5741/GEMS.53.4.438
Streeter E.W. (1892) *Precious Stones and Gems: Their History, Sources and Characteristics*. 5th edition, George Bell & Sons, London.
Turnier R.B., Berg R.B., Kitajima K., Palke A.C., Valley J.W. (2024) Petrogenesis of Montana, USA sapphires inferred from oxygen isotopes and zircon inclusions. *Journal of Petrology*, Volume 65, No. 10, article no. egae107, http://dx.doi.org/10.1093/petrology/egae107

Characterization of Emeralds from Zhen'an County in Shaanxi, China

Yi Guo, Xiao-Yan Yu, and Yu-Yu Zheng

In 2017, the first emerald deposit in the Qinling Orogenic Belt was found in Zhen'an County, Shaanxi Province, China. This study presents a comprehensive analysis of the gemological, spectroscopic, and trace element characteristics of a select set of Zhen'an emerald samples based on standard and advanced gemological methods, including gem microscopy, ultraviolet/visible/near-infrared spectroscopy, Fourier-transform infrared spectroscopy, Raman spectroscopy, and laser ablation–inductively coupled plasma–mass spectrometry. Microscopic studies revealed that Zhen'an emerald exhibits longitudinal striations and inclined growth steps on its hexagonal prism faces and contains an abundance of two-phase (gas/liquid) fluid inclusions. A variety of mineral inclusions were identified, including phlogopite, plagioclase, scheelite, calcite, talc, and hematite. Some crystals display color zoning, with a deeper green rim containing elevated vanadium and iron. Zhen'an emerald's dominant chromophore is vanadium, and the material is characterized by a high vanadium concentration, notably low chromium, a moderate iron concentration, and an elevated ratio of gallium to cesium. These unique geochemical signatures of Zhen'an emerald, along with their internal features, could be a robust tool for discerning emerald from this deposit.

Prominent emerald-producing regions in Asia encompass Panjshir in Afghanistan; Swat in Pakistan; Rajasthan in India; Malipo in Yunnan, China; and Davdar in Xinjiang, China, which are within or adjacent to the Himalayan Orogenic Belt (Marshall et al., 2012; Zheng et al., 2019; Guo et al., 2020; Yu et al., 2020; Qin et al., 2022; Chen et al., 2023; Cui et al., 2023). In 2017, emerald was also discovered within the Qinling Orogenic Belt in central China, in Zhen'an County of the Shaanxi Province (Dai et al., 2017, 2018).

Sporadic reports of emerald occurrences in Zhen'an County first emerged in 2017. The emeralds in those reports were primarily found in deep drilling samples. Recent discoveries of emerald outcrops in the area, including those found in 2025, have established Zhen'an as the third emerald deposit in China. The emeralds extracted from local tungsten-beryllium mines in Zhen'an County are sourced from quartz or quartz-calcite veins and are often associated with minerals such as mica, scheelite, and wolframite (Dai et al., 2017, 2018, 2019). The emerald crystals range in color from light bluish green to vivid bluish green, displaying a slight deepening of hue from core to rim, and are characterized by abundant fluid inclusions—particularly two-phase (gas/liquid) fluid inclusions (Dai et al., 2018, 2019; Dong et al., 2023a). Most emeralds are translucent and have many cracks, but a few are transparent and of gem quality (figure 1). The gem-quality crystals typically measure approximately 5 mm. Recently,

In Brief

- Emeralds in Zhen'an are sourced from quartz or quartz-calcite veins within the tungsten deposits in the Qinling Orogenic Belt, Central China.
- Zhen'an emeralds contain a variety of mineral inclusions, including phlogopite, plagioclase, scheelite, and calcite, and abundant two-phase (gas/liquid) fluid inclusions.
- Unique zigzag linear inclusions frequently occur in pairs and are related to structural features formed during crystal growth.
- Vanadium-dominant Zhen'an emeralds have an extremely low ratio of chromium to vanadium and an elevated ratio of gallium to cesium.

See end of article for About the Authors and Acknowledgments.
Gems & Gemology, Vol. 61, No. 4, pp. 354–373,
http://dx.doi.org/10.5741/GEMS.61.4.354

Figure 1. A 32 ct emerald rough (16 × 13 × 21 mm) from Zhen'an County was cut in half, and the bottom half (16 × 13 × 11 mm, 17 ct) was polished along the cut and set in 18K gold. Photos by Kun Hu (left) and Xiao-Yan Yu (right).

emeralds of roughly 20 × 20 mm and 10 × 60 mm have been sporadically discovered.

Emerald is defined as a green variety of beryl colored by chromium and/or vanadium. Vanadium dominates as the primary chromophore in emerald from only a few deposits; notable examples are emeralds from Malipo in Yunnan, China (Hu and Lu, 2019; Zheng et al., 2019); Byrud in Eidsvoll, Norway (Loughrey et al., 2013); and Lened, Canada (Lake et al., 2017). The chromophore composition of Zhen'an emerald is comparable to that of Malipo emerald; in both cases, the vanadium content is significantly higher than the chromium content (Dai et al., 2018; Yu et al., 2021; Dong et al., 2023b). The aluminum within the emerald is octahedral in coordination and is substituted by elements including magnesium, iron, manganese, chromium, and vanadium (Dai et al., 2018).

For this study, 26 emerald samples were collected from Zhen'an County (southern Shaanxi Province, Central China) by authors X-YY and YG as well as local miners and farmers. Surface micromorphology, inclusion characteristics, spectral features, and chemical composition of the samples were systematically measured and analyzed using standard gemological testing, spectroscopic methods, and quantitative analysis. These results were used to elucidate the gemological properties and color mechanism and, crucially, to aid in the geographic origin determination of emeralds from this new deposit.

HISTORY AND GEOLOGY

Emeralds in China have been found in three deposits: Malipo in Yunnan, Davdar in Xinjiang, and Zhen'an in Shaanxi (Marshall et al., 2012; Dai et al., 2017, 2018, 2019; Hu and Lu, 2019; Zheng et al., 2019; Cui et al., 2023; Peng et al., 2023). Zhen'an in Shaanxi represents the most recent discovery among the three and is the sole emerald deposit within the central Qinling Orogenic Belt in China.

Following the discovery in Zhen'an of a beryl and wolframite syngenetic mineral association, Dai (2017, 2018, and 2019) discovered another mineral association of emerald and scheelite in the Hetaoping tungsten-beryllium mine in Zhen'an. Over the past few decades, local villagers have reported the occasional unearthing of green stones resembling beryl, although the true nature of these stones was unknown. In recent years, some villagers and/or miners have kept specimens of beryl mined from nearby tungsten deposits (figure 2).

The Hetaoping tungsten-beryllium deposit, which hosts emeralds, is situated in western Zhen'an

Figure 2. Emerald crystals from a single quartz vein. Left: Emerald from a quartz vein and its country rock phlogopite schist. Right: The quartz vein shown within the white dotted line in the left image, showing the associated minerals (mainly white quartz and calcite). Photos by Yi Guo.

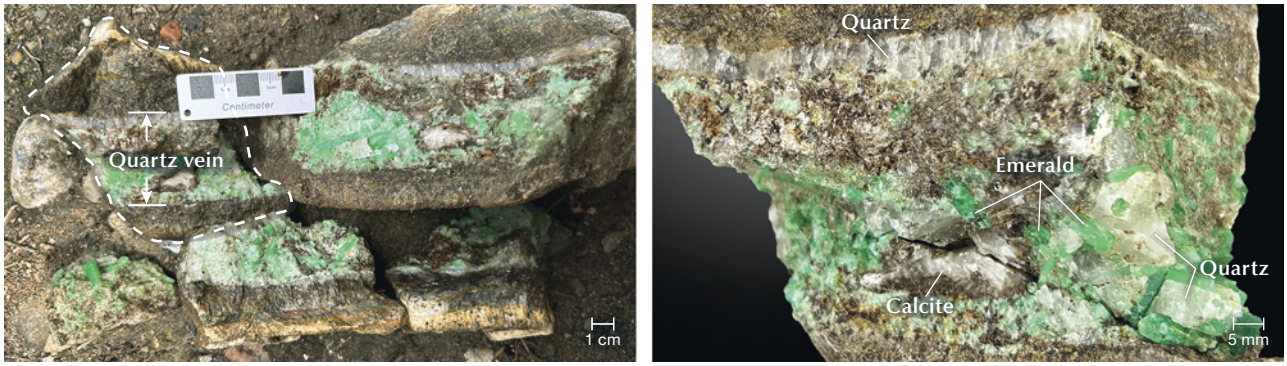

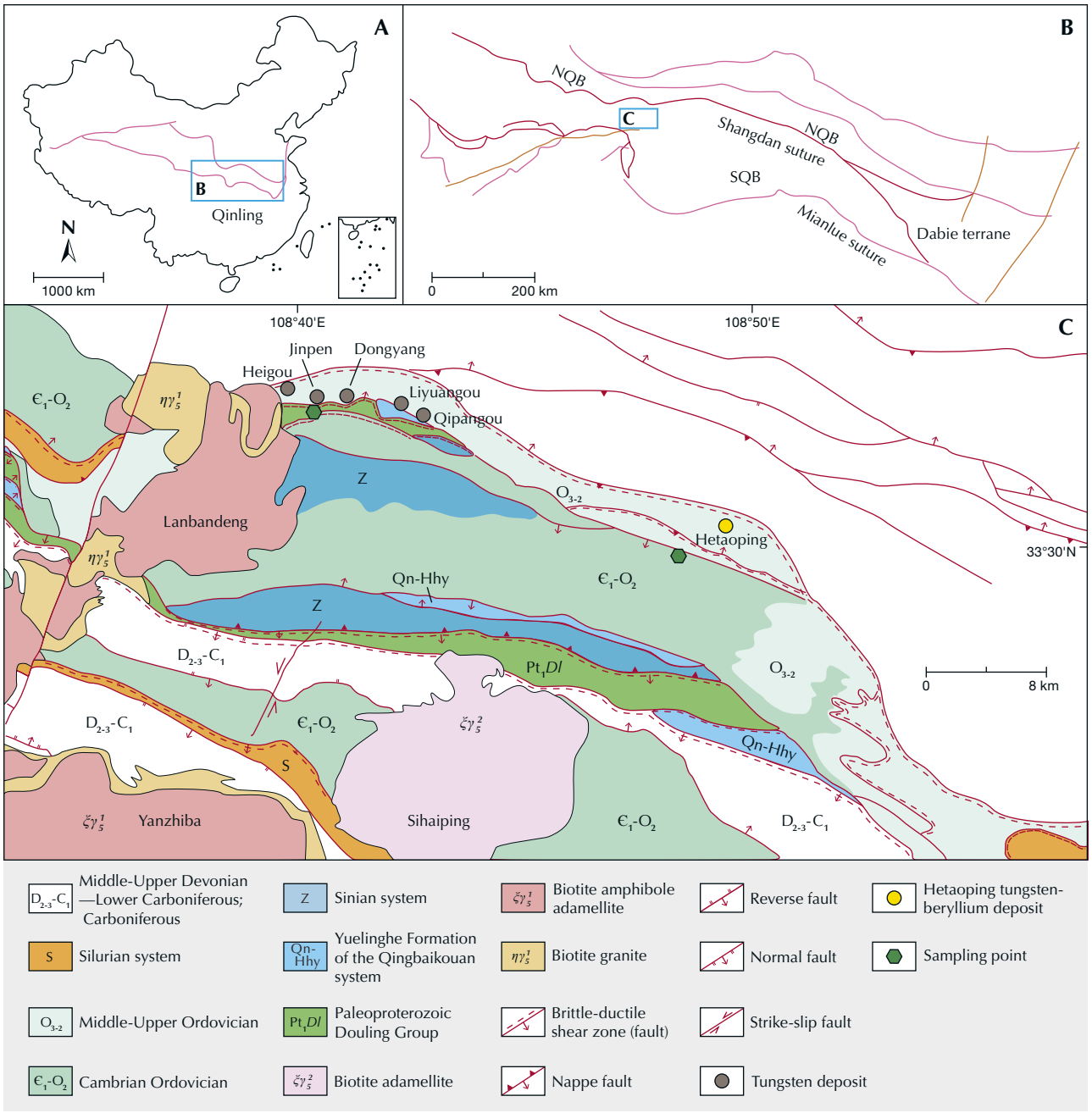

Figure 3. Geotectonic structure of the Qinling Orogenic Belt and regional geology of the Zhen'an area (modified from Dong et al., 2012, and Dai et al., 2019). A: The location of the Qinling Orogenic Belt within China. B: Tectonic divisions of the Qinling Orogenic Belt. C: Emerald mines within Zhen'an.

County. Currently, all the known emerald deposits in Zhen'an County are found within the tungsten mining districts, located tectonically in the South Qinling Belt between the Shangdan and Mianlue suture zones (figure 3). The South Qinling Belt is a significant component of the Qinling Orogenic Belt in central China and belongs to the passive continental margins (Zhang et al., 1997; Xu et al., 2012; Dai et al., 2018, 2019; He et al., 2024; Dai et al., 2024). The outcropping strata in this area predominantly consist of Paleozoic carbonate rocks and Mesozoic magmatic rocks, mainly intermediate to felsic igneous rocks such as Dongjiangkou and Yanzhiba granites (Zhang et al., 1996; Xu et al., 2012). The development of tectonic structures including fold, thrust-nappe, and strike-slip faults provided channels

Figure 4. The Zhen'an emerald mines are located in the South Qinling Belt. A: En route to emerald mines in the Qinling Mountains. B: Author Xiao-Yan Yu points to the quartz vein outcrop. C: Columnar emerald aggregate with green mica in the quartz vein. Photos by Yi Guo (A and B) and Xiao-Yan Yu (C).

for the migration of mineralizing hydrothermal fluids, and also resulted in a large number of tensile and torsional secondary fault structures that became the main ore-bearing spaces (Zhang et al., 1997; Xu et al., 2012). The Yuehe fault is the most important tungsten-beryllium ore-controlling fault (Dai et al., 2018; He et al., 2024).

The emerald deposits are situated on different slopes of the Qinling Mountains, from Hetaoping to Dongyang (figure 4A). Emeralds from Zhen'an are mainly hosted within quartz veins (figures 2, 4B, and 4C) and quartz-calcite veins (figure 5). Most of the emerald crystals range from 0.5 to 2.0 cm in length, with a few longer than 5 cm, including the largest

Figure 5. Two emerald specimens from quartz-calcite veins. A and B: Specimen containing emeralds and associated minerals such as white calcite, off-white quartz, and brown phlogopite. The calcite fluoresces moderately red (early crystallization, larger particles) and strongly blue (later filling crystallization, xenomorphic granular and smaller) under short-wave ultraviolet light. C: Emeralds with associated minerals such as white calcite, white or gray quartz, gray phenakite, and brown phlogopite. Photos by Sheng-Hao Zhu (A) and Yi Guo (B and C).

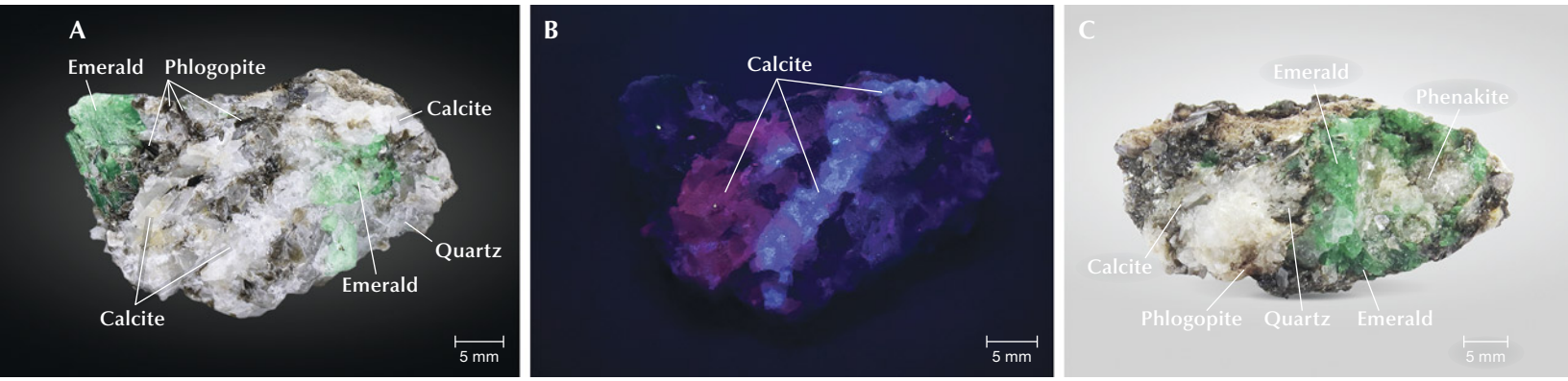

Figure 6. The largest known emerald crystal from Zhen'an to date, weighing 34.34 g and measuring 6.3 cm long, with associated quartz and albite. Photo by Xiao-Yan Yu.

crystal found to date at 6.3 cm long (figure 6). The associated minerals primarily include quartz, scheelite, wolframite, and chromium mica (Dai et al., 2017, 2018, 2019). The argon-argon dating method has yielded plateau ages of 201.4 ± 2.10 Ma for fuchsite and 196.6 ± 2.38 Ma for phlogopite (Dai et al., 2019). The elevated vanadium content in these emeralds may have originated from vanadium-bearing carbonaceous slate and phlogopite schist within the region, and the source of beryllium is believed to be derived from hidden felsic magmatic intrusions (Dai et al., 2018).

MATERIALS AND METHODS

Samples. A total of 26 emerald samples from Zhen'an County, Shaanxi Province, China (figure 7) were examined. Six emerald samples (ESC-8-01, ESC-8-02, ESC-8-03, ESC-9-02, ESC-9-03, and ESC-9-04 were collected in the field from a variety of mines by authors X-YY and YG. The remainder (ESC-01 through ESC-20) were selected from more than 200 emerald crystals collected by an enthusiast who obtained them from local miners and farmers over the past several years. These samples include both partially fractured and well-formed euhedral columnar single crystals exhibiting a typical beryl crystal morphology.

Standard Gemological Testing. Conventional gemological analyses of the samples were performed at the Gemological Research Laboratory of China University of Geosciences, Beijing. Each sample was examined using a refractometer, Chelsea filter, long-wave (365 nm) and short-wave (254 nm) ultraviolet (UV) lamps, and an apparatus for determining specific gravity using the hydrostatic method. Internal and external features were observed with a GI-MP22 gemological microscope utilizing darkfield, bright-field, and oblique illumination techniques. To best capture the inclusion scenes, some photomicrographs were enhanced by focus stacking techniques.

Spectroscopic Methods. Ultraviolet/visible/near-infrared (UV-Vis-NIR) spectra were recorded using a Shimadzu UV-3600 spectrophotometer in diffuse reflection mode. The results were expressed in terms of absorbance, which was accomplished by converting the directly obtained reflectance using the Kubelka-Munk transformation. The instrument was equipped with an ISR-3100 60 mm diameter integrating sphere. Measurements were taken at a sampling interval of 1 nm, using a slit width of 20 nm, and covering a wavelength range from 300 to 900 nm.

Raman spectra were acquired using a Horiba LabRAM HR Evolution Raman spectrometer at the Gemological Research Laboratory of China University of Geosciences, Beijing, employing an argon-ion laser with 532 nm excitation. The spectral range covered was 4000 to 100 cm^{-1}, with an integration time of 5 s and accumulation of up to 3 scans. The Raman shifts were calibrated using monocrystalline silicon prior to testing, with a tolerance of ±0.5 cm^{-1}.

For minerals that could not be identified solely by Raman analysis, particularly those with low hardness, the destructive KBr pellet transmission method of infrared spectroscopy was employed. Infrared spectroscopy was performed using a Bruker Tensor 27 Fourier-transform infrared (FTIR) spectrometer, with the resolution set at 4 cm^{-1} and a scanning range of 4000 to 400 cm^{-1}.

Trace Element Chemistry. *In situ* trace element measurements were conducted using a Thermo-Finnigan Element II sector field inductively coupled plasma–mass spectrometer paired with an NWR193UC laser ablation system at the National Research Center for Geoanalysis, Chinese Academy of Geological Sciences (CAGS), Beijing. The ablation spots on the emerald samples measured 40 μm and were

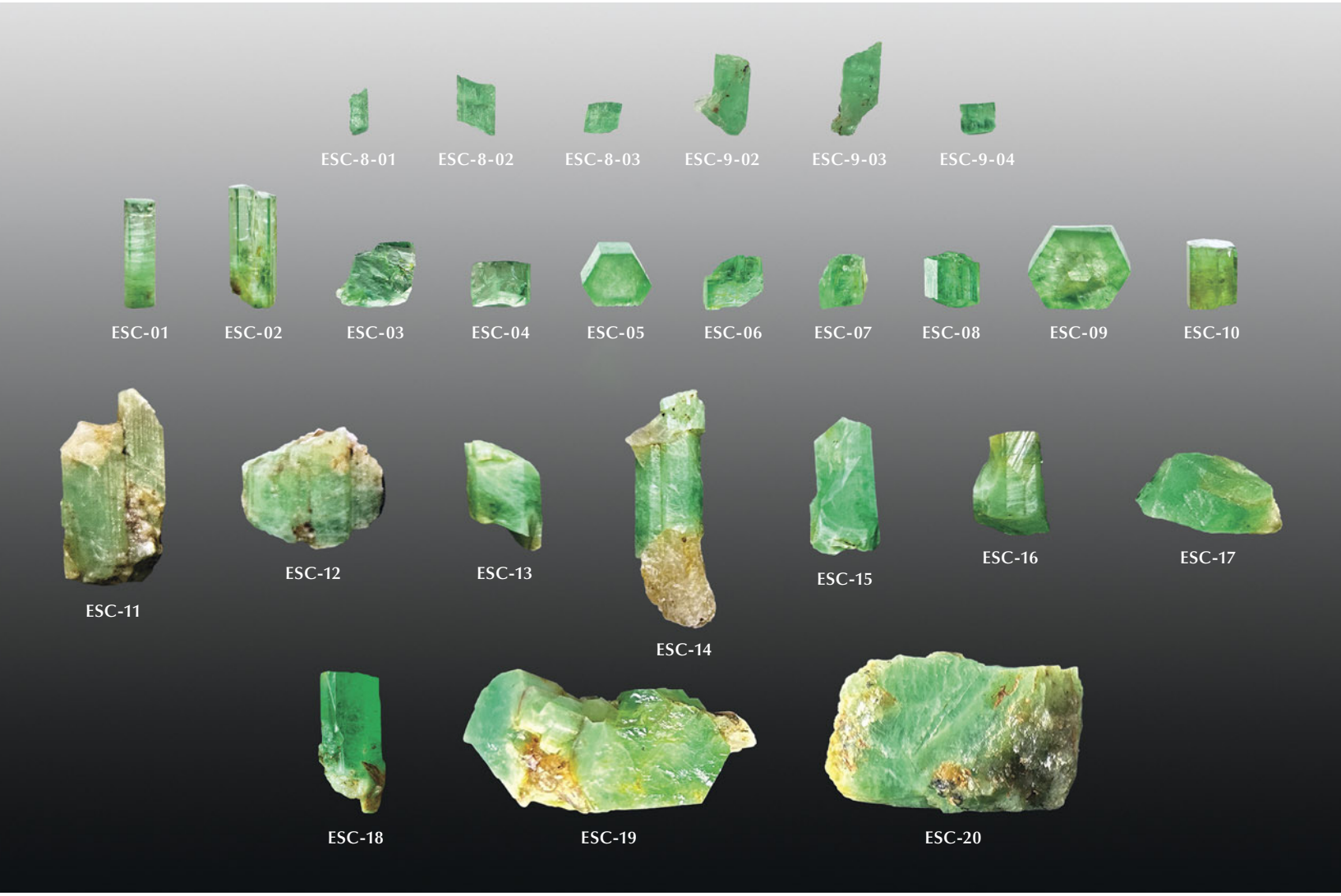

Figure 7. Emerald samples (ranging from 0.21 to 37.10 ct) from Zhen'an, Shaanxi, China. The first row displays transparent emerald crystals, the second row presents transparent to translucent emeralds, and the third and fourth rows show translucent to opaque samples. Photos by Yi Guo.

performed using a repetition rate of 20 Hz and a laser energy density of approximately 5 J/cm^2. Helium was used as the carrier gas for the aerosol generated by laser ablation. The instrument was optimized by ablating NIST SRM 612 to achieve maximum signal intensity for lanthanum and thorium (4×10^5 cps), while maintaining oxide production (ThO^+/Th^+) well below 0.2%. Each analysis lasted for 80 s: 20 s for background acquisition, 40 s for data acquisition during ablation, and 20 s for post-ablation washout. Trace element concentrations were calculated offline using Iolite software for internal standardization, with NIST 610 and KL-2G serving as external calibration standards (GeoReM preferred values) (Woodhead et al., 2007; Paton et al., 2011).

RESULTS

Gemological Properties. The Zhen'an emerald samples used in this study displayed a light to medium saturation of green, with a yellow or blue tone.

The refractive index of the samples ranged from 1.568 to 1.578 for the extraordinary direction (n_e) and from 1.576 to 1.587 for the ordinary direction (n_o), yielding a birefringence of 0.008 to 0.009, consistent with emerald's uniaxial negative character. The

TABLE 1. Gemological properties of emeralds from Zhen'an, Shaanxi, China.

Color	Light to medium yellowish green to bluish green
Clarity	Slightly to heavily included
Refractive indices	n_o = 1.576–1.587; n_e = 1.568–1.578
Birefringence	0.008–0.009
Specific gravity	2.68–2.70
Pleochroism	Medium yellowish green or green (o-ray) and green or bluish green (e-ray)
Fluorescence	Inert to long- and short-wave UV radiation
Chelsea filter	No reaction
External features[a]	• Hexagonal prism *m* faces (sometimes with *a* faces) and double-sided parallel *c* faces • Longitudinal striations, sloping growth steps, and etch figures • Color zoning perpendicular to the *c*-axis ranges from a green rim to a near-colorless core
Internal features	• Healed fissures with two-phase fluid inclusions • Two-phase fluid inclusions containing a gas bubble • Mineral inclusions: phlogopite, plagioclase, scheelite, calcite, and hematite

[a]*Basal pinacoid* c *{0001}, first-order hexagonal prism* m *{10$\bar{1}$0}, and second-order hexagonal prism* a *{11$\bar{2}$0} (Schmetzer and Martayan, 2023).*

specific gravity of the samples varied between 2.64 and 2.72, while the specific gravity of emerald crystals devoid of other associated minerals falls predominantly within the range of 2.68 to 2.70. All samples were unresponsive under the Chelsea color filter and inert under both long- and short-wave UV radiation. A summary of the gemological properties is provided in table 1.

Microscopic Characteristics. Emerald crystals from Zhen'an are generally associated with quartz, muscovite, phlogopite, calcite, albite, scheelite, fluorite,

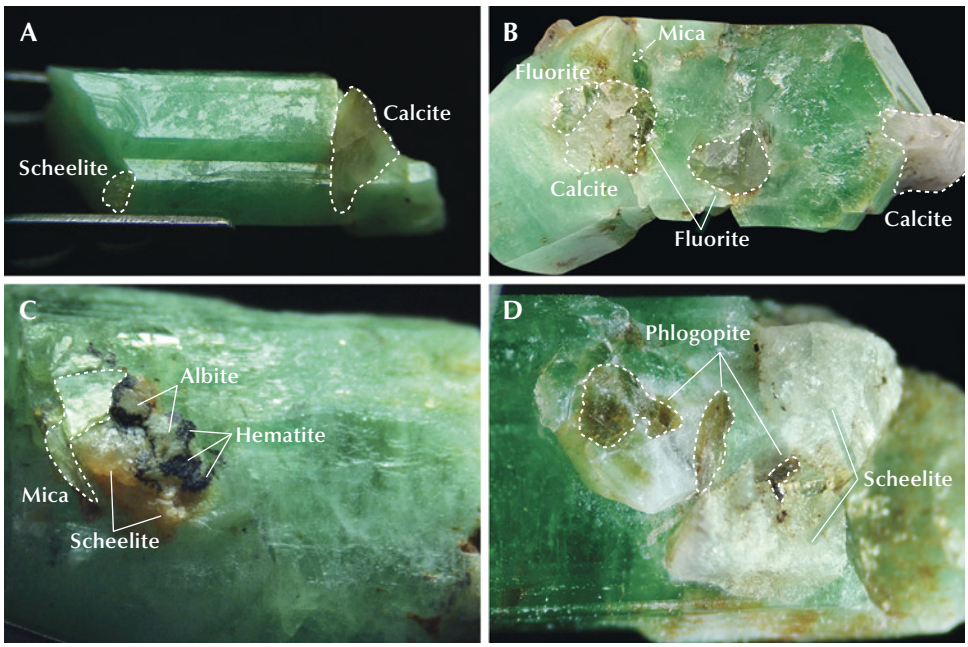

Figure 8. Emerald crystals from Zhen'an with associated minerals. A: ESC-14 and its associated transparent minerals scheelite and calcite. B: ESC-19 with calcite, mica, and fluorite. C: ESC-20 with mica, albite, scheelite, and hematite. D: ESC-18 with scheelite and phlogopite. All associated minerals were identified by Raman analysis. Photomicrographs by Yi Guo; fields of view 20.36 mm (A), 21.45 mm (B), 14.29 mm (C), and 7.78 mm (D).

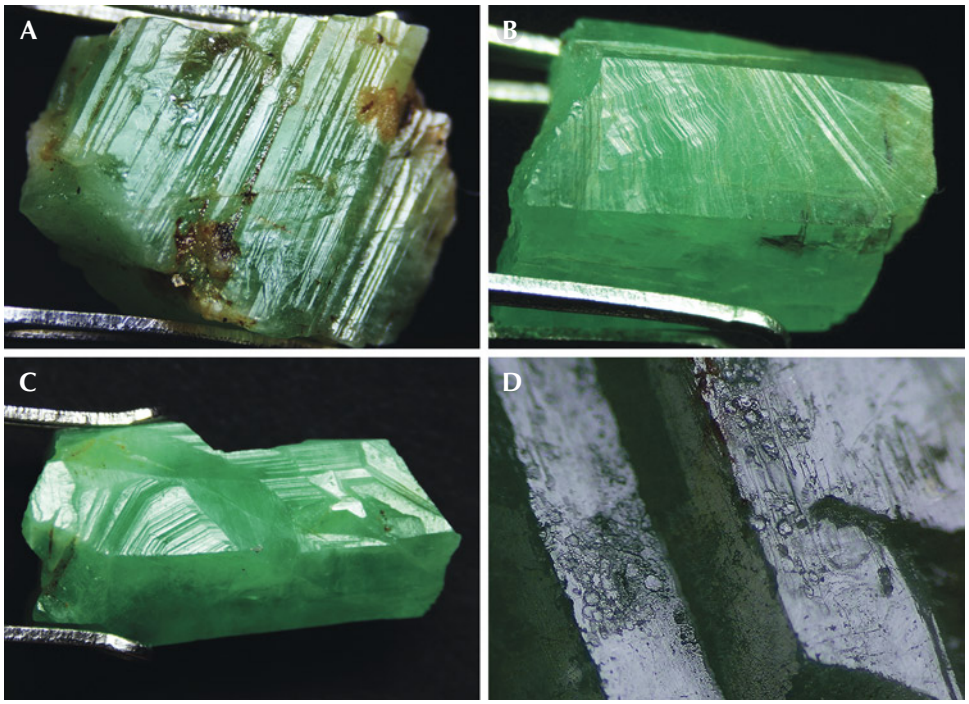

Figure 9. Microtopography of emerald crystals from Zhen'an. A: Longitudinal striation of hexagonal faces (ESC-12). B: Inclined stripes on hexagonal prism face (ESC-16). C: Angular growth steps of one of the m *hexagonal prism faces (ESC-15). D: Hexagonal etch feature (ESC-19). Photomicrographs by Yi Guo; fields of view 14.20 mm (A and C), 11.12 mm (B), and 4.05 mm (D).*

and hematite. In this assemblage, mica is green or brown, and calcite and albite are white or yellow (figure 8).

Some of the emeralds studied had distinct hexagonal color zoning around the *c*-axis, ranging from a green rim to a near-colorless core (again, see figure 7), or flat color bands visible on the prismatic plane. A series of rectilinear stripes (combination striations) parallel to the *c*-axis were visible on the hexagonal column faces (figure 9A). Additionally, oblique striations were observed on the prismatic faces of certain samples (figure 9B), interpreted as growth steps rather than combination striations (Schmetzer and Martayan, 2023). Notably, these growth steps exhibited angular characteristics sometimes approaching an angle of 120° (figure 9C). A variety of etch features were seen on the surface of one of the hexagonal basal pinacoidal faces: irregular etch pits and hexagonal etch pits (figure 9D). Growth steps were observed at the edge of the prismatic face. Incomplete cleavage parallel to the bottom *c* face was seen on the surface.

Distinct linear zigzag inclusions, oriented parallel to the *c*-axis, were identified first within sample ESC-02 (figure 10). Found in four emerald samples, the linear zigzag inclusions appeared in pairs.

The most common inclusion type in the Zhen'an emeralds studied was a two-phase inclusion with a

Figure 10. Two linear zigzag inclusions extending along the direction of the c*-axis, viewed with brightfield illumination (left) and oblique illumination (right). Photomicrographs by Yi Guo; fields of view 5.07 mm (left) and 1.70 mm (right).*

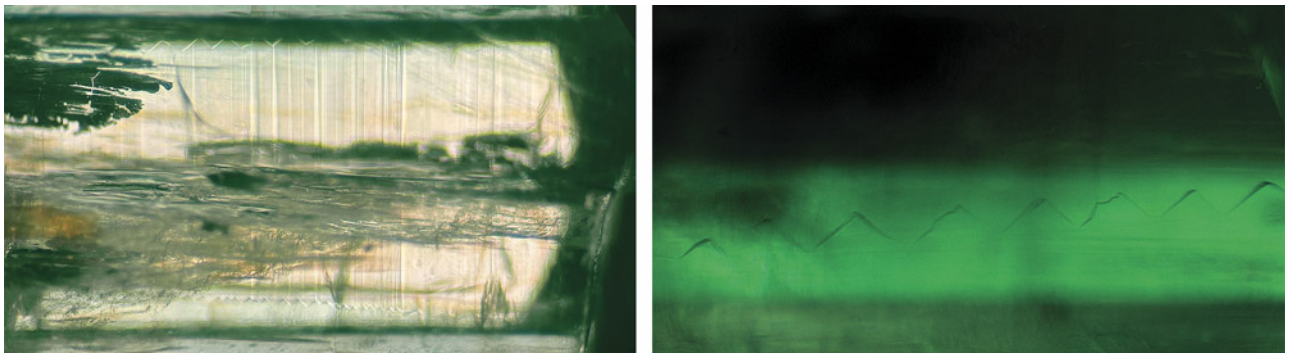

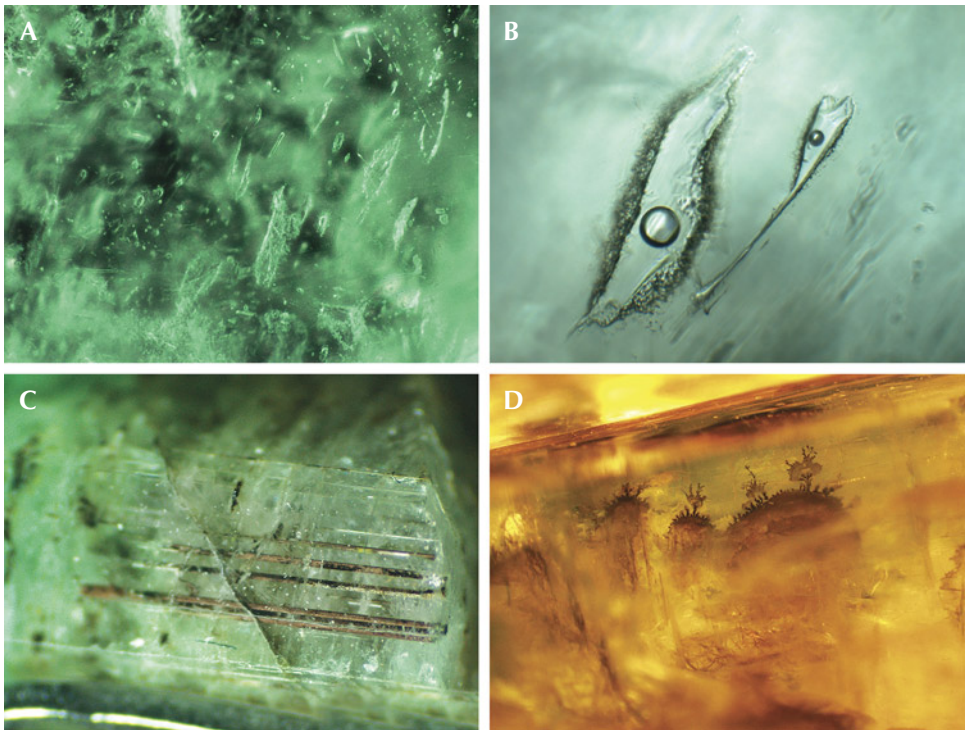

Figure 11. Inclusions in Zhen'an emeralds. A: Fluid inclusion group (ESC-09). B: Irregular isolated two-phase fluid inclusion with an eye-like morphology (ESC-04). C: Colorless transparent tubular inclusions and brown tubular inclusions filled with hematite and magnetite (ESC-05). D: Brown dendritic inclusions filling fissures (ESC-10), which are tentatively identified as dendritic pyrolusite. Photomicrographs by Yi Guo (A and B) and Xiao-Yan Yu (C and D); fields of view: 2.02 mm (A), 0.38 mm (B), 5.0 mm (C), 2.9 mm (D).

gas bubble suspended in fluid (figure 11). These two-phase inclusions were several to hundreds of micrometers in length and a few to tens of micrometers in width. The inclusions exhibited a variety of forms, including elongated, tubular, needle-like, long-tailed, eye-like, and various irregular shapes. Some were clustered in groups within the confines of a healed fissure surface (figure 11A), while others were found in isolation (figure 11B). The tubular inclusions were parallel to the *c*-axis, which measured approximately 4 mm in length, and some subsequently had been filled with black hematite and magnetite adhered to the inner walls of the voids (figure 11C). Secondary inclusions also occur in other morphologies (figure 11D).

The components of isolated primary two- or three-phase fluid inclusions in Zhen'an emeralds were identified by Raman spectroscopy. An eye-like two-phase fluid inclusion, measuring approximately 0.10 mm in length, was subjected to Raman analysis (figure 12). The results suggested water (H_2O) as the liquid phase (identified by a wide absorption band near 3400 cm^{-1}) and carbon dioxide (CO_2) as the gas phase (identified by peaks at 1289 and 1393 cm^{-1}). The Raman spectra of other two- or three-phase fluid inclusions revealed only the identity of the gas phase (figures 13 and 14), which indicated that the components could be CO_2 (1287 and 1389 cm^{-1}) plus nitrogen (2330 cm^{-1}), or CO_2 (1280 and 1385 cm^{-1}) plus methane (2911 cm^{-1}).

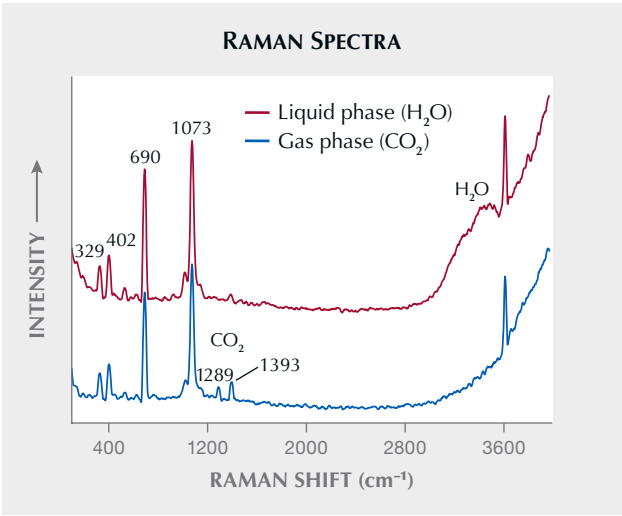

Figure 12. Raman spectra showing the gas and liquid phases of an irregular fluid inclusion (about 0.10 mm in length) in a Zhen'an emerald (ESC-04; see figure 11B). The gas phase is CO_2 (1289 and 1393 cm^{-1}), and the liquid phase is H_2O (about 3400 cm^{-1}). Spectra are offset vertically for clarity.

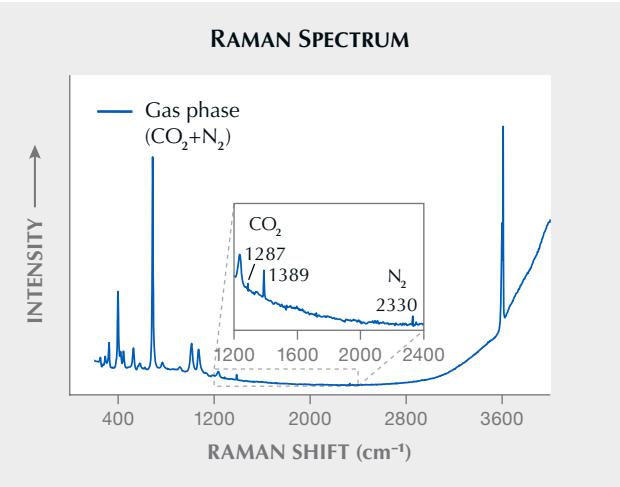

Figure 13. Raman spectrum showing the gas phase of an irregular fluid inclusion (about 0.03 mm in length) in a Zhen'an emerald (ESC-04). The gas phase is a mixture of CO_2 (1287 and 1389 cm^{-1}) and N_2 (2330 cm^{-1}).

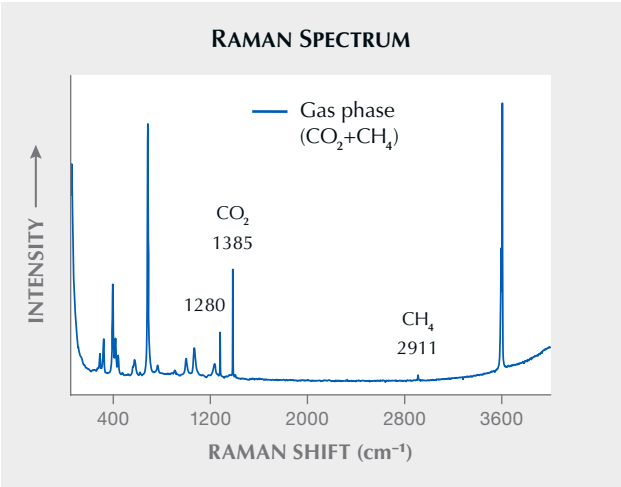

Figure 14. Raman spectrum showing the gas phase of an irregular fluid inclusion (about 0.05 mm in length) in a Zhen'an emerald (ESC-09). The gas phase is a mixture of CO_2 (1280 and 1385 cm^{-1}) and CH_4 (2911 cm^{-1}).

Mineral inclusions in the Zhen'an emeralds studied were abundant, with plagioclase and phlogopite particularly prevalent (figure 15). Plagioclase inclusions occurred in clusters, while phlogopite inclusions were observed in the form of lamellar rectangles and hexagons. Euhedral scheelite and rounded calcite inclusions were also encountered within the emerald crystals. Among the aforementioned mineral inclusions, calcite, plagioclase, and scheelite were all colorless, while phlogopite was nearly colorless with a slight brownish tint. In addition, at one end of sample ESC-05, brown-yellow, greasy, lustrous talc columns (indicated by FTIR) filled the emerald crystals; some of these were exposed and fractured. Brown and brown-black hematite inclusions were also found, usually in the form of irregularly shaped flakes.

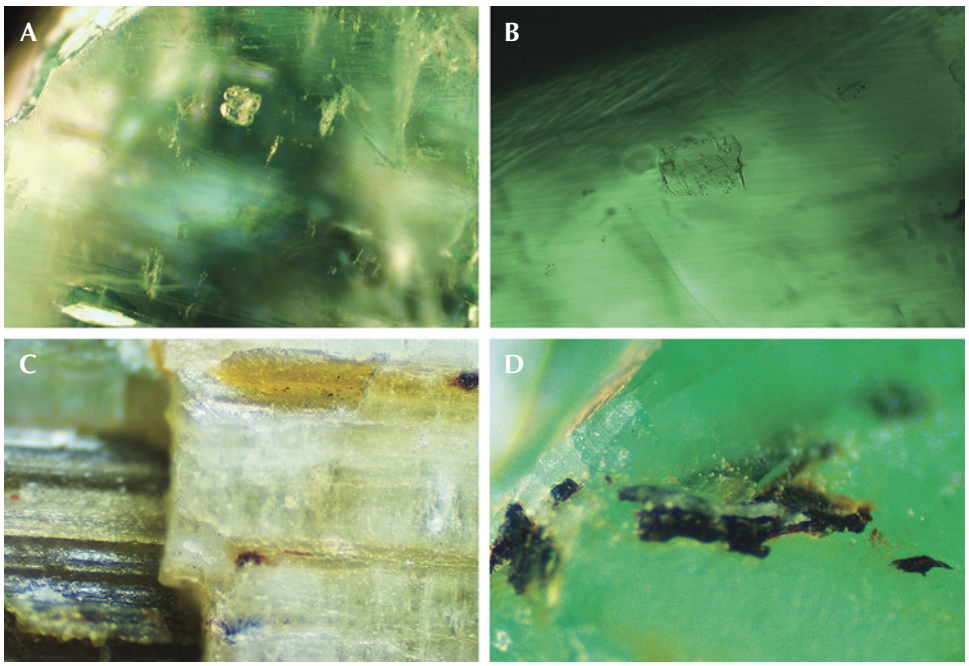

Figure 15. Mineral inclusions in Zhen'an emeralds. A: White calcite inclusions (ESC-9-04). B: Sheetlike rectangular phlogopite inclusion (ESC-9-04). C: Brown-yellow columnar talc inclusions (ESC-05). D: Brown to black flaky hematite inclusions (ESC-9-02). The above minerals (except C) were identified by Raman analysis. Photomicrographs by Yi Guo (A–C) and Xiao-Yan Yu (D); fields of view 1.55 mm (A), 0.88 mm (B), 2.9 mm (C), and 2.03 mm (D).

Trace Element Chemistry. The emerald samples were classified into two groups based on color: bluish green (22 samples) and yellowish green (ESC-07, ESC-10, ESC-16, and ESC-19). From each category, two samples were randomly selected for trace element analysis. For each sample, three to four spots were randomly chosen for laser ablation–inductively coupled plasma–mass spectrometry (LA-ICP-MS) testing, and the results are shown in table 2.

Concentrations of alkali metals in the emerald samples from Zhen'an, from highest to lowest, were sodium (5802–7948 ppm, with an average of 6636 ppm), cesium (715–1585 ppm, average 1188 ppm), lithium (279–627 ppm, average 400 ppm), potassium (90–716 ppm, average 193 ppm), and rubidium (17–42 ppm, average 26 ppm). The combined content of these alkali metal elements varied between 7650 and 9583 ppm, with an average of 7897 ppm.

Beryl that is colored green by chromium and/or vanadium is considered emerald. In these emeralds, vanadium ranged from 1047 to 3031 ppm (average 2252 ppm); chromium did not exceed 178 ppm (average 42 ppm); and iron varied between 951 and 1968 ppm (average 1210 ppm). The chromium content of ESC-19 was below the detection limit. It is evident

TABLE 2. Trace element composition (in ppm) of four Zhen'an emeralds by LA-ICP-MS (range and average).

	Bluish green		Yellowish green		
Element	ESC-05 (4 spots)	ESC-20 (4 spots)	ESC-07 (3 spots)	ESC-19 (4 spots)	Detection limit (ppm)
Li	546–623 (586)	322–347 (330)	306–321 (314)	279–627 (369)	3.0
Na	6300–6662 (6499)	5802–6988 (6520)	6117–6642 (6440)	6403–7948 (7085)	11
Mg	4205–4521 (4358)	4096–5383 (4941)	5027–5299 (5188)	4934–5532 (5144)	2.8
K	155–166 (159)	90–716 (257)	145–154 (151)	166–268 (204)	13
Sc	7–9 (8)	27–45 (35)	20–23 (22)	9–44 (27)	0.4
Ti	34–40 (37)	24–37 (30)	29–33 (31)	32–87 (47)	1.9
V	1047–1191 (1120)	2398–3031 (2676)	2655–2809 (2754)	1450–2837 (2461)	0.2
Cr	16–27 (22)	113–178 (140)	4–6 (5)	bdl[a]–4 (—)	3.9
Mn	14–19 (17)	14–27 (20)	22–27 (25)	27–45 (33)	3.4
Fe	951–1010 (986)	925–1359 (1175)	1103–1236 (1150)	1204–1968 (1532)	32
Zn	62–68 (66)	24–33 (28)	27–29 (28)	33–107 (59)	2.5
Ga	14–16 (15)	22–26 (24)	24–26 (25)	16–33 (26)	0.2
Rb	22–27 (25)	17–26 (23)	29–30 (29)	23–42 (31)	0.1
Cs	922–1016 (974)	989–1388 (1165)	1369–1420 (1398)	715–1585 (1217)	0.1
Li + Na + K + Rb + Cs	7958–8426 (8246)	7650–9014 (8297)	8005–8516 (8334)	8214–9583 (8908)	—
Mg + Mn + Fe + Zn	5233–5620 (5428)	5290–6798 (6165)	6181–6592 (6391)	6366–7588 (6769)	—
Cr/V	0.014–0.025 (0.019)	0.041–0.070 (0.052)	0.0015–0.0022 (0.0019)	0–0.0016 (0.0007)	—

[a]*bdl = below detection limit.*

that the total concentration of monovalent cations ($Li^+ + Na^+ + K^+ + Rb^+ + Cs^+$) consistently surpasses that of divalent cations ($Mg^{2+} + Mn^{2+} + Fe^{2+} + Zn^{2+}$), even if all iron, including Fe^{3+}, is regarded as Fe^{2+}. This observation may suggest a substitution of Li^+ for Be^{2+} at the beryllium site within the crystal structure of emeralds from Zhen'an (Groat et al., 2008). However, this explanation alone is insufficient to account for all observed chemical characteristics. Additionally, it may imply the presence of Al^{3+} substituting for Si^{4+} at the silicon site.

Some samples showed obvious color zoning, which was explored by looking at the trace element concentrations across these zones for two different samples. The trace element concentrations of samples ESC-09 and ESC-10 with obvious color zones are given in table 3. Figure 16 illustrates the seven analytical spots on ESC-09, the five analytical spots on ESC-10, and the associated elemental variations. Overall, the chromium concentration exhibited considerable fluctuation. Within the near-colorless core of the emerald, the concentrations of manganese and chromium displayed notable variability, whereas the levels of magnesium, vanadium, cesium, iron, zinc, rubidium, and scandium remained relatively stable. Progressing from the core to the periphery of the emerald crystal, where the green hue intensified, a pronounced increase in the concentrations of vanadium, cesium, iron, manganese, gallium, and scandium was detected, along with a significant decline in zinc levels.

The content of most elements (except for chromium) showed no significant fluctuations in the core, indicating a relatively stable growth environment during the emeralds' initial crystallization stage (Yu et al., 2020). The variations in trace elements from the core to the rim suggested fluid evolution during the crystallization process or multistage mineralization of the emeralds (Yu et al., 2020; Cui et al., 2023). Additionally, the changes in chromophore elements confirmed vanadium as the primary chromophore in Zhen'an emeralds.

TABLE 3. Trace element composition (in ppm) of two Zhen'an emeralds with color zoning by LA-ICP-MS.

	ESC-09							ESC-10					
	Green rim	Near-colorless core					Green rim	Green rim	Near-colorless core			Green rim	Detection limit
Element	1	2	3	4	5	6	7	1	2	3	4	5	(ppm)
Li	309	644	671	553	663	518	346	286	380	367	421	310	3.0
Na	6080	6726	6790	6275	6937	6077	5210	7153	4986	4706	5690	6548	11
Mg	4697	4592	4545	4446	4654	4614	3975	5842	3516	3559	4214	5111	2.8
Sc	13	4	3	4	4	4	14	34	6	8	8	31	0.4
Ti	36	42	33	28	31	21	29	67	26	27	30	38	1.9
V	2500	1014	989	953	1022	941	2517	3003	958	956	1070	2709	0.2
Cr	4	13	bdl[a]	19	bdl	26	6	9	7	bdl	10	bdl	3.9
Mn	22	20	8	15	6	14	18	36	7	13	15	22	3.4
Fe	1213	790	778	779	835	878	1075	1507	606	724	760	1157	32
Zn	34	83	79	61	81	69	25	33	54	53	53	33	2.5
Ga	28	16	16	15	15	16	29	29	15	16	18	27	0.2
Rb	26	27	29	24	28	25	24	34	17	17	21	30	0.1
Cs	1377	971	968	983	1019	953	1617	1443	692	629	740	1350	0.1

[a]*bdl = below detection limit.*

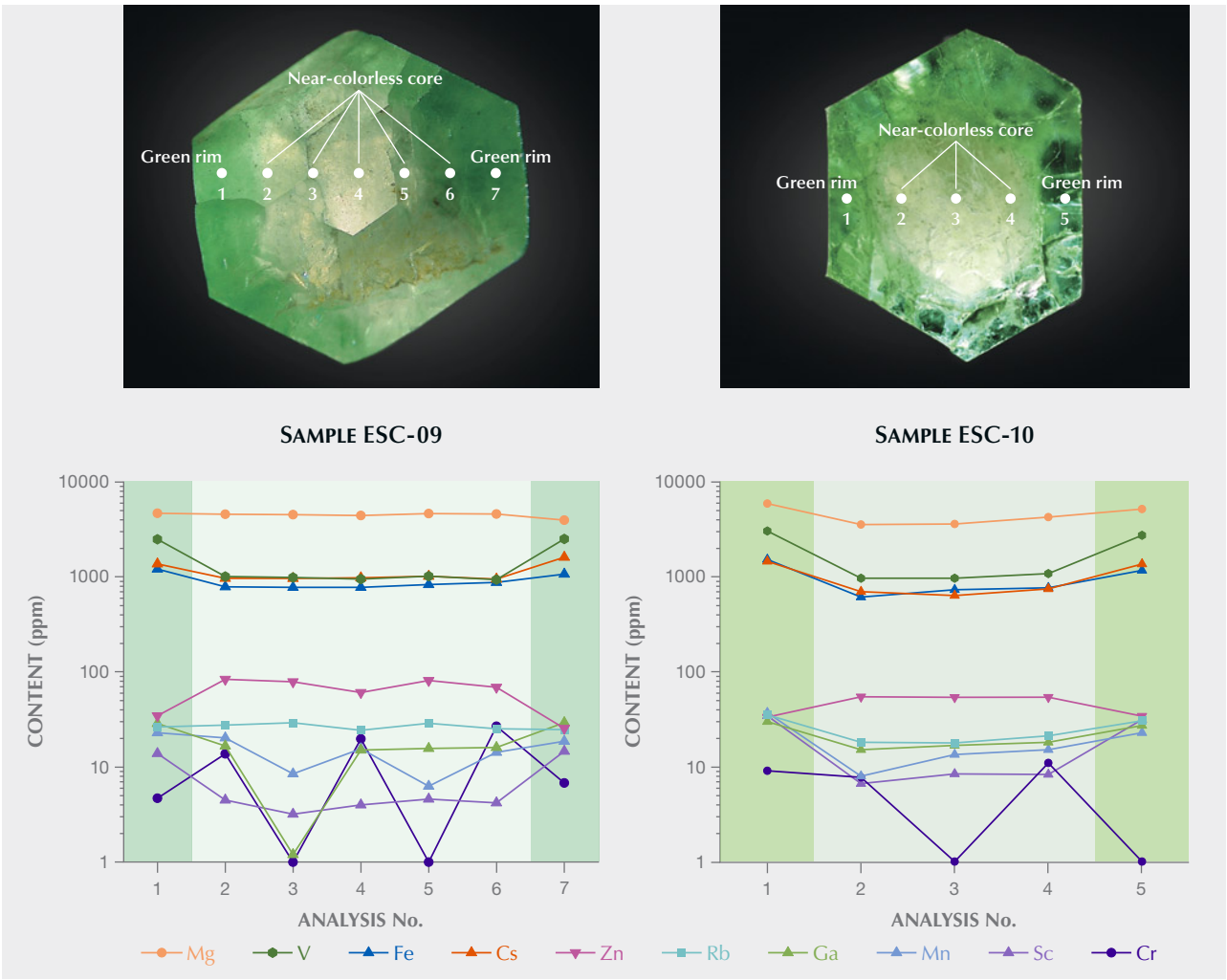

Figure 16. Color-zoned emeralds ESC-09 (left) and ESC-10 (right) with green rims and near-colorless cores with corresponding LA-ICP-MS trace element analyses. White circles indicate the spot positions. Photos by Yi Guo; fields of view 12.92 mm (left) and 9.23 mm (right).

UV-Vis-NIR Absorption Spectroscopy. The spectra of 11 oriented emerald samples (ESC-8-03, ESC-9-04, ESC-01, ESC-02, and ESC-04 through ESC-10) were collected both parallel to the *c*-axis and perpendicular to the *c*-axis in diffuse reflection mode. They each exhibited distinctive vanadium-absorption spectra. The representative UV-Vis-NIR spectra of Zhen'an emerald sample ESC-09 are shown in figure 17.

Four characteristic absorption bands were detected: a weak band around 373 nm, a sharp band around 429 nm, and two broad bands around 600–680 and 750–900 nm. The absorption around 373 nm was

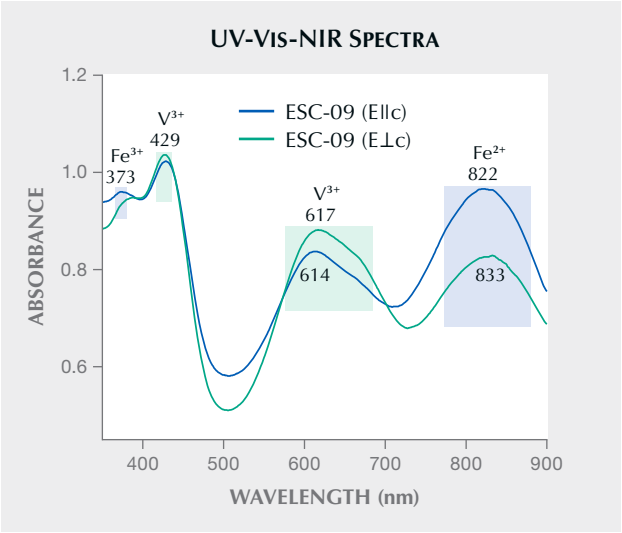

Figure 17. UV-Vis-NIR spectra of Zhen'an emerald ESC-09 taken with unpolarized light parallel and perpendicular to the c-axis.

assigned to Fe^{3+} (Saeseaw et al., 2019). The two absorption maxima around 429 and 617 nm were assigned to V^{3+}, according to the absorption of vanadium-doped synthetic emerald and emerald from Malipo, Yunnan (Schmetzer et al., 2006; Hu and Lu, 2019, respectively). These absorption features of V^{3+} ions were prominent in all the emerald samples tested. The absorption maximum around 830 nm was caused by Fe^{2+} (Wood and Nassau, 1968).

The differences in the UV-Vis-NIR spectra obtained from the two orientations were primarily reflected in the V^{3+} absorption broad band near 615 nm and the Fe^{2+} absorption broad band around 830 nm. Additionally, a noticeable difference in the Fe^{3+} absorption at 373 nm and V^{3+} absorption at 429 nm was observed: when the measurement was taken parallel to the *c*-axis, the absorption intensity of Fe^{3+} was closer to that of V^{3+} at 429 nm, whereas when the measurement was taken perpendicular to the *c*-axis, the Fe^{3+} absorption appeared more like a shoulder peak adjacent to the sharp V^{3+} absorption peak at 429 nm.

Raman Spectroscopy. The Raman spectra of Zhen'an emeralds were measured perpendicular to the *c*-axis. The Raman spectra of the carefully polished regions on *m* faces from all 23 emerald samples were acquired. All of the spectra were nearly identical, and a representative spectrum is shown in figure 18. The characteristic absorption bands of emerald around 526, 685, and 1068 cm^{-1} were caused by Al-O, Be-O, and Si-O stretching vibrations, respectively (Łodzinski et al., 2005). The Raman spectra indicated that both types of water exist in Zhen'an emeralds—type I and type II—and the Raman features of type I (3606 cm^{-1}) were generally more intense than those of type II (3597 cm^{-1}). A lattice vibration related to the beryl structure, specifically the silica tetrahedra in six-membered rings, shows characteristic bands at 322, 395, and 445 cm^{-1}.

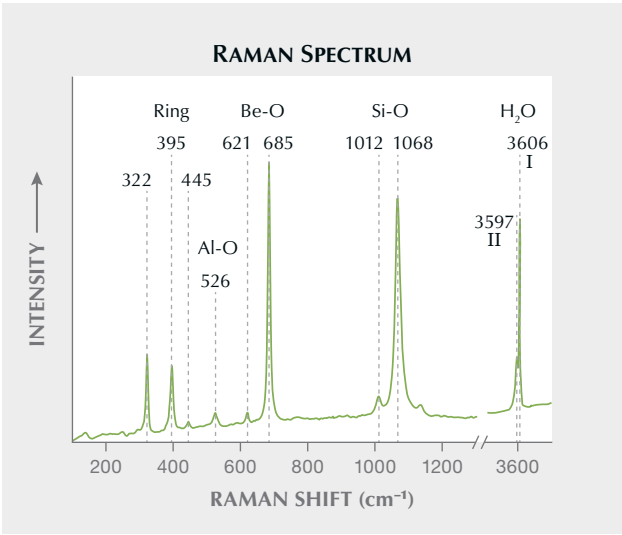

Figure 18. Raman spectrum of Zhen'an emerald (ESC-04) perpendicular to the c*-axis. "Ring" denotes the hexagonal ring within the crystal structure of emerald.*

DISCUSSION

Microscopic Characteristics. In addition to the longitudinal striations on the prismatic faces, inclined stripes are generally seen on some long, parallel hexagonal prism faces parallel to the *c*-axis of the emeralds from Zhen'an. These inclined stripes exhibit an overall stepped pattern rather than complete parallelism, with some individual stripes also displaying a stepped morphology (again, see figure 9B). Hence, they are interpreted as growth steps preserved on crystal planes during crystal development via a layer-by-layer growth mechanism. The hexagonal prism faces parallel to the *c*-axis of an emerald crystal are often visible with longitudinal striations and sometimes growth steps (Hu and Lu, 2019; Schmetzer and Martayan, 2023). The presence of longitudinal striations and the prevalence of growth steps on the hexagonal cylinder may be indicative of a distinctive characteristic exhibited by Zhen'an emerald.

The morphology of linear inclusions with a zigzag shape, which extend parallel to the *c*-axis, resemble the helical inclusions observed in Colombian emerald (Okada and Sirithеerakul, 2019) and the zigzag growth line inclusions in aquamarine (Gao et al., 2023). However, no fluid inclusions were found surrounding the linear zigzag inclusions within Zhen'an emeralds (again, see figure 10), suggesting that they are more likely attributed to crystal structure and growth than to fluid inclusions. Therefore, such inclusions can also be referred to as zigzag growth lines.

The emeralds from Zhen'an are rich in fluid inclusions, especially gas-liquid two-phase fluid inclusions with less than 50% of the fluid-filled cavity volume occupied by bubbles. The compositions of the gas phases identified include carbon dioxide, carbon dioxide plus nitrogen, or carbon dioxide plus methane. Although no fluid inclusions containing daughter crystals have been identified thus far, the

presence of abundant mineral inclusions has been observed, including phlogopite, plagioclase, scheelite, calcite, and hematite, which also serve as associated minerals. These inclusions were commonly observed in the Zhen'an emerald samples, whereas Malipo emeralds, which also exhibit high vanadium content, typically display distinctive dravite (Jiang et al., 2019; Long et al., 2021). This characteristic feature aids in distinguishing emeralds originating from these two mining regions with microscopic examination. Furthermore, the presence of distinct mineral inclusions also serves as an indicator of the heterogeneous nature of the surrounding rock and divergent formation environments within the two mining regions (Jiang et al., 2019; Long et al., 2021).

Color Mechanism. The primary chromogenic element responsible for the green color of Zhen'an emerald is vanadium rather than chromium. Despite the overlapping absorption bands of vanadium and chromium around 620 nm, the broad absorption band at 617 nm in Zhen'an emerald (again, see figure 17), which lacks the sharp bands around 640 and 682 nm, is primarily attributed to vanadium (Wood and Nassau, 1968; Hu and Lu, 2019; Saeseaw et al., 2019). This characteristic vanadium spectrum is similar to that of Malipo emeralds from Yunnan Province, which helps distinguish them from emeralds found in Afghanistan, Pakistan, India, and Davdar in China (Wood and Nassau, 1968; Hu and Lu, 2019; Guo et al., 2020; Qin et al., 2022; Yang et al., 2022; Chen et al., 2023). Furthermore, the shift of the Fe^{3+} absorption band in the UV-Vis-NIR spectra can be used to help distinguish between Zhen'an emerald and Malipo emerald.

The green coloration in the color-zoned emerald samples is directly related to the presence of V^{3+}, with no obvious positive correlation with Cr^{3+} (again, see figure 16). Consequently, Zhen'an emeralds are classified as vanadium-dominant emerald (Groat et al., 2008).

Figure 19. Comparison of the chromium to vanadium ratio of emeralds with vanadium content in higher vanadium and lower chromium. The ratio of Zhen'an emeralds is lower than 0.1, and the ratio of Malipo emeralds is lower than 0.2. Other sources are from Zheng et al. (2019), Hu and Lu (2019), Bai et al. (2019), Rondeau et al. (2008), Lake et al. (2017), Saeseaw et al. (2014) (presented as averages), and Aurisicchio et al. (2018).

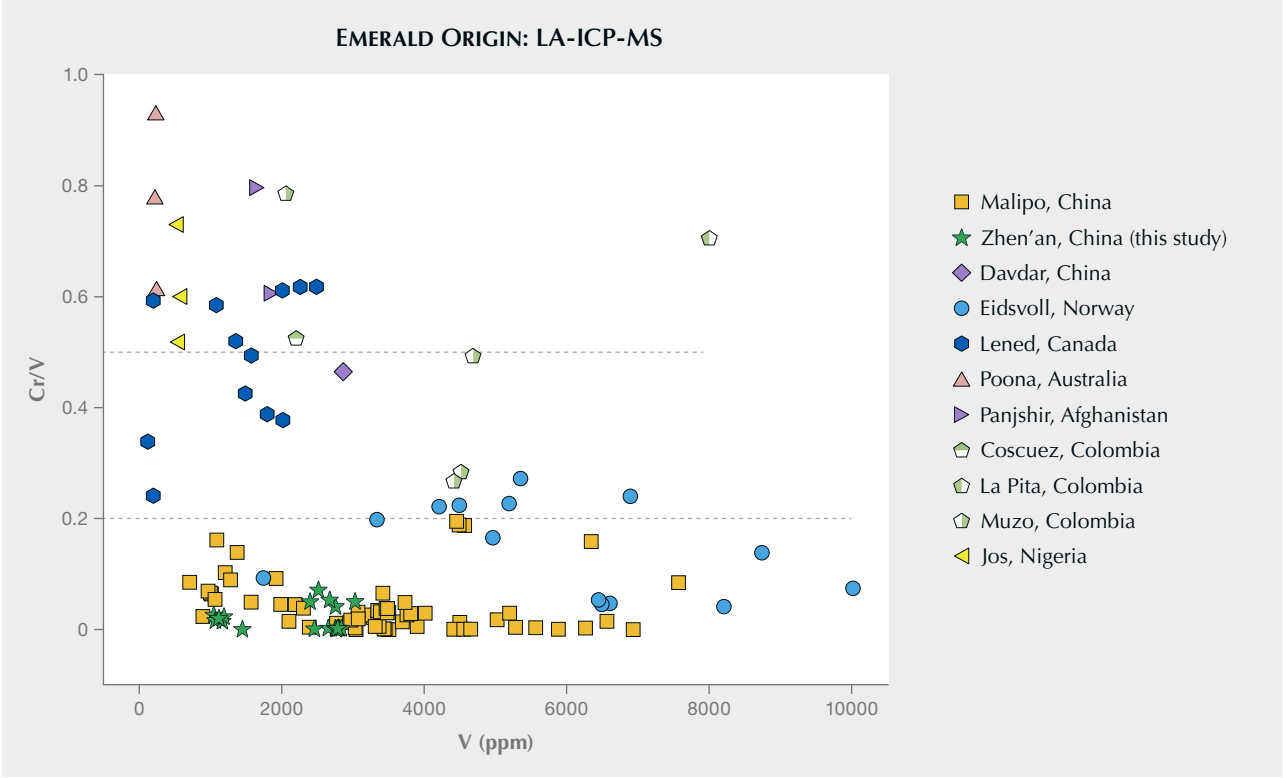

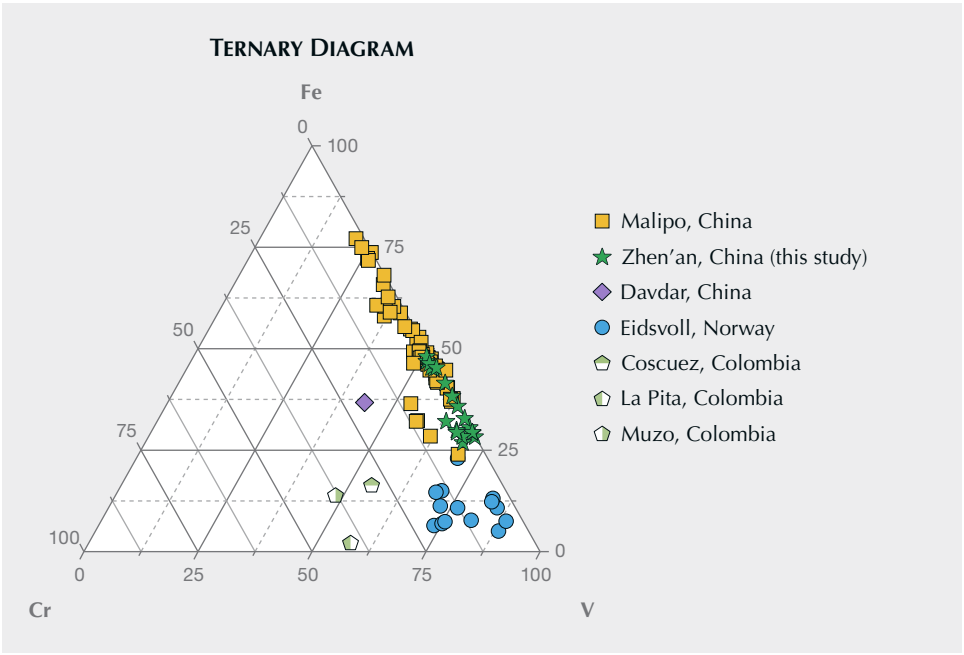

Figure 20. Ternary diagram showing trace element content (in ppm) for emeralds from Zhen'an and other localities. Zhen'an emeralds (green stars) have high vanadium, very low chromium, and medium iron content. Other sources are from Zheng et al. (2019), Hu and Lu (2019), Bai et al. (2019), Rondeau et al. (2008), and Saeseaw et al. (2014) (presented as averages).

Geographic Origin Determination. The total alkali metal content (Li + Na + K + Rb + Cs) of the emeralds from Zhen'an ranges from 7650 to 9583 ppm (average 7897 ppm), which fully overlaps with but on average is lower than that of the emeralds from Malipo, whose content ranges from 7164 to 13469 ppm (Bai et al., 2019; Hu and Lu, 2019; Zheng et al., 2019; Yu et al., 2020; Zheng et al., 2024). Additionally, the absorption strength of type I water is generally higher than that of type II water (again, see figure 18), suggesting a relatively lower alkali metal content in Zhen'an emerald samples (Bersani et al., 2014; Moroz et al., 2000). However, it should be noted that the Raman spectra of water in emeralds from Malipo show three patterns, differing from those of Zhen'an.

In color-zoned Zhen'an emeralds, there is a notable increase in the vanadium, iron, and cesium contents, while the zinc content demonstrates a decrease from core to rim. Additionally, the chromium content, which is always low, fluctuated irregularly from the near-colorless core to the green rim (again, see figure 16). The variation trends of vanadium and iron contents were consistent with those reported by Dai et al. (2018), whereas variations in magnesium content for the samples in this study indicated both increases (ESC-10) and decreases (ESC-09). Therefore, further sample data are required to investigate the variation trend of magnesium content. Moreover, the increasing trends of vanadium, cesium, iron, gallium, and manganese contents from core to rim are consistent with the changes of emeralds with color zoning from Malipo (Yu et al., 2020). Notably, this study also identified a unique downward trend in zinc from core to rim.

Trace element analysis serves as a crucial tool for determining emerald origin (Saeseaw et al., 2019). Zhen'an emerald is characterized by its distinctive trace element signature, which includes high vanadium, relatively low chromium, and moderate iron content, as well as elevated levels of lithium and cesium. Significantly, the chromium content in Zhen'an emerald is substantially lower than its vanadium content, which is a key feature to help differentiate it from emeralds of other origins. The ratio of chromium to vanadium changes with vanadium content, as shown in figure 19, which can distinguish Zhen'an emerald from those from other sources: Poona (Australia), Jos (Nigeria), Panjshir (Afghanistan), Muzo (Colombia), Coscuez (Colombia), La Pita (Colombia), and Lened (Canada). However, there is still some overlap among these mines. Malipo (Yunnan, China) and Eidsvoll (Norway) also exhibit a ratio of chromium to vanadium below 0.2, which is consistent with Zhen'an emeralds.

Figure 20 shows the vanadium-iron-chromium (ppm) ternary diagram of emerald from vanadium-rich mining areas. The very low chromium content causes Zhen'an emerald to fall near the iron-vanadium line, partially overlapping with Malipo emerald. As opposed to Zhen'an emerald, Eidsvoll emerald has high vanadium, low chromium, and low iron.

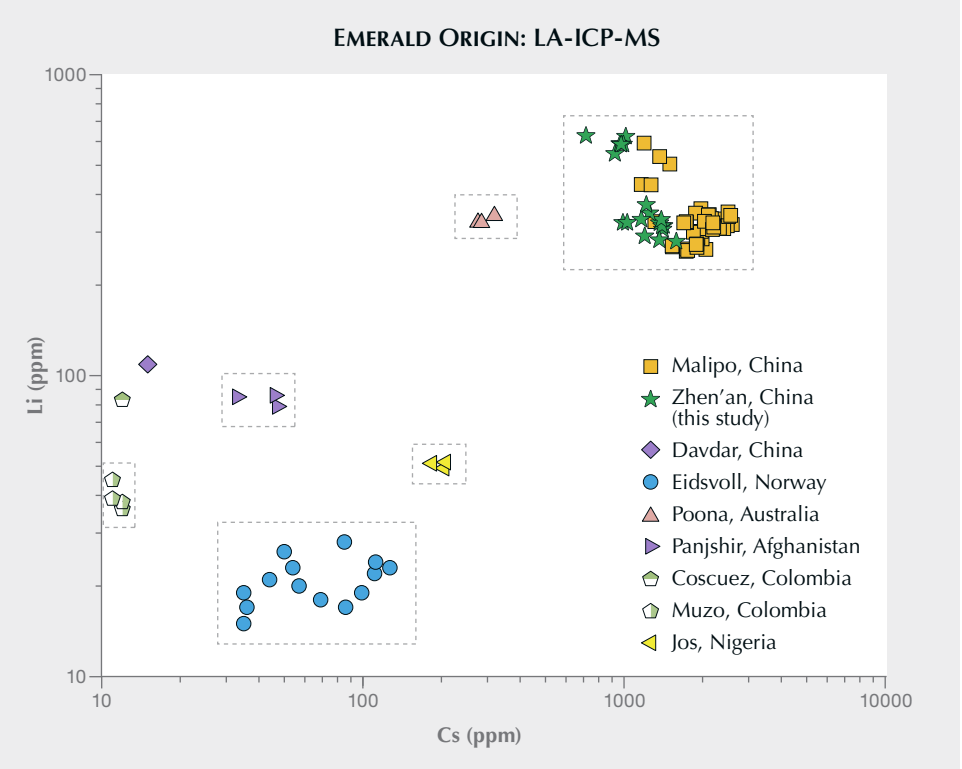

Figure 21. Logarithmic comparison of lithium vs. cesium trace element content for emeralds from Zhen'an and other localities. The emeralds from Zhen'an have higher lithium and cesium content. Other sources are from Zheng et al. (2019), Hu and Lu (2019), Bai et al. (2019), Rondeau et al. (2008), Saeseaw et al. (2014) (presented as averages), and Aurisicchio et al. (2018).

To further distinguish the provenance of vanadium-dominant emeralds, a lithium versus cesium diagram (figure 21) was plotted. Emeralds from Zhen'an are marked by their higher levels of both lithium and cesium, setting them apart from emeralds from other deposits such as Davdar (Xinjiang, China),

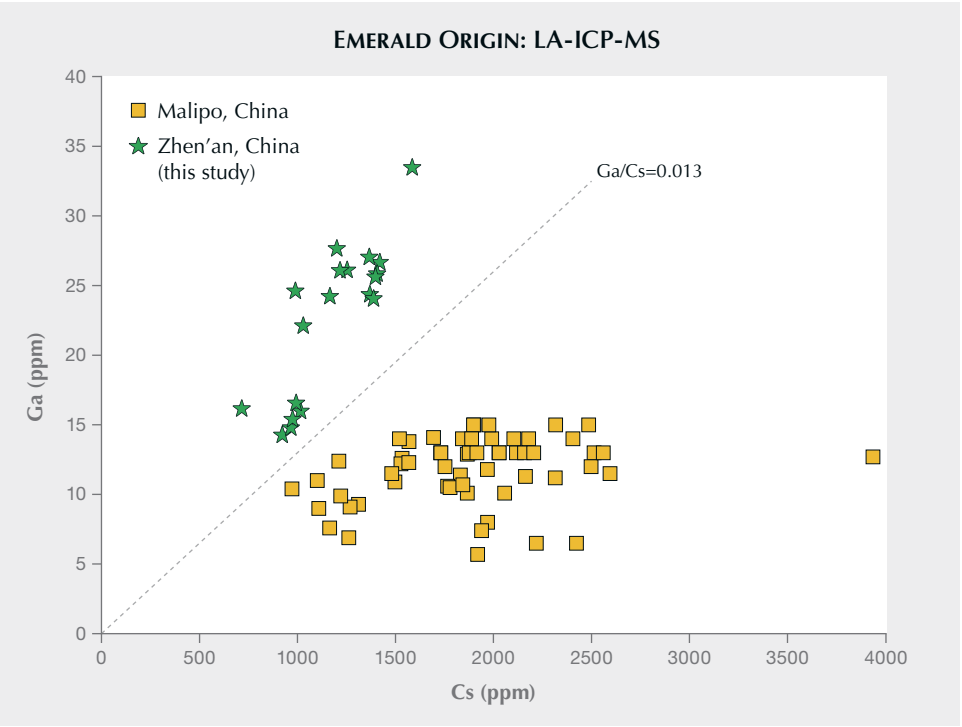

Figure 22. Comparison of gallium vs. cesium trace element content for emeralds from Zhen'an and Malipo. The gallium to cesium ratio of emerald from Zhen'an is higher than that of emerald from Malipo, and they are located on both sides of the auxiliary line (Ga/Cs = 0.013). Data for Malipo emerald is from Zheng et al. (2019) and Hu and Lu (2019).

Eidsvoll (Norway), Poona (Australia), Jos (Nigeria), Panjshir (Afghanistan), Muzo (Colombia), and Coscuez (Colombia).

The challenge in distinguishing emeralds from Zhen'an and Malipo arises from the significant overlap shown in the above plots. However, a potential solution lies in considering the ratio of gallium to cesium, as illustrated in figure 22. By establishing a threshold of Ga/Cs = 0.013 (with a range of 0.012 to 0.014 also considered acceptable), a clear distinction can be made: Zhen'an emeralds are positioned above this threshold line, while Malipo emeralds fall below it.

Emeralds from Zhen'an can be distinguished from emeralds of other origin using the above series of trace element plots, allowing the separation of vanadium-dominant emeralds.

CONCLUSIONS

Emerald from Zhen'an is mainly found in quartz or quartz-calcite veins and associated with minerals such as muscovite, phlogopite, albitite, scheelite, fluorite, and phenakite. The emerald crystals exhibit an intact hexagonal columnar shape with inclined growth steps on hexagonal prism faces. Abundant internal two-phase fluid inclusions (gas phase of carbon dioxide, carbon dioxide plus nitrogen, or carbon dioxide plus methane; liquid phase of water) and mineral inclusions (phlogopite, plagioclase, scheelite, calcite, talc, and hematite) are present within the crystals. Occasionally distinctive zigzag growth lines appear in pairs within these emeralds.

The vibrant green color of Zhen'an emerald primarily arises from the significant presence of vanadium, which exhibits a distinct absorption spectrum in the visible range. Alkali metal content in Zhen'an samples ranges from 7650 to 9583 ppm (average 7897 ppm). Correspondingly, Raman absorption of type I water (3606 cm^{-1}) is stronger than that of type II water (3597 cm^{-1}).

Emeralds from Zhen'an are characterized by their abundant vanadium (1047–3031 ppm), lithium (279–627 ppm), and cesium (715–1585 ppm) contents; iron concentrations ranging from 951 to 1968 ppm; chromium levels typically below 180 ppm; and a gallium to cesium ratio greater than 0.013. Plots such as the ratio of chromium to vanadium versus vanadium, the vanadium-iron-chromium ternary diagram, and plots of cesium versus lithium and cesium versus gallium are particularly useful for differentiating Zhen'an emerald from vanadium-dominant emerald from other origins.

ABOUT THE AUTHORS

Yi Guo holds a master's degree in geology, Dr. Yu-Yu Zheng holds a doctorate in geology, and Dr. Xiao-Yan Yu (yuxy@cugb.edu.cn, corresponding author) is a professor and doctoral supervisor of gemology and mineralogy, at the School of Gemmology, China University of Geosciences in Beijing.

ACKNOWLEDGMENTS

The authors would like to thank Kun Hu for providing samples and valuable information. We are grateful to Zhi-Zhong Li and Yue-Hong Du for their help with the field trip. We express our gratitude to Ye Yuan for the support and assistance provided with the spectral testing and the determination of instrument parameters. Additionally, our appreciation goes to Yi Zhang, Guang-Ya Wang, and Si-Yu Yan for their help with the Raman testing. We sincerely thank Xue-Nan Zhao for photo sharpness optimization. This research was supported by the China Geological Survey Project (grant no. DD20190379-88) and the National Natural Science Foundation of China Project (grant no. 27812022003).

REFERENCES

Aurisicchio C., Conte A.M., Medeghini L., Ottolini L., De Vito C. (2018) Major and trace element geochemistry of emerald from several deposits: Implications for genetic models and classification schemes. *Ore Geology Reviews*, Vol. 94, pp. 351–366, http://dx.doi.org/10.1016/j.oregeorev.2018.02.001

Bai F., Pan H.H., Li X.M. (2019) Replacement degree of Al^{3+} and Cr/V ratio in high-V emeralds from Malipo, Yunnan, China. *Arabian Journal of Geosciences*, Vol. 12, article no. 377, http://dx.doi.org/10.1007/s12517-019-4465-2

Bersani D., Azzi G., Lambruschi E., Barone G., Mazzoleni P., Raneri S., Longobardo U., Lottici P.P. (2014) Characterization of emeralds by micro-Raman spectroscopy. *Journal of Raman Spectroscopy*, Vol. 45, No. 11-12, pp. 1293–1300, http://dx.doi.org/10.1002/jrs.4524

Chen Q., Bao P., Li Y., Shen A.H., Gao R., Bai Y., Gong X., Liu X. (2023) A research of emeralds from Panjshir Valley, Afghanistan. *Minerals*, Vol. 13, No. 1, article no. 63, http://dx.doi.org/10.3390/min13010063

Cui D., Wu Q., Liao Z.T., Qi L.J., Zhou Z.Y., Zhang L.M., Zhong Q., Liu Y.C., Li L. (2023) Growth heterogeneity and zonation characteristics of emeralds from Davdar, Xinjiang. *Earth Science Frontiers*, Vol. 30, No. 2, pp. 401–414, http://dx.doi.org/10.13745/j.esf.sf.2021.11.9 [in Chinese].

Dai H.Z., Wang D.H., Wang C.H., Huang F. (2017) New discovery of quartz vein-type of wolframite ores in the Qinling—Daba Area, Central Orogenic Belt, China. *Rock and Mineral Analysis*, Vol. 36, No. 5, pp. 559–560, http://dx.doi.org/10.15898/j.cnki.11-2131/td.201709040137 [in Chinese].

Dai H.Z., Wang D.H., Liu L.J., Huang F., Wang C.H. (2018) Study on emerald-level beryl from the Zhen'an W-Be polymetallic deposit in Shaanxi province by Electron probe microanalyzer and micro X-ray diffractometer. *Rock and Mineral Analysis*, Vol. 37, No. 3, pp. 336–345, http://dx.doi.org/10.15898/j.cnki.11-2131/td.201712140193 [in Chinese].

———(2019) Metallogenic epoch and metallogenic model of the Hetaoping W-Be deposit in Zhen'an County, South Qinling. *Acta Geologica Sinica*, Vol. 93, No. 6, pp. 1342–1358, http://dx.doi.org/10.19762/j.cnki.dizhixuebao.2019158 [in Chinese].

Dai L.Q., Zhao K., Zhao Z.F., Sun G.C., Gong B., Ma L.T. (2024) Slab subduction and pull link magmatism at active and passive continental margins. *Geophysical Research Letters*, Vol. 51, No. 1, article no. e2023GL106218, http://dx.doi.org/10.1029/2023GL106218

Dong J.Y., Huang F., Wang D.H. (2023a) Geochemical characteristics and geological significance of beryl in different types of beryllium deposits. *Acta Petrologica Sinica*, Vol. 39, No. 7, pp. 2153–2166, http://dx.doi.org/10.18654/1000-0569/2023.07.16 [in Chinese].

Dong J.Y., Huang F., Wei N. (2023b) Characteristics of fluid inclusions in beryl from different beryllium deposits in China. *Acta Geoscientica Sinica*, Vol. 44, No. 4, pp. 635–648, http://dx.doi.org/10.3975/cagsb.2022.122901 [in Chinese].

Dong Y.P., Liu X.M., Zhang G.W., Chen Q., Zhang X.N., Li W., Yang C. (2012) Triassic diorites and granitoids in the Foping area: Constrains on the conversion from subduction to collision in the Qinling orogen, China. *Journal of Asian Earth Sciences*, Vol. 47, pp. 123–142, http://dx.doi.org/10.1016/j.jseaes.2011.06.005

Gao Y., Sun X., Zhao Y., Deng K. (2023) Gem News International: Aquamarine with zigzag growth line inclusions. *G&G*, Vol. 59, No. 3, pp. 394–395.

Groat L.A., Giuliani G., Marshall D.D., Turner D. (2008) Emerald deposits and occurrences: A review. *Ore Geology Reviews*, Vol. 34, No. 1-2, pp. 87–112, http://dx.doi.org/10.1016/j.oregeorev.2007.09.003

Guo H., Yu X., Zheng Y., Sun Z., Ng M.F.-Y. (2020) Inclusion and trace element characteristics of emeralds from Swat Valley, Pakistan. *G&G*, Vol. 56, No. 3, pp. 336–355, http://dx.doi.org/10.5741/GEMS.56.3.336

He H., Tian H., Han K., Yang X., Zhao Y., Chao H. (2024) Study on fluid inclusions and stable isotopics of W-Mo ore deposits in the Ningshan-Zhen'an area, South Qinling, China. *Scientific Reports*, Vol. 14, article no. 16440, http://dx.doi.org/10.1038/s41598-024-67432-9

Hu Y., Lu R. (2019) Unique vanadium-rich emerald from Malipo, China. *G&G*, Vol. 55, No. 3, pp. 338–352, http://dx.doi.org/10.5741/GEMS.55.3.338

Jiang X., Yu X.Y., Guo B.J., Xu C. (2019) A study of mineral inclusions in emeralds from Malipo, Yunnan Province, China. *ACTA Petrologica et Mineralogica*, Vol. 38, No. 2, pp. 279–286 [in Chinese].

Lake D.J., Groat L.A., Falck H., Mulja T., Cempírek J., Kontak D., Marshall D., Giuliani G., Fayek M. (2017) Genesis of emerald-bearing quartz veins associated with the Lened W-skarn mineralization, Northwest Territories, Canada. *Canadian Mineralogist*, Vol. 55, No. 4, pp. 561–593, http://dx.doi.org/10.3749/canmin.1700025

Łodzinski M., Sitarz M., Stec K., Kozanecki M., Fojud Z., Jurga S. (2005) ICP, IR, Raman, NMR investigations of beryls from pegmatites of the Sudety Mts. *Journal of Molecular Structure*, Vol. 744, pp. 1005–1015, http://dx.doi.org/10.1016/j.molstruc.2004.12.042

Long Z.Y., Yu X.Y., Zheng Y.Y. (2021) Ore formation of the Dayakou emerald deposit (Southwest China) constrained by chemical and boron isotopic composition of tourmaline. *Ore Geology Reviews*, Vol. 135, article no. 104208, http://dx.doi.org/10.1016/j.oregeorev.2021.104208

Loughrey L., Marshall D., Ihlen P., Jones P. (2013) Boiling as a mechanism for colour zonations observed at the Byrud emerald deposit, Eidsvoll, Norway: Fluid inclusion, stable isotope and Ar-Ar studies. *Geofluids*, Vol. 13, No. 4, pp. 542–558, http://dx.doi.org/10.1111/gfl.12051

Marshall D., Pardieu V., Loughrey L., Jones P., Xue G. (2012) Conditions for emerald formation at Davdar, China: Fluid inclusion, trace element and stable isotope studies. *Mineralogical Magazine*, Vol. 76, No. 1, pp. 213–226, http://dx.doi.org/10.1180/minmag.2012.076.1.213

Moroz I., Roth M., Boudeulle M., Panczer G. (2000) Raman microspectroscopy and fluorescence of emeralds from various deposits. *Journal of Raman Spectroscopy*, Vol. 31, No. 6, pp. 485–490, http://dx.doi.org/10.1002/1097-4555(200006)31:6<485::AID-JRS561>3.0.CO;2-M

Okada T., Siritheerakul P. (2019) Micro-World: Helical inclusion in Colombian emerald. *G&G*, Vol. 55, No. 2, p. 262.

Paton C., Hellstrom J., Paul B., Woodhead J., Hergt J. (2011) Iolite: Freeware for the visualisation and processing of mass spectrometric data. *Journal of Analytical Atomic Spectrometry*, Vol. 26, No. 12, pp. 2508–2518, http://dx.doi.org/10.1039/C1JA10172B

Peng L.R., Segers M., Yang M.Y. (2023) Emerald and green beryl from Shaanxi province, China. *Journal of Gemmology*, Vol. 38, No. 7, pp. 648–650.

Qin L.J., Yu X.Y., Guo H.S. (2022) Fluid inclusion and chemical composition characteristics of emeralds from Rajasthan area, India. *Minerals*, Vol. 12, No. 5, article no. 641, http://dx.doi.org/10.3390/min12050641

Rondeau B., Fritsch E., Peucat J.J., Nordrum F.S., Groat L. (2008) Characterization of emeralds from a historical deposit: Byrud (Eidsvoll), Norway. *G&G*, Vol. 44, No. 2, pp. 108–122.

Saeseaw S., Pardieu V., Sangsawong S. (2014) Three-phase inclusions in emerald and their impact on origin determination. *G&G*, Vol. 50, No. 2, pp. 114–132, http://dx.doi.org/10.5741/GEMS.50.2.114

Saeseaw S., Renfro N.D., Palke A.C., Sun Z.Y., McClure S.F. (2019) Geographic origin determination of emerald. *G&G*, Vol. 55, No. 4, pp. 614–646, http://dx.doi.org/10.5741/GEMS.55.4.614

Schmetzer K., Martayan G. (2023) Morphology of Colombian emerald: Some less-common cases and their growth and dissolution history. *G&G*, Vol. 59, No. 1, pp. 46–71, http://dx.doi.org/10.5741/GEMS.59.1.46

Schmetzer K., Schwarz D., Bernhardt H.J., Häger T. (2006) A new type of Tairus hydrothermally-grown synthetic emerald, coloured by vanadium and copper. *Journal of Gemmology*, Vol. 30, No. 1-2, pp. 59–74.

Wood D.L., Nassau K. (1968) The characterization of beryl and emerald by visible and infrared absorption spectroscopy. *American Mineralogist*, Vol. 53, No. 5-6, pp. 777–800.

Woodhead J.D., Hellstrom J., Hergt J.M., Greig A., Maas R. (2007) Isotopic and elemental imaging of geological materials by laser ablation inductively coupled plasma-mass spectrometry. *Geostandards and Geoanalytical Research*, Vol. 31, No. 4, pp. 331–343, http://dx.doi.org/10.1111/j.1751-908X.2007.00104.x

Xu Z.Q., Yang J.S., Li H.Q., Wang R.R., Cai Z.H. (2012) Indosinian collision-orogenic system of Chinese continent and its orogenic mechanism. *Acta Petrologica Sinica*, Vol. 28, No. 6, pp. 1697–1709 [in Chinese].

Yang Y.L., Shen X.T., Fan Y.R., Huang W.Z., Pei J.C. (2022) UV-Vis-NIR spectroscopic characteristics of vanadium-rich hydrothermal synthetic emeralds from Russia. *Spectroscopy and Spectral Analysis*, Vol. 42, No. 4, pp. 1199–1203, http://dx.doi.org/10.3964/j.issn.1000-0593(2022)04-1199-05 [in Chinese].

Yu X.Y., Zheng Y.Y., Zhang T.Y., Guo H.S., Long Z.Y., Wan J.X., Zhang C. (2020) The genesis of color zonation of emerald from Dayakou, Yunnan Province: Implication for multi-stage

mineralization. *Earth Science Frontiers*, Vol. 27, No. 5, pp. 116–125, http://dx.doi.org/10.13745/j.esf.sf.2020.5.48 [in Chinese].
Yu X.Y., Long Z.Y., Zhang Y., Qin L.J., Zhang C., Xie Z.R., Wu Y.R., Yan Y., Wu M.K., Wan J.X. (2021) Overview of gemstone resources in China. *Crystals*, Vol. 11, No. 10, article no. 1189, http://dx.doi.org/10.3390/cryst11101189
Zhang G.W., Meng Q.R., Yu Z.P., Sun Y., Zhou D.W., Guo A.L. (1996) Orogenic process and dynamic characteristics of Qinling orogenic belt. *Science in China (Series D)*, Vol. 26, No. 3, pp. 193–200 [in Chinese].
Zhang G.W., Dong Y.P., Yao A.P. (1997) The crustal compositions, structures and tectonic evolution of the Qinling orogenic belt. *Geology of Shaanxi*, Vol. 15, No. 2, pp. 1–14, [in Chinese].
Zheng Y.Y., Yu X.Y., Guo H.S. (2019) Major and trace element geochemistry of Dayakou vanadium-dominant Emerald from Malipo (Yunnan, China): Genetic model and geographic origin determination. *Minerals*, Vol. 9, No. 12, article no. 777, http://dx.doi.org/10.3390/min9120777
Zheng Y.Y., Yu X.Y., Xu B., Guo H.S., Yan Y., Zhang Y., Tang J., Zhao S.Y. (2024) A review of research on emerald origin determination. *ACTA Petrologica et Mineralogica*, Vol. 43, No. 3, pp. 525–561, http://dx.doi.org/10.20086/j.cnki.yskw.2024.0304 [in Chinese].

Thank You, Reviewers

GEMS & GEMOLOGY requires each manuscript submitted for publication to undergo a rigorous peer review process, in which each paper is evaluated by at least three experts in the field prior to acceptance. This is essential to the accuracy, integrity, and readability of *G&G* content. In addition to our dedicated Editorial Review Board, we extend many thanks to the following individuals who devoted their valuable time to reviewing manuscripts in 2025.

Non-Editorial Board Reviewers

Dudley Blauwet • Si Athena Chen • Gagan Choudhary • Céline Rose David • Shiyun Jin • Edward Liu • Joe Dan Lowry • Virgil Lueth • Cidgem Lule • Scott Sucher • Frederick Lin Sutherland • Rachelle Turnier • Wim Vertriest • Mingxing Yang • Alexandre Zaitsev

An Evaluation of Turquoise from The Mona Lisa Mine in Arkansas

Alexander A. Goodsuhm

Turquoise from the Mona Lisa mine, located in Polk County in the U.S. state of Arkansas, gained renewed interest in 2018 when Avant Mining promoted the re-opening of the mine, displaying an approximately 111 kg stabilized turquoise nugget at the AGTA GemFair in Tucson, Arizona. The unique location and geologic setting of the mine led many to question whether this material was turquoise and how it could have formed. Phosphate minerals are prevalent in Arkansas, but the lack of an obvious copper source in this area was considered an obstacle to turquoise formation. In this study, samples obtained during multiple visits to the mine were analyzed to identify their chemistry and structure. X-ray diffraction, Raman spectroscopy, ultraviolet/visible/near-infrared and Fourier-transform infrared spectroscopy, and mass spectrometry results were obtained and combined with geologic observations and measurements to comprehensively characterize Mona Lisa turquoise. Copper was identified as a major elemental component of all tested samples, with copper oxide concentrations ranging from 1.71 to 6.18 wt.%. The presence of copper in major element amounts warrants the use of the term *turquoise* in a gemological context, although the broad range of concentrations suggests solid-solution relationships between turquoise-group minerals, highlighting the inherent heterogeneity and complex mineralogy of turquoise deposits.

Few gemstones have a history as extensive and diverse as turquoise. From ancient civilizations in China and the pharaohs of Egypt to modern designers, this opaque gemstone has captured the imagination of cultures and communities everywhere. In the United States, turquoise has long been associated with Native American cultures. While mines across arid regions in Arizona, New Mexico, Nevada, Colorado, and California have storied histories and archaeological importance, many of these sites today are increasingly depleted. Turquoise remains in great demand, with global and domestic markets placing a premium on stones with recognized mine origins. Although isolated sedimentary turquoise mineralization has been observed and recorded in the U.S. outside the American Southwest, such as in Clay County, Alabama (Harwood and Hajek, 1978), mining those sites has not been economically practical. However, in 2018, a previously inactive turquoise claim—the Mona Lisa mine—in the Ouachita Mountains of western Arkansas was purchased by Avant Mining LLC, and "Mona Lisa turquoise" reentered the marketplace (figures 1–3). Limited information exists about the

Figure 1. Left: Rough and cut turquoise and matrix from the Mona Lisa mine, Polk County, Arkansas. Rock samples are untreated, while the polished slab and cabochons (4.16–37.19 ct) are stabilized. Right: "Lightning bolt" untreated turquoise in matrix specimen (27.90 ct) from the Mona Lisa mine. Photos by Emily Lane.

See end of article for About the Authors and Acknowledgments.
Gems & Gemology, Vol. 61, No. 4, pp. 374–391,
http://dx.doi.org/10.5741/GEMS.61.4.374

Figure 2. Stabilized Mona Lisa turquoise set in silver. Photo courtesy of White Horse Resale; necklace courtesy of Vernon and Clarissa Hale.

Mona Lisa mine, leading to skepticism about the mine's validity as a commercial turquoise source.

The presence of turquoise in western Arkansas had been previously documented (Sinkankas, 1997), but the extent and nature of the deposit had not been fully described. The wetter climate of the Ouachita Mountains (compared to the American Southwest) causes accelerated weathering of phosphate minerals, including turquoise. Arkansas also lacks the past igneous activity and related copper porphyry deposits found in the geology of more commonly known turquoise mining locations. The absence of abundant copper mineralization in Arkansas has led to speculation that the turquoise from the Mona Lisa mine is not turquoise but rather a pale green to blue copper-deficient mineral, planerite, of the turquoise group. Planerite is one of several phosphate minerals frequently found in Arkansas. A more complete mineralogical description and evaluation of the Mona Lisa mine is the focus of this study, to determine whether the material is turquoise. When characterizing turquoise sources, archaeological implications must also be considered. Although there is no record of Mona Lisa turquoise use by indigenous tribes, turquoise artifacts found at regional Caddo archaeological sites in East Texas—which have been attributed to trade with the

Figure 3. "Old stock" stabilized green Mona Lisa turquoise in novaculite matrix set in a silver ribbon pendant. Photo courtesy of White Horse Resale.

American Southwest—offer the slight possibility that Mona Lisa turquoise was mined by Native Americans in southwest Arkansas.

This research represents the most comprehensive historical, geological, and mineralogical evaluation of Arkansas's Mona Lisa mine, with detailed characterization and analyses of material from this source. Multiple trips to the mine from 2020 to 2022 resulted in extensive field observations, mapping, and sample collection. Raman spectroscopy and X-ray diffraction (XRD) techniques were employed to confirm the identity of the turquoise and its accompanying matrix. Moreover, Fourier-transform infrared (FTIR) and ultraviolet/visible/near-infrared (UV-Vis-NIR) spectroscopy were used to identify the chromogenic components and reveal any possible treatment of loose cabochons (which is commonly encountered in turquoise samples). Geochemical data were utilized

In Brief

- The Mona Lisa mine is a turquoise occurrence in Polk County, Arkansas, USA.
- X-ray diffraction, Raman spectroscopy, ultraviolet/visible/near-infrared and Fourier-transform infrared spectroscopy, and mass spectrometry results were used to characterize material from the Mona Lisa mine.
- While the area lacks a well-known copper source, copper was identified as a major elemental component in the tested samples, warranting use of the name *turquoise* in a gemological context.
- This turquoise occurrence is unique in its location and mineralogy and has the potential to increase its production in the coming years.

to identify major element compositions, which were compared to established turquoise-group minerals. The scope of this research increases the understanding of the Mona Lisa mine, a modern source of American turquoise.

HISTORY

In 1877, phosphate minerals in Arkansas were first described from a variscite locality in Montgomery County (Chester, 1877). In 1883, Arkansas wavellite was discovered and reported by George Kunz (1883), and mining for "phosphate rock" in multiple Arkansas counties began in the twentieth century (Stroud et al., 1969). In the years prior to World War II, geoscientists with the Work Progress Administration (WPA) and other government agencies uncovered other aluminum phosphate localities as they explored the potential for manganese resources in western Arkansas (Barwood and deLinde, 1989). The Mona Lisa mine site, located on the ridge of Little Porter Mountain, first opened in 1958 for mining phosphate for agricultural fertilizers. Broader-scale phosphate mining in other Arkansas counties (e.g., Searcy, Van Buren, Independence, Pulaski) decreased the demand for such material, leading to the Mona Lisa site's closure before 1963 (Stroud et al., 1969). In 1974, the mine was rediscovered by Jack McBride, who reportedly built a cabin near the mine (Wigley, 2006). Later reports indicated that the mine was leased at the time to multiple parties over the course of the year, the rights belonging to McBride, James McBroom, and the Newton Company, Inc., respectively. The mine was known by many names in the 1970s, including "the McBride," "Newton Company," "Blue Bird," "McBroom," and "Mona Lisa" (Sinkankas, 1997). Prior to 1978, turquoise production involved the use of a simple vertical shaft to intersect the turquoise zone (at a depth of about 9 m), followed by digging horizontal tunnels to find the extent of the deposit (Ericksen et al., 1983). Cumulative turquoise production reportedly did not exceed 272 kg during that period of production (Ericksen et al., 1983).

Charles "Chuck" Mayfield learned of the mine in the late 1970s, filing several claims while prospecting for samples in the area (Smith, 1981). Following the turquoise boom of the 1970s, Mayfield began mining the turquoise commercially in 1981 (Fellone, 1983). At this time, Jack Wigley, a construction contractor from Dallas, Texas, became involved with the operation, working with a backhoe and limited blasting in addition to hand tools. By 1982, both Wigley and Mayfield had described the discovery of an enormous turquoise nugget weighing approximately 172 kg. During this initial period, some turquoise from the mine was accurately marketed as "Arkansas turquoise" (figure 4), while the material was also sold as "Southwestern turquoise," resulting in difficulty evaluating the true amount and value of production from the Mona Lisa mine (Archuleta and Renfro, 2018). Wigley (2006) stated that his unfamiliarity

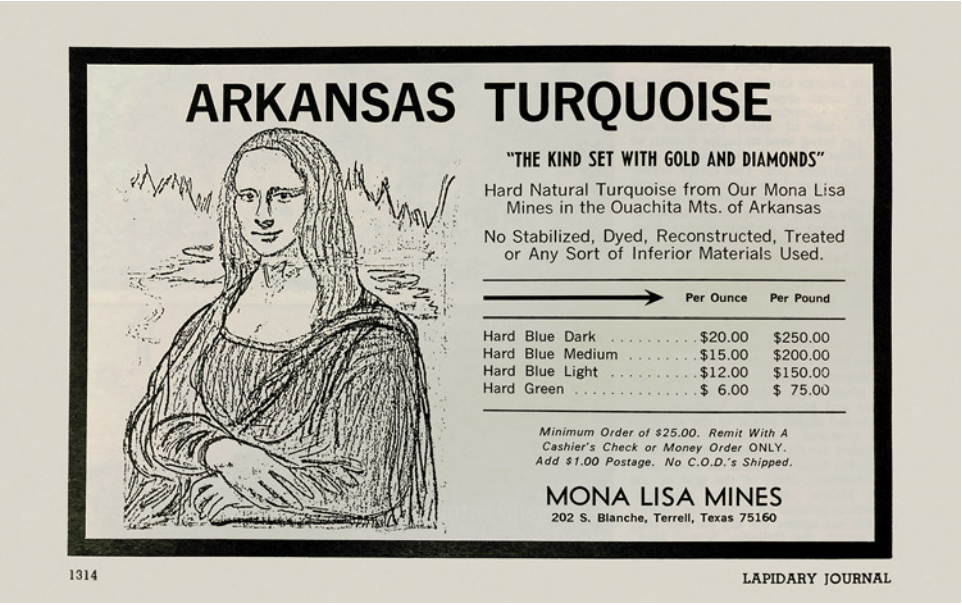

Figure 4. A 1980 advertisement for Arkansas turquoise in Lapidary Journal.

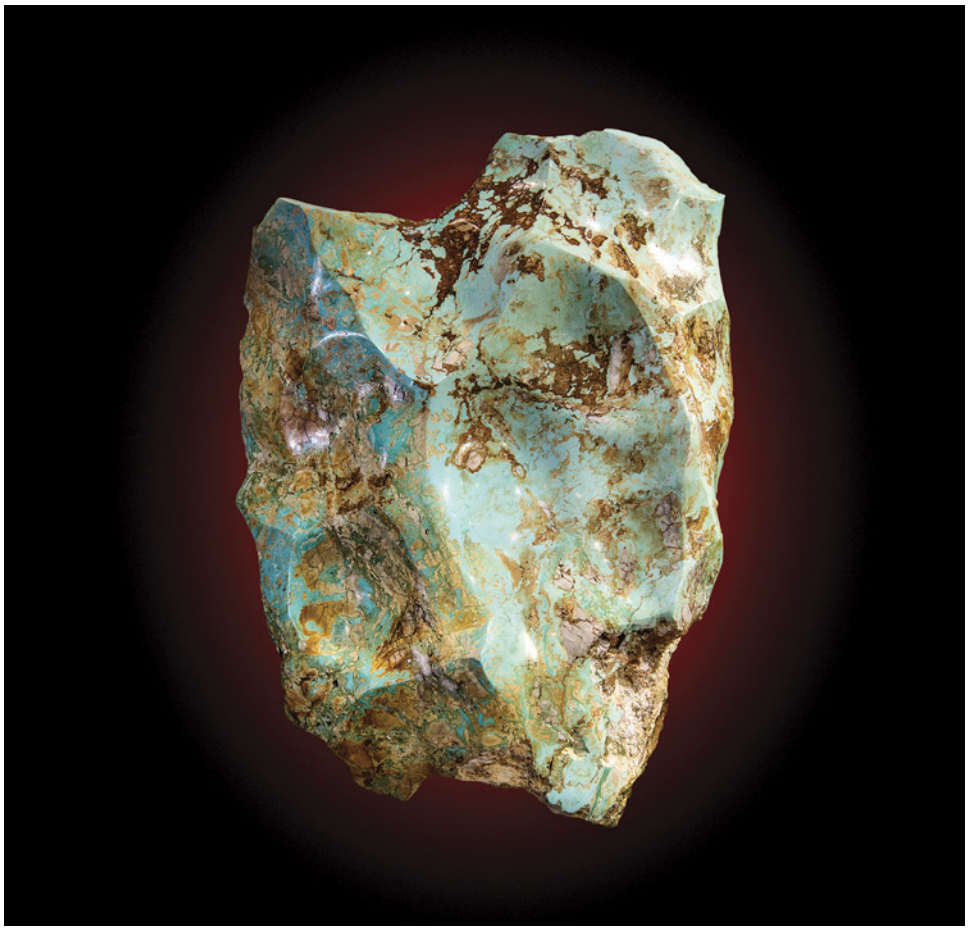

Figure 5. This 111 kg stabilized turquoise nugget, measuring approximately 1 m × 50 cm × 30 cm, was originally recovered from the Mona Lisa mine in the 1980s. Polished in 2018 by Michael Beck (Copper Canyon Lapidary & Jewelry, Sedona, Arizona). Photo by Robert Weldon.

with turquoise mining led to significant material being lost; lower-grade material was simply discarded when it could have been impregnated to allow cutting and polishing. Increased competition from other sources in the U.S. turquoise market caused operations to close in 1986, and further reports suggested that the open trench had been "mined out." Interestingly, neither Wigley nor Mayfield mentioned each other by name in their respective reports from the site, although it appears they mined turquoise at the Mona Lisa mine during the same time period. From 1989 to 1991, the mine was reclaimed by the National Forest Service (Laney, 2020), and it remained inactive for more than two decades, serving only as a minor collecting locality for informed rockhounds.

In 2017, James Zigras, founder and owner of Avant Mining LLC, purchased the mining claim and leased the subsurface mineral rights from the Bureau of Land Management (Targeted News Service, 2020) where the mine is located in the Ouachita National Forest. A test trench in early 2018 produced 454 kg of turquoise within one week (Archuleta and Renfro, 2018), an amount that encouraged further development. Avant Mining promoted the re-opening of the mine at the 2018 AGTA GemFair in Tucson, Arizona, displaying the extremely large rough turquoise nugget found in the early 1980s. Unearthed at 172 kg, the nugget has since been polymer impregnated and polished, currently weighing 111 kg and touted as the "largest American turquoise nugget ever discovered" (figure 5). Since its reentry into the market, the Mona Lisa mine has been operating sporadically, with minor interruptions caused by the COVID-19 pandemic, inclement weather, and delayed access to equipment. Avant Mining has continued to uncover new areas of turquoise mineralization and occasionally offers fee digs, allowing rockhounds and collectors to visit the site.

CLIMATE AND GEOLOGY

While turquoise is found in varying climates around the world, the climate at the Mona Lisa mine distinctly contrasts with the arid climates in the turquoise mining districts of the American Southwest. The Ouachita Mountains' hilly terrain is

Figure 6. The Mona Lisa mine trench, facing eastward in April 2022. Photo by Alexander Goodsuhm.

characterized as temperate (humid subtropical), with most precipitation in the fall and spring. Total precipitation averages around 150 cm per year in the town of Mena (Polk County seat), roughly 22 km northwest of the mine (U.S. Climate Data, 2022). The annual mean temperature in the Mena area is 16°C (60.8°F), the result of hot summers and mild winters. The plant growth on the mountain ridges is dependent on exposure to sunlight, with some areas densely forested (e.g., shortleaf pines, various hardwoods) and others sparsely.

The Mona Lisa mine currently consists of an approximately 90-meter-long open trench (figure 6) dug into weathered and fractured host rock along the ridge of Little Porter Mountain in Polk County, Arkansas. The trench is located near the contact and transition between the Missouri Mountain Shale and Arkansas Novaculite, with thin beds of shale visible just south of the trench and interbedded in novaculite within the trench.

Arkansas's Late Devonian to Early Mississippian Novaculite Formation (figure 7) consists of multicolor high-purity cryptocrystalline silica that derives its name from the Latin for "razor" due to the prevalent usage of the material for whetstones (Goldstein, 1959). Novaculite is differentiated from chert by its lighter color, lack of lamination and chalcedony, and less organic and clastic material (Goldstein, 1959). The deposition of the Arkansas Novaculite remains a complicated geologic topic, with fossil remains of radiolaria, spores, and sponge spicules offering some

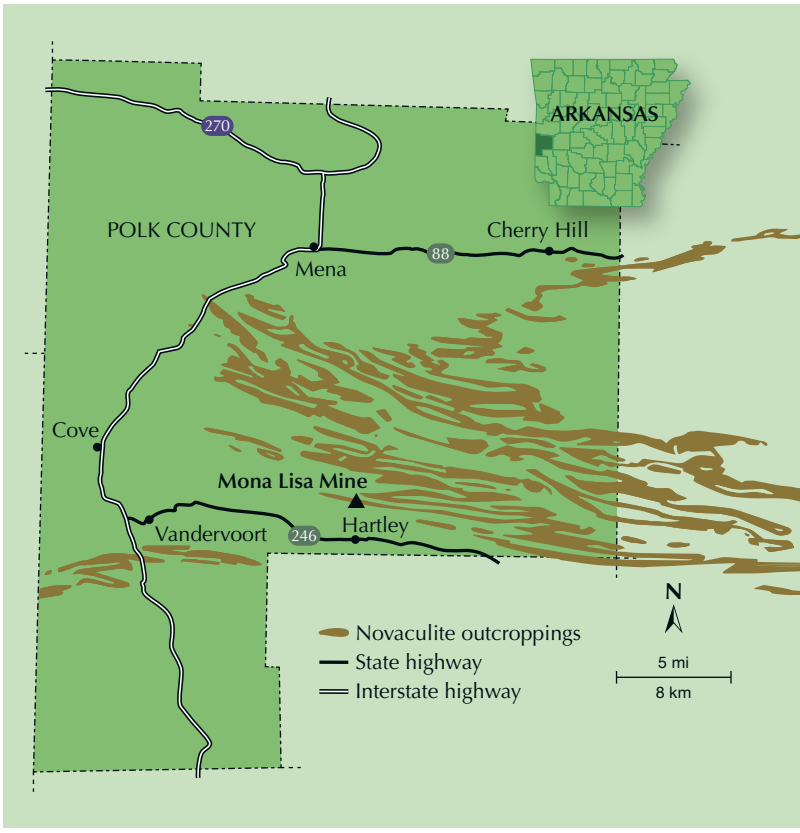

Figure 7. Map of the Mona Lisa mine location in Polk County, Arkansas, showing geologic outcroppings of novaculite in the area. Cartography by Thomas Paradise.

Figure 8. The extent and location of the Ouachita orogenic system. Most of the orogenic belt is blanketed by younger sedimentation, apart from the Ouachita Mountains in Arkansas and Oklahoma. Modified from Harry and Mickus (1998).

evidence that the silica was derived organically (Goldstein, 1959). However, elemental concentrations of the rock show a reasonable resemblance to that of a magmatic body associated with arc volcanism, caused by the deposition of siliceous volcanic ash into the ocean (Philbrick, 2016).

The Early-Middle Paleozoic rocks found in the Ouachita Mountains record the rifting along the southern margin of the North American craton, the beginnings of a complete Wilson Cycle—regressing and transgressing coasts. During the Late Paleozoic, the closing of the ocean basin began, starting with collision in the east—the Appalachian Orogeny—between the North American craton and the African plate (Gutschick and Sandberg, 1983). As this impact continued, an accretionary wedge was thrust on top of the subducting plate, causing extensive faulting and folding (Houseknecht and Matthews, 1985). The brittle deformation provided the means of transport for mineralized veins to form, with radiometric dating of adularia (a variety of potassium feldspar) in the veins confirming Late Pennsylvanian to Early Permian deformation and development (Richards et al., 2002). This tectonic activity during the Ouachita Orogeny (~318 to 271 Mya; figure 8) provided the setting for the unique geologic conditions that facilitated the mobilization and mineralization of phosphates such as turquoise.

Turquoise-Group Minerals. For this study, it was crucial to distinguish between multiple mineral species that may share similar properties and to define *turquoise* accurately. Scanning electron microscopy (SEM), thermogravimetric analysis (TGA), Mössbauer spectroscopy, X-ray diffraction (XRD), electron probe microanalysis (EPMA), Fourier-transform infrared (FTIR) spectroscopy, and Raman spectroscopy have been previously used to analyze the crystallography and chemistry of turquoise (Foord and Taggart, 1998; Frost et al., 2006; Abdu et al., 2011). Prior research on turquoise and related phosphate minerals led to the establishment of the mineralogic turquoise group—a set of turquoise and five similar minerals with minor chemical differences (Foord and Taggart, 1998).

The turquoise group is comprised of turquoise ($CuAl_6(PO_4)_4(OH)_8 \cdot 4H_2O$), planerite ($Al_6(PO_4)_2(PO_3OH)_2(OH)_8 \cdot 4H_2O$), chalcosiderite ($CuFe^{3+}_6(PO_4)_4(OH)_8 \cdot 4H_2O$), faustite ($ZnAl_6(PO_4)_4(OH)_8 \cdot 4H_2O$), aheylite ($(Fe^{2+}, Zn)Al_6(PO_4)_4(OH)_8 \cdot 4H_2O$), and an unnamed iron-bearing end member ($Fe^{2+}Fe^{3+}_6(PO_4)_4(OH)_8 \cdot 4H_2O$). These mineral species are isostructural, with limited differences in unit cell dimensions. The general chemical formula for the turquoise-group minerals is commonly expressed as $A_{0-1}B_6(PO_4)_4(OH)_8 \cdot 4H_2O$ (Abdu et al., 2011). The A site is occupied by divalent cations, typically Cu^{2+}, Zn^{2+}, and/or Fe^{2+}, while the B site houses the trivalent cations Al^{3+} or Fe^{3+}. The range in metal compositions at the A and B sites is responsible for variation in color in turquoise-group minerals (Abdu et al., 2011). All members of the turquoise group form in the triclinic crystal system, representing the space group $P\bar{1}$, with the only symmetrical element being a point of inversion. Focusing on the crystallography of turquoise-group minerals requires additional nomenclature to

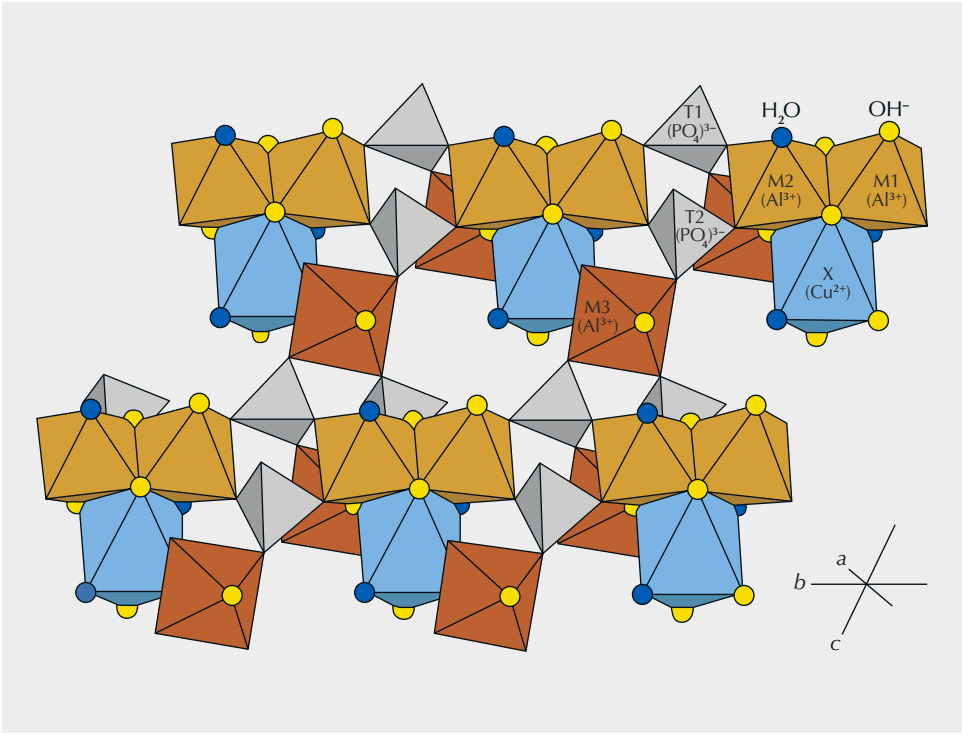

Figure 9. An illustration of the triclinic crystallographic structure of turquoise with structural sites (structural formula: $X(M1_2M2_2M3_2)_{\Sigma=6}(PO_4)_4(OH)_8{\cdot}4H_2O$) and the corresponding ions for ideal turquoise. Modified from Abdu et al. (2011).

describe the structural relationships between the chemical components.

The turquoise-group formula that best represents the crystal structure of the unit cell is $X(M1_2M2_2M3_2)_{\Sigma=6}(PO_4)_4(OH)_8{\cdot}4H_2O$. The structural formula differentiates the positions of the four octahedrally coordinated cation sites. The X, M1, M2, and M3 crystallographic sites are coordinated by oxygen and hydroxide anions. The tetrahedral anionic phosphate groups, characteristic of all phosphate minerals, share corners with the M1 and M2 sites, extending in the crystallographic *b* direction (Abdu et al., 2011). The X octahedra shares an edge with the M1 and M2, while shared corners between the tetrahedral phosphate and the M3 site extend the motif in the *a* and *c* directions (figure 9). The structure is additionally strengthened by hydrogen bonds between $(OH)^-$ groups (Abdu et al., 2011). Resulting from this structure, the X site and the M3 site's differences in spatial arrangement from the M1 and M2 sites permit the substitution of certain elements in particular locations; the X site accepts divalent cations with intermediate ionic radii (Cu^{2+}, Zn^{2+}, Fe^{2+}), as the M sites accept trivalent cations with smaller radii (Al^{3+}, Fe^{3+}), with M3 preferring more frequent substitutions (Abdu et al., 2011). Strict compositional boundaries between turquoise-group end members have not been explicitly defined. Due to solid-solution relationships and the typical micro- to cryptocrystalline nature of turquoise-group minerals, chemical analyses frequently demonstrate heterogeneity and intermediate compositions. Defining compositional boundaries between end members can be complex: the prevalence of site vacancies must be determined for planerite, and the oxidation state of iron must be considered for aheylite and chalcosiderite. As faustite and turquoise differ by their X-site occupancy, using the zinc-to-copper ratio can more directly discriminate between the two.

MATERIALS AND METHODS

Samples. Ten natural turquoise samples with matrix components were donated by Avant Mining for analysis (TQ-A1 through TQ-J1; figure 10). The author selected these samples from an array of material produced by the test trench and found in old mine tailings. Samples were selected intentionally to encompass the range of material found at the mine, with differences in color and hardness (table 1). Based on GIA's colored stone reference collection classification scheme, these samples are C type, collected on-site from the miners (Vertriest et al., 2019). Samples were also collected directly by the author (A type)

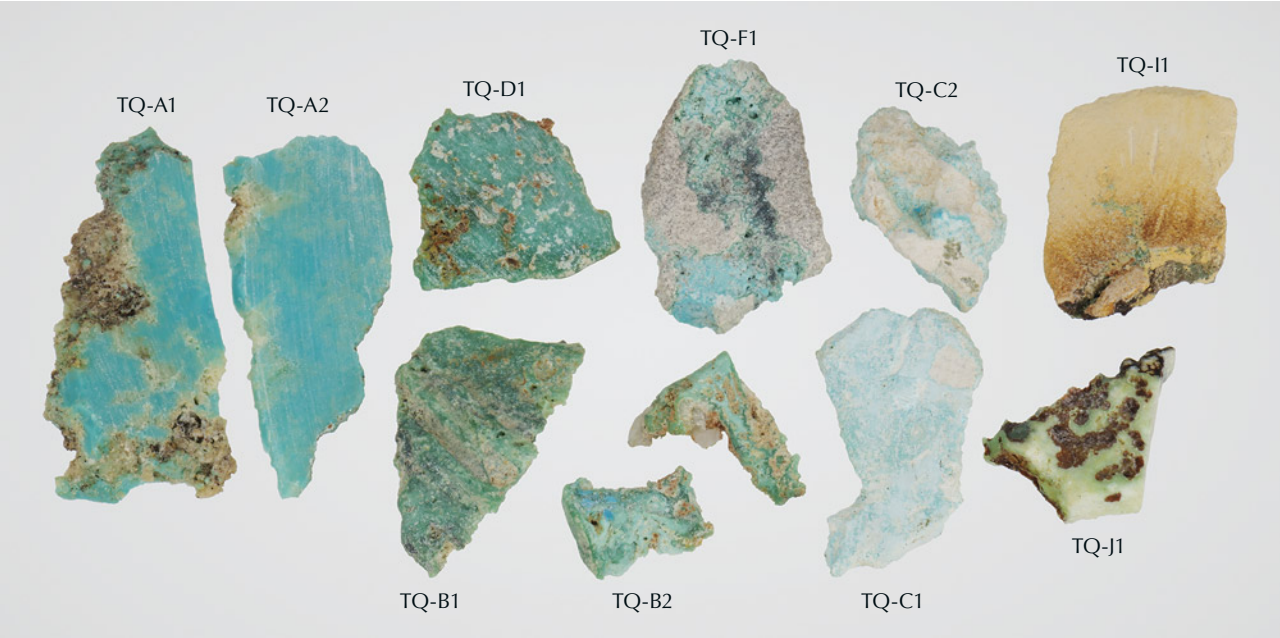

Figure 10. Slabbed natural turquoise samples from the Mona Lisa mine (1.45–7.71 ct). After analysis, sample TQ-B2 broke into two pieces during handling. Photo by Emily Lane.

but were generally too small for full analysis using the methods outlined in this study. Avant Mining also supplied six polymer-impregnated turquoise cabochons (ML-01 through ML-06) and a polymer-impregnated turquoise and matrix slab, demonstrating stabilized examples of the material now available on

TABLE 1. Color, hardness, and results of X-ray diffraction and Raman spectroscopy for ten untreated Mona Lisa turquoise slabs.

Sample no.	Color	Hardness	XRD (TGM)[a]	XRD (matrix)	Raman (TGM)	Raman (matrix)
TQ-A1	Greenish blue	5.5–6.0	Turquoise	nd[b]	Turquoise	nd
TQ-A2	Greenish blue	4.5–5.0	Faustite	nd	Turquoise	nd
TQ-B1	Bluish green	6.0	Turquoise	nd	Turquoise	Quartz
TQ-B2	Green and greenish blue	6.0	nd	Quartz	Turquoise	Quartz
TQ-C1	Greenish blue	5.0–6.0	Turquoise	nd	Turquoise	Quartz
TQ-C2	Greenish blue	4.5–5.0	Faustite	nd	Turquoise	nd
TQ-D1	Blue-green	6.0	Turquoise	nd	Turquoise	Anatase
TQ-F1	Greenish blue	6.0	Turquoise	nd	Turquoise	Quartz
TQ-I1	Blue-green	<2.5	nd	Crandallite	nd	Quartz
TQ-J1	Yellowish green	6.0	Planerite	nd	Planerite	nd

[a]*TGM = turquoise-group mineral.*
[b]*nd = not detected.*

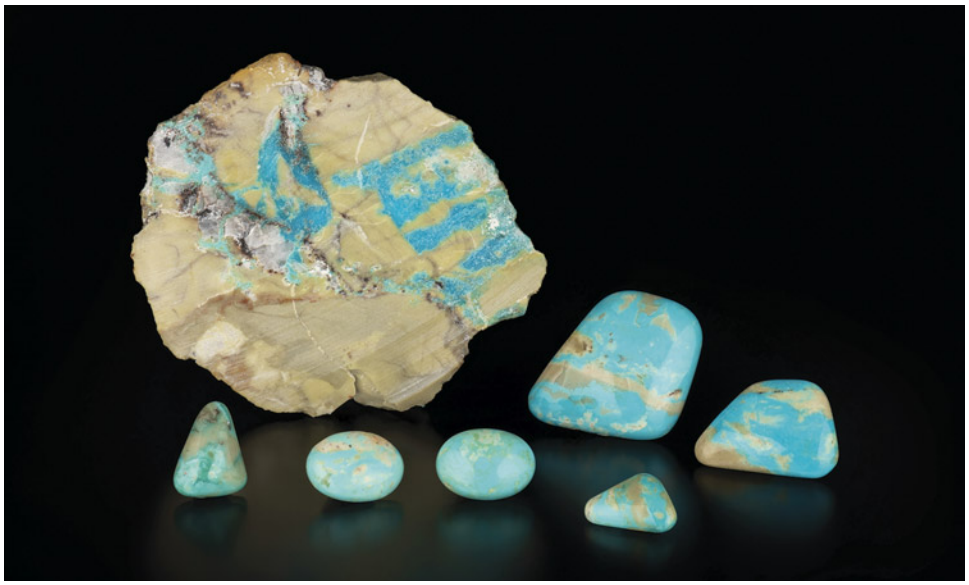

Figure 11. Stabilized turquoise cabochons (ML-01 through ML-06) weighing 4.16–37.19 ct and a 57.9 g slab from the Mona Lisa mine. Photo by Emily Lane; courtesy of Avant Mining LLC.

the market (figure 11). Stabilization refers to the process of impregnating turquoise with polymer, resin, or wax, which can improve the color and usability of a specimen.

Fieldwork. Several field expeditions to the Mona Lisa mine were conducted from 2020 to 2022. To represent the scale of the mine, Thomas R. Paradise, professor of geosciences at the University of Arkansas, and the author constructed an isohypsometric (relative elevation) map from a false datum outside the mine trench. The spatial relationships were preserved using tape measures, Abney and laser levels, and a 10-meter stadia rod. Changes in rock type and widespread fracturing of the host rock were observed. The bedding orientations of the geologic formations were recorded using Brunton compasses and the Stereonet Mobile application (Allmendinger et al., 2017). At the time of the visits, the mine was inactive, and little *in situ* turquoise was observable. Turquoise mineralization patterns in the trench suggested the turquoise formed in preexisting fractures and voids in the host rock (figure 12). Therefore, the existing fractures in the host Arkansas Novaculite formation represented the most efficient channels for mineralization. Gregory Dumond, associate professor of geosciences at the University of Arkansas, and the author measured the orientations of more than 200 fractures within the Mona Lisa mine trench.

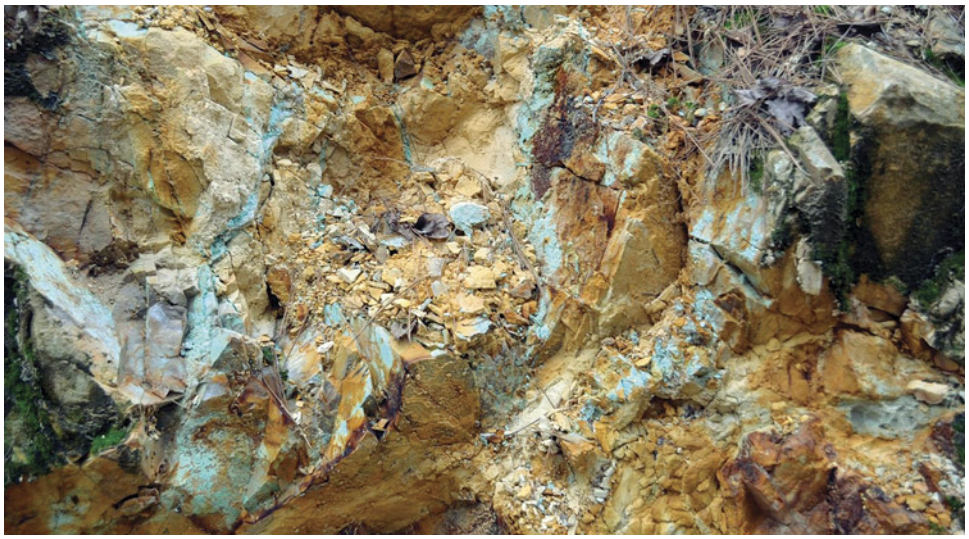

Figure 12. Turquoise mineralization in host novaculite at the Mona Lisa mine, facing south from the center of the trench. Photo by Thomas Paradise.

Physical Properties. Sample colors were recorded under daylight-equivalent lighting. Hardnesses were determined using Mohs hardness pencils calibrated to every 0.5 unit on the Mohs hardness scale.

UV-Vis-NIR Spectroscopy. UV-Vis-NIR spectra were collected on untreated and treated samples at GIA in Carlsbad, California, using a GIA UV-Vis-NIR spectrometer in the 250–985 nm wavelength range. Spectra were recorded in a reflective configuration, using a Labsphere certified reflectance standard for establishing the background. Three averages per analysis were collected, with an integration time of 100 ms and resolution bandwidth of 0.7–0.8 nm.

FTIR Spectroscopy. Transmission IR spectra from the six stabilized samples and ten rough untreated samples were collected at GIA with a Thermo Nicolet 6700 FTIR spectrometer over a 600–6500 cm^{-1} range. The KBr pellet method was used to allow transmission through the samples. Spectral resolution was set at 4 cm^{-1}, with 64 scans per analysis.

X-Ray Diffraction. Ten samples were cut into small slabs and analyzed by Andrian V. Kuchuk from the University of Arkansas Nanocenter for XRD patterns on a Malvern Panalytical X'Pert^3 Materials Research Diffractometer. Sample slabs (not powdered samples) were analyzed directly to preserve the specimens. XRD is a quick tool to identify mineral crystal structures; this conventional technique has been used in many turquoise studies due to the link between structure and chemistry (Foord and Taggart, 1998). Samples were scanned between the 5.04° to 50.96° 2θ angles with a step size of 0.015° every 0.6 seconds. The radiation was sourced from a copper anode with a wavelength of 1.5406 Å. The PANalytical X'Pert HighScore mineral software was used to process the data and identify the mineral phases. QUALX2.0 diffraction software (Altomare et al., 2008, 2015) was used to better differentiate sample spectra when they could be compared to crystal structures within public databases (e.g., POW_COD; Gražulis et al., 2012; Altomare et al., 2015). Peaks were matched with the dominant crystal phases after background correction based on figure of merit of the database entries.

Raman Spectroscopy. Raman analysis was conducted by the author at Baylor University in Texas using a Thermo Scientific DXR Raman microscope fitted with a 10× objective, 532 nm laser, 25 μm pinhole, and 1800 lines/mm grating. Analyses were conducted at room temperature (~21°C) with a spot size of 2.1 μm. As documented in other Raman studies of turquoise, fluorescence correction was applied with adjusted laser power (from 8.0 to 1.0 mW) to account for peak saturation and to limit disturbances (Dumańska-Słowik et al., 2020). In previous research, the Raman signature of turquoise was mapped by Frost et al. (2006), Čejka et al. (2015), and Dumańska-Słowik et al. (2020), whereby each vibrational mode can be attributed to types of bonding within the turquoise sample. Then the RRUFF library (Lafuente et al., 2015) was queried for reference spectra to compare with the Mona Lisa material.

Geochemistry. Two natural turquoise samples were chemically analyzed by laser ablation–inductively coupled plasma–mass spectrometry (LA-ICP-MS) at GIA. Samples TQ-C1 and TQ-D1 were selected for analysis for their differing appearances, confirmed identities by Raman and XRD as members of the turquoise group, and suitability for the methodology (chalkier samples caused issues with establishing a clean background in the sample chamber). The system links a Thermo Fisher iCAP Qc ICP-MS with an Elemental Scientific Lasers 213 nm laser. Three spots measuring 55 μm in diameter were collected on two samples with a fluence of ~10 J/cm^2 and a 10 Hz repetition rate. Spot locations were chosen on areas of the samples with minimal visible matrix influence. Two samples of untreated Sleeping Beauty turquoise (Globe, Arizona), donated by the Turquoise Museum (Albuquerque, New Mexico), were also analyzed to directly compare Mona Lisa mine material with turquoise from a well-known source. Three external standards—NIST 610, GSD-1G, and GSE-1G—were used in conjunction with ^{27}Al as an internal standard. Ideal turquoise phosphorus concentrations (P_2O_5 = 34.90 wt.%) were assumed during data processing according to stoichiometric calculations. The data was then converted to wt.% oxides in order to view major element concentrations. Varying oxidation states, especially of iron substituting into turquoise's formula at multiple sites, complicates the conversion of wt.% data to atoms per formula unit. Due to the imprecise nature of those calculations based on LA-ICP-MS data, the focus here is solely on the oxides and how they relate to the turquoise mineral group.

RESULTS

Gemological Characteristics. Within the Mona Lisa mine trench, the appearance of the material varied

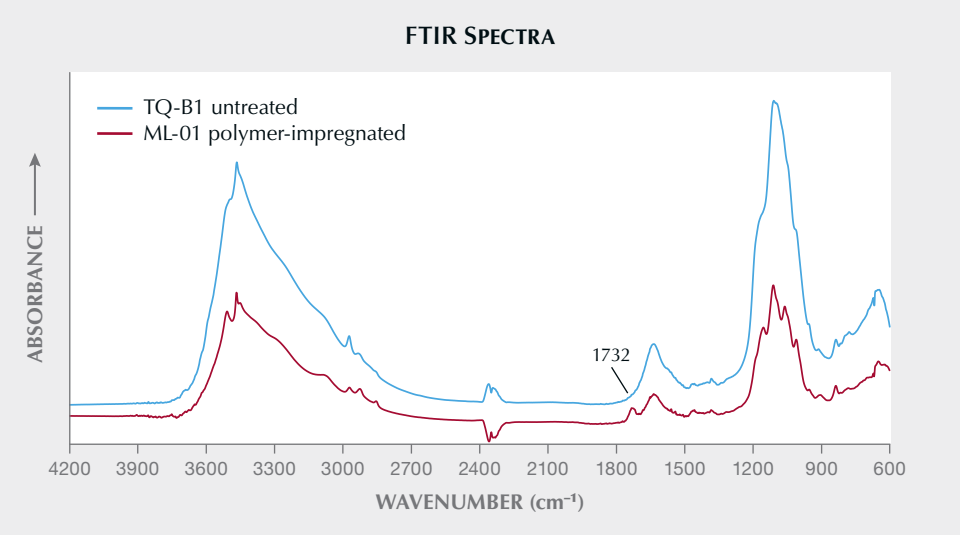

Figure 13. FTIR spectra of untreated (TQ-B1) and polymer-impregnated (ML-01) Mona Lisa turquoise. The carbonyl band at ~1732 cm^{-1} identifies the presence of polymer. Spectra are offset vertically for clarity.

from chalky and pale colored (material requiring stabilization) to harder, more saturated greenish blue turquoise (not requiring stabilization). Sample colors ranged from yellowish green to greenish blue (again, see table 1). Samples ranged in hardness from <2.5 for chalky turquoise to 6 for more coherent samples. The hardness of turquoise is generally between 5 and 6 on the Mohs scale.

Example IR spectra (figure 13) display typical turquoise bands based on OH (~3509 cm^{-1}), H_2O (~1635 cm^{-1}), and PO_4 (~1059 and 1110 cm^{-1}) stretching (band assignments from Čejka et al., 2015). Polymer-impregnated samples were distinguishable from untreated samples by the carbonyl band at ~1732 cm^{-1}. UV-Vis-NIR data from the same samples were collected in the 250–987 cm^{-1} range and identify the roles of iron and copper in the turquoise's color (figure 14). The absorption band at ~429 nm is caused by Fe^{3+}, while the broad band centered around 685 nm is a Cu^{2+} feature (Chen et al., 2012).

Fieldwork. The constructed isohypsometric map and depth model of the Mona Lisa mine are presented in figure 15. The map was constructed using a false datum on the southwestern edge of the trench. Two dominant fracture populations were recorded: steeply westward-dipping (n = 63; average strike and dip: 193.42°, 80.85°) and steeply eastward-dipping (n = 65; average strike and dip: 2.48°, 79.01°). Seam diagrams (figure 16) depicting the patterns of turquoise mineralization within the trench show that the orientation of seams follows these prevalent

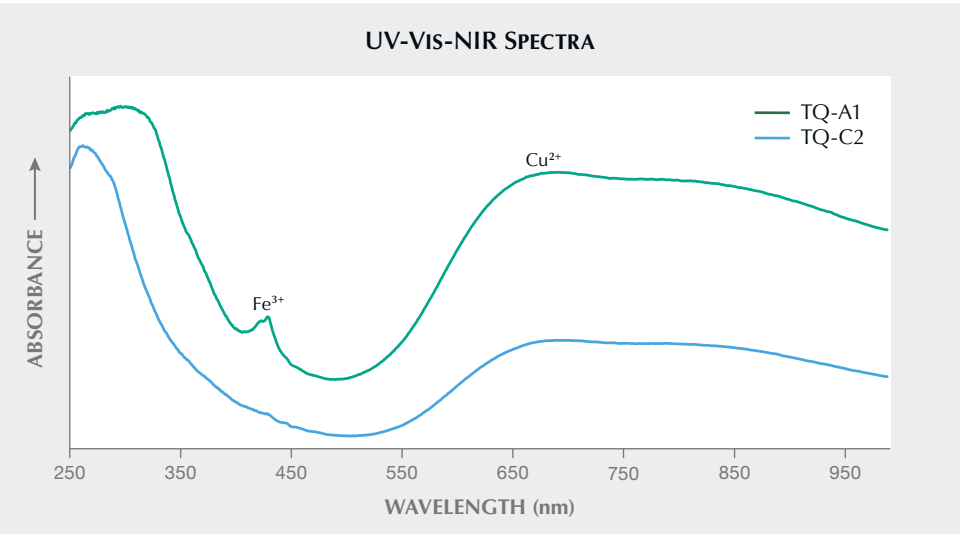

Figure 14. UV-Vis-NIR spectra of two pieces of Mona Lisa turquoise. The bands relating to the Fe^{3+} and Cu^{2+} chromophores are labeled. The pale blue sample (TQ-C2) shows a much weaker Fe^{3+} band. Spectra are offset vertically for clarity.

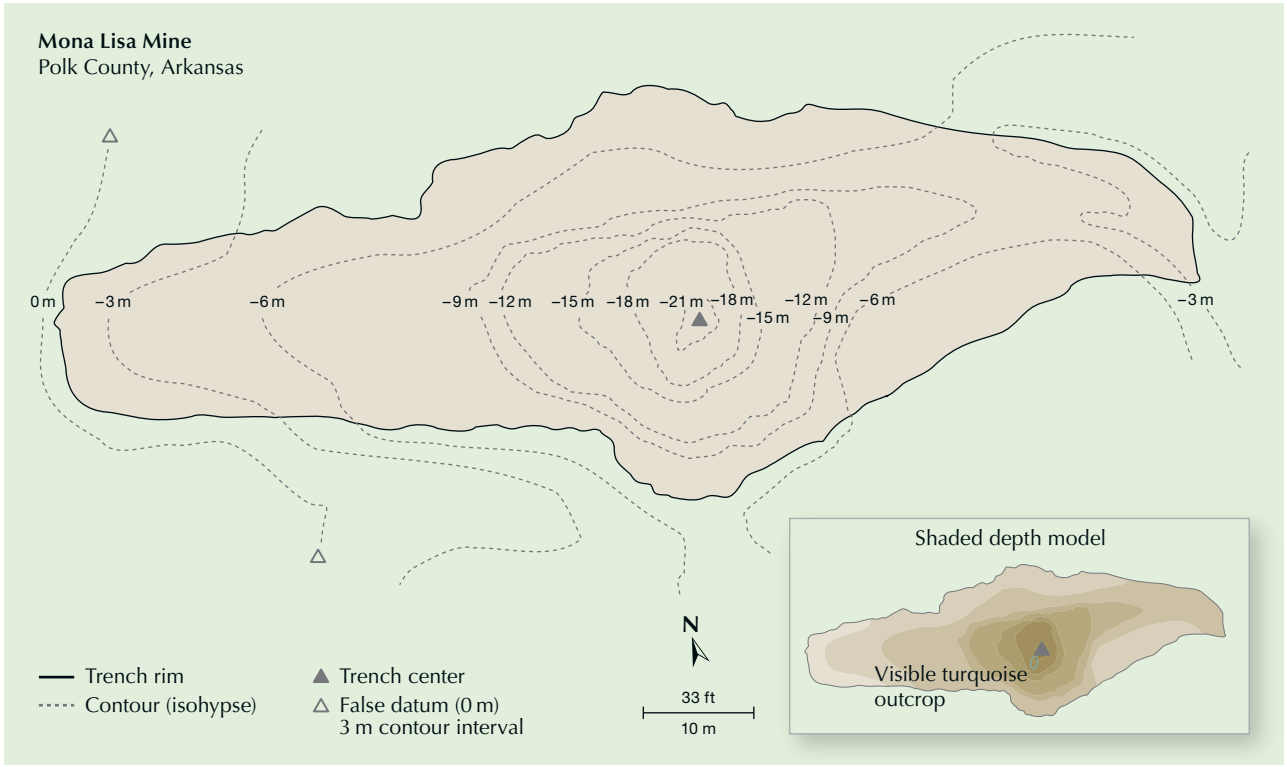

Figure 15. Topographic mapping conducted in March 2021. Isohypsometric map constructed by Thomas Paradise and Alexander Goodsuhm.

near-vertical fractures. The turquoise seams, however, are often not continuous. Other minerals within the veins include quartz, iron oxides, and manganese oxides.

Mineralogy Data. Eight of ten samples tested with XRD matched with turquoise-group minerals (five turquoise, two faustite, and one planerite). An example turquoise-matching diffractogram (sample TQ-C1)

Figure 16. Mona Lisa turquoise precipitating within the chalky white weathered novaculite matrix. Photos taken in September 2019 from the deepest part of the trench facing the north side, shown along with corresponding seam diagrams. Photos courtesy of Avant Mining LLC; digitization by Thomas Paradise.

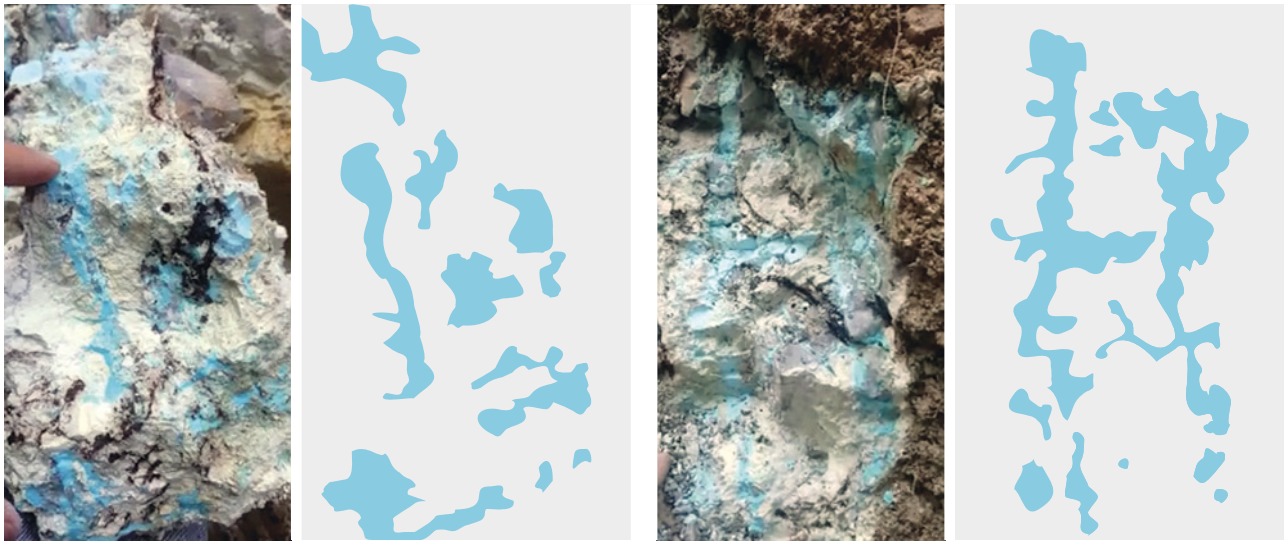

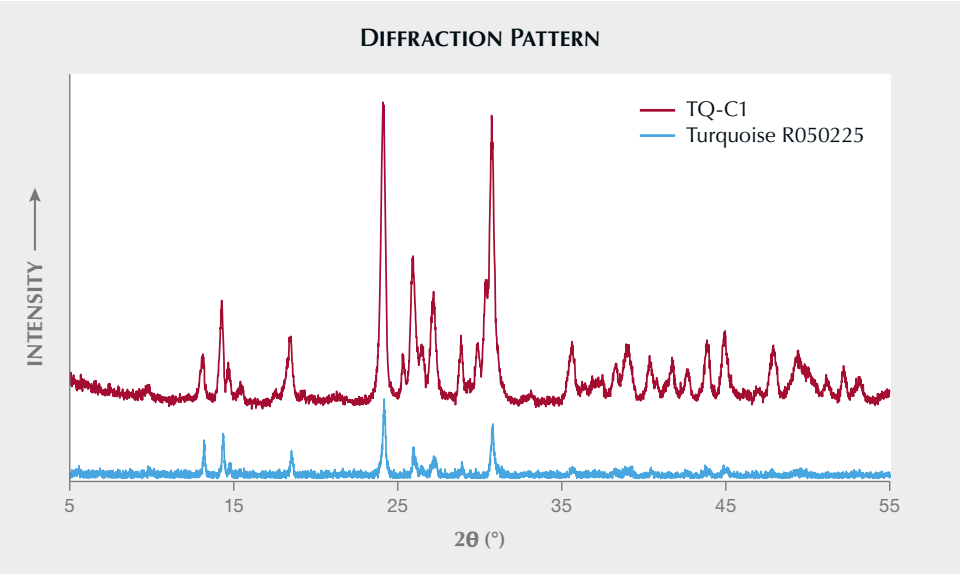

Figure 17. Example X-ray diffractogram of untreated turquoise from the Mona Lisa mine (sample TQ-C1), compared to a turquoise reference sample from the RRUFF database. Spectra are offset vertically for clarity.

is shown in figure 17. The other two samples had more dominant diffraction patterns related to the matrix material, which overwhelmed any potential turquoise signal. Nine of the ten samples matched with turquoise-group minerals using Raman spectroscopy (eight turquoise and one planerite). When possible, the matrix material was also tested; identified phases are shown with the complete results in table 1. Samples TQ-A1, TQ-A2, TQ-B1, TQ-B2, TQ-C1 (figure 18), TQ-C2, TQ-D1, and TQ-F1 matched turquoise Raman reference spectra.

Chemical Composition. Three LA-ICP-MS spots each were collected on samples TQ-C1 (greenish blue areas) and TQ-D1 (blue-green areas), which were confirmed as structural turquoise by Raman spectroscopy and XRD. Table 2 contains the major element concentrations in wt.% oxides of these samples, averaged

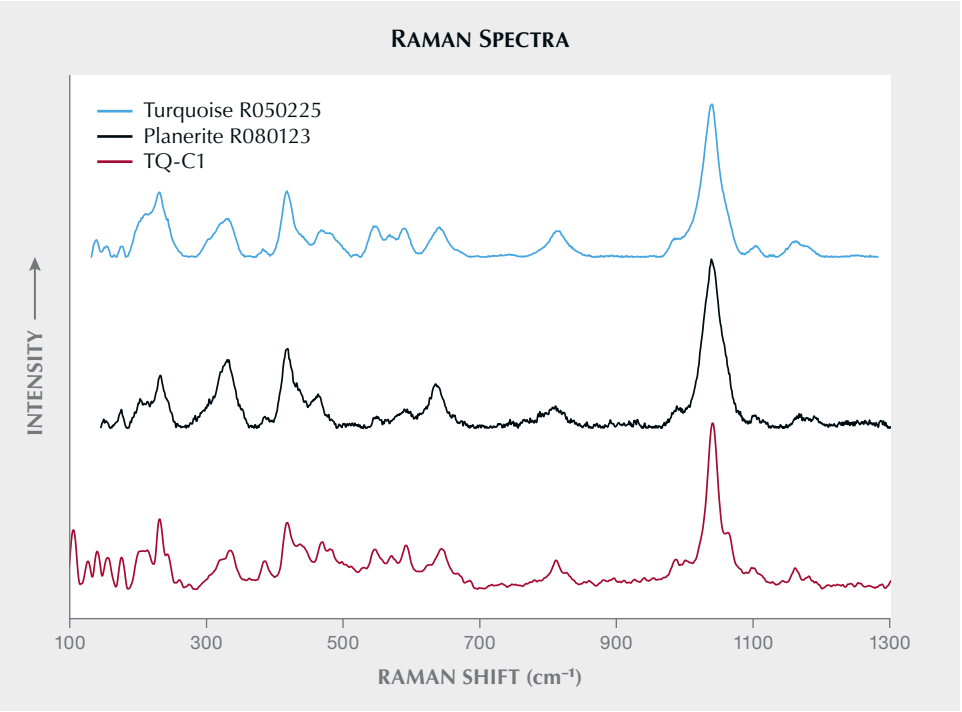

Figure 18. Turquoise and planerite Raman reference spectra from the RRUFF database, compared with the measured spectrum of Mona Lisa turquoise sample TQ-C1. Spectra are offset vertically for clarity.

concentrations from the Sleeping Beauty samples, averaged Iranian turquoise chemistry determined by EPMA (Gandomani et al., 2020), and theoretically ideal turquoise chemistry (Foord and Taggart, 1998) for comparison. Values for Al_2O_3 and P_2O_5 shown from this study are assumed based on turquoise stoichiometry. The CuO content varies significantly, ranging from 1.71 to 6.18 wt.% in these samples. Iron and zinc readily substitute within the turquoise group; Fe_2O_3 ranged from 0.55 to 0.87 wt.% and ZnO from 0.029 to 0.34 wt.%. H_2O content (calculated as the difference from 100%) was high for sample TQ-D1 (23.37–25.15 wt.%) and lower for TQ-C1 (17.06–18.67 wt.%). CaO was detected with high concentrations (1.33–6.30 wt.%) for TQ-C1, but only in trace amounts for TQ-D1.

DISCUSSION

Mineralogy. Out of the ten Mona Lisa samples tested, seven had conclusive matches with XRD reference patterns for turquoise (again, see figure 17). The other three analyses revealed the presence of crandallite (a calcium aluminum phosphate) and quartz in the matrix material (dominant matrix signal prevented the collection of clear turquoise diffraction patterns for these samples) and identified the pale yellowish green sample slab (TQ-J1) as the turquoise-group mineral planerite. Out of the ten Mona Lisa turquoise samples, nine were identified conclusively as turquoise-group minerals through comparison with the Raman reference spectra from the RRUFF database (again, see figure 18; Lafuente et al., 2015). The presence of copper as a major elemental component

TABLE 2. Major element oxide data (in wt.%) obtained by LA-ICP-MS for two untreated Mona Lisa turquoise samples (TQ-D1 and TQ-C1), two untreated Sleeping Beauty turquoise samples (SB-S and SB-L), and published Iranian turquoise chemistry from multiple mines.

Sample no.	Na_2O	Al_2O_3[a]	SiO_2	P_2O_5[a]	K_2O	CaO	Fe_2O_3	CuO	ZnO	H_2O[b]	Total
TQ-D1 SP1	0.011	37.60	bdl[c]	34.90	0.035	0.0039	0.55	1.71	0.029	25.15	100
TQ-D1 SP2	0.022	37.60	0.057	34.90	0.050	0.0072	0.87	3.07	0.060	23.37	100
TQ-D1 SP3	0.011	37.60	bdl	34.90	0.034	0.0043	0.65	1.99	0.033	24.78	100
TQ-C1 SP1	0.031	37.60	0.12	34.90	0.087	5.02	0.72	4.03	0.32	17.17	100
TQ-C1 SP2	0.029	37.60	0.094	34.90	0.076	1.33	0.79	6.18	0.34	18.67	100
TQ-C1 SP3	0.027	37.60	0.11	34.90	0.088	6.30	0.73	2.92	0.29	17.06	100
SB-S (avg. of 6 analyses)	0.011	37.60	0.17	34.90	0.090	0.056	0.66	6.88	0.015	19.63	100
SB-L (avg. of 6 analyses)	0.008	37.60	0.29	34.90	0.090	0.056	0.38	6.71	0.32	19.65	100
Detection limit (wt.%)	0.0002	—	0.007	—	0.0001	0.0008	0.0002	0.00001	0.00002	—	—
Iranian turquoise (Gandomani et al., 2020) determined by EPMA	—	35.07	0.42	34.26	0.072	0.051	3.16	7.01	—	18.20	98.24
Ideal turquoise (Foord and Taggart, 1998)	—	37.60	—	34.90	—	—	—	9.78	—	17.72	100

[a] *Al_2O_3 and P_2O_5 are assumed and used as internal standards for normalization.*
[b] *H_2O content was calculated by the difference from 100%.*
[c] *bdl = below detection limit.*

differentiates turquoise from all other turquoise-group minerals, which have similar crystallographic dimensions and cannot be easily separated using standard structural testing.

In the turquoise group, solid-solution relationships between mineral end members are common. The substitution of copper, zinc, and vacancies in the X site causes the turquoise-planerite solid-solution series and the probable turquoise-faustite solid-solution series. Concentration data from this study indicated the presence of copper, zinc, and iron as major elements in some samples, with higher average concentrations of copper. However, the highest measured CuO content in this study was 6.18 wt.%, while ideal turquoise would have >9 wt.% (Foord and Taggart, 1998). These lower concentrations indicate that vacancies fill many octahedrally coordinated X sites in Mona Lisa material. Ideal planerite only has vacancies in its X site, with no copper or zinc. Copper has been detected in planerite samples in concentrations up to 3.41 wt.%, while samples with 3.92 wt.% copper have been described mineralogically as an intermediate planerite-turquoise (Foord and Taggart, 1998). The presence of vacancies in Mona Lisa samples provides evidence that the samples are intermediate members of the turquoise-planerite series. Compositional boundaries for the use of the names *turquoise* and *planerite* have not been previously defined or characterized. The H_2O content of the two tested samples also provides a hint at the planerite-turquoise relationship. A fully occupied X site corresponds to a lower water content for turquoise (~17.72 wt.%), while vacancies correspond to higher water content (~21.56 wt.%) (Foord and Taggart, 1998). Using this relationship, TQ-D1 can be inferred to have fewer occupied X sites than TQ-C1. Iron concentrations were also analyzed, but these concentrations do not distinguish between Fe^{2+} and Fe^{3+}. Because iron can fill the X site (Fe^{2+}, aheylite) or the M1-3 sites (Fe^{3+}, chalcosiderite), the valence state of the iron is important to consider when evaluating solid-solution relationships between turquoise and iron-bearing turquoise-group minerals. Assuming all iron as Fe^{3+}, Mona Lisa and Sleeping Beauty turquoise compositions were plotted on a ternary diagram (figure 19). Although turquoise from both localities contains iron, it remains chemically much closer to the turquoise end member than the chalcosiderite end member. The major elemental concentrations of iron are interpreted as an indicator of further substitution within the crystal structure, and additional testing is necessary to determine site assignments.

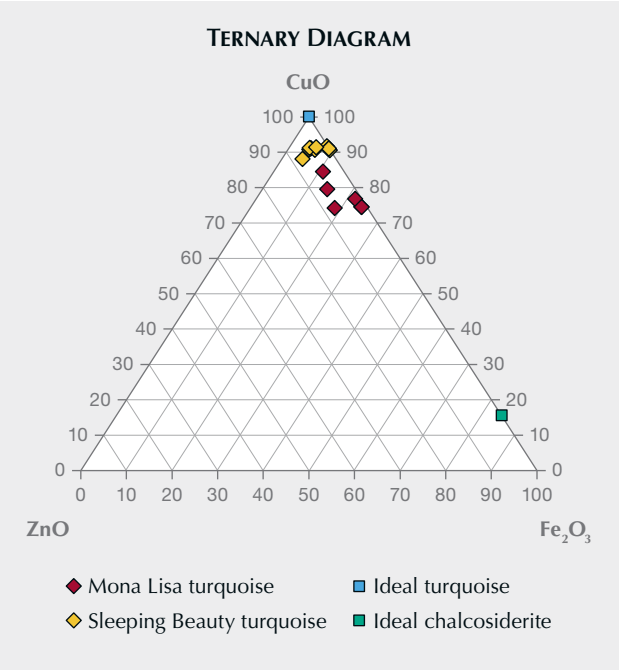

Figure 19. Ternary diagram showing untreated Mona Lisa and Sleeping Beauty turquoise chemistry determined in this study, with ideal turquoise and chalcosiderite for reference.

The possibility of a calcium end member in the turquoise group has been considered since "coeruleolactite" was initially described in 1871 (Peterson, 1871). Note that sample TQ-C1 had significant concentrations of calcium. It is likely, though, that this represents a mixture of turquoise and another mineral in the analysis. Crandallite, a calcium aluminum phosphate mineral—$CaAl_3(PO_4)(PO_3OH)(OH)_6$—was identified from XRD patterns of the matrix material found at the mine. A mixture of crandallite and turquoise in the ablated spot could provide the elevated calcium concentrations that were observed. The heterogeneity of the turquoise itself and the matrix is a problem for accurate chemical analysis and reproducibility, by LA-ICP-MS or wet chemistry bulk composition mass spectrometry.

Importance in the Trade. The color, hardness, and location of Mona Lisa turquoise contribute to its economic value. The color variations within the material are likely caused by alteration and the presence of iron. Mona Lisa turquoise varies significantly in hardness, with some samples able to be cut and polished without stabilization. The physical properties of the mined material are likely dependent on both the mineralization conditions and exposure to weathering.

The matrix pattern of Mona Lisa turquoise is also a distinguishing characteristic. In cut and polished stones, the matrix appears light tan, with some patches of white and brown, such as in the beads shown in figure 20. Mona Lisa turquoise generally lacks the distinctive spiderweb pattern that can add value to certain samples, but the nondescript appearance of the Mona Lisa matrix promotes focus on the turquoise color itself. Localized sulfide mineralization does occur in the Ouachita Mountains, but sulfides were not observed at the Mona Lisa mine or within the matrix material.

The provenance of a colored gemstone can impact its value in the trade. Specific turquoise mines in the American Southwest, Iran, and China produce material of higher market value due to rarity and name recognition. Origin determination of turquoise samples is complicated by multiple factors: the heterogeneity of the material at each site, turquoise's cryptocrystalline nature, and the sheer number of turquoise-producing mines, many of which are now defunct (and thus difficult to acquire reliable material from). An extensive collection of turquoise from numerous important turquoise-producing regions and mines would need to be analyzed prior to making origin conclusions for an unknown stone.

Figure 20. A Mona Lisa turquoise necklace with a matched suite of stabilized beads (diameter of largest bead is 35 mm). Photo by Thomas Paradise.

The Mona Lisa mine's location increases the rarity and value of the material, because turquoise from Arkansas has been previously unconfirmed or passed off as economically insignificant. However, the value of Mona Lisa turquoise will depend heavily on increased marketing, as the site remains relatively unknown. Until the Mona Lisa mine becomes a known and respected locality for turquoise collectors and dealers, the demand for and subsequent worth of this material will remain lower than that from well-known sources, despite its rarity and peculiarity. Mona Lisa turquoise specimens with the highest value per carat are those hard enough to be cut and polished directly from the mine, which, like with most turquoise mines, is only a small fraction of the material.

CONCLUSIONS

The Mona Lisa mine is a unique turquoise occurrence because of its location in Arkansas—a lesser-known locale. Gemological evaluation, X-ray diffraction, Raman spectroscopy, and elemental concentrations confirmed that the material is within the turquoise mineral group and has a significant copper component—and thus can be classified as turquoise. The zinc, copper, and iron concentrations also established that the turquoise-group members faustite, planerite, and chalcosiderite potentially can also be found at this location. At the Mona Lisa mine, turquoise mineralized along the ridge of Little Porter Mountain within near-vertical conjugate fractures in weathered novaculite, adjacent to a geologic contact with the Missouri Mountain Shale. The question of how turquoise formed at the site remains: aluminum and phosphorus were likely derived from deep-water shale units (including the Missouri Mountain Shale), while copper mineralization has been described in adjacent areas, often associated with manganese

mineralization (Stone and Bush, 1984). In Polk County, manganese deposits are found in the Arkansas Novaculite, with chemical analysis indicating up to 1.40 wt.% copper in manganese-rich samples (Ericksen et al., 1983). With mineralizing fluids traveling along geologic contacts and fractures, the weathering of the shales and manganese ores could have provided the components for turquoise mineralization at the Mona Lisa mine.

At the site, turquoise is mined from a 90-meter-long open trench that deepens toward the center. Compared with many well-known mines in the American Southwest, where turquoise is found associated with economically viable copper deposits, the Mona Lisa mine is a small-scale surface mining operation. At the time of this writing, the site is not operating commercially, but new mineralizations are being uncovered. With the discovery of a copper source in the area, the potential for additional deposits of turquoise would increase. Because the gemological value of turquoise often depends on mine name recognition, historical significance, and rarity, increased public awareness of Mona Lisa turquoise may one day be associated with its increasing value, as it represents a renewed, distinctive source of American turquoise.

ABOUT THE AUTHOR

Alexander A. Goodsuhm is a research associate at GIA in Carlsbad, California.

ACKNOWLEDGMENTS

The author thanks James Zigras and Avant Mining LLC for access to the Mona Lisa mine and samples and the Turquoise Museum (Albuquerque, New Mexico) for providing samples from the Sleeping Beauty mine. Thomas R. Paradise, Adriana Potra, and Gregory Dumond from the University of Arkansas assisted with fieldwork and the writing process, and their comments were greatly appreciated. Kenneth Befus is also thanked for allowing use of the Raman microscope at Baylor University. Ziyin Sun and Aaron Palke provided insights into the methodology for data collection at GIA. The author is especially appreciative of the constructive suggestions and comments provided by the peer reviewers, which considerably improved the article.

REFERENCES

Abdu Y.A., Hull S.K., Fayek M., Hawthorne F.C. (2011) The turquoise-chalcosiderite $Cu(Al,Fe^{3+})_6(PO_4)_4(OH)_8 \cdot 4H_2O$ solid-solution series: A Mössbauer spectroscopy, XRD, EMPA, and FTIR study. *American Mineralogist*, Vol. 96, No. 10, pp. 1433–1442, http://dx.doi.org/10.2138/am.2011.3658

Allmendinger R.W., Siron C.R., Scott C.P. (2017) Structural data collection with mobile devices: Accuracy, redundancy, and best practices. *Journal of Structural Geology*, Vol. 102, pp. 98–112, http://dx.doi.org/10.1016/j.jsg.2017.07.011

Altomare A., Cuocci C., Giacovazzo C., Moliterni A., Rizzi R. (2008) QUALX: A computer program for qualitative analysis using powder diffraction data. *Journal of Applied Crystallography*, Vol. 41, No. 4, pp. 815–817, http://dx.doi.org/10.1107/S0021889808016956

Altomare A., Corriero N., Cuocci C., Falcicchio A., Moliterni A., Rizzi R. (2015) QUALX2.0: A qualitative phase analysis software using the freely available database POW_COD. *Journal of Applied Crystallography*, Vol. 48, No. 2, pp. 598–603, http://dx.doi.org/10.1107/S1600576715002319

Archuleta J.-L., Renfro N. (2018) Gem News International: Turquoise from western Arkansas. *G&G*, Vol. 54, No. 1, p. 86.

Barwood H.L., deLinde H. (1989) Arkansas phosphate minerals: A review and update. *Rocks & Minerals*, Vol. 64, No. 4, pp. 294–299, http://dx.doi.org/10.1080/00357529.1989.11761770

Čejka J., Sejkora J., Macek I., Malíková R., Wang L., Scholz R., Xi Y., Frost R.L. (2015) Raman and infrared spectroscopic study of turquoise minerals. *Spectrochimica Acta Part A: Molecular and Biomolecular Spectroscopy*, Vol. 149, pp. 173–182, http://dx.doi.org/10.1016/j.saa.2015.04.029

Chen Q., Yin Z., Qi L., Xiong Y. (2012) Turquoise from Zhushan County, Hubei Province, China. *G&G*, Vol. 48, No. 3, pp. 198–204, http://dx.doi.org/10.5741/gems.48.3.198

Chester A.H. (1877) On the identity of the so called peganite of Arkansas with the variscite of Breithaupt and callainite of Damour. *American Journal of Science and Arts*, Vol. S3-13, No. 3, pp. 295–296, http://dx.doi.org/10.2475/ajs.s3-13.76.295

Dumańska-Słowik M., Wesełucha-Birczyńska A., Natkaniec-Nowak L., Gaweł A., Włodek A., Kulmaczewska K. (2020) Blue or green? Turquoise–planerite species from Carico Lake Valley in Nevada, the United States: Evidence from Raman spectroscopy. *Journal of Raman Spectroscopy*, Vol. 51, No. 2, pp. 346–356, http://dx.doi.org/10.1002/jrs.5761

Ericksen G.E., Patterson S.H., Dunn Jr. M.L., Harrison D.K. (1983) Mineral resources of the Caney Creek Wilderness, Polk County, Arkansas. *Studies Related to Wilderness*, Geological Survey Bulletin 1551, pp. 1–41.

Fellone F. (1983) There's turquoise in them thar hills! *Arkansas Gazette,* Little Rock, June 12.

Foord E., Taggart J.E. (1998) A reexamination of the turquoise group: The mineral aheylite, planerite (redefined), turquoise and coeruleolactite. *Mineralogical Magazine*, Vol. 62, No. 1, pp. 93–111, http://dx.doi.org/10.1180/002646198547495

Frost R.L., Reddy B.J., Martens W.N., Weier M. (2006) The molecular structure of the phosphate mineral turquoise—A Raman spectroscopic study. *Journal of Molecular Structure*, Vol. 788, No. 1-3, pp. 224–231, http://dx.doi.org/10.1016/j.molstruc.2005.12.003

Gandomani E.M., Rashidnejad-Omran N., Emamjomeh A., Vignola P., Hashemzadeh T. (2020) Electron microprobe study of turquoise-group solid solutions in the Neyshabour and Meydook mines, northeast and southern Iran. *Canadian Mineralogist*, Vol. 58, No. 1, pp. 71–83, http://dx.doi.org/10.3749/canmin.1900004

Goldstein Jr. A. (1959) Cherts and novaculites of Ouachita facies.

Silica in Sediments, Society of Economic Paleontologists and Mineralogists, Special Publication No. 7, pp. 135–149.
Gražulis S., Daškevič A., Merkys A., Chateigner D., Lutterotti L., Quirós M., Serebryanaya N.R., Moeck P., Downs R.T., Le Bail A. (2012) Crystallography Open Database (COD): An open-access collection of crystal structures and platform for world-wide collaboration. *Nucleic Acids Research*, Vol. 40, Issue D1, pp. D420–D427, http://dx.doi.org/10.1093/nar/gkr900
Gutschick R.C., Sandberg C.A. (1983) Mississippian continental margins on the conterminous United States. In Stanley D.J. and Moore G.T., Eds., *The Shelf Break: Critical Interface on Continental Margins*, Society of Economic Paleontologists and Mineralogists, Special Publication 33, pp. 79–96.
Harry D.L., Mickus K.L. (1998) Gravity constraints on lithosphere flexure and the structure of the late Paleozoic Ouachita Orogen in Arkansas and Oklahoma, south central North America. *Tectonics*, Vol. 17, No. 2, pp. 187–202, http://dx.doi.org/10.1029/97TC03786
Harwood H., Hajek B. (1978) Mineralogical Notes: Notes on some new occurrences in Alabama. *Mineralogical Record*, Vol. 9, No. 6, pp. 388–391.
Houseknecht D.W., Matthews S.M. (1985) Thermal maturity of carboniferous strata, Ouachita Mountains. *American Association of Petroleum Geologists Bulletin*, Vol. 69, No. 3, pp. 335–345, http://dx.doi.org/10.1306/ad4624e3-16f7-11d7-8645000102c1865d
Kunz G.F. (1883) Perofskite and wavellite from Arkansas. *New York Academy of Science*, Vol. 3, pp. 17–18.
Lafuente B., Downs R.T., Yang H., Stone N. (2015) The power of databases: The RRUFF project. In T. Armbruster and R.M. Danisi, Eds., *Highlights in Mineralogical Crystallography*, W. De Gruyter, Berlin, pp. 1–30, https://rruff.info/about/downloads/HMC1-30.pdf
Laney S.E. (2020) Turquoise in the Ouachita Mountains. *Mineral News*, Vol. 36, No. 9, pp. 1–14.
Peterson T. (1871) Coeruleolactit ein neues Mineral von Rindsberg, bei Katzenellenbogen, in Nassau and Zur. Kenntnis der Thonerdehydrophosphate. *Neues Jahrbuch für Mineralogie*, Vol. 353, No. 9 [in German].
Philbrick J.B.S. (2016) *A Geochemical Analysis of the Arkansas Novaculite and Comparison to the Siliceous Deposits of the Boone Formation*. Master's Thesis, University of Arkansas, 60 pp.
Richards I.J., Connelly J.B., Gregory R.T., Gray D.R. (2002) The importance of diffusion, advection, and host-rock lithology on vein formation: A stable isotope study from the Paleozoic Ouachita orogenic belt, Arkansas and Oklahoma. *Geological Society of America Bulletin*, Vol. 114, No. 11, pp. 1343–1355, http://dx.doi.org/10.1130/0016-7606(2002)114%3C1343:tiodaa%3E2.0.co;2
Sinkankas J. (1997) *Gemstones of North America, Volume III*. Geoscience Press, Tucson, AZ.
Smith D. (1981) Mona Lisa mine makes state's turquoise king smile. *Arkansas Gazette*, Little Rock, November 29.
Stone C.G., Bush W.V. (1984) General geology and mineral resources of the Caddo River Watershed. *Arkansas Geological Commission*, Information Circular 29, pp. 18–22.
Stroud R.B., Arndt R.H., Fulkerson F.B., Diamond W.G. (1969) Mineral resources and industries of Arkansas. *U.S. Bureau of Mines*, Bulletin 645.
Targeted News Service (2020) Rep. Westerman Hosts DOI Deputy Secretary MacGregor. *Targeted News Service*, Washington, DC.
U.S. Climate Data (2022) Climate Mena - Arkansas. *U.S. Climate Data, version 3.0*. Accessed 4/16/2022. http://www.usclimatedata.com/climate/mena/arkansas/united-states/usar0376
Vertriest W., Palke A.C., Renfro N.D. (2019) Field gemology: Building a research collection and understanding the development of gem deposits. *G&G*, Vol. 55, No. 4, pp. 490–511, http://dx.doi.org/10.5741/GEMS.55.4.490
Wigley J. (2006) Arkansas turquoise: How I became a gem miner. *Rock & Gem*, Vol. 36, No. 4, pp. 28–30.

Lab Notes

Figure 1. This 0.59 ct near-colorless octagonal step-cut armenite measuring 6.01 × 4.07 × 3.33 mm marks the first time this mineral has been submitted to a GIA laboratory. Photo by Diego Sanchez.

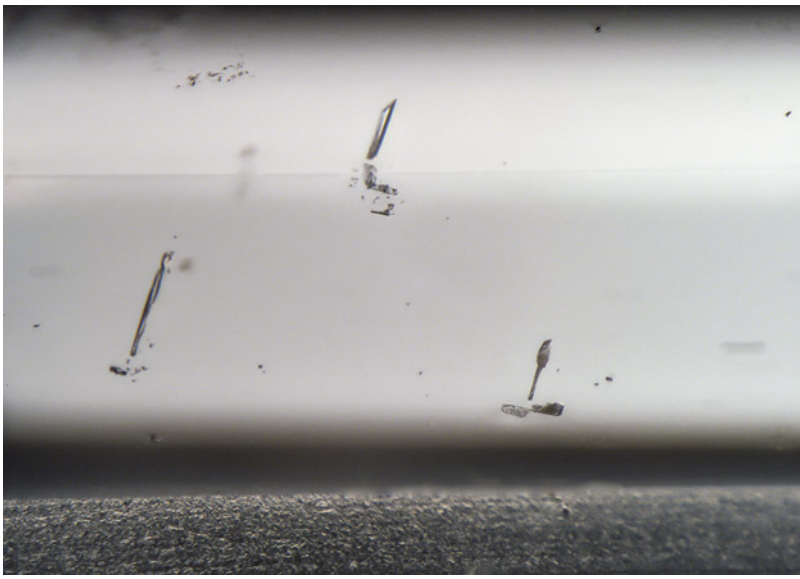

Figure 2. Negative crystal inclusions were observed in the submitted armenite. Photomicrograph by Britni LeCroy; field of view 2.77 mm.

Rare Faceted ARMENITE

A 0.59 ct near-colorless octagonal step-cut stone was recently submitted to the Carlsbad laboratory (figure 1). Standard gemological testing measured a refractive index of 1.550–1.555 (birefringence of 0.005), a biaxial optic figure, and a hydrostatic specific gravity of 2.77. Microscopic examination revealed negative crystals (figure 2), colorless particles, and a small fingerprint breaking the pavilion surface. These properties were consistent with those reported for armenite. The submitted stone was then compared to a near-colorless armenite reference specimen belonging to the GIA Museum, which showed a similar microscopic appearance along with internal stress fractures. Raman and infrared spectra collected on both stones were a near-perfect match, further supporting the armenite identity of the stone.

Armenite is a rare orthorhombic silicate with a formula of $BaCa_2Al_6Si_9O_{30}{\cdot}2(H_2O)$. Originally identified in Norway in 1939, it has since been found in Canada (Quebec), Australia (New South Wales), Scotland, the Czech Republic, Switzerland, the United States (Washington), and Italy (Sardinia). It usually forms as veins within host rocks, including metasomatic basic to intermediate igneous rocks, mineralized skarn and hornfels, and gneisses. The data gathered from this first-time submission of armenite will assist in future identifications.

Britni LeCroy

Editors' note: All items were written by staff members of GIA laboratories.

Gems & Gemology, Vol. 61, No. 4, pp. 392–399.

Figure 3. A 100.15 ct faceted cuprite, measuring 29.37 × 22.29 × 14.09 mm, the largest ever submitted to GIA. Photo by Diego Sanchez.

100 ct CUPRITE with Malachite Inclusions

The Carlsbad laboratory recently examined a 100.15 ct transparent dark red gem submitted for an identification report (figure 3). An over-the-limit refractive index reading and submetallic luster were observed. Raman and infrared spectra were collected on the stone and concluded its identity as cuprite. This is the largest cuprite ever submitted to GIA. While its size alone makes the stone noteworthy, it also possessed photogenic malachite inclusions identified with Raman spectroscopy. Most were in the form of small, concentrically banded green aggregates breaking the surface of the pavilion (figure 4). But the most interesting inclusion was a cluster of dark green transparent malachite crystals breaking the crown (figure 5). Transparent crystals are uncommon for this mineral.

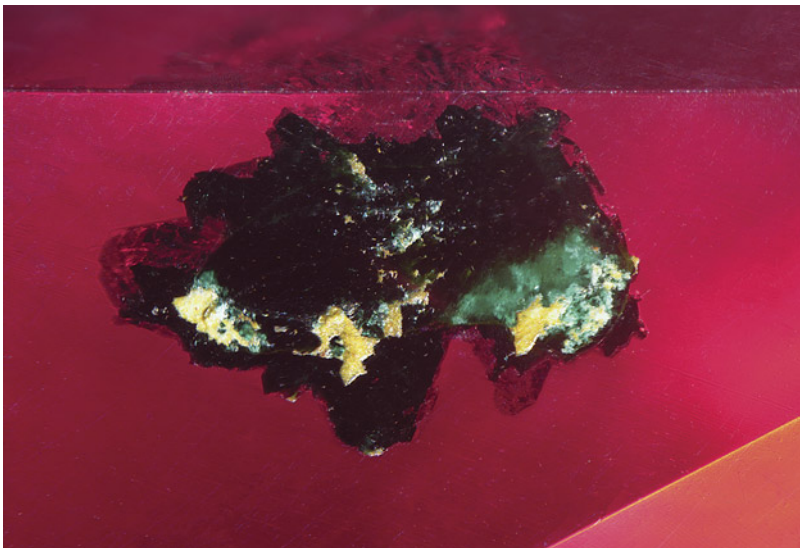

Figure 5. A cluster of dark green transparent malachite crystals breaks the crown of the cuprite. Photomicrograph by Britni LeCroy; field of view 2.81 mm.

Cuprite is an oxide mineral with the simple chemical formula of Cu_2O. It is a secondary mineral that forms in the oxidized zone of copper sulfide deposits. Large, gem-quality specimens are exceptionally rare and are most often sourced from a single deposit in Namibia. Cuprite is often found with malachite, a copper carbonate hydroxide mineral, along with azurite, chalcocite, and limonite. Gem-quality cuprite is mainly considered a collector's stone. While the mineral has an attractive deep red hue and submetallic luster, its Mohs hardness is 3.5–4, making it generally too soft for use in jewelry.

Britni LeCroy

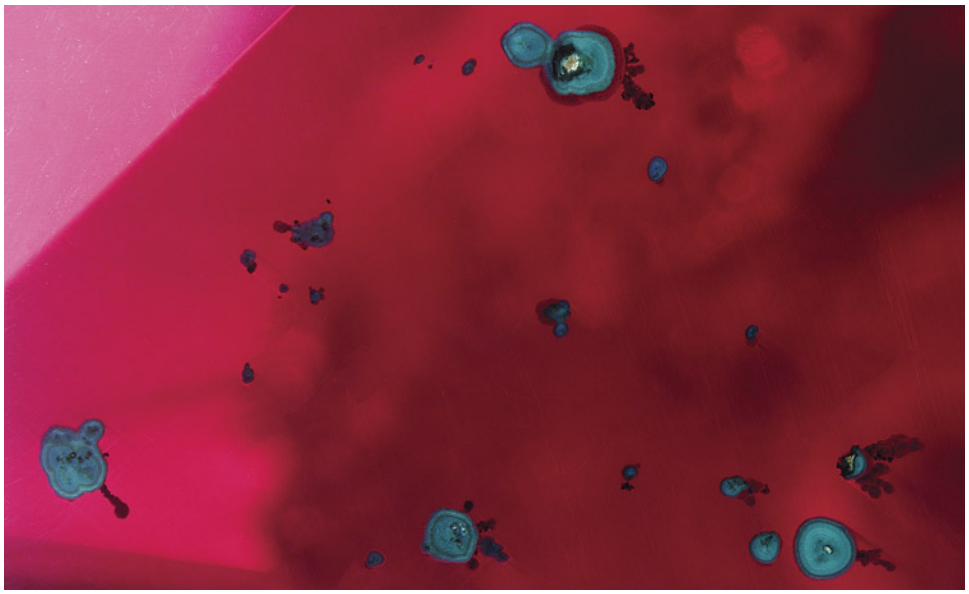

Figure 4. Banded aggregate malachite inclusions were observed breaking the pavilion of the cuprite. Photomicrograph by Britni LeCroy; field of view 4.74 mm.

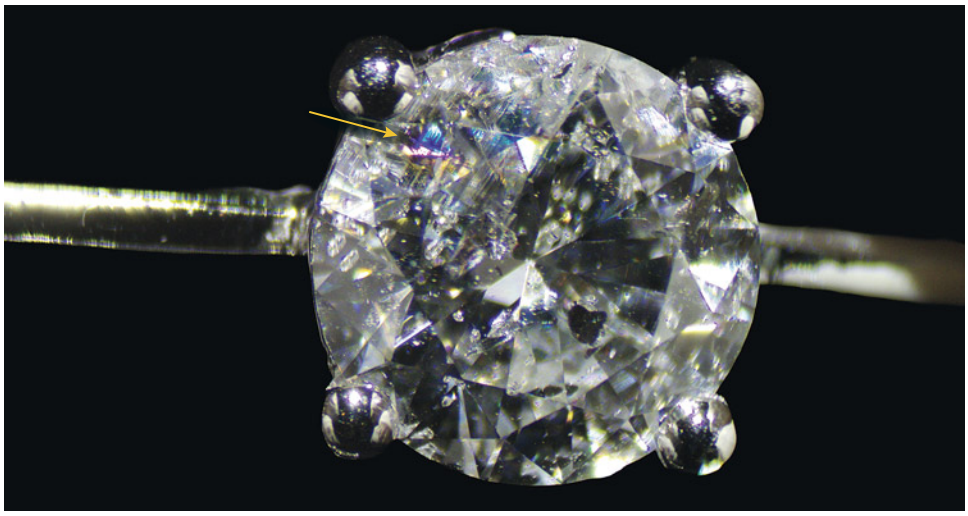

Figure 6. A round brilliant-cut diamond set in the necklace exhibits the flash effect (indicated by arrow) when tilted, a characteristic of fracture filling caused by the presence of a filler within a surface-reaching fracture. Photo by Gaurav Bera.

Fracture-Filled DIAMONDS Detected in Mounted Jewelry

Since the introduction of GIA's Jewelry Analysis Service at the India International Jewellery Show (IIJS) Premiere in August 2025, the Mumbai laboratory has received several intriguing submissions. Among them was a set of mounted items: a pair of earrings and a necklace. The necklace featured 14 round brilliants with a stated weight of 15.27 carats total. The earrings were set with a combination of pear-, oval-, and marquise-shaped stones with a stated weight of 10.84 carats total.

In both the necklace and earrings, the prongs limited access to the pavilion areas and restricted a full view of clarity features. Spectroscopic analysis using the GIA iD100 confirmed that all mounted stones were diamonds and ruled out a laboratory-grown origin. During clarity assessment, bright rainbow-like reflections were observed in two round diamonds from the necklace and in one marquise-shaped diamond from an earring. These features were visible face-up under 10× magnification. At 40× magnification under darkfield and fiber-optic illumination, the phenomenon was identified as the flash effect (figure 6), a visual characteristic typically associated with fracture-filled diamonds (Spring 2018 Lab Notes, pp. 56–57). Flash effects can be challenging to detect, as surface-reaching fractures may show iridescence. Viewing angle is critical for accurate identification; iridescence is typically visible when viewed nearly perpendicular to the fracture plane, whereas the flash effect appears most clearly when viewed parallel to the plane. In addition to the flash effect, a cloudy, milky area was observed across crown facets of the marquise-shaped diamond, further supporting the presence of a filler material within the fracture (figure 7).

Fracture filling is a clarity enhancement treatment used to improve the visual appearance of diamonds by filling surface-reaching fractures with a glass-like substance. The filler material (typically a lead-containing glass) has a refractive index close to that of diamond, reducing the visibility of the fractures and thus giving an appearance of improved clarity (S.F. McClure and C.P. Smith, "Gemstone enhancement and detection in the 1990s," Winter 2000 *G&G*, pp. 336–359). Unlike some clarity treatments that are stable and long-lasting, fracture filling is not permanent; the filler may degrade or become discolored over time, particularly when exposed to ultraviolet light, heat, ultrasonic cleaning, or certain chemicals. The presence of such unstable treatments significantly impacts a diamond's value, durability, and required care. Because of the unstable nature of the filler, GIA does not issue grading reports for diamonds that have undergone fracture filling. Therefore, thorough testing, especially of mounted stones, remains essential for accurate grading and identification. Full disclosure of such treatments is crucial to uphold consumer confidence and ensure market transparency.

Sumit Vardawat, Ashok Prajapati, and Roxane Bhot Jain

Figure 7. A marquise-shaped diamond set in one of the earrings displays a cloudy appearance (indicated by arrow) caused by the presence of filler material within surface-reaching fractures. Photo by Gaurav Bera.

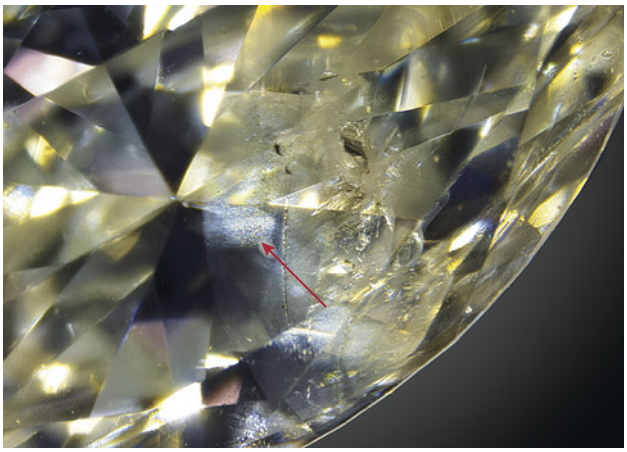

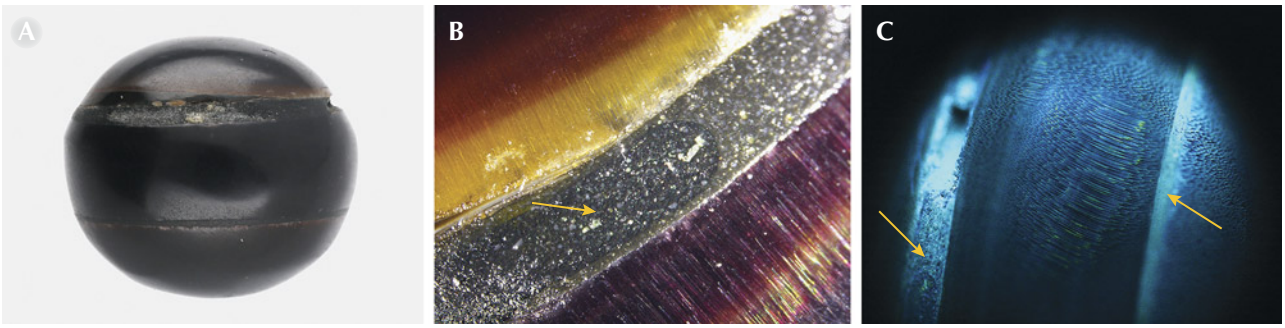

Figure 8. A: An assembled black non-nacreous imitation pearl weighing 10.56 ct and measuring 12.23 × 11.87 × 10.78 mm. B: Bonding agent (indicated by arrow) between the two shell fragments with the polishing lines exhibiting an optical chatoyancy-like effect where colors of pink, yellow, and green were observed. C: Strong bluish green fluorescence observed under the DiamondView showing banding of an unidentified bonding agent (arrows) along with the calcitic columnar structure. Photos by Gaurav Bera (A) and Keaton Talker (B and C); field of view 4.30 mm (B).

Assembled Black IMITATION PEARL

GIA's Mumbai laboratory recently examined an undrilled black near-round bead, weighing 10.56 ct and measuring 12.23 × 11.87 × 10.78 mm, submitted for identification (figure 8A). Initial examination of the specimen indicated that it was an assembled imitation pearl made from shell fragments.

Visually, the specimen consisted of three distinct sections fused together using a dark-colored bonding agent. Under high magnification, some areas revealed columnar structures similar to those observed in non-nacreous pen pearls from the Pinnidae family. Fine lines from working and polishing the specimen were visible across the surface, likely created during the shaping process. Interestingly, under fiber-optic illumination, a chatoyancy-like phenomenon was created by the fine acicular structure of calcite crystals of the shell (figure 8B). When examined using the deep-UV wavelength (<230 nm) of the DiamondView, the three fragments exhibited prominent bands with a bluish reaction and fine cellular hexagonal calcitic columnar features typical of a pen shell (figure 8C; Spring 2017 *G&G* Micro-World, pp. 105–106). The bonding agent displayed a stronger bluish green reaction.

The specimen showed an inert reaction under X-ray fluorescence. Energy-dispersive X-ray fluorescence analysis conducted on the three fragments revealed no traces of manganese but strontium levels of 639, 819, and 904 ppm, respectively, indicating that they were of saltwater origin. Real-time X-ray microradiography (RTX) displayed a distinct banding pattern wherein demarcations were visible between the shell fragments and the bonding agent (figure 9A). The shell fragments exhibited a tight structure. X-ray computed microtomography (μ-CT) imaging showed a more defined banding structure and gas bubbles trapped within the bonding agent (figure 9, B and C). All these characteristics were similar to those previously observed in imitation pearls made of pen shell (Fall 2019 Gem News International, pp. 445–446).

Collectively, the analytical data and observations indicated that the three fragments originated from the same kind of shell, possibly pen shell, and were bonded to create an imitation resembling a whole non-nacreous pen pearl.

Keaton Talker, Roxane Bhot Jain, and Abeer Al-Alawi

Figure 9. A: RTX image showing the three shell fragments fused by a bonding agent (indicated by arrows). B: μ-CT imaging displaying a very tight structure with internal banding (arrow). C: μ-CT imaging showing trapped gas bubbles (white arrows) within the bonding agent (yellow arrow).

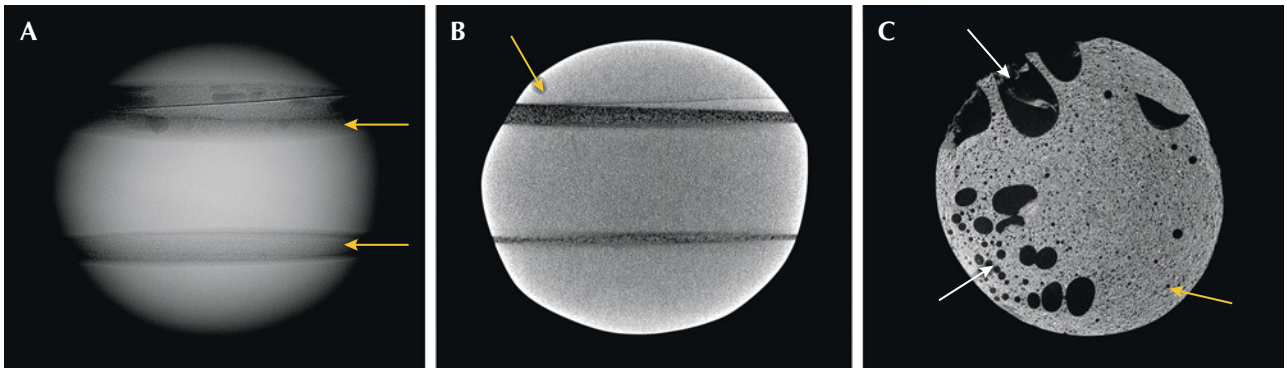

Figure 10. An orangy red translucent friedelite weighing 27.50 ct. Photo by Diego Sanchez.

A Rare FRIEDELITE

The Carlsbad laboratory recently received an orangy red translucent stone weighing 27.50 ct and measuring approximately 22.46 × 22.11 × 7.42 mm (figure 10). Standard gemological testing revealed a spot refractive index of 1.63 and an absorption band between ~535 and 595 nm with a cutoff of ~480 nm using a handheld spectroscope. The stone contained a long but shallow eye-visible fracture that had been stained black by an unknown substance. A cryptocrystalline aggregate structure was observed under the microscope, with the stone remaining light when rotated in the polariscope. The center of the stone displayed a uniform orangy red color. Small white blebs of carbonate mineralization above a veinlet of white and pink carbonate minerals were found along the perimeter of the stone (figure 11). These observations, along with Raman spectroscopy, were consistent with the rare mineral friedelite ($Mn_8^{2+}Si_6O_{15}(OH,Cl)_{10}$).

Figure 11. Small white blebs of carbonate mineralization above a veinlet of white and pink carbonate minerals in a rare orangy red friedelite. Photomicrograph by Michaela Damba; field of view 6.34 mm.

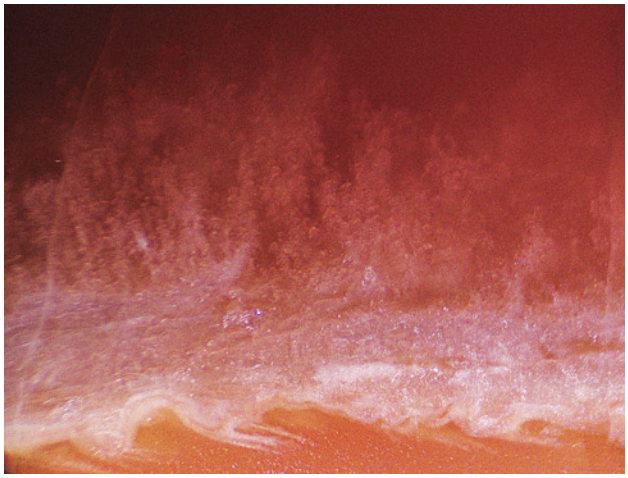

Friedelite was first discovered in 1876 in the manganese mine at Adervielle, in the Vallée du Luron of the Hautes Pyrenees, France, and named after French chemist and mineralogist Charles Friedel. Since its discovery, friedelite occasionally has been found worldwide in other manganese silicate deposits (H.S. Pienaar, "Gem-quality friedelite from the Kalahari manganese field near Kuruman, South Africa," Winter 1982 *G&G*, pp. 221–224). This is the second friedelite GIA has examined to date.

Michaela Damba

Cat's-Eye Boulder OPAL

The Carlsbad laboratory recently encountered a 4.80 ct cushion-shaped double cabochon, measuring 11.65 × 9.87 × 4.71 mm, submitted for identification. The cabochon's specific gravity measured 2.68 with a spot refractive index reading of 1.44, consistent with boulder opal. The stone was characterized as a translucent precious cat's-eye boulder opal with an opaque ironstone matrix base. Its dark gray bodycolor was influenced by a cloudy layer of minute inclusions at the precious opal–ironstone matrix boundary. The uneven boundary and color pattern indicated the stone's natural creation, showing no evidence of assembly or treatment and no fluorescence when exposed to ultraviolet light. The chatoyant play-of-color band stayed dominantly green as a light source moved across the stone, with flashes of blue play-of-color mingling with the green (figure 12). Chatoyant bands in precious cat's-eye opal are not always one color; while more centered and well-defined in comparison to this boulder opal, a solid green chatoyant band has been similarly observed, displaying an "opening" of the eye under two light sources (Summer 2003 Lab Notes, p. 148).

Figure 12. This composite image of a 4.80 ct precious cat's-eye boulder opal shows the progression of the cat's-eye as a light source moves across the stone. Photos by Annie Haynes.

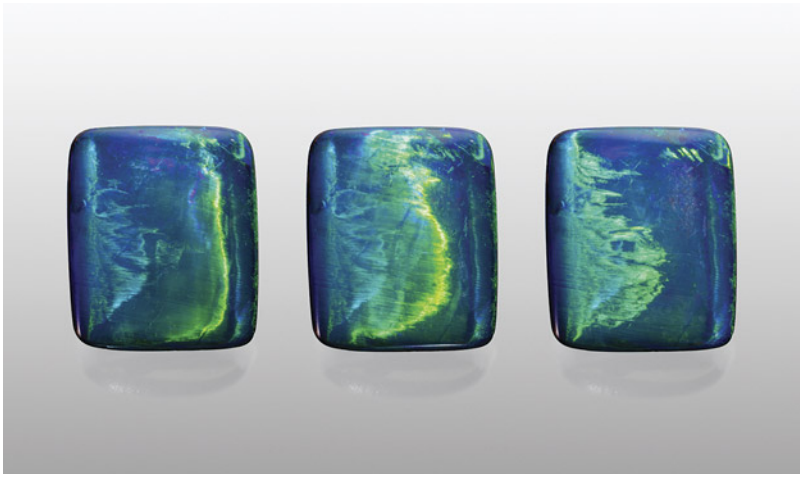

Precious opal is often associated with unique mosaic patterns attributed to its play-of-color. This material can also display other phenomena such as asterism (Summer 2014 Lab Notes, pp. 152–153) or chatoyancy. Both phenomena are quite uncommon due to opal's lack of a definite repeating crystal structure (J.V. Sanders, "The structure of star opals," *Acta Crystallographica*, Vol. A32, 1976, pp. 334–338). Most cat's-eye opals on the market today lack play-of-color; these are referred to as common opals and tend to have a brownish yellow bodycolor. Chatoyancy in common opal is caused by light reflecting off numerous parallel fibrous inclusions, as it is in most other cat's-eye gemstones. Common cat's-eye opal can originate from countries such as Tanzania and Brazil.

GIA laboratories occasionally examine rare precious cat's-eye opals with misalignments in their structure generating linearly arranged play-of-color patches. Precious cat's-eye opal has been sourced from various countries including the United States and Mexico (Winter 1990 Gem News, p. 304), with the sharpness of the eyes and the spectral colors observed varying greatly. Chatoyancy in precious opal can be affected by the cutting quality and orientation.

This cat's-eye boulder opal was reportedly sourced from the Opalton mining area, a locality in Queensland, Australia. Precious opal in boulder rough is rarely visible on the exterior of ironstone concretions. A periphery saw blade impregnated with industrial diamond is used to carefully slice at the edges of the concretion, exposing the opal. Slow grinding with the wheel when fashioning the stone gives definition to the cat's-eye, or "rolling flash" play-of-color pattern.

As the cat's-eye dissipated toward one side of the stone, a broad stroke of bluish green play-of-color resembling an aurora or bioluminescent ocean wave during an algae bloom took form. This unique type of boulder opal is a visually impressive and rare example of precious cat's-eye opal viewed from any face-up angle.

Jeffrey Hernandez

Figure 13. An 8.98 ct white semi-baroque cultured pearl measuring 11.31 × 10.75 × 10.30 mm exhibiting dents and wrinkles on its surface. Photo by Hemal Trivedi.

PEARLS

An Unconventional Bead Cultured Saltwater Pearl

GIA's Mumbai laboratory recently received an undrilled white semi-baroque saltwater nacreous pearl for identification, weighing 8.98 ct and measuring 11.31 × 10.75 × 10.30 mm (figure 13). Externally, the pearl exhibited dents and wrinkles on its surface, similar to those observed in cultured pearls.

Real-time X-ray microradiography (RTX) revealed a tight structure with uniform opacity throughout the pearl and the absence of growth features typical of natural or cultured origin in pearls of this size (figure 14A). The internal

Figure 14. RTX (A) and µ-CT (B) imaging showing the subtle variation in radiopacity between the bead nucleus and the nacre (indicated by arrow). C. µ-CT scan of a bead cultured pearl for comparison showing the demarcation of the bead nucleus with a small organic gap.

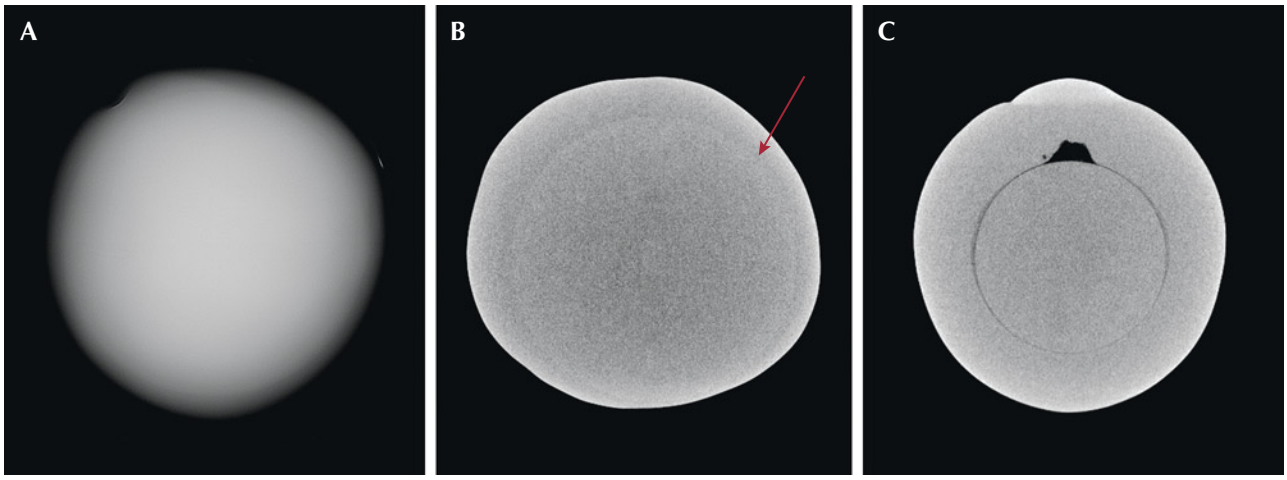

structure was challenging to interpret, requiring further analysis using X-ray computed microtomography (μ-CT) imaging, which also revealed a tight structure. However, a fine round demarcation of a possible bead nucleus was present, exhibiting a subtle variation in its radiopacity with an outer nacre area (figure 14B). This evidence indicated that the pearl was likely bead cultured, though it appeared atypical.

Typically, bead cultured pearls are easily identifiable as they show a characteristic distinct dark gray demarcation of the round bead nucleus used during the cultivation process (figure 14C), and sometimes are accompanied by small organic gaps. The examined pearl exhibited a more blended and uniform opacity throughout, with the bead nucleus appearing more radiopaque than traditional freshwater shell nuclei. The pearl displayed an inert reaction when subjected to X-ray fluorescence (XRF), indicating its saltwater origin. Moreover, this reaction suggests that the bead is of a non-standard material, as typical white saltwater bead cultured pearls with this nacre thickness (again, see figure 14B) usually exhibit weak yellowish green fluorescence under XRF due to trace amounts of manganese from the freshwater shell material of the bead. These observations suggest the potential use of an unconventional bead nucleus for culturing, such as a saltwater shell bead or other organic material (L.E. Cartier and M.S. Krzemnicki, "New developments in cultured pearl production: Use of organic and baroque shell nuclei," *Australian Gemmologist*, Vol. 25, No. 1, 2013, pp. 6–13).

Identifying the material used as the bead nucleus in this pearl remains inconclusive due to the lack of fluorescence and shell banding, coupled with the subtle variations in the radiopacity of the bead nucleus. Significant advancements in techniques and materials used for culturing pearls have resulted in an increased number of challenging pearls submitted for identification to laboratories. In a few cases similar to the pearl examined here, results based entirely on RTX imaging can lead to misidentification. The use of μ-CT imaging has proven to be a pivotal tool in the identification of such challenging pearls (M.S. Krzemnicki et al., "X-ray computed microtomography: Distinguishing natural pearls from beaded and non-beaded cultured pearls," Summer 2010 *G&G*, pp. 128–134).

Pfokreni Nipuni, Abeer Al-Alawi, and Chunhui Zhou

Filled Natural Hollow Heart-Shaped Pearls

Recently, the Mumbai laboratory received a parcel of loose white to light cream baroque pearls identified as filled natural hollow saltwater pearls after visual and chemical examination. Four of these pearls exhibited notable heart-like shapes and an unusual red X-ray fluorescence (figure 15).

The four pearls ranged from 22.47 × 22.00 × 15.73 mm to 35.46 × 27.27 × 24.22 mm in size and weighed 34.30, 52.75, 75.86, and 98.53 ct. They appeared worn and fragile, and their heft slightly exceeded the typical weight for pearls of similar size (Winter 2022 Lab Notes, pp. 480–481). Their surfaces were characterized by significant cracks, grooves, and plugged areas. When viewed under higher magnification, all four pearls revealed areas that were sealed with a piece of shell, bonded together using a yellowish brown resinous adhesive (figure 16A). This adhesive was visible within the cracks and fissures and contained trapped air bubbles (figure 16, B and C). While some surface areas exhibited an overlapping nacre terrace structure, there was also evidence of working observed near the plugged areas.

Real-time X-ray microradiography (RTX) and X-ray computed microtomography (μ-CT) analyses revealed the presence of large cavities filled with foreign materials, with a radiopacity similar to the pearls' nacre. Rectangular and tabular fragments of different sizes used as fillers were visible in the μ-CT images, as well as pieces of cut shell to seal the pearls' openings (figure 17). The smooth outline of these large cavities blended with the external shape of the pearls. In addition, the growth arc pattern of the surrounding nacre was an indicator of their natural formation. GIA has previously encountered similar pearls (Summer 2019 Lab Notes, pp. 251–254).

Energy dispersive X-ray fluorescence spectroscopy showed manganese levels below detection limits and strontium levels ranging from 790 to 1297 ppm, indicating a saltwater origin. When viewed under X-ray fluorescence, all four pearls showed red emission of varying intensity. Although most saltwater pearls are inert, this unusual red

Figure 15. Top: Four heart-shaped filled natural hollow pearls weighing 34.30, 52.75, 75.86, and 98.53 ct (from left to right). Bottom: The pearls exhibit red X-ray fluorescence of varying degrees. Photos by Gaurav Bera and Eram Shaikh.

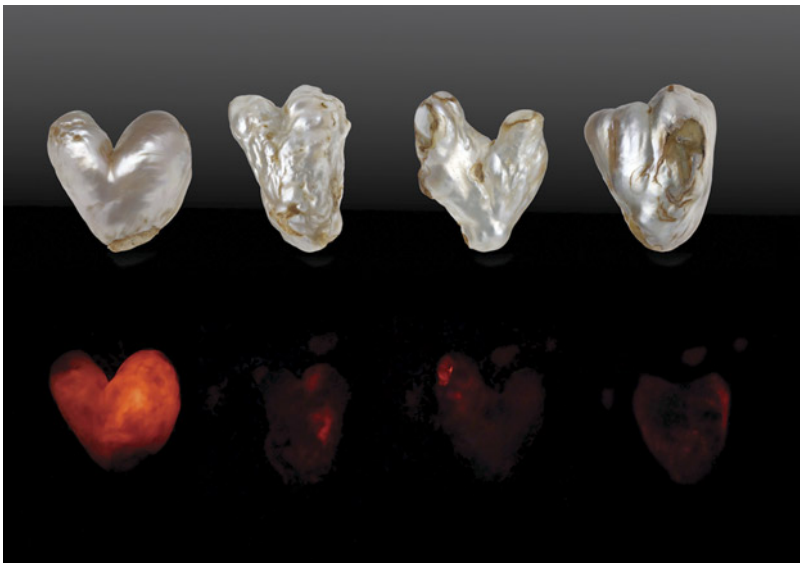

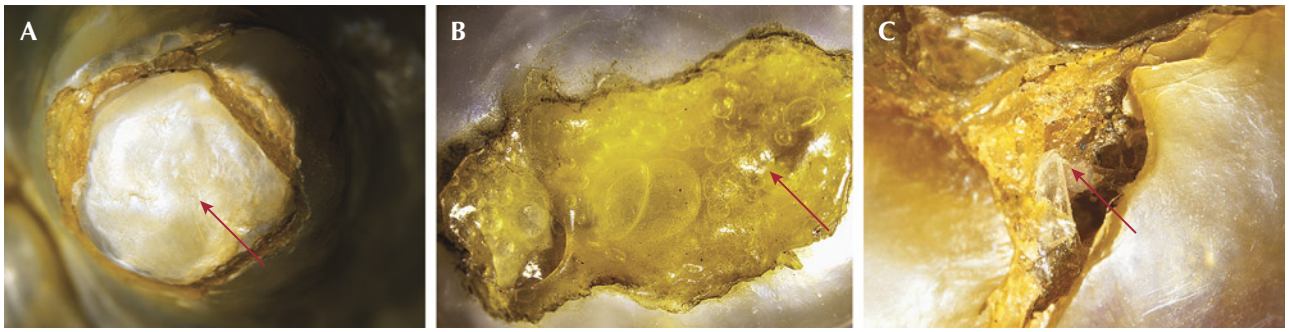

Figure 16. A: Plugged area showing shell piece in the 34.30 ct pearl. B: Trapped gas bubbles in adhesive in the 75.86 ct pearl. C: Adhesive-filled cracks and broken nacre in the 98.53 ct pearl. Photomicrographs by Nitin Wadgaonkar; fields of view 3.00 mm.

reaction could potentially be attributed to the unidentified material inside these filled natural hollow pearls. Under long-wave UV, the pearls showed a moderate bluish reaction, and an inert reaction under short-wave UV radiation.

All four pearls displayed evidence of considerable efforts to improve their durability, including cavity filling, plugging, and working their surfaces to smooth the areas around the plugs. However, despite these interventions, the overall shape, external appearance, and internal structures of the pearls indicate their natural origin. The unique shape and modifications applied to certain areas raise a degree of uncertainty regarding whether they are whole or blister pearls. Nevertheless, their distinctive heart shapes, along with their striking red fluorescence, make these pearls particularly noteworthy.

Eram Shaikh, Nishka Vaz, and Abeer Al-Alawi

Figure 17. Top: RTX images showing the complex internal structure of the four natural hollow pearls filled with unidentified foreign material. Bottom: µ-CT images showing the detailed outline of rectangular and tabular cut fragments used as filler and the pearl openings plugged with shell (indicated with arrows).

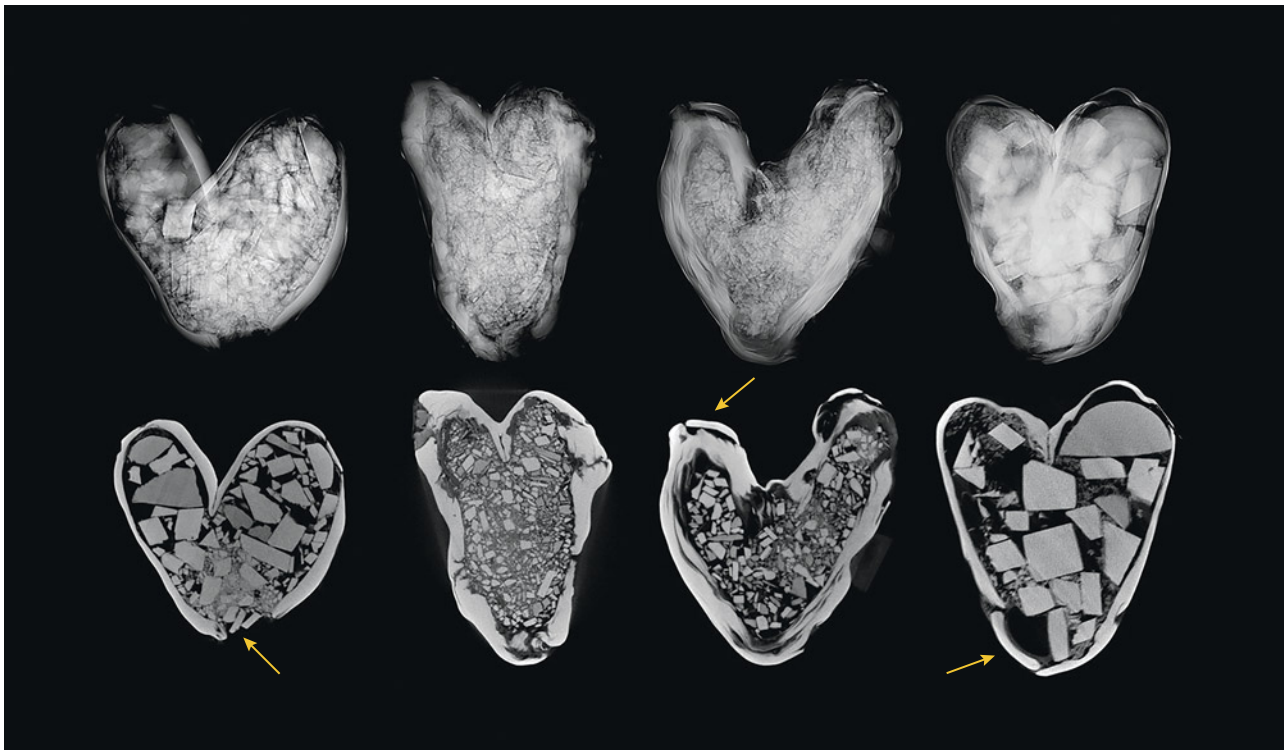

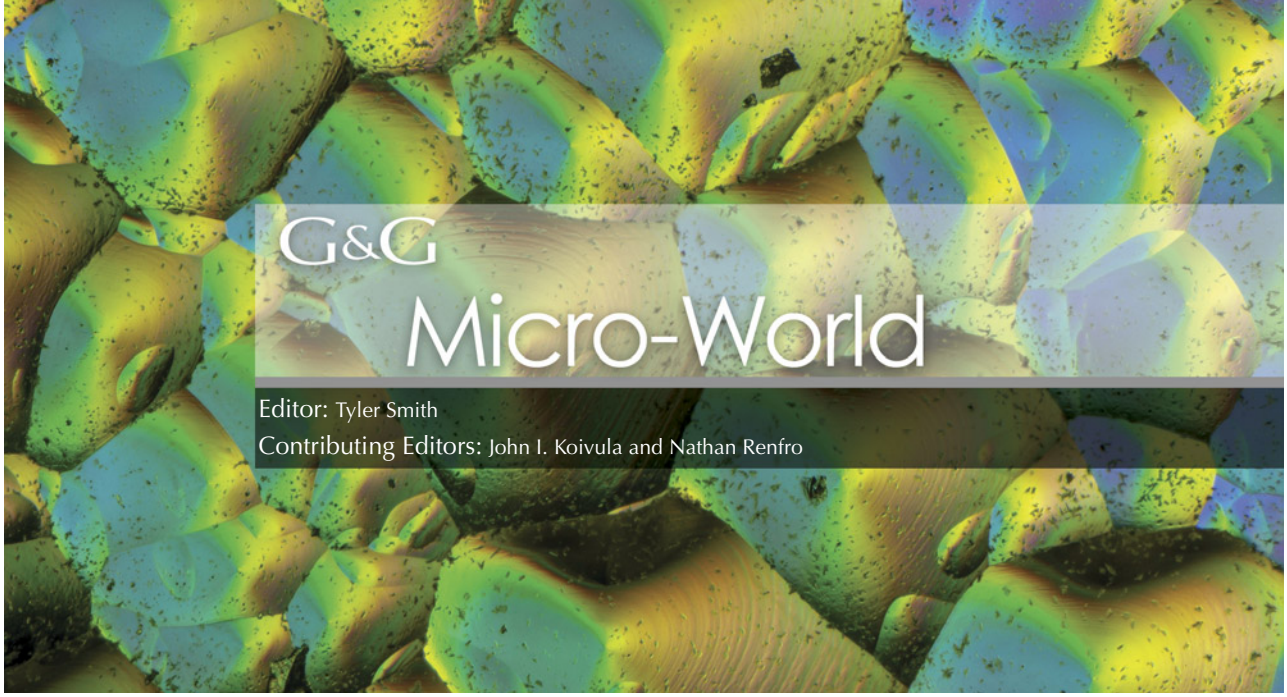

"Bamboo Forest" in Colombian Emerald

A recently examined 1.17 ct green stone exhibited dense tube inclusions running parallel to the *c*-axis (figure 1). The stone was identified as a Colombian emerald based on trace element chemistry measured by laser ablation–inductively coupled plasma–mass spectrometry analysis (S. Saeseaw et al., "Geographic origin determination of emerald," Winter 2019 *G&G*, pp. 614–646), and the profile was similar to that of samples from the Chivor district.

Long growth tubes are common inclusions in colored beryl-group gemstones that form in fluid-rich environments (e.g., Winter 2023 *G&G* Micro-World, p. 503; Fall 2024 Lab Notes, pp. 379–380). In this stone, the linear pavilion facet edges created the illusion of a corridor through a tranquil bamboo forest. The sawtooth graining occasionally observed in Colombian emeralds also was present, reminiscent of sunlight filtering through the bamboo. These impressions were enhanced as the emerald was imbued with a refreshing green color resulting from trace amounts of chromium and vanadium.

Taku Okada
GIA, Tokyo

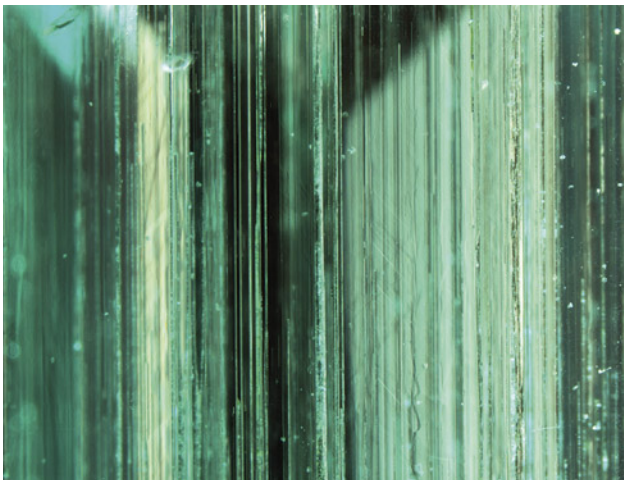

Figure 1. The effect of the pavilion facet edges on the dense tube inclusions in this Colombian emerald creates a scene reminiscent of a bamboo forest. Photomicrograph by Taku Okada; field of view 4.10 mm.

Blooming Bouquet: Thin Films in Russian Emerald

Some gems are enchanting both outside and in. Recently, the Lotus Gemology laboratory received an interesting submission of a 78.01 ct carved Russian emerald. According to the client, the emerald was carved by gemstone engraver Michael Peuster and inspired by art nouveau artist Alphonse Mucha. The woman depicted holds blooming flowers, symbolizing the arrival of spring (figure 2).

Microscopic examination revealed delicate, bouquet-like thin film inclusions on the back of the carving (figure 3). Iridescent thin films are frequently observed in emeralds from Russia, and this specimen showcased several striking

About the banner: Growth hillocks on the surface of this Russian laboratory-grown smoky quartz display vivid interference colors under polarized lighting. Photomicrograph by Nathan Renfro; field of view 10.02 mm. Courtesy of the John I. Koivula inclusion collection.

Gems & Gemology, Vol. 61, No. 4, pp. 400–406.

Figure 2. A Russian emerald carving, approximately 41 × 25 mm, of a woman holding blooming flowers, reportedly fashioned by Michael Peuster. Photo by Ronnakorn Manorotkul; courtesy of Tsarina Jewels.

examples. It was a delightful coincidence to find that the inclusion scene in this stone echoed the floral motif carved into its exterior.

E. Billie Hughes
Lotus Gemology, Bangkok

Figure 4. Near-colorless heulandite crystals resembling worms in an Ethiopian opal exhibiting play-of-color. Photomicrograph by Bawornluk Keeratithanarut; field of view 2.88 mm.

"Worms" in Opal

Opal is an amorphous gemstone known for its unique play-of-color phenomenon. Additionally, opal hosts a wide range of mineral inclusions. Recently, an interesting inclusion was observed in a 22.96 ct Ethiopian opal. Standard gemological testing and Fourier-transform infrared spectroscopy confirmed the opal as natural and untreated. Microscopic examination revealed the presence of near-colorless crystal inclusions (figure 4), matching heulandite of the zeolite group when identified by Raman spectroscopy. These inclusions exhibited a distinctive morphology, resembling worms with elongated, segmented bodies. In some areas, the inclusions appeared twisted, further enhancing their serpentine illusion.

Bawornluk Keeratithanarut
GIA, Bangkok

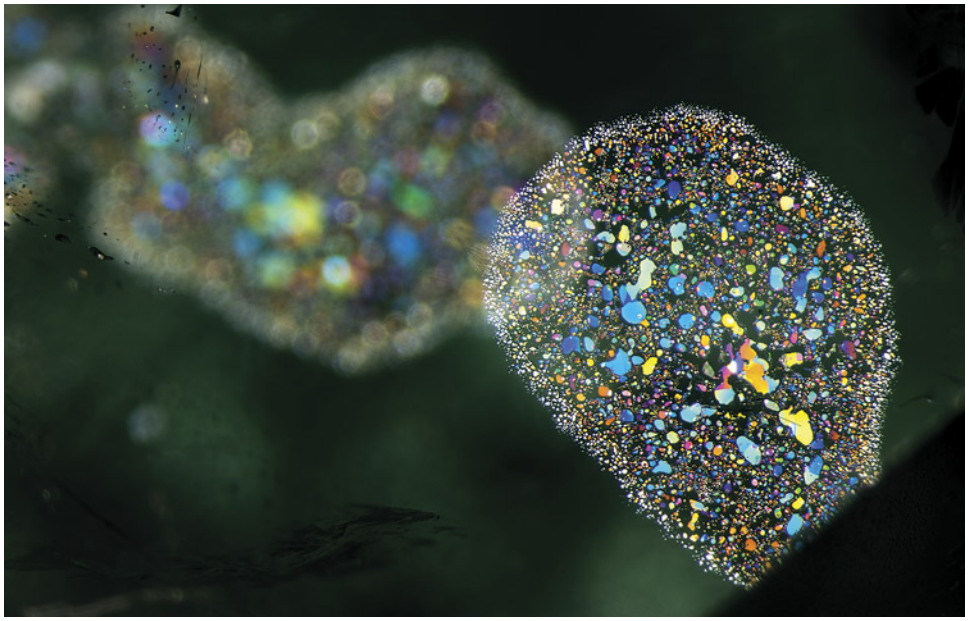

Figure 3. Like an artist's palette, clusters of stacked thin films create a bouquet of color inside this Russian emerald. Photomicrograph by E. Billie Hughes; field of view 5.4 mm.

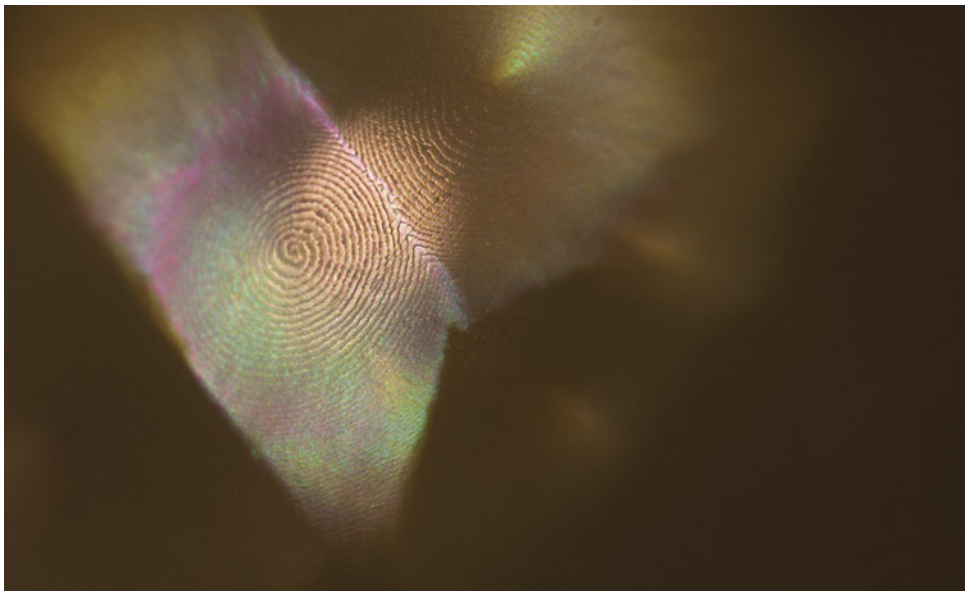

Figure 5. Spiral pattern of nacre platelets observed in each polygon of the mosaic pattern. Photomicrograph by Nishka Vaz; field of view 0.5 mm.

Fingerprint Pattern on a "Hammered" Pearl's Surface

Among a parcel of saltwater natural and cultured pearls, a white near-button, non-bead cultured pearl, weighing 3.18 ct and measuring 8.06 × 7.81 × 6.57 mm, recently stood out due to its unusual external appearance. The pearl's surface exhibited a mosaic of indentations surrounded by ridges, visually similar to the hammered effect seen on metal ornaments (Summer 2024 *G&G* Micro-World, pp. 228–229). Bright spots of light reflected from the center of each polygonal subsurface indentation. Each indentation displayed a spiral pattern of nacre platelets resembling a human fingerprint, with the center of the spiral aligning with the center of each polygon (figure 5). The strong iridescence produced by the nacre platelets was complemented by shimmering flashes of light within the mosaic, which seemed to float just beneath the pearl's surface. This subtle optical effect combined with the beautifully symmetrical nacre spirals makes this pearl noteworthy.

Nishka Vaz and Abeer Al-Alawi
GIA, Mumbai

Hanabi in a Conch Pearl

Conch pearls are often appreciated for their pleasing pink bodycolor and striking flame structures. These pearls can exhibit a variety of flame patterns, from long and narrow to short and broad flames. Recently, the author encountered a conch pearl that displayed truly captivating patterns.

The pink oval conch pearl weighed 5.95 ct and measured 10.68 × 9.22 × 7.38 mm. At first glance, eye-visible flame structures were observed. Microscopic examination under fiber-optic light revealed a fascinating discovery of firework-like flame patterns (figure 6). The combination of these patterns and the warm pink bodycolor of the pearl was reminiscent of *hanabi*, the Japanese word for "fireworks," which illuminate the sky every summer at festivals in Japan.

Flame structures can be explained by the interaction between light and aragonite lamellae microstructures of the pearl (H.A. Hänni, "Explaining the flame structure of non-nacreous pearls," *Australian Gemmologist*, Vol. 24, No. 4, 2010, pp. 85–88). While it is rather common to find flame structures on conch pearls, the patterns exhibited by this specimen were remarkable.

Hazel "Wing Kiu" Fan
GIA, Hong Kong

Figure 6. A 5.95 ct pink oval conch pearl exhibiting firework-like flame patterns. Photomicrograph by Hazel "Wing Kiu" Fan; field of view 5.98 mm.

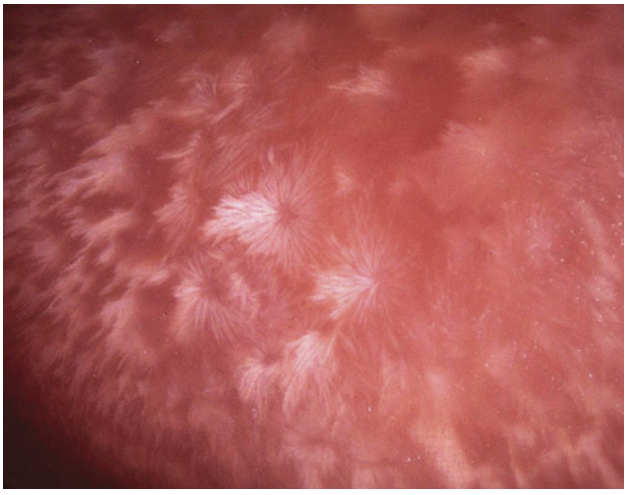

Figure 7. Fibrous mannardite crystals in quartz. Photomicrograph by Liyan He; field of view 2.98 mm.

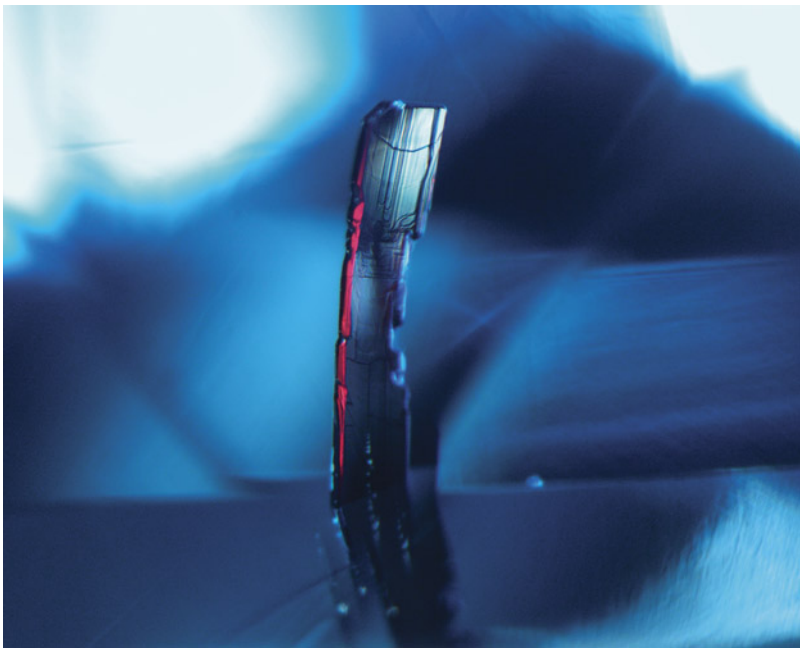

Figure 8. Red prismatic tantalite breaking the surface of a greenish blue sapphire. Photomicrograph by Axle Estrella; field of view 1.93 mm.

Mannardite in Quartz

Recently, the authors investigated a set of three colorless quartz samples, each exhibiting distinctive black fibrous inclusions. Microscopic observation revealed that the metallic opaque crystals were often arranged in parallel or radial formations (figure 7). These inclusions were identified by Raman spectroscopy as the rare mineral mannardite ($Ba(Ti^{4+}_{6}V^{3+}_{2})O_{16}$). Mannardite is a member of the cryptomelane group (hollandite) and is found in Russia, Northwest Kazakhstan, and South China, with these inclusions typically ranging from 15 to 50 μm in width.

This discovery offers new insights into low-temperature hydrothermal mineralization processes, as the coexistence of mannardite with quartz suggests formation under specific redox conditions (X. Fu et al., "Mineralogy and trace element geochemistry of the early Cambrian black shale-hosted Zhongcun vanadium deposit, southern Qinling, China," *Ore Geology Reviews*, Vol. 155, 2023, article no. 105371). These findings contribute to understanding vanadium-rich mineral paragenesis in quartz-bearing systems and highlight Raman spectroscopy's critical role in nondestructive mineral identification at the micrometer scale.

Liyan He
Guangdong Gemstones & Precious Metals Testing Center
Guangzhou, China
Wingtak Lui
Min De Minerals & Gem Research Co. Ltd.
Nanjing, China

Dark Red Tantalite Crystal in Greenish Blue Sapphire

The authors recently examined a 1.80 ct greenish blue sapphire and were surprised to observe a dark red internal protuberance jutting inward from the surface of the pavilion (figure 8). The prismatic inclusion was identified as manganotantalite ($(Mn,Fe)(Ta_2O_6)$; a manganese-enriched iron-tantalum oxide) using Raman spectroscopy, consistent with its red bodycolor. This mineral displayed a blunt termination and etched pinacoidal surfaces. Laser ablation–inductively coupled plasma–mass spectrometry analysis showed that the host sapphire had iron levels of up to 1900 ppma. With a spectroscope, a strong broad absorption around 840–880 nm was observed. These observations are consistent with known occurrences of tantalite in sapphire hosts from basaltic-related origins (S. Promwongnan and C. Sutthirat, "Mineral inclusions in ruby and sapphire from the Bo Welu gem deposit in Chanthaburi, Thailand," Fall 2019 *G&G*, pp. 354–369).

While tantalite itself is not uncommon in sapphires of this type, this inclusion was notable due to its interesting morphology and attractive dark red color, attributed to the presence of manganese, which contrasted with the greenish blue stone (O.I. Lee and E.T. Wherry, "Manganotantalite from Amelia, Virginia," *American Mineralogist*, Vol. 4, No. 7, 1919, pp. 80–83).

Axle Estrella and Joseph Hukins
GIA, New York

Figure 9. Natural 1.36 ct scapolite with saturated blue spindle-shaped lazurite inclusions. Photos by Lhapsin Nillapat (left) and Chinnaphat Buntem; field of view 2.90 mm (right).

Spindle-Shaped Lazurite Inclusions in Scapolite

The author recently examined a 1.36 ct near-colorless, transparent scapolite gemstone containing an abundance of eye-visible vivid blue inclusions (figure 9). These spindle-shaped inclusions were identified as lazurite by Raman spectroscopy. Under microscopic observation, the well-defined symmetrical shapes, sharp boundaries, and intensely saturated blue color of the inclusions were readily observed due to the high clarity of the scapolite host. Lazurite within scapolite is rare and has been reported mainly from the Sar-e-Sang mines in Badakhshan, Afghanistan (S.W. Faryad, "Metamorphic conditions and fluid compositions of scapolite-bearing rocks from the lapis lazuli deposit at Sare Sang, Afghanistan," *Journal of Petrology*, Vol. 43, No. 4, 2002, pp. 725–747).

Chinnaphat Buntem
GIA, Bangkok

Metal Sulfide in Spinel

Recently, a 3.14 ct pink spinel was submitted to the Lotus Gemology laboratory, with encouragement from the owner to examine its inclusions. When viewed under the microscope, the spinel did not disappoint. Suspended within was a richly textured, opaque metallic crystal (figure 10). Although attempts were made to identify the inclusion using micro-Raman spectroscopy, its identity remained inconclusive. However, based on the crystal's appearance, it was likely a metal sulfide. Similar inclusions in spinel have been reported as pyrite (E.B. Hughes et al., "Spinel inclusions: An exercise in aesthetics," *InColor*, No. 43, 2019, pp. 66–73; N. Renfro et al., "Micro-features of spinel," Spring 2021 *G&G*, pp. 46–49).

E. Billie Hughes
Lotus Gemology, Bangkok

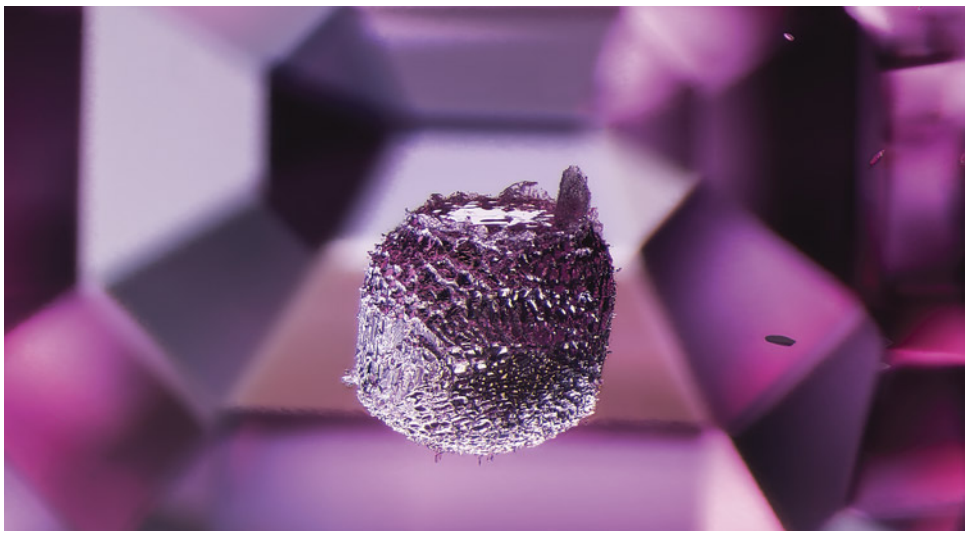

Figure 10. A strikingly textured crystal, likely a metal sulfide, is suspended within a pink spinel; viewed under darkfield and diffuse fiber-optic lighting. The step-cut facets on the stone's pavilion provide a sense of depth to the image. Photomicrograph by E. Billie Hughes; field of view 3.4 mm.

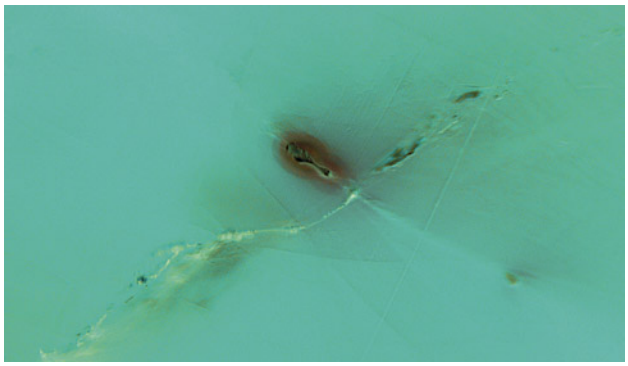

Figure 11. Top view of an altered etch tube in tourmaline resembling a drumstick of a chicken. Photomicrograph by Jamie Price; field of view 1.16 mm.

Whimsical Growth Tubes in Tourmaline

Crystals formed within pegmatitic environments are exposed to hydrothermal fluids that may alter the mineral both externally and internally via fractures or etch channels. The hydrothermal fluids sometimes contain radioactive elements such as uranium, thorium, and radium, which can cause alterations to the host crystal. Evidence of radiation damage is often found in diamond and in copper-bearing tourmaline, referred to as "radiation stains" and "pink sleeves," respectively (J.I. Koivula et al., "Solution-generated pink color surrounding growth tubes and cracks in blue to blue-green copper-bearing tourmalines from Mozambique," Spring 2009 *G&G*, pp. 44–47).

Recently, the author examined a 37.09 ct copper-bearing tourmaline containing many growth tubes that had been altered by radioactive hydrothermal fluids, two of which were intriguing. When viewed directly down the length of the etch tubes, one area resembled a drumstick of a chicken (center of figure 11), while another area looked like the face of a bird with a fuzzy tuft (figure 12).

Jamie Price
GIA, Carlsbad

Figure 12. Top view of an altered etch tube in tourmaline resembling the face of a bird with a fuzzy tuft. Photomicrograph by Jamie Price; field of view 1.48 mm.

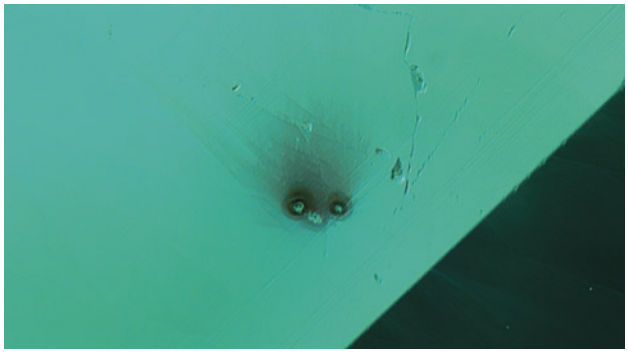

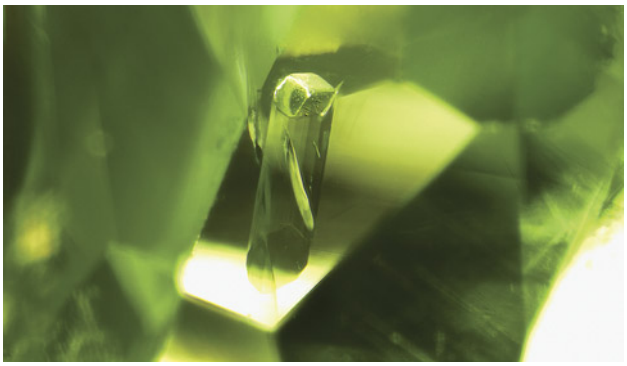

Figure 13. A euhedral tourmaline crystal in a tourmaline host. Photomicrograph by Hikaru Sato; field of view 1.95 mm.

Tourmaline in Tourmaline

The author recently examined a 0.16 ct transparent oval modified brilliant tourmaline containing an included euhedral crystal (figure 13). The inclusion, identified by Raman spectroscopy as tourmaline, displayed a rolled trigonal prism with blunt terminations and associated stress fractures. Tourmaline inclusions in tourmaline have been previously documented (N. Renfro et al., "Micro-features of tourmaline," Summer 2024 *G&G*, pp. 208–210); however, it is rare to see such a perfectly shaped crystal inclusion.

Hikaru Sato
GIA, Tokyo

Quarterly Crystal: β-Quartz Morphology in Beryl

The specimen shown in figure 14, weighing 80.60 ct and measuring approximately 28 × 24 × 22 mm, consists of a

Figure 14. A sharply defined inclusion of α-quartz with β-quartz form is observed within beryl. Photo by Harold Moritz.

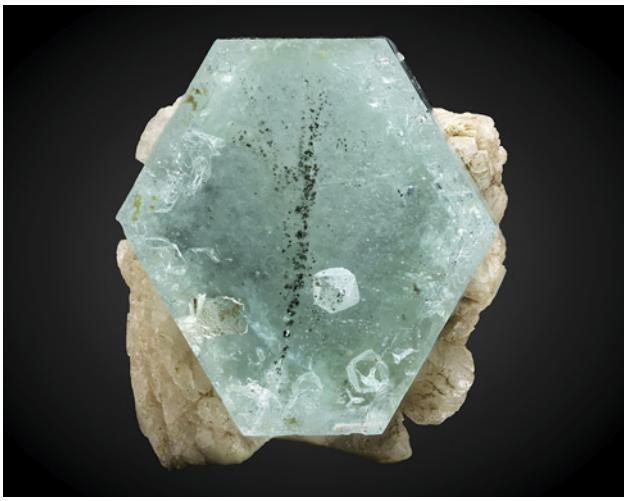

sharp, well-formed aquamarine beryl crystal grown on microcline feldspar crystals. The sample is from Pakistan's Shigar Valley in the Skardu district of Gilgit-Baltistan.

Microscopic examination revealed a single, sharply defined inclusion approximately 3 mm in length (figure 15). The strikingly short bipyramidal morphology is characteristic of β-quartz, the high-temperature polymorph of silicon dioxide, which usually transitions to α-quartz upon cooling below ~570°C (W.L. Bragg and R.E. Gibbs, "The structure of α and β quartz," *Proceedings of the Royal Society of London*. Series A, Vol. 109, No. 751, 1925, pp. 405–427). That transition typically destroys the original crystal shape, making preserved β-quartz morphology exceedingly rare in nature.

In this case, it appears that rapid encapsulation within the growing beryl may have frozen the morphology in place before the reconstructive transition could alter the form. While the inclusion is α-quartz in structure today, as confirmed by Raman spectroscopy, its preserved β-quartz–like shape raises intriguing questions about formation conditions and cooling rates. A literature search failed to reveal any other examples of the β-quartz form preserved within beryl.

Russell E. Behnke
Meriden, Connecticut

Figure 15. The 3 mm β-quartz inclusion pseudomorphed to α-quartz in the beryl host. Photomicrograph by Harold Moritz; field of view 9.00 mm.

Introducing Jewelry Services

Our legacy of trust,
now available for jewelry.

GIA®

New GIA Jewelry Services

For generations, the world has trusted GIA to provide accurate reports for loose gems.

Now, we're bringing our global leadership to new horizons by providing jewelry services.

Expect the same rigorous GIA standards, deep expertise, and advanced technology to add confidence and credibility to every jewelry report.

GIA.edu/jewelryservices

Jewelry provided courtesy of The Clear Cut.

The Diversity of Gemstone Deposits

Aaron C. Palke, James E. Shigley, and Wim Vertriest

It is widely recognized that some gem minerals often occur together in various localities—either in the same host rock or in the same deposit. Gem minerals each require a certain set of physical and chemical conditions for their formation. This edition of the *Colored Stones Unearthed* column will explore where specific gem minerals are found together and the conditions that produce these distinct geological settings.

Background

The most significant historic deposit of fine ruby is undeniably the Mogok Valley in Myanmar (formerly Burma). Yet, this deposit is recognized not only for yielding some of the world's most important ruby, but also for a myriad of other fine gems (figure 1) from blue sapphire to peridot to spinel. Was it a stroke of luck that this relatively small region in Southeast Asia just happens to produce such an amazing diversity of gemstones, or is something more happening beneath the surface? The previous installment of *Colored Stones Unearthed* covered gems found in pegmatites. These pegmatitic deposits virtually always yield a number of different gemstones in the same deposit, rather than being single gem sources. In contrast, some gem deposits are known for producing almost exclusively one species of gemstone (e.g., the Mozambique ruby deposits,

Figure 1. Composite of Burmese gemstones from the Mogok region, from top to bottom: 59.94 ct moonstone, 9.10 ct blue sapphire, 4.67 ct orangy yellow tourmaline, 6.75 ct yellow sapphire, 8.09 ct pink scapolite, 7.19 ct reddish brown zircon, 4.79 ct red spinel, and 1.65 ct ruby. Photos of the moonstone and zircon by Orasa Weldon; all others by Robert Weldon. Courtesy of GIA's Dr. Edward J. Gübelin collection.

Editors' note: Questions or topics of interest should be directed to Aaron Palke (apalke@gia.edu) or James Shigley (jshigley@gia.edu).

Gems & Gemology, Vol. 61, No. 4, pp. 408–414.

TABLE 1. Examples of gems commonly found together.

Type of deposit	Gems found together	Major geographic locales
Marble deposits	Ruby/pink sapphire, spinel	Myanmar, Tanzania (Mahenge), Vietnam
Schist-hosted deposits	Alexandrite, emerald	Russia (Ural Mountains), Tanzania (Lake Manyara)
Pegmatite deposits	Beryl, chrysoberyl, garnet, quartz, spodumene, topaz, tourmaline, etc.	Afghanistan, Brazil, China, Madagascar, Mozambique, Nigeria, Pakistan, Russia, Ukraine, United States, Vietnam, etc.
Alkali basalt/ volcanic deposits	Garnet, ruby, sapphire, black spinel, zircon	Australia, Cambodia, Thailand, United States, etc.
Alluvial/ gravel deposits	Chrysoberyl, feldspar, garnet, ruby, sapphire, spinel, topaz, tourmaline, etc.	Madagascar, Myanmar, Sri Lanka, Tanzania, Vietnam, etc.

the Zambian emerald deposits, the Australian opal fields). In fact, it is quite common for multiple gems to be found in a single deposit (table 1). This contribution to *Colored Stones Unearthed* investigates deposits known for producing multiple gemstone species and places these deposits in a broader geological context.

Why Are Some Gems Found Together?

The assemblage of minerals that form in any situation is determined by the specific geological conditions including pressure, temperature, and local chemical environment. One instance of multiple gem species being found in the same deposit occurs when these species have overlapping chemical components but overall different chemical compositions. The simplest example is the Mogok Valley in Myanmar. Most of the major deposits here are alluvial. While the most well-known gem produced here is ruby, in many of the deposits, ruby and pink or red spinel are found in abundance. Though it is often stated anecdotally that ruby and spinel were indistinguishable until fairly recent mineralogical advancements, local mining communities in Mogok certainly understood these two mineral species were distinct and could distinguish between the two based on crystal morphology and other properties such as hardness. The chemical formulae for ruby (the red variety of corundum) and spinel are Al_2O_3 and $MgAl_2O_4$, respectively. Essentially the only chemical difference between ruby and red spinel, both colored by the presence of trace chromium, is the addition of magnesium to the nearly pure aluminum oxide comprising corundum (ruby). Fine mineral specimens of ruby and red spinel in marble are routinely recovered in Mogok (figure 2). The spinel-bearing specimens occur in a calcite ($CaCO_3$) and dolomite ($CaMg(CO_3)_2$) marble, while ruby-bearing specimens occur in a marble that is nearly pure calcite. These specimens virtually never contain both ruby and spinel due to the fact that spinel crystallizes in these environments at the expense of corundum (ruby) when too much magnesium is present for corundum itself to form.

Figure 2. Ruby crystal in calcite marble (28.03 g; left) and spinel crystal in calcite and dolomite marble (412.40 g; right) from Myanmar. Photos by Robert Weldon; gifts of the Larson family, GIA Museum nos. 24188 and 23669.

Figure 3. Secondary deposits can concentrate gems with very different geological formation conditions, such as quartz and corundum (pink sapphire), which cannot coexist at equilibrium in the earth's crust. Photo by Wim Vertriest.

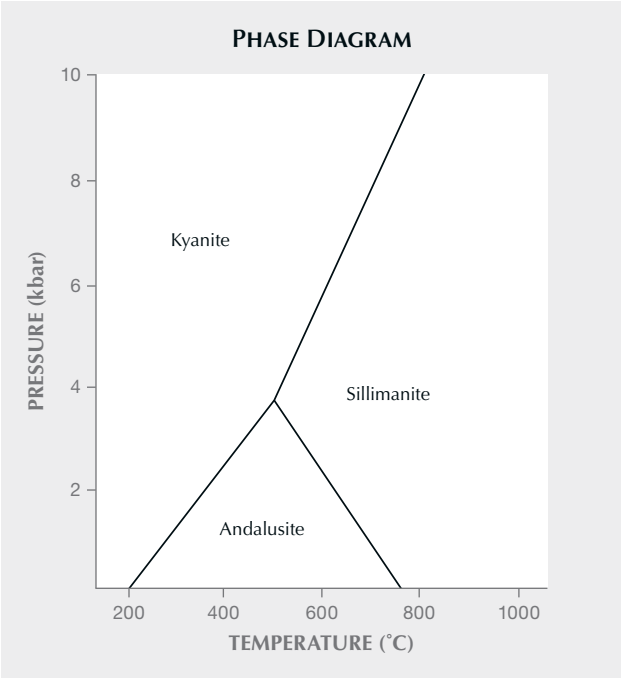

Figure 4. A temperature and pressure phase diagram for aluminosilicate minerals (Al_2SiO_5).

The following section describes several instances in which different gemstones form in a single deposit due to diversity in the chemical environment. The next section covers volcanic deposits, where multiple gems are brought to the surface from great depths by basaltic or other volcanic eruptions. In these cases, the ultimate origin of the different gems found in the same deposit are not clearly understood, but there is almost certainly some genetic link. The final section discusses alluvial or secondary deposits, in which intense, usually tropical, weathering pulls gemstones from multiple geological formations across a broad area, gathering several different gem species together. In many cases, the gems found in these secondary deposits clearly have disparate geological origins involving entirely different formation conditions. The clearest example of this is gem-bearing gravels containing both corundum (ruby or sapphire) and gemmy quartz (figure 3). Under most circumstances, this is impossible as corundum and quartz cannot form in equilibrium at most conditions within the earth's crust[1].

Different Gem Species Due to Chemical Variations

The chemical forces controlling mineralization within the earth have been studied systematically and extensively by geoscientists for more than 100 years. The thermodynamics dictating which minerals form where have largely been unraveled by scientists in experimental laboratories. Geochemists make sense of the results from these lab experiments using tools called phase diagrams, which help visualize the relationships among chemical composition and formation temperature and pressure (depth in the earth). One of the simplest of such diagrams is for the aluminosilicate minerals kyanite, sillimanite, and andalusite, all with the chemical formula Al_2SiO_5 but with different crystal structures. Whether one of these minerals forms instead of another depends on the pressure and temperature of formation. Figure 4 shows the phase diagram for these minerals; if the exact pressure and temperature of formation are known, they can be plotted on this diagram to reveal which of these minerals would have formed in any given geological environment.

Figure 5 shows a more complex phase diagram, determining which beryllium mineral will be stable at a specified temperature and pressure, but with variations in chemical environment. Changes in chemistry are described with the variables a_{SiO_2} and $a_{Al_2O_3}$. These variables are called the "activity" (a) of the chemical components (species)—in this case SiO_2 and Al_2O_3—and are essentially measures of their concentrations or driving forces. For example, the right side of the diagram displays a field for chrysoberyl and a field for beryl. Focusing on the line between the two, if the concentration of SiO_2 at point A in the diagram is increased (or the activity of SiO_2 is increased), the position on the diagram will move to point B, and beryl becomes the stable phase as opposed to chrysoberyl. Once beryl is stable, the concentration of Al_2O_3 could also be increased, causing chrysoberyl to become stable again (point B to point C).

[1]Some exceptional cases of coexisting corundum and quartz assemblages have been documented, although it is unclear if these represent equilibrium or non-equilibrium mineralogical assemblages (Guiraud et al., 1996; Tsunogae and van Reenen, 2006).

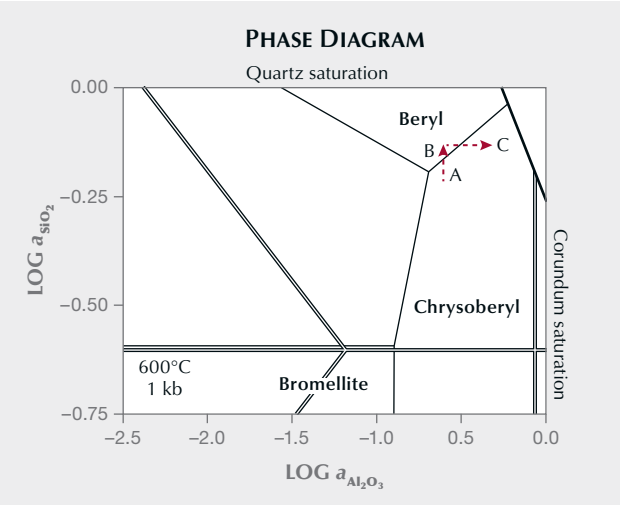

Figure 5. Phase diagram for beryllium-rich minerals as a function of SiO_2 vs. Al_2O_3 activity. Modified from Barton and Young (2002).

The emerald and alexandrite deposits in the Ural Mountains in Russia near Ekaterinburg provide a relevant geological example. Emerald was first discovered here in the 1830s, and later the color-change variety of chrysoberyl, alexandrite, was found and described from the same region (figure 6). Although there are several historic deposits in the area, mining mainly occurs at the Mariinsky-Priisk (formerly Malysheva) mine where emerald is the primary product, with some alexandrite produced as a byproduct. Anecdotal evidence indicates that some deposits were more well known for producing emerald and some more known for alexandrite. While the phase diagram in figure 5 may not exactly correspond to the conditions of formation here, it can serve as a general explanation for how deposits like this form multiple different gem species. Figure 5 indicates that only very special geochemical conditions would allow for both alexandrite and emerald to be produced at the same time, and those conditions exist right along the boundary between the emerald (beryl) and alexandrite (chrysoberyl) fields. Once on that boundary, pushing the concentrations of SiO_2 or Al_2O_3 in either direction will cause either emerald or alexandrite to become unstable, leaving only one of these gems to be formed. It is likely that variations in the chemical conditions from one location in these pegmatite-related, schist-hosted deposits to another resulted in zones of both emerald and alexandrite. The same geological forces were also at play at Lake Manyara in Tanzania, which is mostly known as an alexandrite deposit but also produces emerald. Additionally, recent anecdotal evidence also suggests that some Brazilian emerald mines have started producing small amounts of alexandrite, and the same geological forces may be responsible in those cases.

The previous *Colored Stones Unearthed* installment focused on pegmatites, which can be referenced for a more detailed discussion than what is covered here (Palke and Shigley, 2025). In brief, pegmatitic gem deposits represent a slightly different scenario than described above in that the gems in a pegmatite are generally all found together in the same pockets. One of the distinguishing factors with these pegmatite gemstones is that they all typically have significantly different chemistries. The pegmatitic fluids forming the stones have very unique chemical profiles and contain higher concentrations of many exotic components such as boron, fluorine, and lithium that are not enriched in most geological environments. Therefore, gem minerals such as elbaite tourmaline ($Na(Li_{1.5}Al_{1.5})Al_6(Si_6O_{18})(BO_3)_3(OH)_3(OH)$), topaz ($Al_2(SiO_4)(F,OH)_2$), and spodumene ($LiAlSi_2O_6$) will all form simultaneously as the fluids have all the necessary components for their concurrent formations.

Figure 6. The Russian Ural Mountains host a number of gem deposits producing samples such as emerald (290 ct; left) and alexandrite (2.85 ct; right, shown in daylight equivalent and incandescent illumination). Photos by Robert Weldon; courtesy of R.T. Boyd Limited (left) and GIA's Dr. Edward J. Gübelin collection (right).

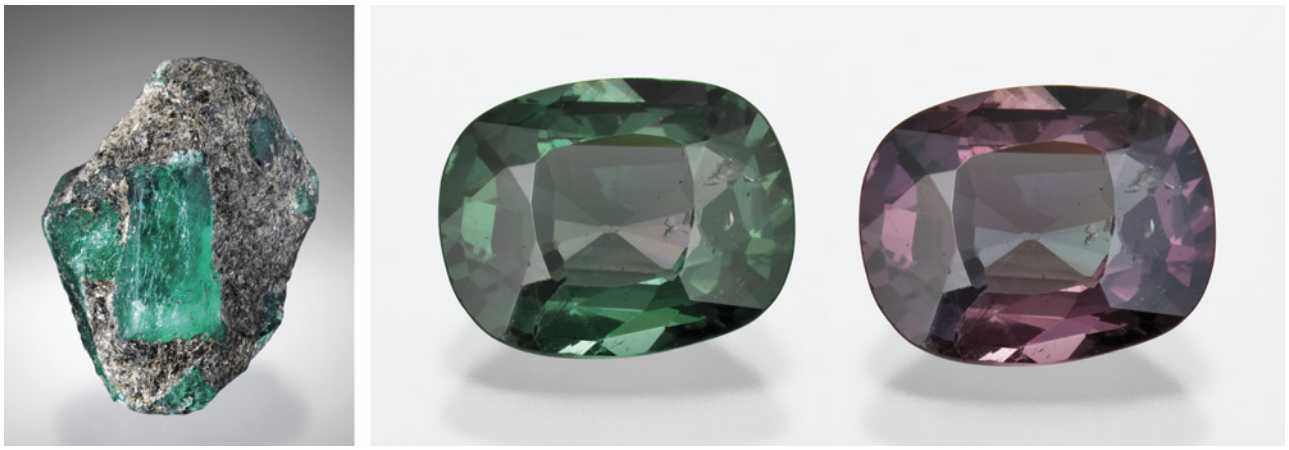

Figure 7. Yellow sapphire from a basalt-related deposit in Australia, ranging in size from approximately 1.44 ct to 8.00 ct. Photo by Robert Weldon; courtesy of Mark Tremonti.

Different Gem Species in Volcanic Deposits

Some of the world's most important colored stone deposits were formed when magmas picked up gems from deep in the earth, later reaching the surface in violent volcanic eruptions. A prime example is basalt-related sapphire found in numerous locales, but most importantly Australia (figure 7), Thailand, Cambodia, Nigeria, and more recently Ethiopia. A ubiquitous mineralogical association in these deposits is gemmy zircon ($ZrSiO_4$). While the zircon found in these deposits is typically dark brown, some of the material is suitable for faceting and finds its way into the gem market. One exception among these deposits is Ratanakiri in Cambodia, which is recognized for yielding gem-quality zircon that can be heated to produce an attractive blue color (figure 8). While Ratanakiri mostly produces gem zircon, subordinate sapphire production also occurs. Though the geological origins of sapphire and zircon are not fully understood, they are generally thought to have formed from some alkali-rich (but not mafic) magmas such as syenites. The formation of zircon and sapphire is likely linked in some way. However, some studies have shown differences in ages and trace element compositions of zircon inclusions in sapphire and the megacrystic zircon, indicating a complex but likely connected genesis (Abduriyim et al., 2012; Sutherland et al., 2015a,b; Vu et al., 2023). While basalt-related sapphire gems are the most common for this type of deposit, Montana sapphire is also of volcanic origin. These secondary Montana sapphire deposits also produce gemmy garnet that, although uncommon in the trade, occasionally end up as gemstones in the hands of avid collectors.

Different Gem Species in Secondary Deposits

Probably the most relevant type of deposit producing multiple different gem species are secondary deposits. In these deposits, gems have been released from their host rocks by

Figure 8. Blue zircon from the Ratanakiri deposit in Cambodia, each measuring 8.8 mm. Photo by Orasa Weldon; courtesy of Tim Roark, Inc.

long-term weathering and erosion. This process destroys much of the rock but has less of an effect on gems (which are durable by definition), effectively freeing them. During this process, they are transported by gravity, commonly aided by the flow of water, and end up in river systems, where they can concentrate and eventually get trapped. This can result in high volumes of gem-quality material found in easily accessible locations.

Some of the richest colored stone deposits can be traced back to major orogenic events when massive continents collided, burying rocks to great depths and creating extreme conditions of pressure and temperature. During these collisional events, multiple different rock formations were buried within the earth, with fluid flow within and between these formations facilitating the transfer of different chemical components needed to form gems. These conditions, in many cases, were perfect for forming a diverse set of gem materials including ruby, sapphire, chrysoberyl, spinel, and garnet. Additionally, these orogenic deposits are typically associated with pegmatitic intrusions, in which case the entire suite of pegmatitic gemstones can be expected (e.g., beryl, topaz, tourmaline, feldspar, and quartz).

Over the span of millions of years, these mountain chains were worn down by weathering and erosion, sometimes leaving more durable minerals concentrated at or near the surface. The presence of multiple different geological formations with distinct chemical and mineralogical compositions in these eroded mountains is the fundamental reason for the diversity of gemstones found in secondary deposits. A generalized geological map of the Mogok region in Myanmar is shown in figure 9. In Mogok, ruby and spinel form in marble (shown in blue in the map), whereas sapphire and other gems are derived from syenites and charnockites (shown in yellow). Pegmatite formations supply additional suites of gemstones. In this type of deposit, the gemstones are produced all together as prolonged periods of weathering break down gem-bearing rocks and concentrate the wear-resistant gems in gravels, often in low-lying valleys or ancient riverbeds. In this case, the gems found in these deposits, such as ruby and blue sapphire, are not necessarily directly related geologically, but

Figure 9. Generalized geological map of Mogok, Myanmar, showing various formations responsible for producing gemstones that have weathered into secondary deposits. Modified from Searle et al. (2020).

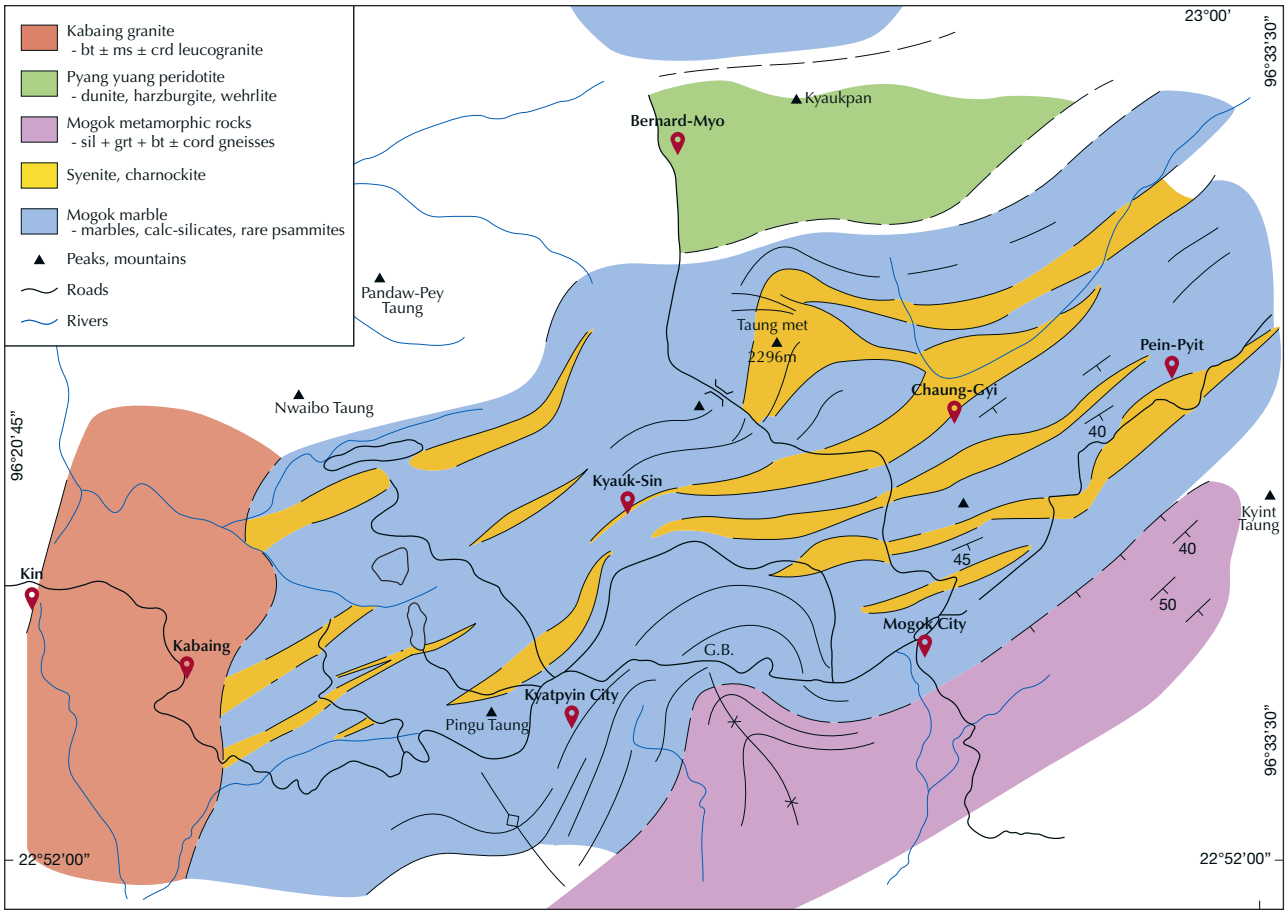

Figure 10. A typical mix of gems including garnet, quartz, topaz, sapphire, chrysoberyl, and zircon found by miners in Ratnapura, Sri Lanka. This secondary deposit includes gems potentially from multiple sources, each with its own distinct geological story, weathered out of host rocks and found together in rivers running through the valleys. Photo by Wim Vertriest.

are found together simply because distinct geological formations weather and break down into the same local sedimentary catchments (figure 10). These deposits are most prevalent throughout East Africa, Southeast Asia, and Sri Lanka.

Summary

The world's colored stone deposits are not equally distributed geographically but often concentrated in specific geological terranes. Many of these fortuitous occurrences are further blessed with not only the presence of gemstones, but also with a large diversity of gem species. These deposits are not purely random, but the product of a unique geological history in which natural forces created just the right conditions for the crystallization, concentration, and preservation of gemstones.

REFERENCES

Abduriyim A., Sutherland F.L., Belousova E.A. (2012) U–Pb age and origin of gem zircon from the New England sapphire fields, New South Wales, Australia. *Australian Journal of Earth Sciences*, Vol. 59, No. 7, pp. 1067–1081, http://dx.doi.org/10.1080/08120099.2012.724031

Barton M.D., Young S. (2002) Non-pegmatitic deposits of beryllium: Mineralogy, geology, phase equilibria and origin. *Reviews in Mineralogy and Geochemistry*, Vol. 50, No. 1, pp. 591–691, http://dx.doi.org/10.2138/rmg.2002.50.14

Guiraud M., Kienast J.-R., Ouzegane K. (1996) Corundum–quartz-bearing assemblage in the Ihouhaouene area (in Ouzzal, Algeria). *Journal of Metamorphic Geology*, Vol. 14, No. 6, pp. 755–761, http://dx.doi.org/10.1111/j.1525-1314.1996.00046.x

Palke A.C., Shigley J.E. (2025) Colored Stones Unearthed: Gem granitic pegmatites. *G&G*, Vol. 61, No. 2, pp. 192–204.

Searle M.P., Garber J.M., Hacker B.R., Htun K., Gardiner N.J., Waters D.J., Robb L.J. (2020) Timing of syenite-charnockite magmatism and ruby and sapphire metamorphism in the Mogok Valley Region, Myanmar. *Tectonics*, Vol. 39, No. 3, article no. e2019TC005998, http://dx.doi.org/10.1029/2019TC005998

Sutherland F.L., Coenraads R.R., Abduriyim A., Meffre S., Hoskin P.W.O., Giuliani G., Beattie R., Wuhrer R., Sutherland G.B. (2015a) Corundum (sapphire) and zircon relationships, Lava Plains gem fields, NE Australia: Integrated mineralogy, geochemistry, age determination, genesis and geographical typing. *Mineralogical Magazine*, Vol. 79, No. 3, pp. 545–581, http://dx.doi.org/10.1180/minmag.2015.079.3.04

Sutherland F.L., Piilonen P.C., Zaw K., Meffre S., Thompson J. (2015b) Sapphire within zircon-rich gem deposits, Bo Loei, Ratanakiri Province, Cambodia: Trace elements, inclusions, U–Pb dating and genesis. *Australian Journal of Earth Sciences*, Vol. 62, No. 6, pp. 761–773.

Tsunogae T., van Reenen D.D. (2006) Corundum + quartz and Mg-staurolite bearing granulite from the Limpopo Belt, southern Africa: Implications for a *P–T* path. *Lithos*, Vol. 92, No. 3-4, pp. 576–587, http://dx.doi.org/10.1016/j.lithos.2006.03.052

Vu D.T.A., Fanka A., Sutthirat C. (2023) Trace element geochemistry and U-Pb dating of zircon inclusions in sapphire from Southern Vietnam: Indicator of basalt-related sapphire formation. *Journal of Asian Earth Sciences*, Vol. 245, article no. 105537, http://dx.doi.org/10.1016/j.jseaes.2022.105537

GIA Colored Stone Reports

Every Gem Carries a Story — We Uncover It.

GIA®

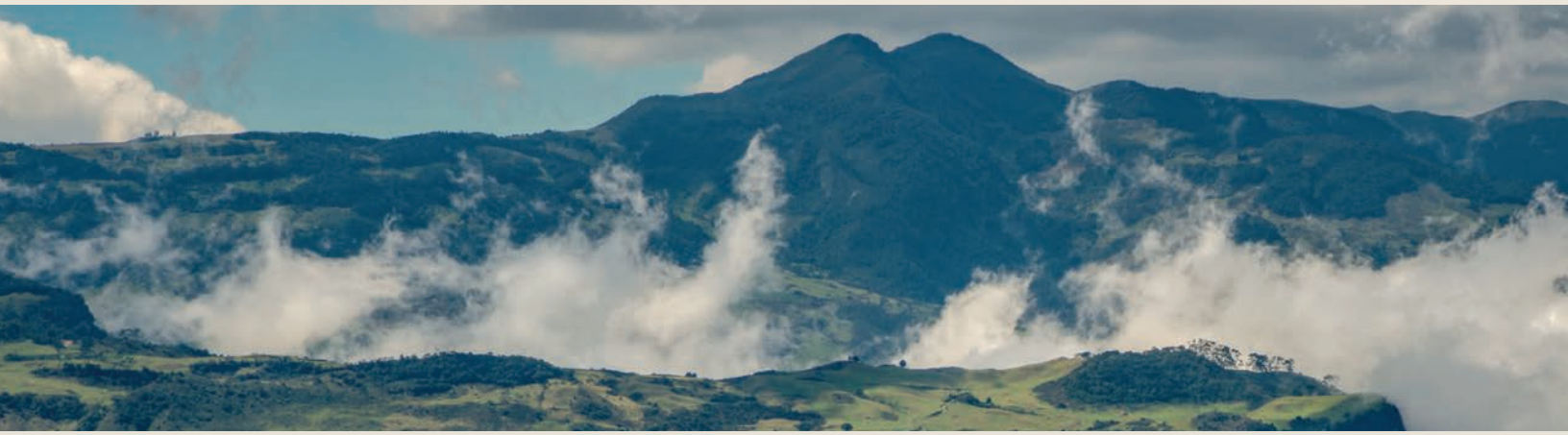

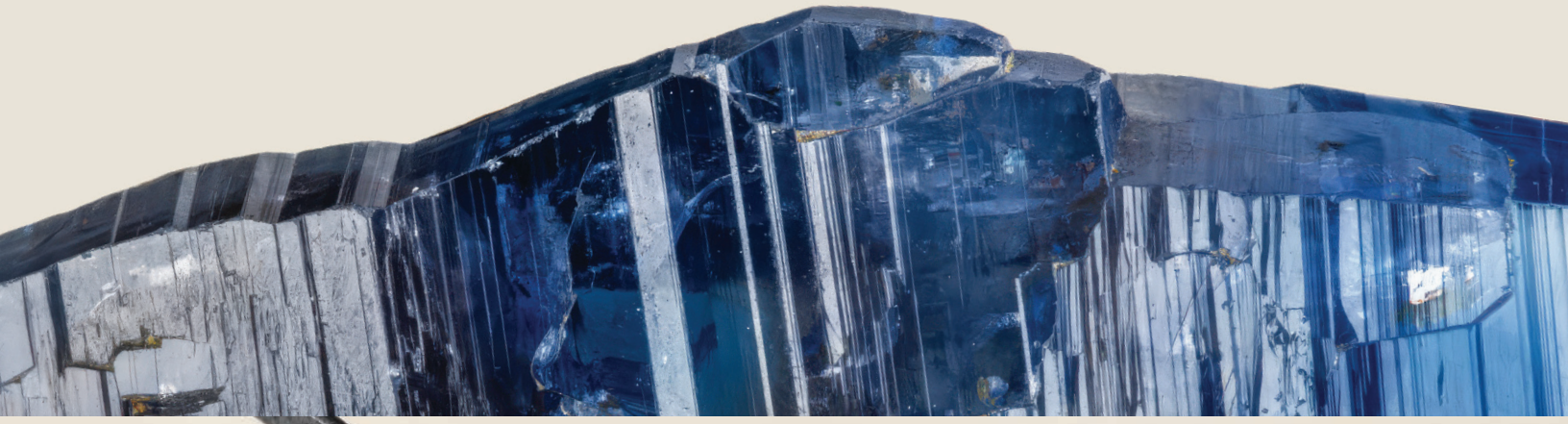

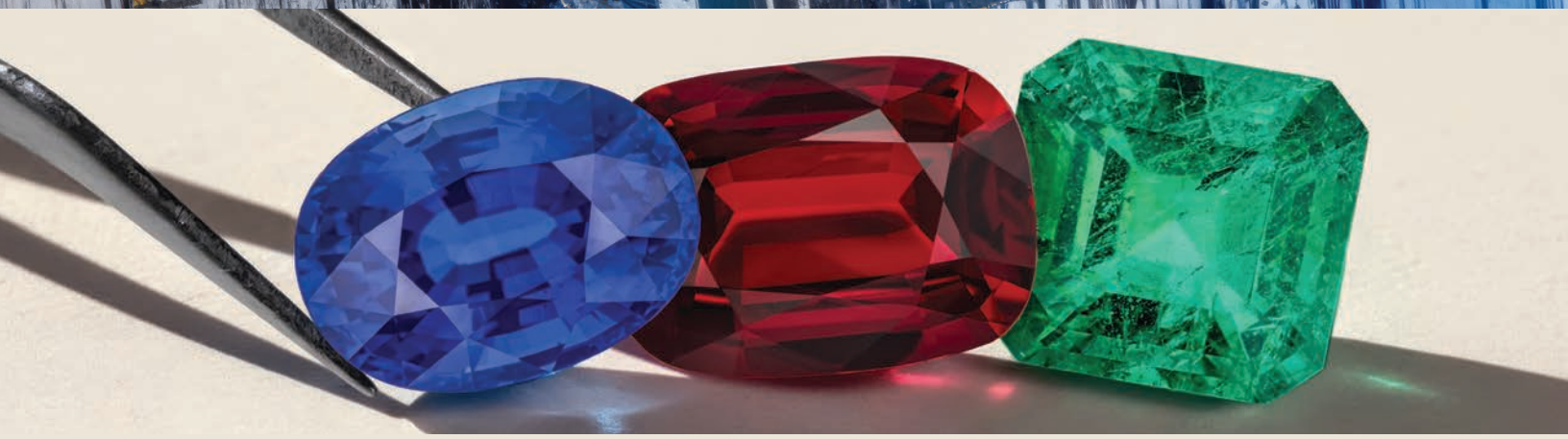

Our unrivaled field gemologists and researchers identify **colored stone treatments and geographic origins** with accuracy and precision, so we can offer you **trusted, industry-leading reports** that help earn customer confidence.

- 28,000+ gem reference samples
- 100+ field expeditions worldwide
- 70+ researchers and gemologists
- A global network of colored stone laboratories

GIA Colored Stone Reports

GIA.edu/coloredstones

GEM NEWS INTERNATIONAL

Contributing Editors
Gagan Choudhary, *IIGJ-Research & Laboratories Centre, Jaipur, India* (gagan.choudhary@iigjrlc.org)
Guanghai Shi, *School of Gemmology, China University of Geosciences, Beijing* (shigh@cugb.edu.cn)

CONVERGE 2025

Converge took place at the Omni La Costa Resort in Carlsbad, California, on September 7–10, 2025. This new event united GIA's gemological research and industry-leading education with the American Gem Society's (AGS) professional development and networking opportunities.

GIA's research sessions featured 24 speaker presentations (see pp. 416–435 of this issue) and more than 30 posters (see pp. 438–444 of this issue), covering broad topics, including colored stones and pearls, diamond identification, diamond and mineral geology, diamond cut, gem characterization, gemology and jewelry, and new technologies and techniques. GIA also offered a number of hands-on sessions including differentiating between natural and laboratory-grown diamonds, an introduction to jewelry forensics, and the photomicrography of gems (see pp. 444–447 of this issue).

SPEAKER PRESENTATIONS

This section provides summaries of the 24 speaker presentations offered at Converge. All entries written by GIA staff.

COLORED STONES AND PEARLS

Colored Stone Treatments in the Twenty-First Century: A Review and Current State of Research

Dr. Aaron Palke (GIA, Carlsbad) observed that a major focus of gemological research is always to improve a laboratory's ability to detect gems accurately and efficiently that are artificially treated to enhance their appearance. As our knowledge grows, laboratories focus on treatments that are increasingly difficult to detect, such as low-temperature heat treatment, chromophore diffusion, and artificial irradiation. Dr. Palke's talk provided a review of the innovative research on colored stone treatment identification in the twenty-first century. He noted that treatments are not inherently bad, but rather are crucial for miners and the industry because most gems need treatment to be marketable. Similarly, treatments do not decrease value because gemstones that require enhancement typically have little worth otherwise. He quipped, "Big, clean, untreated gems make you rich…treated gems pay the bills!"

Dr. Palke noted that gem enhancement is not new; ancient treatments included dyeing and quench crackling, foil backs, boiling amber in oil, and low-temperature heat treatment of sapphire. By the twentieth century, treaters employed sophisticated furnaces with precise temperature and atmosphere control, radiation, and advanced clarity enhancements such as resins and epoxies for emerald and flux and glass fillings for ruby. Gem treatment in the twenty-first century centered on modifications to established treatments, "new recipes," and extending existing enhancements to different types of gems, including lattice diffusion, low-temperature heat treatment, irradiation of pink sapphire, and clarity enhancement for non-emerald gemstones. Although lattice diffusion is not a new treatment—titanium-diffused sapphire appeared in the 1970s to '80s—treaters experimented with introducing other chromophores into gems at high temperatures. Gemological laboratories saw an unusual influx of padparadscha-colored sapphires in the early 2000s and quickly determined their

Editors' note: Interested contributors should send information and illustrations to gandgeditorial@gia.edu.

Gems & Gemology, Vol. 61, No. 4, pp. 416–453.

Figure 1. Gem laboratories saw an unusual influx of padparadscha-colored sapphires in the early 2000s and quickly attributed their color to beryllium diffusion. This group of pink and orangy pink treated sapphires ranges from 0.51 to 0.84 ct. Photo by Kevin Schumacher.

color was due to beryllium diffusion (figure 1). Gem labs also encountered lattice-diffused spinel (first treated with cobalt then nickel) and copper-diffused feldspar. Early production beryllium-diffused sapphire and ruby usually had a thin diffusion rim as beryllium did not diffuse too far into the stone, but treaters soon found the right techniques to diffuse beryllium all the way through. Beryllium treatment usually adds orange, but can also take away blue color. Inclusions in treated stones are often heavily altered, but in general, this is associated with high-temperature heated sapphires.

REFERENCES

Emmett J.L., Scarratt K., McClure S.F., Moses T., Douthit T.R., Hughes R., Novak S., Shigley J.E., Wang W., Bordelon O., Kane R.E. (2003) Beryllium diffusion of ruby and sapphire. *G&G*, Vol. 39, No. 2, pp. 84–135, http://dx.doi.org/10.5741/GEMS.39.2.84

Jollands M., Ludlam A., Palke A.C., Vertriest W., Jin S., Cevallos P., Arden S., Myagkaya E., D'Haenens-Johannson U., Weeramongkhonlert V., Sun Z. (2023) Color modification of spinel by nickel diffusion: A new treatment. *G&G*, Vol. 59, No. 2, pp. 164–181, http://dx.doi.org/10.5741/GEMS.59.2.164

Kane R.E, Kammerling R.C., Koivula J.I., Shigley J.E., Fritsch E. (1990) The identification of blue diffusion-treated sapphires. *G&G*, Vol. 26, No. 2, pp. 115–133.

Rossman G.R. (2011) The Chinese red feldspar controversy: Chronology of research through July 2009. *G&G*, Vol. 47, No. 1, pp. 16–30, http://dx.doi.org/10.5741/GEMS.47.1.16

Field Gemology: A Foundation to Better Understand Gemstones

Wim Vertriest (GIA, Bangkok) presented the exciting topic of field gemology. For more than 15 years, GIA has visited mining locales around the globe to collect gems for scientific research (figure 2). Collecting samples with a high reliability of stated provenance and treatments is critical for any research institution, since the quality of scientific data is directly related to the quality of the samples. Vertriest quoted famed naturalist Sir David Attenborough to illustrate that the research library associated with collections is almost of greater importance than the objects themselves. Important information also comes from the circumstances of documentation that should accompany every scientifically collected specimen. GIA's colored stone

Figure 2. Besides gemological and geologic aspects, the practice of field gemology allows gemologists to understand the culture, political dynamics, and trade complexities related to gemstones. Here field gemologists Wim Vertriest (seated center) and Aaron Palke (seated right) examine rough material from Wa Khan Sho, near Mogok, which produces ruby, sapphire, and spinel. Photo by Robert Weldon.

reference collection is well-documented in terms of origin (provenance) and treatment status. It presently contains 30,165 samples—primarily ruby, sapphire, emerald, and spinel, but also other gems including opal and garnet.

Vertriest posed the question of why jewelers, cutters, hobbyists, clients, wholesalers, and retailers should care that GIA invests in field gemology. To answer this question, he introduced the "four pillars" of field gemology, starting with the first: understanding the gems. This means characterizing the gems in terms of their identification, inclusions, chemistry, extent or absence of treatment, and often their geographic origin, if possible. As an aside, Vertriest noted that there are no bad treatments, only bad disclosure. The second pillar is understanding the earth. This means assimilating the environmental and health impacts of mining gems and the working conditions of the miners, as well as deciphering the geological processes at work and why gems are found where they are.

The third pillar is understanding how people trade gems. Who works with the stones, how do they move through the supply chain, where is the value added, and which skills add to those values? Vertriest cited Mozambique's Winza ruby deposit as an example. Connoisseurs regard its top-quality rubies as the world's finest, but apart from this tiny percentage, the rest are unusable without treatment. That Mozambique rubies react so well to treatment is one of the key reasons for the success of this material: "B-grade" goods can be made attractive and sellable. If there is no market for low-grade gems, mining will stop and the highest value material will not be found. In other words, treatment is one way to "upgrade" lower-quality material; it allows us to get more value out of the full mine run by producing a range of gems at different price points, which keeps the gem supply chain alive. The fourth pillar is understanding the source. This refers to the context of where the gemstones come from and the people who work with them, along with the meaning these specific gems hold for those who handle and make their livelihoods from them. Vertriest noted that the trade places a lot of value on the origin of certain gemstones without knowing what that means. If you try to understand the source, what makes a certain place so special in terms of its people, culture, and politics becomes clear, because these factors often dictate supply to the trade.

Field gemology allows gemologists to understand the intricacies, dynamics, and complexities that are related to gemstones. Forming a holistic view of a gem and what it represents is critical for any modern gemologist wanting to address the gem industry's current challenges.

REFERENCES

Hsu T., Lucas A., Pardieu V. (2015) Splendor in the Outback: A visit to Australia's opal fields. *G&G*, Vol. 51, No. 4, pp. 418–427, http://dx.doi.org/10.5741/GEMS.51.4.418

Hsu T., Lucas A., Kane R.E., McClure S.F., Renfro N.D. (2017) Big Sky country sapphire: Visiting Montana's alluvial deposits. *G&G*, Vol. 53, No. 2, pp. 215–227, http://dx.doi.org/10.5741/GEMS.53.2.215

Vertriest W., Girma D., Wongrawang P., Atikarnsakul U., Schumacher K. (2019) Land of origins: A gemological expedition to Ethiopia. *G&G*, Vol. 55, No. 1, pp. 72–88, http://dx.doi.org/10.5741/GEMS.55.1.72

Vertriest W., Palke A.C., Renfro N.D. (2019) Field gemology: Building a research collection and understanding the development of gem deposits. *G&G*, Vol. 55, No. 4, pp. 490–511, http://dx.doi.org/10.5741/GEMS.55.4.490

The Value of Pearl Impact

Pierre Fallourd (Onegemme, Perth, Western Australia) addressed the origin and societal and environmental impact of cultured pearls, rather than the physical attributes, that contribute to their perceived worth. The presentation focused on the mission to measure, manage, and share the value of pearls' social and environmental impact. Fallourd noted that origin and impact are emerging as equally important factors throughout the jewelry value chain; pearl is the one gem that exemplifies the need for humans and nature to coexist in harmony.

Traditionally, pearls are valued based on their appearance using GIA's 7 Pearl Value Factors: size, shape, color, luster, surface, nacre, and matching. Fallourd posed the concept of pearl as the first "nature positive" gem, adding that the pearl farming-to-retail supply chain has the potential to make a positive impact on climate change, water quality, biodiversity, habitat, and society. Fallourd identified how a well-run, ecologically conscious cultured pearl farm might offset climate change and improve water quality and marine habitat. Both pearls and oyster shells capture carbon and produce mother-of-pearl, which is a widely used, long-lasting decorative product. Oysters extract nutrients, in the form of nitrogen and phosphorus, and heavy metals to improve water quality. One metric ton of farmed oysters can remove 10 kg of nitrogen, 0.5 kg of phosphorus, and 0.7 kg of heavy metals. A farm of 40,000 oysters turns over >2,000,000 liters (nearly one Olympic-sized swimming pool) every hour. Pearl oysters house diverse and abundant epifauna that adds to the ecosystem; a 1-hectare farm might produce more than one extra metric ton of catchable fish by providing additional spawning habitats.

Pearling and pearl farming are labor-intensive and create direct skilled employment often in remote locations. Communities also benefit through fair trade, creation of wealth, and transfer of knowledge. However, there are risks to be mitigated; badly run farms can produce excess sewage, increase sediment, and encourage overfishing, invasive species, and disease, while emissions reduction and use of renewable energy might be costly. The social and environmental benefits of marine pearl farming vary according to species, processes, and location. Every opportunity comes with an attached risk that should be monitored and moderated. The benefits can exceed the cost to the communities and ecosystems for each hectare farmed. Their value can be measured and managed, and pearl farming can deliver value throughout the entire pearl supply

chain, leading to a virtuous cycle. If provenance and best practices can be demonstrated, retailers have additional storytelling resources to engage and enthuse consumers.

REFERENCE

Alleway H. (2023) Gem News International: An environmental, social, and governance assessment of marine pearl farming. *G&G*, Vol. 59, No. 3, pp. 404–406.

Pearl Testing and Research at GIA: A Brief History and Recent Updates

In this presentation, **Dr. Chunhui Zhou** (GIA, New York) provided a brief history of GIA's advances in pearl testing technology and research, which have helped GIA solve various identification challenges for this unique and timeless biogenic gem. Dr. Zhou traced GIA's pearl testing legacy back to the 1930s, when Japanese akoya cultured pearls were first successfully commercialized, and the ability to separate natural pearls from their cultured counterparts presented gemological laboratories with a major identification challenge. In the 1930s, GIA used the endoscope, an optical device that revealed the presence of a bead nucleus under the nacre of a cultured pearl. In the 1940s, GIA elaborated this device into the Pearloscope, which also detected the shell-banding structure in the beads. By the 1950s, X-ray equipment was obligatory for pearl identification, and pearl testing amounted to more than 90% of the GIA Gem Testing Laboratory's business. Dr. Zhou emphasized that the importance of pearls to the industry has continued to drive four primary areas of pearl-related research at GIA: a pearl's natural or cultured nature (figure 3), whether it was produced in a saltwater or freshwater environment, the type of mollusk that produced it, and whether the mollusk produces nacreous, porcelaneous, or non-nacreous pearls. A fifth consideration, if present, is the degree and type of treatment. Dr. Zhou highlighted the various research publications GIA scientists have contributed over the years, many of which are listed below.

REFERENCES

Homkrajae A., Manustrong A., Nilpetploy N., Sturman N., Lawanwong K., Kessrapong P. (2021) Internal structures of known *Pinctada maxima* pearls: Natural pearls from wild marine mollusks. *G&G*, Vol. 57, No. 1, pp. 2–21, http://dx.doi.org/10.5741/GEMS.57.1.2

Nilpetploy N., Lawanwong K., Kessrapong P. (2018) Non-bead cultured pearls from *Pinctada margaritifera*. *GIA Research News*, April 27, https://www.gia.edu/ongoing-research/non-bead-cultured-pearls-from-pinctada-margaritifera

Scarratt K., Sturman N., Tawfeeq A., Bracher P., Bracher M., Homkrajae A., Manustrong A., Somsa-ard N., Zhou C. (2017) Atypical "beading" in the production of cultured pearls from Australian *Pinctada maxima*. *GIA Research News*, February 13, https://www.gia.edu/gia-news-research/atypical-beading-production-cultured-pearls-australian-pinctada-maxima

Sturman N., Homkrajae A., Manustrong A., Somsa-ard N. (2014) Observations on pearls reportedly from the Pinnidae family (pen pearls). *G&G*, Vol. 50, No. 3, pp. 202–215, http://dx.doi.org/10.5741/GEMS.50.3.202

Sturman N., Bergman J., Poli J., Homkrajae A., Manustrong A., Somsa-ard N. (2016) Bead-cultured and non-bead-cultured pearls from Lombok, Indonesia. *G&G*, Vol. 52, No. 3, pp. 288–297, http://dx.doi.org/10.5741/GEMS.52.3.288

Figure 3. Modern gemological laboratories use real-time X-ray imaging systems to assess the transparency of gem materials, which is especially important for distinguishing natural from cultured pearls. Photo by Nuttapol Kitdee.

An Overview of the Natural Gulf Pearl Trade

Abeer Al-Alawi (GIA, Mumbai) provided an overview of the natural pearl trade in the Persian (Arabian) Gulf. Historically, this area—particularly Bahrain, Qatar, Kuwait, and the United Arab Emirates (UAE)—was considered the center of the natural pearl trade. Pearl diving was an essential livelihood of many communities in the Gulf, which were renowned for producing some of the world's finest natural pearls, known among Indian traders as "Basra pearls," a term that remains in use to this day. Traders transported Persian Gulf pearls from the port town of Basra in southern Iraq by sea on *dhows* and other vessels to India, where they were processed, sorted, drilled, and strung before being sold in Europe and other markets worldwide.

The period between 1850 and 1930 marked the peak of natural pearl fishing in the Persian Gulf, when the area supplied perhaps 70–80% of the world's natural pearls. During this time, Bahrain was the epicenter of the natural pearl trade. Al-Alawi noted that Bahrain had the richest pearling beds followed by Kuwait and Qatar. Two important sites are considered the "home of pearling" in the UAE: Dubai and Abu Dhabi. Julfar, now known as Ras Al Khaimah in the UAE, was one of the most important pearling centers and was recognized for producing the best quality pearls due to its location between the main pearl banks and Hormuz. The pearling beds were typically at depths between 6 and 20 meters, with deeper areas reaching up to 30 meters. Traditionally, the diving season was from April to September. Divers remained under water for 60 to 90 seconds using a nose clip. Larger pearling ships required a crew of 60 to 80, including a captain, captain's assistant and crew head, singer (one of the most important roles), diver, trainee, puller, and cook. At the end of the season, shares would be distributed by function; the diver would take two shares and the puller only one, while the singer would take two shares for his distinguished role on board.

In the nineteenth and early twentieth centuries, most Gulf pearls were shipped to and processed in Bombay (now Mumbai), India, which has been a significant pearl manufacturing, processing, and trading hub for centuries. To showcase the high-quality Basra pearls, Bombay traders would sort the pearls, string them with silk threads, and tie them together at both ends using decorative metallic cords of various colors. These bunches were in great demand in Europe's pearl markets and were sold as "Bombay bunches." By the mid-1930s, three factors caused natural pearl revenues to plunge more than 70%: the economic impact of the Great Depression, the discovery of oil in the Persian Gulf, and the advent of commercial quantities of Japanese akoya cultured pearls. However, Al-Alawi highlighted the present-day resurgence of interest in natural pearls driven by a growing appreciation for their rarity and unique history (figure 4).

REFERENCES

Hohenthal T.J. (1938) The Bombay pearl market—Summary of a report. *G&G*, Vol. 2, No. 9, pp. 159–160.

Kennedy L., Homkrajae A. (2023) Gem News International: Spotlight on natural nacreous pearls. *G&G*, Vol. 59, No. 1, pp. 112–113.

Lesh C. (1980) Born in the depths: The perfect pearl. *G&G*, Vol. 16, No. 11, pp. 356–365.

Figure 4. The majority of these loose natural pearls are from the Pinctada radiata *mollusk. They were recently collected off the coast of Kuwait in the Persian (Arabian) Gulf. Photo by Robert Weldon.*

An Overview and Update on the GIA 7 Pearl Value Factors Classification System

Cheryl (Ying Wai) Au (GIA, Hong Kong) opened by posing the question of how we should describe the beauty or the quality of pearls in language that everyone can understand. Similar to the Four *C*s for diamonds, GIA developed the GIA 7 Pearl Value Factors. This system offers consistency and provides customers with the knowledge needed to make an informed purchase. We can apply it to all nacreous pearls, including the four major cultured pearl types in the market: akoya, South Sea, Tahitian, and freshwater (figure 5). Au summarized GIA's long history with pearls. The Institute began offering pearl identification services in 1949, a few years before the introduction of diamond grading. *Gems & Gemology* published the first paper discussing pearl value factors and classification in 1942, though it focused on natural pearls. In 1967, the GIA 7 Pearl Value Factors were first identified and described by Richard T. Liddicoat Jr. with an emphasis on cultured pearls. Today, a GIA Pearl Identification Report provides extensive information including pearl quantity, weight, size, shape, color, overtone, natural or cultured identity, mollusk type, saltwater or freshwater environment, and any detectable treatments.

In 2021, GIA launched a Cultured Pearl Classification Report that clearly states the 7 Pearl Value Factors of the submitted pearl items. Au covered recent updates to some terms adopted by GIA including the recently expanded nacre quality scale, and defined each value factor:

1. Size is determined by weighing and measuring the pearl. Pearl size is expressed in millimeters and pearl weight in carats (typically), both to two decimal places. Different pearl types have different size ranges. For example, akoya pearls are generally smaller with a typical size range of 6–9 mm, and South Sea pearls might range from 13–20 mm.
2. GIA classifies pearls into seven main shapes: round, near-round, drop, oval, button, semi-baroque, and baroque.
3. Pearl colors have three different components: bodycolor, overtone, and orient. Bodycolor combines hue, tone, and saturation. GIA uses 19 hue names for pearls. Tone is the relative lightness or darkness of a color, ranging from white, through various shades of gray, to black. Saturation is the relative weakness or strength of color, first neutral, then from very light to strong. Overtone is a single translucent color overlying a pearl's bodycolor, while orient is any combination of multiple overtone colors or iridescence overlying a pearl's color.
4. Luster describes the intensity and sharpness of reflections seen on a pearl's surface. After comparison with specific pearl luster masters, GIA classifies a pearl's luster grade as Excellent, Very Good, Good, Fair, or Poor. Different pearl types have varying inherent luster ranges, so an Excellent luster for one type might only be Very Good for another.
5. Surface classification describes the degree of spotting on a pearl's surface, and also considers the number,

Figure 5. The GIA 7 Pearl Value Factors classification system is applicable across the whole pearl supply chain, from buyers checking the quality of pearls at an auction to consumers shopping for pearls at the retail level. Photo by Wim Vertriest.

severity, and positioning of visible blemishes. After comparing to pearl surface masters and judging the surface condition, a pearl's surface is classified into one of four categories: clean, lightly spotted, moderately spotted, and heavily spotted.

6. Nacre grades are based on three elements: thickness, continuity, and condition. GIA's nacre grade reflects the condition of a pearl's nacre, which affects luster, surface, and sometimes durability. The pearl's nacre layer should meet required minimum thickness standards for each pearl type: for akoya this is at least 0.15 mm, for Tahitian at least 0.80 mm, and for South Sea at least 1.50 mm. Pearls with thin nacre show a chalky appearance and the beads are readily visible under strong lighting. Nacre continuity is the lack of disruptions or "movement" in nacre layering, or in other words, the smoothness and "cleanliness" of the pearl. Nacre condition includes any post-harvest considerations, such as processing, polishing, and working, as well as wear and damage.
7. Matching is defined as the uniformity of appearance in strands and multiple pearl groups or items. Well-matched, high-quality pearl sets show uniformity of color and shape, while lower-quality sets display greater variation in shape and color.

REFERENCES

Ho J.W.Y., Shih S.C. (2021) Pearl classification: The GIA 7 Pearl Value Factors. *G&G*, Vol. 57, No. 2, pp. 135–137, http://dx.doi.org/10.5741/GEMS.57.2.135

Liddicoat R.T. Jr. (1967) Cultured-pearl farming and marketing. *G&G*, Vol. 12, No. 6, pp. 162–172.

Rietz P.C. (1942) The classification and sales possibilities of genuine pearls. *G&G*, Vol. 4, No. 1, pp. 9–12.

——— (1942) The classification and sales possibilities of genuine pearls. *G&G*, Vol. 4, No. 2, pp. 25–28.

DIAMOND IDENTIFICATION

Distinguishing Diamonds: Understanding the Differences Between Natural and Laboratory-Grown Diamond Formation and Their Unique Stories

Dr. Ulrika D'Haenens-Johansson (GIA, New York) outlined the momentous transformation in the diamond industry over the past 20 years due to the advent of commercial laboratory-grown diamonds (LGDs), discussing the differences in natural and LGD formation and highlighting the resulting clues that they provide, which allow conclusive separation (figure 6). Production of LGDs has surged significantly with pronounced improvements in their size and quality; forecasted 2025 production is approximately 30 million carats of LGD gem rough. Despite sharing key crystal properties with natural diamonds, LGDs have fundamentally distinct formation mechanisms and stories from diamonds that formed millions to billions of years ago deep within the earth.

Dr. D'Haenens-Johansson noted that LGDs are widely available and have garnered a lot of press coverage, resulting in a mixture of both highly informed and misinformed clients and retailers, which creates considerable confusion and mistrust. "Bad actors" can intentionally mix LGDs with natural diamonds, or it might happen inadvertently. Dr. D'Haenens-Johansson stressed that clear differentiation of both products is key.

Natural diamonds are old, having formed 90 million to 3.5 billion years ago. For comparison, the extinction of dinosaurs happened 65 million years ago, and the age of Earth is 4.56 billion years. Natural diamonds form within the earth from carbon-containing fluids and rocks at greater depths than any other gemstone. Most derive from rocks 150–200 km below the earth's surface, but some originate deeper: 700 km. They are brought up to the surface by ancient volcanic eruptions in kimberlite pipes. Natural diamonds are rare; it takes roughly 100,000 metric tons of ore to find a single one-carat D-color flawless diamond (a grade of >0.01 carat/metric ton).

LGDs are mass-produced in factories. Their composition and crystal structure are the same as natural diamond, with essentially the same physical, chemical, and optical properties. They can be differentiated because they have a fundamentally different origin from natural diamonds. LGDs are produced by two main methods: high-pressure, high-temperature (HPHT), accounting for 20% of production, and chemical vapor deposition (CVD) representing 80%. HPHT synthesis uses a press that mimics the conditions of natural diamond growth, but not the chemistry.

Figure 6. The different growth conditions of natural and laboratory-grown diamonds provide distinctive clues that allow gemologists to conclusively separate them. Here laboratory-grown CVD (left) and HPHT (middle) rough diamonds are pictured next to a natural rough diamond (right). Photos by Robert and Orasa Weldon; courtesy of the GIA Sir Ernest Oppenheimer Student collection (left).

LGD growth occurs at pressures of 5–6 GPa and temperatures of 1300–1600ºC over durations of days to months. CVD synthesis uses a gaseous carbon source with hydrogen, diamond seed plates, microwaves to activate plasma and low pressures (one twentieth to one quarter atmospheres) and temperatures of 700–1200ºC to build up LGDs layer-by-layer over a period of days to months.

GIA has been researching synthetic diamonds since their inception. Robert Crowningshield was the first gemologist to inspect General Electric's gem-quality specimens in the 1970s. GIA continues to analyze LGDs from the trade and also conduct in-house synthesis of CVD LGDs. GIA has developed a fundamental understanding of the material and its evolution over time and can recognize the difference between natural diamonds and LGDs. Humans cannot reproduce natural diamond formation and residence conditions, so natural diamonds and LGDs are not identical. They each contain clues of their origin that allow us to clearly separate them using laboratory services and screening equipment.

REFERENCES

Ardon T., McElhenny G. (2019) Lab Notes: CVD layer grown on natural diamond. *G&G*, Vol. 55, No. 1, pp. 97–99.

Eaton-Magaña S., Breeding C.M. (2018) Features of synthetic diamonds. *G&G*, Vol. 54, No. 2, pp. 202–204, http://dx.doi.org/10.5741/GEMS.54.2.202

Eaton-Magaña S., Shigley J.E. (2016) Observations on CVD-grown synthetic diamonds: A review. *G&G*, Vol. 52, No. 3, pp. 222–245, http://dx.doi.org/10.5741/GEMS.52.3.222

Eaton-Magaña S., Shigley J.E., Breeding C.M. (2017) Observations on HPHT-grown synthetic diamonds: A review. *G&G*, Vol. 53, No. 3, pp. 262–284, http://dx.doi.org/10.5741/GEMS.53.3.262

Eaton-Magaña S., Hardman M.F., Odake S. (2024) Laboratory-grown diamonds: An update on identification and products evaluated at GIA. *G&G*, Vol. 60, No. 2, pp. 146–167, http://dx.doi.org/10.5741/GEMS.60.2.146

Wang W., Persaud S., Myagkaya E. (2022) Lab Notes: New record size for CVD laboratory-grown diamond. *G&G*, Vol. 58, No. 1, pp. 54–56.

Screening and Detection of Synthetic Diamonds

Dr. David Fisher (De Beers, Maidenhead, United Kingdom) acknowledged that laboratory-grown diamonds (LGDs) are now an established part of the jewelry trade and gave a brief history of diamond synthesis from the 1950s, citing the many advances in quality and size that have made LGDs a commercial commodity in today's markets. The talk outlined the approaches taken to date to address the challenge along with the developments that have allowed the application of screening technology to the wide range of sizes affected by LGD production. Dr. Fisher emphasized the need to extend screening capability beyond the laboratory and into retail, where the ability to clearly demonstrate a diamond's natural origin could assist retailers in the promotion of natural diamonds.

The presentation outlined the many options for diamond verification instruments (DVIs) available to the trade. Some of the screening methods these devices use include absorption, fluorescence, or phosphorescence, often relying on the N3 defect (a vacancy surrounded by three nitrogen atoms, which appears in the vast majority of natural diamonds, but is absent in LGDs and diamond simulants). Dr. Fisher also described the pressures the trade exerts on manufacturers of DVIs, including cost, compact size, accuracy of screening, and volume, especially where melee-size diamonds are concerned. The Natural Diamond Council's (NDC) Assure Program verifies the performance of commercially available DVIs used to separate natural diamonds and LGDs. All instruments are rigorously tested by an independent third-party laboratory using a standard methodology and various sample sizes of natural diamonds, LGDs, and diamond simulants. Key metrics include false-positive rate (wrongly identifying a synthetic diamond as natural) and the referral rate (correctly identifying a stone that needs further testing). NDC publishes results online, which are available to anyone in the diamond trade. Dr. Fisher noted that the optimal false-positive rate is 0%; it is "really bad" if any LGDs are passed as natural. Of the 32 DVIs tested in the first iteration of the Assure Program (2019), only 14 (32%) gave a 0% false-positive rate. By Assure 2.0 (2025), the false-positive rate was much better: 15 out of 18 (83%) returned a zero false-positive rate.

REFERENCES

Crowningshield R. (1971) General Electric's cuttable synthetic diamonds. *G&G*, Vol. 13, No. 10, pp. 302–314.

De Beers Diamond Verification Instruments: https://verification.debeersgroup.com/diamond-verification-instruments/

Eaton-Magaña S., D'Haenens-Johansson U.F.S. (2012) Overview and Update: Recent advances in CVD synthetic diamond quality. *G&G*, Vol. 48, No. 2, pp. 124–127.

Eaton-Magaña S., Shigley J.E. (2016) Observations on CVD-grown synthetic diamonds: A review. *G&G*, Vol. 52, No. 3, pp. 222–245, http://dx.doi.org/10.5741/GEMS.52.3.222

Fisher D. (2018) Addressing the challenges of detecting synthetic diamonds. *G&G*, Vol. 54, No. 3, pp. 263–264.

Natural Diamond Council ASSURE Program: https://www.naturaldiamonds.com/council/assure-testing-program/

Shigley J.E., Fritsch E., Stockton C.M., Koivula J.I., Fryer C.W., Kane R.E. (1986) The gemological properties of the Sumitomo gem-quality synthetic yellow diamonds. *G&G*, Vol. 22, No. 4, pp. 192–208.

Shigley J.E., Fritsch E., Stockton C.M., Koivula J.I., Fryer C.W., Kane R.E., Hargett D.R., Welch C.W. (1987) The gemological properties of the De Beers gem-quality synthetic diamonds. *G&G*, Vol. 23, No. 4, pp. 187–206.

Shigley J.E., Fritsch E., Koivula J.I., Sobolev N.V., Malinovsky I.Y., Pal'yanov Y.N. (1993) The gemological properties of Russian gem-quality synthetic yellow diamonds. *G&G*, Vol. 29, No. 4, pp. 228–248.

Wang W., Hall M.S., Moe K.S., Tower J., Moses T.M. (2007) Latest-generation CVD-grown synthetic diamonds from Apollo Diamond Inc. *G&G*, Vol. 43, No. 4, pp. 294–312.

Wang W., D'Haenens-Johansson U.F.S., Johnson P., Moe K.S., Emerson E., Newton M.E., Moses T.M. (2012) CVD synthetic diamonds from Gemesis Corp. *G&G*, Vol. 48, No. 2, pp. 80–97, http://dx.doi.org/10.5741/GEMS.48.2.80

DIAMOND AND MINERAL GEOLOGY

Determining a Diamond's Country of Origin: Dream or Reality?

Dr. Michael Jollands (GIA, New York) questioned whether gemological laboratories might develop methods to determine a diamond's country of origin just as many have for colored gems such as sapphire, ruby, and emerald, which are generally submitted without any documentation. In this talk, Dr. Jollands discussed the challenges of determining a diamond's country of origin, the pitfalls of some proposed methods, and future opportunities for tracing a diamond's mine-to-market path. Most colored stones form up to a few tens of kilometers below the earth's surface, where there can be major geologic differences from place to place. In contrast, diamonds form much deeper in the lower lithosphere or mantle, hundreds of kilometers below the surface. Here, there are only minor differences between different parts of the earth.

For colored gems, laboratories use several methods for determining origin: inclusions or visual observations, trace element chemistry (energy-dispersive X-ray fluorescence or laser ablation–inductively coupled plasma–mass spectrometry), and spectroscopy. Trace elements exist in gems in very small amounts at the parts-per-billion (ppb) or parts-per-million (ppm) level and are not normally part of the crystal. Some well-known trace elements in diamond are nitrogen, hydrogen, boron, silicon, oxygen, and nickel. Many other elements can exist in fluid inclusions inside diamonds. These inclusions may be visible or invisible, and unevenly distributed, and the elements they contain are generally present at the parts-per-million to parts-per-trillion levels. Analysis is extremely challenging and destructive, even with new, highly sensitive equipment.

Published work and GIA's own testing show complete overlap between the trace element chemistry of diamonds from different locations. Some differences do exist, but these are associated with different diamond-forming fluids, which are not geographically specific. In contrast, colored stones often show very clear separation between samples from different geographic origins. For example, copper-bearing tourmaline from different locales can be separated using gallium, lead, copper, strontium, and zinc levels. To the best of current knowledge within GIA and the academic community, no similar separation exists for diamonds. Gemologists routinely use three kinds of spectroscopy: infrared (IR), ultraviolet/visible/near-infrared (UV-Vis-NIR), and photoluminescence (PL). Only IR spectroscopy shows promise. One set of defects associated with nitrogen and hydrogen may be useful because their spectra can be used to determine how long the diamond sat in the earth at a given temperature. Diamonds from different locations have different time and temperature histories. Although a current global dataset of around one million stones shows some correlation, samples from the same location can fall across the whole plot, with overlap between diamond ages from different locations.

Dr. Jollands concluded that many diamonds lack visible inclusions, trace elements are very challenging to measure, and characteristics completely overlap between sources. Spectroscopy offers no geographical separation, and tracing stones from source to consumer appears to be the only viable method for tracking diamond origin today (figure 7). This brings many challenges, including tagging stones at every step and stopping inadvertent or deliberate swapping of stones, but these can be overcome, whereas geologic limitations cannot.

REFERENCE

Smith E.M., Smit K.V., Shirey S.B. (2022) Methods and challenges of establishing the geographic origin of diamonds. *G&G*, Vol. 58, No. 3, pp. 270–288, http://dx.doi.org/10.5741/GEMS.58.3.270

Figure 7. Once rough diamonds such as these from Angola enter the supply chain and are mixed with diamonds from other mines, determining their geographic origin is currently impossible. Photo by Robert Weldon; courtesy of Diamond Trading Antwerpen.

Lithospheric Diamonds and Their Mineral Inclusions: A Glimpse into the Ancient Earth's Mantle

Dr. Mei Yan Lai (GIA, Carlsbad) began by explaining how kimberlite and lamproite eruptions sample Earth's mantle to bring diamonds to the surface. The extreme hardness and chemical inertness of diamond enable it to serve as a probe into the composition of Earth's mantle and as a recorder of geotectonic history spanning millions to billions of years. Approximately 99% of recovered diamonds form in the subcratonic lithospheric mantle at depths of 140–200 km. While these depths cannot be directly sampled by any physical method, mantle rocks and occasionally diamond have erupted to the surface by deep-seated kimberlite volcanism.

The two mantle rocks for lithospheric diamond formation are peridotite (primarily made of olivine, enstatite, and chrome diopside, along with accessory minerals such as spinel, garnet, and sulfides) and eclogite (mostly garnet and omphacite with accessory minerals such as kyanite, coesite, rutile, corundum, and sulfides). Diamonds can be monocrystalline, fibrous, or polycrystalline. Monocrystalline diamonds typically display octahedral shapes, but can be cubic, twinned (e.g., macles), or irregular in shape. Diamond crystals can also undergo dissolution, transitioning from octahedral to dodecahedral forms, depending on the extent of resorption. Surface features including trigons or tetragons, hillocks, deformation lines, or hexagons are signs of dissolution and may be preserved on the girdles of polished diamonds. Mineral inclusions in diamond are signatures of the mantle rocks they grew in and can be identified by Raman spectroscopy. Characteristic inclusions of peridotitic diamonds are purple garnet, bright green chrome diopside, colorless enstatite, olivine, and dark red chromite. Eclogitic diamonds might contain orange garnets (figure 8), grayish green omphacites, colorless coesite, brownish orange rutile, or blue kyanite.

Dr. Lai explained the circumstances under which scientists employ a technique called chemical geothermobarometry to estimate the pressure and temperature conditions of the mantle. They analyze the chemical composition of pairs of coexisting mineral inclusions such as garnet and olivine in peridotitic diamonds or garnet and omphacite in eclogitic ones. Iron and magnesium partition themselves between these minerals in a way that is highly dependent on temperature. After measuring each mineral's iron-magnesium ratio, scientists use experimentally derived equations to calculate the formation temperature.

The eruption ages of diamond-bearing kimberlites and lamproites range from around 20 million to 1 billion years. Scientists use radioactive decay systems to infer diamond age. Unfortunately, the half-life of carbon-14 is too short and cannot be used for objects older than 57,000 years. Radioactive decay systems with longer half-lives are used instead (41 billion years for rhenium-osmium in sulfide minerals and 106 billion years for samarium-neodymium in garnets and clinopyroxene). Dr. Lai concluded by placing natural diamonds in context with Earth's 4.56-billion-year timeline. Peridotitic diamonds from Canada's Ekati mine (3.5 billion years old) and eclogitic ones from Botswana's Jwaneng mine (2.9 billion years old) bracket the onset of plate tectonics (about 3 billion years ago). Dr. Lai noted that natural diamonds are among the oldest and most remarkable objects to wear and long predate the extinction of the dinosaurs (65 million years ago) and the advent of our own species, *Homo sapiens*, a mere 300,000 years ago.

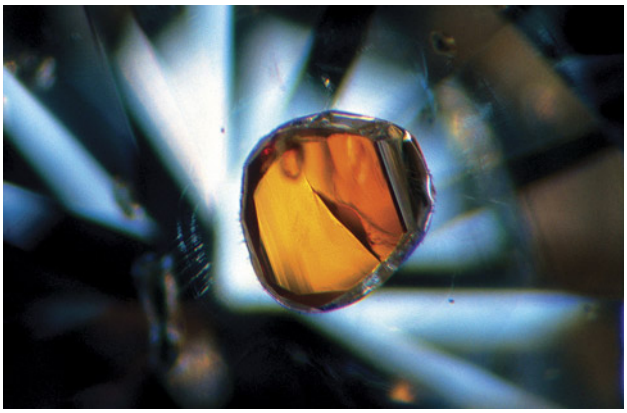

Figure 8. This transparent orange almandine pyrope garnet typifies an eclogitic origin for its host diamond. Photomicrograph by John I. Koivula; field of view 3.6 mm.

REFERENCES

Hardman M.F., Lai M.Y. (2023) Gem News International: Diamondiferous mantle eclogite: Diamond surface features reveal a multistage geologic history. *G&G*, Vol. 59, No. 3, pp. 402–404.

Kirkley M.B., Gurney J.J., Levinson A.A. (1991) Age, origin, and emplacement of diamonds: Scientific advances in the last decade *G&G*, Vol. 27, No. 1, pp. 2–25, http://dx.doi.org/10.5741/GEMS.27.1.2

Shirey S.B., Shigley J.E. (2013) Recent advances in understanding the geology of diamonds. *G&G*, Vol. 49, No. 4, pp. 188–222, http://dx.doi.org/10.5741/GEMS.49.4.188

Superdeep Diamonds: Exceptional Gems with an Incredible Backstory

Dr. Evan Smith (GIA, New York) described research led by GIA in the past decade revealing that many high-quality type II gem diamonds, known for their purity, come from unusually extreme depths inside the earth. Known as superdeep diamonds, this rare geological category of diamond originates from depths of 300–800 km. All gem diamonds form much deeper in the earth (around 140 to 200 km) than colored gems (only up to a few tens of kilometers), but only some are superdeep. These represent 1–2% of mined diamonds and ascend in low-density rocks to depths of about 200 km, where they might be brought to the surface in kimberlites. The depths these diamonds originated from are determined by their mineral inclusions

that represent the pressure and temperature conditions of their formation. Scientists recognized ferropericlase and majoritic garnet in the 1980s and used high-pressure experiments as a basis for comparison to confirm their deep origin in the mantle. These discoveries provide a bigger picture of diamonds; lithospheric diamonds crystallize from carbon-containing fluids at depths of 150 to 200 km, whereas superdeep or sublithospheric diamonds form at depths of 300 to 800 km and subduction of oceanic lithosphere is a key ingredient in their formation. Ringwoodite, a high-pressure version of olivine, is stable at depths of 520 to 660 km in Earth's mantle, so the discovery of a hydrous ringwoodite inclusion in a superdeep diamond is evidence of subducted water. Unlike most lithospheric diamonds, which contain nitrogen and are therefore type I, superdeep diamonds are type IIa—containing essentially no nitrogen with levels of <5 parts per million (ppm)—or IIb, which contain traces of boron. Type I lithospheric diamonds represent 98% of all gem diamonds, whereas type IIa (1–2%) and IIb (<0.02%) are incredibly rare. Some of the world's most valuable gems are type IIa superdeep diamonds, including the 530.2 ct Cullinan I diamond set in the Sovereign's Scepter with Cross, part of the British Crown Jewels.

Scientists use the acronym CLIPPIR to describe these big gems: Cullinan-like, Large, Inclusion-Poor, Pure, Irregular, and Resorbed. The inclusions in CLIPPIR diamonds are associated with deeply subducted oceanic plates. Some of these inclusions are metallic (a mix of iron, nickel, carbon, and sulfur), and molten during diamond growth, representing the diamond-forming medium. Superdeep diamond genesis results from the warming and deformation of altered oceanic lithosphere at depth. Three fluid-generating mechanisms are important to diamond formation: the melting of carbonates, the release of water, and the evolution of a metallic melt. The ideas associated with natural diamond are some of the most unique in all geosciences: they form as a result of large-scale movements of plate tectonics; they are ancient (up to 3.5 billion years old); they are the deepest-derived objects you can touch; and they reach the earth's surface in strange volcanoes. Diamonds are a window into the hidden processes of the planet's interior, giving them both a tremendous scientific value and a fascinating natural history.

REFERENCES

Eaton-Magaña S., Breeding C.M., Shigley J.E. (2018) Natural-color blue, gray, and violet diamonds: Allure of the deep. *G&G*, Vol. 54, No. 2, pp. 112–131, http://dx.doi.org/10.5741/GEMS.54.2.112

Shirey S.B., Shigley J.E. (2013) Recent advances in understanding the geology of diamonds. *G&G*, Vol. 49, No. 4, pp. 188–222, http://dx.doi.org/10.5741/GEMS.49.4.188

Smith E.M., Shirey S.B., Nestola F., Bullock E.S., Wang J., Richardson S.H., Wang W. (2016) Large gem diamonds from metallic liquid in Earth's deep mantle. *Science*, Vol. 354, No. 6318, pp. 1403–1405, http://dx.doi.org/10.1126/science.aal1303

Smith E.M., Shirey S.B., Wang W. (2017) The very deep origin of the world's biggest diamonds. *G&G*, Vol. 53, No. 4, pp. 388–403, http://dx.doi.org/10.5741/gems.53.4.388

Gem Mineral Evolution: Gemology in the Context of Deep Time

Dr. Robert M. Hazen (Carnegie Institution Earth and Planets Laboratory, Washington, DC, and George Mason University, Fairfax, Virginia) placed gem minerals in the context of mineral evolution. The range and diversity of Earth's minerals are a consequence of more than 4.5 billion years of new physical, chemical, and ultimately biological processes. The concept of mineral evolution represents a new framing of mineralogy for education and public engagement. It explains the change over time of the diversity of mineral species, their relative abundance, and compositional ranges, along with their grain sizes and shapes. It also explains why smaller bodies in our solar system, such as Mars and our own moon, have less diverse assemblies of minerals. Dr. Hazen noted that mineral evolution focuses exclusively on near-surface mineral phases (<3 km in depth), as these are accessible on Earth and most likely to be observed on other planets and moons.

Ten mineral evolution stages were identified over a period of 4.5 billion years, starting with just 25 mineral species and 16 chemical elements, and leading to >6,000 minerals and 72 essential elements today. Dr. Hazen related each stage to major events in Earth's history, including the heat and impact of planetary accretion, the transition from a "dry" to a "wet" planet through volcanism and outgassing of water and other volatiles, and the formation of granite and the onset of plate tectonics to oxygenation and the rise of life. At each stage, the range of possible minerals increases, including gems. Peridot appears around 4.55–4.35 billion years ago, as the young planet's internal heat drove volcanism and outgassing of water. Pegmatite gems such as beryl, spodumene, and tourmaline (figure 9) occur as granite forms through crustal remelting and differentiation around the 3.5-billion-year mark. With the onset of plate tectonics around 3 billion years ago, conditions became suitable for the formation of gem corundum, garnet, and jadeite. With the dawn of life, the rise of photosynthesis, and the production of an oxygen-rich atmosphere between 2.5 and 1.85 billion years ago, gem minerals such as azurite, malachite, and turquoise became possible. At each stage of mineral evolution, the range, diversity, and number of minerals increased. Dr. Hazen explained that each mineral or gem specimen is a treasure trove of information, revealing rich detail about formation processes and times.

Dr. Hazen introduced applications of powerful analytical and visualization methods to the characterization of mineral origins and the prediction of new mineral deposits, noting that we have entered a new age of mineral informatics where multidimensional analysis and visualization of mineral systems are leading to insights into the co-evolution of Earth and life. The talk concluded with a proposal that the diversity and distribution of minerals on Earth is a planetary-scale biosignature.

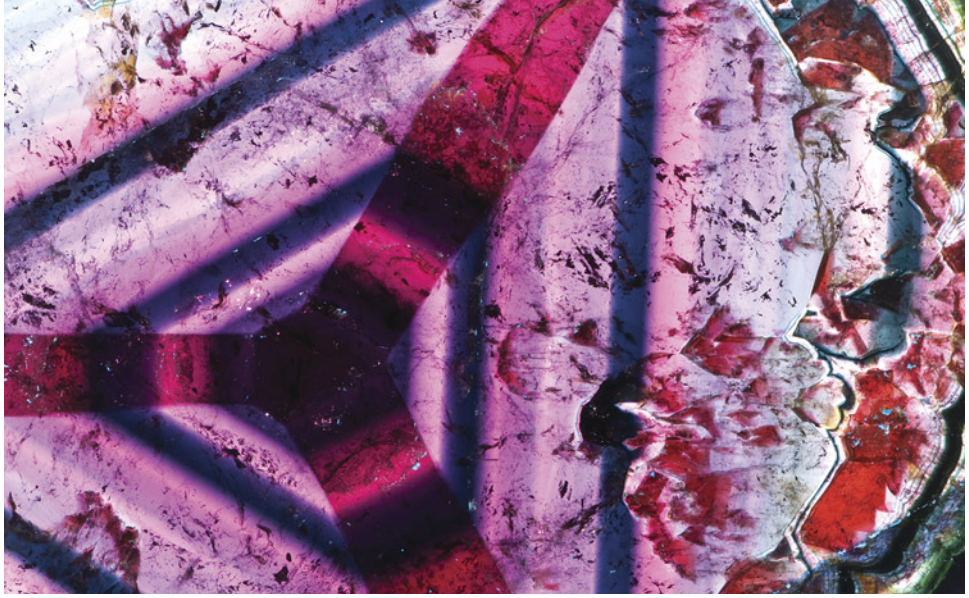

Figure 9. In a microcosm of mineral evolution, the color zoning in this liddicoatite tourmaline slice from Madagascar reflects changes in chemistry during growth. Photo by Robert Weldon.

REFERENCES

Hazen R.M. (2010) Evolution of minerals. *Scientific American*, Vol. 302, No. 3, pp. 58–65.

Hazen R.M., Morrison S.M. (2020) An evolutionary system of mineralogy. Part I: Stellar mineralogy (>13 to 4.6 Ga). *American Mineralogist*, Vol. 105, No. 5, pp. 627–651, http://dx.doi.org/10.2138/am-2020-7173

Hazen R.M., Papineau D., Bleeker W., Downs R.T., Ferry J.M., McCoy T.J., Sverjensky D.A., Yang H. (2008) Mineral evolution. *American Mineralogist*, Vol. 93, No. 11-12, pp. 1693–1720, http://dx.doi.org/10.2138/am.2008.2955

DIAMOND CUT

Modern Diamond Design

Dr. Jim Conant (GIA, Las Vegas) explored how new computational tools help navigate the vast design space of possible facet arrangements for polished diamonds, enabling both novel cuts and optimization of traditional cuts for light performance. Dr. Conant explained the basics of diamond optical performance and the work behind the creation of some new diamond cuts. The foundation of all diamond cut analysis is the concept of "virtual facet pattern." This helps interpret and model the various optical phenomena that contribute to or detract from the beauty of a cut diamond. It accounts for attributes such as brightness, light leakage, "crushed ice," "dark zone" patterns, fire, and scintillation, as well as enabling the creation of new diamond cuts, faceting arrangements, and cut geometries.

Virtual facets are the complex shifting patterns of little polygons that the observer sees, similar to a hall of mirrors, as a moving diamond's facet geometry reflects light back to the eye. Taking a single virtual facet near the edge of the table of an ideal cut round brilliant as an example, Dr. Conant explained that light striking the inside surface of a diamond at all but the steepest angles reflects off the internal surface like a mirror. As the remaining light enters the gem, it refracts as it passes through the crown, reflects twice off the pavilion, and finally travels out of the stone from the crown back to the observer's eye. Because this light meets several different facets along the way, it fragments into several columns. From the observer's perspective, each virtual facet collects light from a different region in the environment.

Dr. Conant explained that a diamond's appearance is quite sensitive to slight differences in pavilion angle; at 41.4 degrees, the beam path no longer exits the crown but reflects back down to the pavilion where it collects light from underneath the diamond, leading to "partial leakage." Showing the example of a poorly cut pear-shaped diamond cut to match the shape of the rough and maximize weight, Dr. Conant noted that sometimes leakage is even more obvious when the beam immediately exits through the pavilion without any reflections. The stone's poor appearance results from a too shallow pavilion, allowing light to leak out the bottom and create a "dark zone." Leakage detracts from a diamond's appearance, especially when it creates a big and blocky pattern. This is an example of a virtual facet drawing light from a dark place in the environment.

Next, Dr. Conant touched upon "crushed ice," the part of some diamond fancy shapes composed of thousands of tiny virtual facets. These tiny virtual facets draw light from a randomized subset of the environment and correspond to differing focal lengths. Rather than distinct, geometric facets with crisp edges and high contrast between light and dark areas, crushed ice features many small, irregular facets that blend light in a shimmering way, like shattered glass. Diamonds with little variation in brightness can appear less appealing than those with some contrasting dark regions. However, some dark features are universally disliked. Classic "bow tie" patterns can be appealing when less severe and more transient. The more persistent a dark zone is across different tilts, viewing distances, and lighting environments, the more likely it is to be perceived as negative.

REFERENCE

Reinitz I.M., Gilbertson A., Blodgett T., Hawkes A., Conant J., Prabhu A. (2024) Observations of oval-, pear-, and marquise-shaped diamonds: Implications for fancy cut grading. *G&G*, Vol. 60, No. 3, pp. 280–304, http://dx.doi.org/10.5741/GEMS.60.3.280

Toward a Fancy Cut Grade

For **Jason Quick** (GIA, Las Vegas), diamond cut is more than symmetry and light; it shapes style, taste, and personality. How can GIA help define and teach the design factor? Fancy cuts offer seemingly limitless design possibilities that defy exhaustive exploration (figure 10). However, exploring this vast array of potential fancy-cut designs enables rather than constrains innovation. Quick reflected that both AGS and GIA have a long history of diamond-cut research leading to today's Project Everest. This collaboration started with high-level meetings in 2020, led to the integration of both research teams in 2022, and to AGS Labs formally becoming GIA's Diamond Cut R&D Lab in 2023.

GIA's upcoming fancy cut grading system will use ray tracing on 3D wireframe models to assess light performance and will prioritize diamond beauty over fixed proportion ranges. This system must solve challenges for retailers, and by necessity, be packaged with education that makes the system intuitive to use and explain to consumers. He noted that diamond cut planning involves three stages: (1) mapping of rough, (2) planning, and (3) polishing. Mapping involves 3D plotting of inclusions (size, type, and location) along with color estimation. Planning produces permutations of size and cutting style to maximize yield and quality in terms of the Four *C*s. This provides an estimate of potential gem value and marketability (liquidity). Polishing transforms the diamond through sawing, bruting (shaping), blocking, and final polishing into a finished gem.

Recent advances in GIA cut research encompass cut space (mathematical models of all possible faceting arrangements), optics (simulations of light moving through faceted diamonds), and metric development (modeling and quantifying optical phenomena, such as "crushed ice" and "bow ties"). The objective of the system is to produce fancy-cut designs that deliver high performance across the most commonly encountered lighting environments and that maintain superior performance face-up, when tilted, and from various viewing distances. To support manufacturers, GIA is developing Facetware "software as a service" (SaaS), enabling the submission of 3D models for preliminary cut grade assessments to assist diamond designers and manufacturers. This system will provide cut analysis (a provisional cut grade, including symmetry evaluation), plans to support decisions before polishing, and scans to support quality control metrics after polishing.

REFERENCES

Blodgett T., Gilbertson A., Geurts R., Goedert B. (2011) Length-to-width ratios among fancy shape diamonds. *G&G*, Vol. 47, No. 2, p. 129.

Reinitz I.M., Gilbertson A., Blodgett T., Hawkes A., Conant J., Prabhu A. (2024) Observations of oval-, pear-, and marquise-shaped diamonds: Implications for fancy cut grading. *G&G*, Vol. 60, No. 3, pp. 280–304, http://dx.doi.org/10.5741/GEMS.60.3.280

GIA "Excellent" Fancy Recutting Solutions

Janak Mistry (Lexus, Surat, India) looked forward to the introduction of GIA's fancy cut grading system, noting that the industry must prepare to manufacture fancy cut diamonds to "nicer makes" that receive better grades from the new GIA system and appeal to well-educated buyers. Leading laboratories have certified 8–10 million fancy-shaped diamonds over the last two decades. The majority were polished to retain mass rather than to optimize beauty and will likely require recutting to match clients' expectations. A similar challenge arose in 2005–2006 when AGS and GIA introduced cut grading for round brilliants, prompting some manufacturers to recut inventory.

Figure 10. Fancy-shaped diamonds such as these offer a multiplicity of design possibilities for consumers to explore. Photos by Robert Weldon.

Mistry's talk explored the implications of fancy cut grading through case studies on light performance and potential recut strategies. To demonstrate this process, Mistry selected a number of diamonds that performed poorly in the proposed new GIA system (beta version) and recut them to a GIA Excellent cut grade. The first example was a 0.51 ct oval with a very strong dark "bow tie" pattern. The best recutting plan option in the new system reduced the weight by 0.04 ct but removed the bow tie and improved the cut and symmetry grades to Excellent, resulting in a value addition of 22% and a far more marketable gem. The second example was a 0.96 ct emerald cut with Very Good cut, Fair symmetry, and Good polish. Its clarity was only I_1 due to a deep cavity on the gem's table. Recutting to the best solution reduced weight by almost 0.14 ct, but resulted in the removal of the cavity, which improved clarity from I_1 to SI_2, produced Excellent grades for cut, symmetry, and polish, and made the gem much brighter and pleasingly symmetrical. Mistry noted that the combination of these improvements was a value addition of 73%.

REFERENCES

Moses T.M., Johnson M.L., Green B., Blodgett T., Cino K., Geurts R.H., Gilbertson A.M., Hemphill T.S., King J.M., Kornylak L., Reinitz I.M., Shigley J.E. (2004) A foundation for grading the overall cut quality of round brilliant cut diamonds. *G&G*, Vol. 40, No. 3, pp. 202–228, http://dx.doi.org/10.5741/GEMS.40.3.202

Reinitz I.M., Gilbertson A., Blodgett T., Hawkes A., Conant J., Prabhu A. (2024) Observations of oval-, pear-, and marquise-shaped diamonds: Implications for fancy cut grading. *G&G*, Vol. 60, No. 3, pp. 280–304, http://dx.doi.org/10.5741/GEMS.60.3.280

GEM CHARACTERIZATION

Rare and Radiant: The Science and Beauty of Fancy-Color Diamonds

Dr. Sally Eaton-Magaña (GIA, Carlsbad) explored the rainbow of natural diamonds and their varied causes of color, highlighting some of the most rare and magnificent diamonds that GIA has evaluated. Every natural diamond has a unique story of its creation written into its atomic-scale defects and inclusions (figure 11). Most receive the ingredients for color within the earth as they form. Impurities of nitrogen, boron, nickel, and hydrogen produce yellow, yellowish green, violet, and blue colors, while abundant tiny inclusions create black or white colors. Once they reach the earth's surface, diamonds can be exposed to radioactive minerals that might color them green or blue. By contrast, the majority of natural pink diamonds colored by the 550 nm absorption band derive their color from the geologic forces of mountain-building events deep within the earth.

Natural yellow diamonds are the most common fancy colors, while pure orange diamonds are among the rarest. Both are colored by atomic-level structural defects associated with nitrogen impurities. Four groups of defects cause color in nearly all yellow and orange diamonds: cape defects (N3 and associated absorptions), isolated nitrogen defects, the 480 nm visible absorption band, and H3 defects. Some of the spectacular yellow to orange diamonds seen at GIA include the 30.54 ct Arctic Sun, the 128.54 ct Tiffany Yellow, and the 5.54 ct Fancy Vivid orange Pumpkin.

Natural blue diamonds are among the rarest and most valuable gems, and many come from very specific mines: South Africa's Cullinan and Australia's Argyle. While boron impurities are often associated with blue color, some blue and gray to violet colors also originate from simple structural defects produced by radiation exposure or from more complex defects involving hydrogen. Examples of remarkable blue diamonds include the 45.52 ct Hope, the 31.06 ct Wittelsbach-Graff, the 15.10 ct De Beers Blue, and the 20.46 ct Okavango Blue.

Dr. Eaton-Magaña then discussed the four major causes of color for green diamonds. Radiation exposure is the most common and can create vivid pure green colors. Some yellow-green diamonds owe their bodycolor to the combination of the H3 defect and green fluorescence, or to hydrogen- or nickel-related defects. Among the most famous green diamonds are the 41 ct Dresden Green, the 5.51 ct Ocean Dream, and the 5.03 ct Fancy Vivid green Aurora Green.

There are two primary causes of color for pink to red diamonds. The so-called "Golconda" pinks get their color from nitrogen vacancy centers, while the overwhelming majority of natural pink diamonds (about 99.5%) get theirs from an absorption band centered on 550 nm. This absorption band is created when the diamond experiences stresses at high pressure and temperature and plastically deforms,

Figure 11. Fancy-color diamonds, such as these examples from the Aurora Butterfly of Peace, owe their spectacular hues to many causes, including tiny amounts of impurities, atomic-level structural defects, or plastic deformation deep in the earth. Photos by Robert and Orasa Weldon.

typically due to mountain-building events. The 34.65 ct Fancy Intense pink Princie, the 11.15 ct Fancy Vivid pink Williamson Pink Star, the 5.11 ct Moussaieff Red, and the 2.33 ct Winston Red are examples of famous pink to red natural diamonds GIA has examined over recent years.

REFERENCES

Breeding C.M., Shigley J.E. (2009) The "type" classification system of diamonds and its importance in gemology. *G&G*, Vol. 45, No. 2, pp. 96–111, http://dx.doi.org/10.5741/GEMS.45.2.96

Breeding C.M., Eaton-Magaña S., Shigley J.E. (2020) Naturally colored yellow and orange gem diamonds: The nitrogen factor. *G&G*, Vol. 56, No. 2, pp. 194–219, http://dx.doi.org/10.5741/GEMS.56.2.194

Eaton-Magaña S., Breeding C.M., Shigley J.E. (2018) Natural-color blue, gray, and violet diamonds: Allure of the deep. *G&G*, Vol. 54, No. 2, pp. 112–131, http://dx.doi.org/10.5741/GEMS.54.2.112

Eaton-Magaña S., Ardon T., Smit K.V., Breeding C.M., Shigley J.E. (2018) Natural-color pink, purple, red, and brown diamonds: Band of many colors. *G&G*, Vol. 54, No. 4, pp. 352–377, http://dx.doi.org/10.5741/GEMS.54.4.352

Eaton-Magaña S., Ardon T., Breeding C.M., Shigley J.E. (2019) Natural-color fancy white and fancy black diamonds: Where color and clarity converge. *G&G*, Vol. 55, No. 3, pp. 320–337, http://dx.doi.org/10.5741/GEMS.55.3.320

The Impact of Fluorescence on the Appearance of Gemstones

Dr. Christopher M. Breeding (GIA, Carlsbad) explained that fluorescence in minerals has long been a subject of intrigue and fascination. For gemstones, it is sometimes considered a benefit and other times a flaw. Fluorescence can affect the appearance of some gemstones, and thus their values, even in normal lighting conditions. Dr. Breeding defined fluorescence as the emission of electromagnetic radiation from a substance stimulated by the absorption of incident electromagnetic radiation. The emission persists only as long as the stimulating radiation is continued. Phosphorescence is any emission that continues after the stimulating radiation is stopped. In gemology and mineralogy, fluorescence is commonly associated with excitation by an ultraviolet (UV) light source. Gemologists use a number of specific wavelengths of UV light, including long-wave at 365 nm, short-wave at 254 nm, and deep-UV (<230 nm, as used by the DiamondView device). Any wavelength of light, including visible light, can induce fluorescence.

Dr. Breeding noted that connoisseurs consider rubies from Myanmar's (formerly Burma's) Mogok region among the finest available. They owe their vibrant red hues to a combination of absorption and fluorescence, both caused by chromium atoms in their structure (figure 12). The trade values strongly fluorescent "Pigeon's Blood" Burmese rubies, and the most exceptional stones have sold for more than US$1 million per carat. Rubies with high iron levels have weak fluorescence, and the trade tends to value them less highly. Research at GIA using filters that only allow chromium fluorescence to pass through shows that the impact of fluorescence on ruby's red color may be overstated.

Figure 12. The larger of these two rubies from Namya, Myanmar, weighing 7.5 ct (left) and 4.5 ct (right), is pictured under long-wave fluorescent light. These high-quality gems from Kachin State are often mistaken for Mogok rubies due to their similar quality. Photo by Wim Vertriest.

Conversely, the trade applies discounts of 10 to 30% to colorless or near-colorless diamonds with strong or very strong fluorescence. Dr. Breeding noted a common trade perception that D–G color diamonds with strong fluorescence sometimes exhibit a noticeable luminescence, which can give a diamond a "hazy" appearance. As a result, many near-colorless diamonds sell at a discount simply because they have strong blue fluorescence. Observations at GIA among high clarity, D–G color, highly fluorescent diamonds demonstrate that facet junctions remain clear and crisp under UV lighting. On the other hand, the hazy or cloudy appearance in fluorescent diamonds intensifies under UV. Strong blue fluorescence does not cause a diamond to appear hazy on its own, but it may increase the haziness of a stone with light scattering structural defects or inclusions. Experiments using a technique called modulation transfer function (MTF), which measures an optical system's ability to transfer contrast from an object to an image, allow us to evaluate and quantify haziness in diamond. GIA will add comments to grading reports for many fluorescent diamonds beginning in late 2025.

To conclude, Dr. Breeding explained that pearls can be treated with blue-fluorescing optical brighteners to enhance their appearance, and that perceptions about gemstone fluorescence and appearance, even deeply rooted ideas, are not always reality.

REFERENCES

D'Haenens-Johansson U.F.S., Eaton-Magaña S., Towbin W.H., Myagkaya E. (2024) Glowing gems: Fluorescence and phosphorescence of diamonds, colored stones, and pearls. *G&G*, Vol. 60, No. 4, pp. 560–580, http://dx.doi.org/10.5741/GEMS.60.4.560

Zhou C., Tsai T.-H., Sturman N., Nilpetploy N., Manustrong A., Lawanwong K. (2020) Optical whitening and brightening of pearls: A fluorescence spectroscopy study. *G&G*, Vol. 56, No. 2, pp. 258–265, http://dx.doi.org/10.5741/GEMS.56.2.258

Phenomenal Gemstones: A Brief Overview of the Nanostructures Behind the Optical Spectacles

Dr. Shiyun Jin (GIA, Carlsbad) focused on gem materials that display special optical phenomena including asterism, chatoyancy, aventurescence, iridescence, and color change. Gems with these distinctive properties have attracted the attention of gem lovers and scientists for centuries. Yet scientists have only characterized most of the nanostructures underlying these optical effects in the last few decades, thanks to the development of electron microscopy. Dr. Jin referred to the Summer 2025 *Gems & Gemology* paper, a comprehensive 60-page article documenting more than two dozen types of phenomenal gems with nearly 300 references for those seeking to know more. Dr. Jin noted that the paper provides necessary clarifications because many terms used in the trade to describe phenomenal gems are often poorly defined and subjective. However, the roots of this confusion are understandable: a gemstone might display multiple phenomena; gemologists often use many terms to describe the same phenomena; the same phenomenon might also look dissimilar in different stones; and different phenomena, with disparate underlying causes, may appear similar.

Dr. Jin briefly touched on well-understood phenomena including opalescence (the milky or hazy appearance due to diffuse scattering of light by nanoparticles), asterism and chatoyancy (the star and cat's-eye effects caused by oriented light-scattering needles), and aventurescence (the specular reflections from isolated, typically flat or "platy" inclusions within a transparent gem). A longer segment of the talk covered phenomena due to thin-film interference of reflected light from repeated arrays of transparent thin platy minerals, where the color depends on the thickness of the layers. This includes the blue flashes of labradorescence, the rainbow of orient or overtone shown by nacreous pearls, the iridescence of shell, and play-of-color in opals (figure 13). Iridescence is not exclusive to gems; the flashing colors seen in a pigeon's feathers, a butterfly's wing, or on the surface of a soap bubble are due to the same cause.

Next, Dr. Jin focused on inconsistencies in terms mineralogists, gemologists, and the gem trade use to describe feldspars with iridescence. Mineralogists generally separate iridescent feldspars into three categories based on their bulk chemical composition: labradorite, peristerite, and moonstone. Moonstone, for example, is named after its white or silver iridescent glow that resembles moonlight. Unfortunately, the trade applies the term *moonstone* haphazardly to any light-colored feldspar, such as transparent labradorite displaying a desaturated multicolor iridescence, which is often sold as "rainbow moonstone." This adds confusion to an already complicated subject. Dr. Jin encouraged the use of more general terms such as *iridescence* and *play-of-color* over specific terms such as *labradorescence*. He stressed that phenomena should be defined based on the underlying texture and physics processes instead of vague descriptions of appearance.

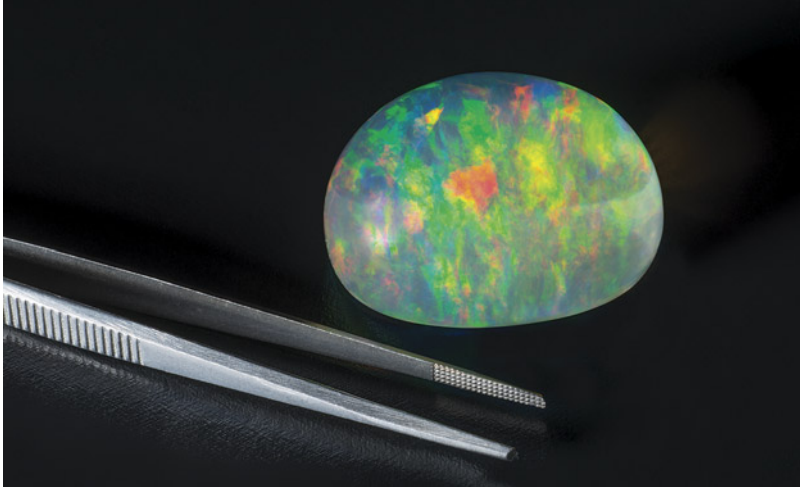

Figure 13. This 264.44 ct Ethiopian opal displays a spectacular play-of-color phenomenon. Photo by Robert Weldon; courtesy of Tewodros Sintayehu, Orbit Gems, and Bill Marcue, DW Enterprises.

REFERENCE

Jin S., Renfro N.D., Palke A.C., Shigley J.E. (2025) Structures behind the spectacle: A review of optical effects in phenomenal gemstones and their underlying nanotextures. *G&G*, Vol. 61, No. 2, pp. 110–170, http://dx.doi.org/10.5741/GEMS.61.2.110

GENERAL GEMOLOGY

The Science That Makes Gems Shine: Understanding Metrology at GIA

Dr. Yun Luo (GIA, Carlsbad) began by differentiating *metrology*, the science of measurement and its application, from *meteorology*, the study of the weather, and explaining its relevance to GIA. Dr. Luo explored how metrology underpins GIA's research and laboratory services through rigorous validation, verification, and intra- and inter-laboratory testing of various measurement instruments. Precision and accuracy are at the heart of every gemstone measurement and evaluation GIA undertakes. Metrology ensures consistency and reliability across GIA's global laboratories. Dr. Luo explained how the three pillars of traceability (every result must link back to a recognized reference), reference standards (the agreed reference everyone measures against), and accuracy (how close a measurement is to the true value) ensure that the measurements of a diamond taken at one GIA laboratory match those of the same diamond if submitted to another GIA location. Dr. Luo defined accuracy as the closeness to a desired target value and precision as the consistency and repeatability of the results achieved. Both are essential for reliable measurements. Uncertainty is the level of confidence we have in the result, and calibration is the process of correcting systematic error. Together, precision, uncertainty, and calibration transform a number on a screen into a scientifically sound and meaningful measurement. Dr. Luo reminded the audience that measurement without an estimate of uncertainty is meaningless.

Every instrument has a range of reproducibility or tolerance. Reproducibility measurements allow metrologists

to track the performance of each device and assess whether any of them need extra attention. Testing a gemstone at GIA includes measurement of carat weight, dimensions, color, clarity, fluorescence, spectrometry, imaging, and chemical analysis. These measurements have to be accurate, precise, and consistent across all of GIA's labs. What makes GIA stand out is that metrologists verify instruments daily before evaluating client stones, regularly submit unannounced blind control stones to check accuracy, have well-defined standards and inter-lab tests for global consistency, and capture hourly data during business hours at all GIA laboratories to ensure quality.

REFERENCE

Nelson D.P., Reinitz I.M. (2024) Metrology at GIA. *G&G*, Vol. 60, No. 4, pp. 596–603, http://dx.doi.org/10.5741/GEMS.60.4.596

The Vault and Beyond: The Exciting Lives of Museum Specimens

Dr. Rachelle Turnier (GIA, Carlsbad) offered a behind-the-scenes look at the GIA Museum to highlight the essential roles its exhibits and specimens play in GIA's mission. When Robert M. Shipley founded GIA in 1931, he needed specimens for teaching. In those early days, there was no distinct "museum," but rather simply an "education collection." Over the years, the collection grew as diamonds and gemstones were loaned or purchased. Eventually some of the loans became gifts. In 1976, Dr. Vincent Manson, GIA's "director of dreams," had a vision for separate museum and education collections. A former curator at New York's American Museum of Natural History, he recognized the value of GIA's pieces and their many potential uses and separated them into two collections.

However, it was not until 2000 that GIA created a formal museum department. The catalyst was undoubtedly the 1997 opening of the Carlsbad campus. GIA is a living museum, with more than 100 exhibits spread throughout the Carlsbad campus to serve the students, public, and employees. Of the 50,000 specimens in the collection, 75% are donations from alumni, industry leaders, and retiring enthusiasts who donate their treasures knowing they will be used and appreciated (figure 14). The Sir Ernest Oppenheimer Student collection is perhaps the most foundational donation. Loaned in 1933, then later donated in 1955, it consists of more than 1,500 carats of diamonds, worth $20,000 at the time. Its spectacular diamond crystals, both loose and in matrix, would be valued at several million dollars if donated today. Through donations and purchases, GIA acquired additional important collections including the Dr. Kurt Nassau Synthetic collection, the Dr. Frederick H. Pough Synthetic collection, a collection of Pierre Touraine's Southwest-inspired jewelry, and in 2005, the Dr. Edward J. Gübelin collection. Recent donations include pre-Columbian jewelry, a collection of 850 polished gem and mineral eggs, the models and findings of

Figure 14. This past GIA Museum birthstone exhibit at the San Diego International Airport represents one way GIA promotes its mission to engage, inspire, and educate the public about gemology. Photo by Kevin Schumacher.

Peter Lindeman, who worked for important jewelry brands including Tiffany & Co., and a significant donation of high-end jewelry ranging from an Egyptian necklace fabricated around 1500 BCE to Victorian high-end jewelry from brands such as Cartier, Tiffany & Co., and Fabergé.

While GIA's Museum collection serves to educate students and inspire visitors on public tours, it is also a crucial resource for GIA's scientists. GIA researchers draw on the collection for experiments and research purposes, including using gemstones of known localities to develop new geographic origin services, studying gems for causes of color, and even for developing laboratory standards.

REFERENCES

GIA Museum: https://www.gia.edu/gia-museum
Atlantis: https://www.gia.edu/gia-museum-exhibit-atlantis
Hauser Mineral Collection: https://www.gia.edu/gia-museum-exhibit-hauser-mineral-collection
Pierre Touraine Jewelry: https://www.gia.edu/gia-museum-exhibit-pierre-touraine-jewelry
Riches in the Rocks: https://www.gia.edu/gia-museum-exhibit-riches-in-the-rocks
Tiger's-Eye Quartz: https://www.gia.edu/gia-museum-exhibit-tigers-eye-quartz

Exploring the Behind-the-Scenes of the Smithsonian National Gem Collection

Dr. Gabriela Farfan (Smithsonian National Museum of Natural History, Washington, DC) shared how research, "behind-the-scenes" teams, and iconic exhibits work together to spark curiosity about the natural world, highlighting the new Winston Fancy Color Diamond collection—including

the 2.33 ct Winston Red—which was unveiled in 2025. The Smithsonian National Museum of Natural History is part of the U.S. national collection of museums, has no admission charge, and sees more than 6 million visitors per year. Its gems and minerals are a gateway to science for many visitors. In Dr. Farfan's reckoning, a gem is a mineral that has been transformed by an artist, and the Institution's many such gem icons include the 45.52 ct Hope diamond, the 48.68 ct "Whitney Flame" topaz, the 10,363 ct Dom Pedro aquamarine, the 75.47 ct Hooker emerald, and the Marie Antoinette diamond earrings. Dr. Farfan noted that the National Gem and Mineral Collection contains approximately 385,000 specimens, of which more than 10,000 are gemstones. The Institution's role is to preserve mineral and gem specimens for generations to come.

Although all the Smithsonian's specimens come via donations, other museums may request loans for exhibits, and scientists can request samples for study. Recent acquisitions include the 55.08 ct Kimberley diamond (2019); the 116.76 ct "Lion of Merelani" tsavorite garnet (2023); a 30.50 ct spessartine garnet, a 12.85 ct bicolor zoisite, a spectacular morganite carving of cockatoos (2024); and a 13.34 ct Paraíba tourmaline and a 73.55 ct lavender spinel (2025). Dr. Farfan explained how the collection is expanded by filling its "holes." This includes adding new mineral species, covering representation of specific localities, responding to popular research topics, including unique gemstones, and making significant "upgrades" for exhibitions. The Winston Fancy Color Diamond collection donated in 2025 is one such example. It encompasses 118 diamonds in all colors of the rainbow. Forty of these diamonds, ranging from 0.4 to 9.5 ct, are now on exhibit. Of these, the Winston Red, a 2.33 ct old mine brilliant cut diamond with an unmodified Fancy Red hue, is the most well-known.

A group of researchers from the Smithsonian, GIA, and the École des Mines de Paris (Paris School of Mines) undertook a 2025 study of the Winston Red to answer specifics about the gem, namely the cause of its unique pure red hue, and its history, geographic origin, and rarity. Dr. Farfan outlined the results of the team's research. Analyses confirmed the presence of plastic deformation bands, and dislocation network patterns classified the Winston Red as a type IaAB (A) Group 1 "pink" diamond. To achieve its red color and dense dislocation networks, the Winston Red diamond likely experienced immense strain in Earth's mantle. Although the team traced the Winston Red back to 1938, its old mine brilliant cut suggests a richer story. Based on its mineralogical characteristics and history, Dr. Farfan concluded that the likely geographic origin of the stone is Venezuela or Brazil and called out the recent Spring 2025 *Gems & Gemology* article on the gem.

REFERENCES

Chapin M., Pay D., Shigley J., Padua P. (2013) The Smithsonian gem and mineral collection. *GIA Research News*, November 14, https://www.gia.edu/gia-news-research-smithsonian-gem-mineral-collection

Crowningshield R. (1989) Grading the Hope diamond. *G&G*, Vol. 25, No. 2, pp. 91–94.

Farfan G.A., D'Haenens-Johansson U.F.S., Persaud S., Gaillou E., Feather R.C. II, Towbin W.H., Jones D.C. (2025) A study of the Winston Red: The Smithsonian's new fancy red diamond. *G&G*, Vol. 61, No. 1, pp. 16–42, http://dx.doi.org/10.5741/GEMS.61.1.16

Gaillou E., Post J.E. (2007) An examination of the Napoleon diamond necklace. *G&G*, Vol. 43, No. 4, pp. 352–357.

King J.M., Shigley J.E. (2003) An important exhibition of seven rare gem diamonds. *G&G*, Vol. 39, No. 2., pp. 136–143.

NEW TECHNOLOGIES AND TECHNIQUES

Revealing the Hidden World of Diamond in 3D

Dr. Daniel Jones (GIA, New Jersey) explained that all diamonds possess an interior "hidden world" that reveals their growth history, information about their chemical composition, and evidence of post-growth events. In this talk, Dr. Jones explored the unseen world of diamond, showing the structures of growth using photoluminescence with a newly developed GIA 3D imaging system. This system allows for high-resolution 3D mapping of the internal structure of diamonds using defect photoluminescence and high-powered lasers. It also identifies defects using spectroscopy.

Natural diamonds grow deep in the earth over a period of millions to billions of years and are subject to changing environments, which cause subtle, sometimes imperceptible changes to their atomic structure. Dr. Jones asked the audience to liken diamond growth to tree rings, showing layers radiating outward with the oldest part in the center. A diamond's growth history can be viewed using complex imaging techniques. Dr. Jones remarked how visual observations can be useful in analyzing diamond, and that spectroscopy, a method for determining the existence of atomic-scale color centers, can be applied across the bulk or at specific points of a diamond. Some of these color centers create visible color through absorption, and others emit light through fluorescence when excited via a laser light source. Using a combination of visual observation, spectroscopy, and 3D scanning, gemologists can visualize the structures of natural diamonds in their full crystallographic majesty.

Unlike a human eye or a conventional camera, which "sees" only three broad bands of light (red, green, and blue), hyperspectral data as captured by an imaging spectrometer contains hundreds of narrow, continuous spectral bands across a wide part of the electromagnetic spectrum beyond the visible range into the infrared and ultraviolet. This creates a hyperspectral "data cube" where two dimensions are spatial (X + Y), and the third (Z) is spectral, which allows for characterization of the diamond based on its unique "spectral fingerprint." Critically, this process is nondestructive, making analysis much more viable. Dr. Jones

explained that the downside is the amount of data generated and the processing power required to render it into a three-dimensional model. Dr. Jones showed several examples of the technique including video renderings revealing defects and structure in both rough and faceted natural diamonds, allowing the rotation of the image around its axes to show three-dimensional structure. This allows the observer unprecedented resolution and access to the gems' internal growth patterns. Dr. Jones demonstrated the technique with examples of high-pressure, high-temperature (HPHT) and chemical vapor deposition (CVD) laboratory-grown diamonds, which also revealed their distinctive structures and defect patterns.

REFERENCES

Eaton-Magaña S., Breeding C.M. (2016) An introduction to photoluminescence spectroscopy for diamond and its application in gemology. *G&G*, Vol. 52, No. 1, pp. 2–17, http://dx.doi.org/10.5741/GEMS.52.1.2

Eaton-Magaña S., Jones D.C., Turnier R.B., Breeding C.M. (2024) Shining a light on gemstone properties: An exploration of photoluminescence spectroscopy. *G&G*, Vol. 60, No. 4, pp. 494–517, http://dx.doi.org/10.5741/GEMS.60.4.494

Art and Algorithm: Advances in Generative AI and Jewelry Design

Michael Magee (GIA, Carlsbad) explored recent advances in both generative artificial intelligence (AI) technology and regulations, demonstrating how jewelry designers and retailers can leverage these powerful tools responsibly for innovation. While initially controversial, many ethical and regulatory challenges surrounding AI tools have begun to find resolution. Magee explained how generative AI learns patterns from large datasets, identifies underlying structures and elements, and generates something new and unique based on this input (figure 15). The talk covered general models such as ChatGPT (Open AI), Gemini (Google), and Copilot (Microsoft); image generators including Midjourney, Leonardo, and Firefly (Adobe); and provided examples with jewelry-specific applications such as Dzine, Bez, GemArt AI, and Blng.

Magee discussed a recent U.S. Copyright Office report that identified key copyrightability issues related to AI-generated outputs. The existing legal framework governing copyright protection in the U.S. requires human authorship, as established by the Copyright Clause in the Constitution. No court has recognized copyright for works created solely by non-humans. In fact, the U.S. District Court ruled that while human contributions must be assessed on a case-by-case basis to determine authorship, works generated without human involvement do not meet the authorship requirement. The report emphasizes that prompts alone do not provide sufficient control for copyright eligibility. Human authors are entitled to copyright for their contributions, including selection, coordination, and arrangement of AI-generated material.

Figure 15. AI tools that can generate photorealistic images from text prompts are becoming more widely used to rapidly iterate jewelry designs. While designers can benefit from these tools' capabilities, they must be aware of their flaws. This image output includes irregularly shaped gems and "floating" bezels.

Magee explained that the distinction lies in whether AI is used to enhance human expression or if it makes expressive choices independently, and that there is a divergence of opinion on the extent of human contribution required for copyright protection.

Next, Magee illustrated some of the current capabilities of AI applications, showing a range of designs along with the written and visual prompts—including the speaker's own hand-drawn sketches—that produced them. The products included photorealistic images and a near-cinematic 5-second video that could be used in a luxury jewelry commercial. Current challenges in using generative AI for jewelry design include creating desirable and original designs, understanding manufacturability to create usable 3D models, and energy consumption. Per a recent *MIT Technology Review* article, the electricity needed to generate 15 chat questions, render an image using 10 attempts, or produce three 5-second videos amounts to approximately 2.9 kWh, equivalent to the electricity necessary to power an e-bike for 100 miles, run a microwave for 3.5 hours, or drive a small electric car for 12 miles.

Magee emphasized that designers must work harder to create desirable and original designs rather than simply using prompts together with data "scraped" from other images and sources, and went on to suggest creating custom training for an AI application using up to 20 images

with a consistent style, photos, or better yet, the designer's original digital renderings. He explained that using the designer's own hand or digital sketching is best because this incorporates human creativity and expression into designs. To make designs manufacturable, Magee suggested vetting the AI renderings for both outlandish and subtle errors. To ensure good quality control, the AI must be trained with accurate 3D models in order to calculate dimensions or estimate material weights accurately. Currently, AI-generated 3D models show poor surface quality, uneven dimensions, and improper segregation of parts.

Magee concluded by observing that good design still relies on knowledgeable individuals to catch both wildly impossible and subtly wrong AI-rendered images, provide CAD models or other manufacturing data for 3D, create accurate weight and cost estimates, and decide which tools are right for the job and the designer's brand. Future directions will include better 3D model generation, plugins for Rhino and other jewelry-specific CAD programs, cost estimates, bill-of-materials (BOM) lists from images, and further integration into the customer experience.

REFERENCES

Magee M.D. (2024) Generative artificial intelligence as a tool for jewelry design. *G&G*, Vol. 60, No. 3, pp. 330–347, http://dx.doi.org/10.5741/GEMS.60.3.330

O'Donnell J., Crownhart C. (2025) We did the math on AI's energy footprint. Here's the story you haven't heard. *MIT Technology Review*, May 20, https://www.technologyreview.com/2025/05/20/1116327/ai-energy-usage-climate-footprint-big-tech/

United States Copyright Office (2024–2025) Copyright and Artificial Intelligence. Part 1: Digital Replicas (July 2024) https://www.copyright.gov/ai/Copyright-and-Artificial-Intelligence-Part-1-Digital-Replicas-Report.pdf

———Part 2: Copyrightability (January 2025) https://www.copyright.gov/ai/Copyright-and-Artificial-Intelligence-Part-2-Copyrightability-Report.pdf

———Part 3: Generative AI Training (May 2025) https://www.copyright.gov/ai/Copyright-and-Artificial-Intelligence-Part-3-Generative-AI-Training-Report-Pre-Publication-Version.pdf

Innovative Spectroscopic Instrumentation for Gemstone Screening and Identification

Dr. Tsung-Han Tsai (GIA, New Jersey) described how GIA is developing new gem testing instrumentation. The talk focused on fluorescence spectroscopy for diamond screening, pearl testing, and colored stone identification, as well as image-assisted Raman and photoluminescence equipment for diamond jewelry identification and multi-excitation photoluminescence spectroscopy for gemstone analysis. Conventional luminescence observation uses filtered long-wave (365 nm) and short-wave (254 nm) ultraviolet light. The mercury lamps used have limitations: Their emission spectra typically include a mixture of all mercury lines, which can interfere with luminescence observations, and the filters they use degrade over time. Nonetheless, they provide powerful UV excitation (~200 μW) at an affordable cost. Making luminescence measurements with spectroscopy leads to more objective conclusions than visual observations and allows for automation and more rapid screening. Gemstone screening maintains transparency in the gem market by helping prevent undisclosed mixing of laboratory-grown and treated color diamonds and simulants, which would threaten the price of natural gems, undermine consumer confidence, and cause legal and regulatory issues. Any screening technology must meet certain identification challenges, manage high volumes of gems, be compact enough to be practical, and be cost-effective.

Approximately 97% of natural diamonds show blue fluorescence caused by the N3 color center (a crystallographic defect in diamond consisting of a vacancy surrounded by three nitrogen atoms). Other less common fluorescence colors include yellow, green, white, orange, and red. While the N3 defect appears in the vast majority of natural diamonds, its absence in laboratory-grown diamonds (LGDs) and diamond simulants allows a 100% referral rate of these materials with fluorescence screening. Similarly, most natural-color pink diamonds only show the N3 defect, while the NV^0 center (a defect consisting of a nitrogen atom that has replaced a carbon atom and an adjacent missing carbon atom) is characteristic of multi-treated and laboratory-grown diamonds but rare in untreated pink ones (about 0.6% of rare, so-called "Golconda" diamonds). This allows fluorescence screening a positive identification rate of 99.8% for natural-color pink diamonds and a 100% referral rate for pink LGD and multi-treated pink diamonds. GIA's iD100 is an example of a newer compact fluorescence screening device. It offers automatic diamond identification for colorless to near-colorless, blue to green, brown, and pink to red diamonds, displays results in approximately 2 seconds, and is suitable for loose and mounted samples (>0.9 mm) in any cut. Fluorescence screening also shows some promise for mineral identification and detection of color treatments in pearls.

REFERENCES

D'Haenens-Johansson U.F.S., Eaton-Magaña S., Towbin W.H., Myagkaya E. (2024) Glowing gems: Fluorescence and phosphorescence of diamonds, colored stones, and pearls. *G&G*, Vol. 60, No. 4, pp. 560–580, http://dx.doi.org/10.5741/GEMS.60.4.560

Eaton-Magaña S., Ardon T., Smit K.V., Breeding C.M., Shigley J.E. (2018) Natural-color pink, purple, red, and brown diamonds: Band of many colors. *G&G*, Vol. 54, No. 4, pp. 352–377, http://dx.doi.org/10.5741/GEMS.54.4.352

Moses T., Reinitz I.M., Johnson M.L., King J.M., Shigley J.E. (1997) A contribution to understanding the effect of blue fluorescence on the appearance of diamonds. *G&G*, Vol. 33, No. 4, pp. 244–259.


CONVERGE
Presenting Sponsor
Jewelers Mutual


GIA Research
The goal of the research program goal is to improve the identification of natural, synthetic and treated gem materials in support of the GIA Laboratory:
• Scientists, technicians and gemologists
• An array of gem-testing and scientific instrumentation
• Standard data-collection procedures at multiple locations
• A searchable information database on all types of gems

CONVERGE™

AGS CONCLAVE X GIA SYMPOSIUM

◆ SEPTEMBER 7 - 10, 2025 ◆
CARLSBAD, CA

Photos by Emily Lane, Mimi Travis, and Russel Samson.

POSTER PRESENTATIONS

More than 30 posters covering broad topics related to the industry were presented at Converge 2025. Presenters were on hand to interact with Converge attendees to share their gemological knowledge (figure 1). In the poster presentations outlined below, only the principal, or first-listed author, appears. All entries were written by GIA staff. To view photos of the posters, visit https://www.gia.edu/gems-gemology/winter-2025-gemnews-converge-posters

COLORED STONES AND PEARLS

Gemological Characterization of Emeralds from North Carolina, USA

Nicole Ahline | GIA, Carlsbad

North Carolina's emerald deposits are among the few recognized in North America, best known because they are historically significant and gemologically distinct due to their chemistry and color zoning. This poster provides the context of the geological environment the emeralds formed in, an overview of their standard gemological properties, inclusion photomicrographs, and chemistry.

Emerald Report Features at GIA Laboratories

Alex Goodsuhm | GIA, Carlsbad

Since December 2024, GIA has offered optional filler identification on its emerald origin reports. This poster details the new service, which is available in addition to the standard report information and includes identification of the stone and the degree of filler. Currently offered at no cost, the service provides the filler information in the following format: Type A (oils and other naturally occurring materials such as Canada balsam, cedarwood oil, and paraffin) and Type B (artificial resins such as Opticon, Permasafe, and Araldite).

Explorations in Brazil: GIA's 102nd Field Expedition

Dr. Aaron Palke | GIA, Carlsbad

This poster focuses on a recent GIA field gemology expedition to Brazil, which remains a colored stone mining powerhouse. The objective was to bolster GIA's colored stone reference collection with representative samples of white opal from Piauí State and emerald from Campos Verdes, Goiás State, and to revisit the legendary copper-bearing tourmaline deposits in Paraíba. The opal samples, which resemble Australian opal, will help support an upcoming new GIA opal report, and the emerald samples are of interest because their chemistry and inclusion suites can resemble gems from other locations including Pakistan, Afghanistan, and Colombia.

Field Gemology and GIA's Colored Stone Reference Collection

Wim Vertriest | GIA, Bangkok

This poster summarizes GIA's field gemology expeditions and the nature of the Institute's colored stone reference collection. A map shows the locations of mining areas visited to date and the types of gem materials collected. Short summaries provide the reference collection's focus along with an explanation of the six sample categories (A–F), based on proximity to the mine when collected by the field gemologist.

Figure 1. On hand to interact with Converge poster session attendees, GIA's Nathan Renfro, Nicole Ahline, John Koivula, and librarian emerita, Dona Dirlam represent a wealth of gemological and geoliterary experience. Photo by Emily Lane.

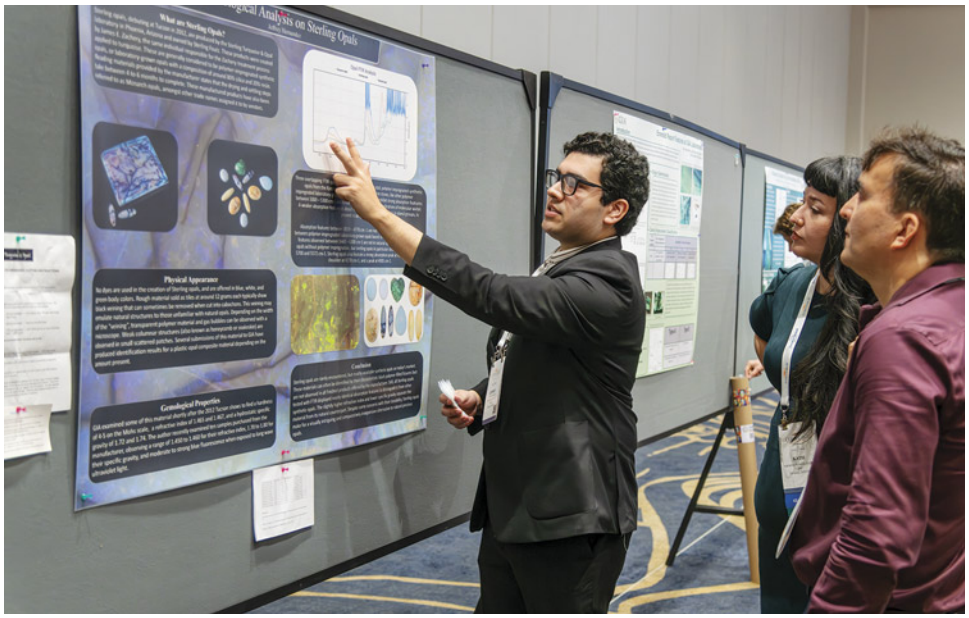

Figure 2. Jeffrey Hernandez interprets the distinctive absorption peaks of Sterling synthetic opal to show how these features allow gemologists to identify this material. Photo by Emily Lane.

Glass Ceramics as Imitation Gems

Dr. Wasura Soonthorntantikul | GIA, Bangkok

Glass ceramics are materials consisting of crystalline phases dispersed in an amorphous glass matrix, which combine properties of glass and ceramics. While mainly produced for industrial purposes, these materials are very suitable for use as imitation gems. They are tougher and more wear-resistant than regular glass and are inexpensive to produce in any color or transparency. This poster outlines how glass ceramics are made, their gemological properties, and possible identification challenges.

Advances in Jadeite Origin Determination at GIA

Alex Goodsuhm | GIA, Carlsbad

Due to the increase in supply of high-quality Guatemalan jadeite/omphacite jade (known as *fei cui* in the trade) reaching gem markets, GIA recently conducted a study of untreated Guatemalan and Burmese (Myanmar) material. Trace element chemistry analysis using laser ablation–inductively coupled plasma–mass spectrometry followed by application of machine learning revealed differences that, when coupled with observations, allow separation and permit origin determination of both sources.

Gemological Analysis on Sterling Opals

Jeffrey Hernandez | GIA, Carlsbad

The author presented a gemological characterization of Sterling synthetic opals along with context about their origin, physical appearance, production process, and place in the market (figure 2). This distinctive material, essentially polymer-impregnated laboratory-grown opal, is readily identified by characteristic black polymer-filled fissures and its distinctive Fourier-transform infrared absorption peaks.

Gemological Characteristics of Natural Pearls from Windowpane Oysters (Placunidae Family) from Indonesia

Karan Rajguru | GIA, Mumbai

This poster provides an overview of the gemological characteristics of natural pearls from windowpane oysters, which are widely distributed along the coasts of India, Indonesia, the Philippines, and China. Observations include surface structures and real-time X-ray microradiography and X-ray computed microtomography of the pearls' interiors. Spectroscopic and trace element analyses are also presented, confirming these pearls are composed of calcite rather than aragonite.

Organic-Rich Cores in South Sea Non-Bead Cultured ("Keshi") Pearls

Nishka Vaz | GIA, Mumbai

The authors present a study of 43 South Sea "keshi" non-bead cultured (NBC) pearls from the *Pinctada maxima* mollusk using real-time X-ray microradiography, X-ray computed microtomography, and Raman spectroscopy. Examination revealed a variety of internal structures including cores with light gray nuclei, seedlike features, off-round nuclei, and multiple cores and nuclei, which are key indicators of NBC pearls from this mollusk. Raman spectroscopy confirmed that the cores primarily combine conchiolin and aragonite nacre.

Hydrogen-Related Peaks in the Infrared Spectra of Corundum: What Are They, and What Can They Tell Us?

Dr. Michael Jollands | GIA, New York

In corundum, most infrared absorption bands relate to hydrogen in defects associated with a small number of other trace elements: beryllium, magnesium, nickel, iron, cobalt, titanium, tin, vanadium, and silicon. The exact positions of these bands correlate to the atomic structures of these defects. The author outlines how specific bands can correspond to different localities, heat treatment conditions, or laboratory-grown material. The nature of these bands can be determined by combining atomic modeling with analysis of trace element concentrations.

Nanoparticles in Natural Beryllium-Bearing Sapphires

Dr. Shiyun Jin | GIA, Carlsbad

Trace element analysis of gem corundum is important because it helps us understand which chromophores color them and often informs country of origin determination. Although beryllium is most often associated with diffusion treatment, it does occur naturally in corundum, where it is always associated with heavy high field strength elements (HHFSEs) such as niobium, tantalum, and tungsten. These elements are found in primary nano-inclusions that precipitate out of the corundum as irregular-shaped clouds or milky bands as it cools. This poster presents an analysis of the distribution and nature of these particles.

Diversity in Kashmir Sapphires

Sudarat Saeseaw | GIA, Bangkok

Kashmir's blue sapphire mines owe their legendary status to a relatively short window of production in the 1880s and 1890s. What little production has emerged since then has been of much lower quality than that of this early period. The trade identifies old production as "Classic" and more recent material as "New Kashmir." GIA recently had the opportunity to study a suite of 400 sapphires sourced from old collections and more recent finds near the mines. As both types contain very similar inclusion patterns, they are likely from the same deposit. This poster presents a representative set of photomicrographs from this research.

Chromophore Simulation of Copper-Bearing Tourmaline

Dr. Yusuke Katsurada | GIA, Tokyo

Paraíba tourmaline owes its blue to green color to the presence of trace amounts of copper and manganese. Although the influence of copper, which creates an absorption between 600 and 1000 nm, is relatively well understood, the role of manganese has not yet been studied in detail. Following experimental analysis of the other chromophores that contribute to color in elbaite tourmaline, the authors propose a model to predict their influence in addition to copper. The addition of iron creates a darker blue, manganese (Mn^{3+}) a violet to purple, and manganese plus titanium (Mn-Ti) a greenish blue to green color.

Figure 3. Dona Dirlam's poster presentation on the wealth of gem and ornamental materials associated with the Taj Mahal. Photo by Emily Lane.

The Evolution of Persian Turquoise Classification from Past to Present

Dr. Niloofar Mousaviapak | Claude Bernard University, Lyon, France

This poster examines the evolution of Iranian turquoise classification. Originally, naming and valuation were linked to the name of the mine producing the turquoise, but during the Qajar Period (1794–1925), factors such as the texture, presence of matrix, and depth of color were introduced, making the description of quality and appearance more consistent. This poster is centered on a chart that shows how ancient, Qajar, and modern terminology correlate.

DIAMONDS

Correlations Between Spectroscopic Characteristics and Growth Parameters of Nitrogen-Doped CVD Diamond

Dr. Matthew Dale | De Beers, Maidenhead, United Kingdom

This poster summarizes a photoluminescence (PL) spectroscopy and luminescence imaging study of specially grown chemical vapor deposition (CVD) diamonds, exploring correlations between the intensities of different PL features and the nitrogen concentrations and growth rates of the samples.

The Current Gemological Landscape of Laboratory-Grown Diamonds

Dr. Sally Eaton-Magaña | GIA, Carlsbad

This work surveys the current production of laboratory-grown diamonds (LGDs), showing how color, clarity, cut grades, and color distribution have changed over time (2015–2025) using both high-pressure, high-temperature (HPHT) and chemical vapor deposition (CVD) methods. The poster outlines the advanced testing methods used by GIA to conclusively identify LGDs, the services provided by the GIA laboratory, and the growth of CVD diamonds at GIA.

Fluorescence Lifetime Analysis and Mapping of a Hydrogen-Rich Diamond

Dr. Paul Johnson | GIA, New York

This poster presents details of a custom-built instrument designed to measure the lifetime of diamond color centers over picosecond to millisecond timescales, along with analysis of a hydrogen-rich, type Ia diamond sample specially prepared for this study. The sample, a natural diamond crystal from Zimbabwe fashioned into a 0.92 ct cube and subsequently heated and irradiated, contains a stellate-shaped cloud inclusion.

Reflecting on Fancy-Cut Diamond Patterning

Dr. James Conant | GIA, Las Vegas

The author provides a visual guide to various aspects of fancy-cut diamond patterns, beginning with generating symmetrical diamond designs and determining the degree of symmetry to create a three-dimensional model. This allows for the modeling of light and demonstrates the visual appearance of virtual facets and the evaluation of any patterning, such as "bow ties" or "crushed ice," that a particular design might display.

Spatial Distribution of Defects in Natural C-Center–Bearing Diamonds

Taryn Linzmeyer | GIA, Carlsbad

A C-center is a crystallographic defect in which a single isolated nitrogen atom substitutes for a carbon atom within a diamond's crystal structure. Diamonds with this defect are called type Ib and are rare in nature because residence in Earth's mantle tends to cause the defects to aggregate into pairs (A-centers) or clusters of four nitrogen atoms surrounding a vacancy (B-centers). C-centers might cause vibrant yellow to orange colors, making these diamonds valuable to the gem trade. In this study, the authors use photoluminescence and Fourier-transform infrared spectroscopy to characterize these rare natural diamonds.

GENERAL GEMOLOGY

10,000 Years of Collecting Malachite

Dona Dirlam | Geo-Literary Society, Redwood Falls, Minnesota

This poster features a list of important malachite deposits by country and a timeline of malachite references in historic literature flanking an image of the GIA Museum's specimen "Atlantis," a stunning 70 × 20 cm array of green malachite spires coated with blue chrysocolla from the Star of the Congo mine in Lubumbashie, Haute-Katanga, Democratic Republic of the Congo.

The Elephants Are Winning

Charles Carmona | Guild Laboratories, Los Angeles

Although the global elephant population has started to rebound following historic lows between 1990 and 2010, they are still threatened by the illegal ivory trade and human-elephant conflict, including encroachment of livestock into elephant habitats and habitat fragmentation driven by human population growth. This poster contrasts the modest rebound in elephant numbers with the serious decline in the global coral population driven by overharvesting and climate change, and creates awareness of other endangered species.

Gem Mineral Localities at the Time of the Taj Mahal

Dona Dirlam | Geo-Literary Society, Redwood Falls, Minnesota

Long-established maritime and land trade routes, including the Silk Road, enabled Shah Jahan and other Mughal rulers to amass mineral and gem resources, resulting in remarkable jewelry pieces and spectacular monuments such as the Taj Mahal in the 1600s and 1700s. Centered on a map illustrating historic gem sources and the routes that connected the gem trade to the Mughal markets, this poster features examples of emerald, diamond, and spinel jewelry pieces produced during this opulent period (figure 3).

For more information, see Dirlam D.M., Rogers C.L., Weldon R. (2019) Gemstones in the era of the Taj Mahal and the mughals. *G&G*, Vol. 55, No. 3, pp. 294–319, http://dx.doi.org/10.5741/GEMS.55.3.294

The Global Trade Routes and Localities of Gemstones According to 17th–18th Century Armenian Sources

Dr. Sona Tajiryan | Los Angeles

This poster illuminates the early modern (1500s–1800s) gem trade by way of previously unpublished archival sources. It documents the practices of Armenian merchants

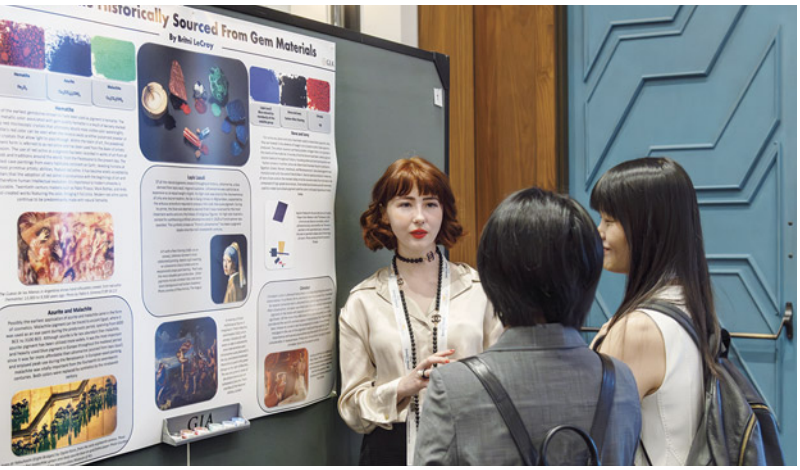

Figure 4. Britni LeCroy links gem-derived pigments to pivotal works of art in human history. Photo by Emily Lane.

who were central to the transcontinental movement of gems at the time. A map shows the major trade routes of the most sought-after gems—ruby, pearl, sapphire, turquoise, lapis lazuli, amber, and coral—from mines or manufacturing centers and onward to hubs of consumption, illustrating the sophistication of these early modern trading networks.

Inclusion Chronicles: A Pursuit of Photomicrography

Randall Lightfoot | Mayflower Estate Buying & Consulting, Towson, Maryland

This poster is a reminder of the wonders within gems as revealed by the practice of photomicrography. The author, winner of Gem-A's 2023 Photographer of the Year Award, presents a set of gemstone inclusion photomicrographs as an inspiration to others to explore and record the interior of gems.

The Literature of Gem-Bearing Granitic Pegmatites

Dona Dirlam | Geo-Literary Society, Redwood Falls, Minnesota

Pegmatites have fascinated scientists since the dawn of mineralogy. This poster explores the term's origin in early literature, beginning with its coining by French mineralogist René Just Haüy. The authors provide pointers to more modern references, plus a list of the world's major gem pegmatite districts along with specific examples of important pegmatites from the literature—Brazil's Pederneira pegmatite and the Emmons pegmatite from the U.S. state of Maine. Also included is a QR code linking to a unique pegmatite bibliography provided by GIA's Dr. James Shigley.

For more information, see Palke A.C., Shigley J.E. (2025) Colored Stones Unearthed: Gem granitic pegmatites. *G&G*, Vol. 61, No. 2, pp. 192–204.

Mineral-Driven Technology and Aesthetics: Material Basis and Cultural Expression of Chinese and Western Colored Glaze Crafts

Dr. Shangjia Wen | Gemmological Institute, China University of Geosciences, Wuhan

Minerals have often served as vehicles for human technological innovation and cultural expression. This poster explores the use of the copper mineral malachite, source of the copper pigment used to color ancient Egypt's turquoise blue Faience (circa 3000 BCE) as well as the vibrant green glazed ceramics produced by the Changsha Kiln during the Tang Dynasty (eighth to ninth century).

Pigments Historically Sourced from Gem Materials

Britni LeCroy | GIA, Carlsbad

This presenter examines the pivotal role of six gem and mineral materials—hematite, azurite, malachite, lapis lazuli, bone and ivory, and cinnabar—as the sources for pigments throughout human history (figure 4). The poster cites examples using these pigments, from red ochre–outlined handprints in ancient caves to master works by Vermeer, Titian, Malevich, and Degas, showing how gem materials and human ingenuity infuse art through the ages.

For more information, see LeCroy B. (2022) Gems on canvas: Pigments historically sourced from gem materials. *G&G*, Vol. 58, No. 3, pp. 318–337, http://dx.doi.org/10.5741/GEMS.58.3.318

Revision of the GIA Pearls Course

Dr. Tao Hsu | GIA, Carlsbad

This poster outlines the updated GIA Pearls eLearning course and Pearl Lab Class, showing a list of each assignment's contents. The updated course includes the addition of two new assignments covering natural nacreous pearls and natural non-nacreous pearls, respectively, addressing a gap in the curriculum.

An Update on the GIA Library's Rare Book Digitization Project

Dianna Parsons | GIA, Carlsbad

With more than 50,000 books and 1,000 magazine and journal titles on topics related to gemstones and jewelry, GIA's Richard T. Liddicoat Gemological Library and Information Center is the largest, most complete library of its kind. This poster spotlights the library's work digitizing rare books, outlining the digitization system used and citing examples of works publicly available through this initiative. Works cited and accessible by QR codes include Clinton's *The Story of a Pearl Oyster* (1914), Schmidt's *Diamond Gold and Silver Invoice* (1702), John Brogden's

Jewellery, Original Watercolor Drawings for Decorative Jewellery (1885), and Nawab Ahsanullah's *Dacca Collection* (circa 1900).

Young's Durability Scale

Kennon Young | Vermont Gemological Laboratory, Burlington

The author proposes a rating system for the durability of gemstones, which considers three properties: Mohs hardness (35%), fracture toughness (45%), and inclusions (20%). This produces a practical scale of 1 through 10 with opal, fluorite, and pearl at one end (1–2) and chrysoberyl, jadeite, corundum, and nephrite at the other (9–10).

NEW TECHNOLOGIES AND TECHNIQUES

Advanced Data Analysis and Machine Learning: Applications in Gem Identification

Dr. Matthew Hardman | GIA, Carlsbad

Natural and laboratory-grown diamonds (LGDs) can be indistinguishable to the unaided eye, and practical considerations dictate that they must be separated by nondestructive analytical techniques. The author demonstrates how a combination of photoluminescence spectroscopy and machine learning can allow evaluation and simplification of this spectral data by presenting a study of 1,121 natural diamonds and 1,178 chemical vapor deposition LGDs.

Polish to Rough Matching: Delivering Objective Assurance

Mayank Jain | DiaDNA AI Labs, Surat, India

The author presents a potential solution for rough-to-polished diamond traceability from mine to market. With many touchpoints in diamond manufacturing and multiple changes of hand thereafter, tracking a diamond from rough to a finished gem in jewelry is one of the industry's greatest challenges. The author proposes a solution involving high-resolution scanning followed by automated matching using artificial intelligence.

An Extended Application of Quantitative Description Methods for Color Cause of Chrysoberyl

Xinxin Gao | University of Chinese Academy of Sciences, Beijing

Guided by recent research into the chromophores of corundum, the authors present a parallel study of iron- and chromium-bearing chrysoberyl, driven by the similarities in the two minerals' chemistry, structure, and ultraviolet/visible/near-infrared (UV-Vis-NIR) spectral features. Results are presented as calculated color circles and UV-Vis-NIR absorption cross sections for both chromophores in chrysoberyl.

Figure 5. Artitaya Homkrajae explains how machine learning combined with trace element chemistry can enhance the pearl identification process. Photo by Emily Lane.

Identification of Known *Pinctada maxima* Pearls Using Trace Element Analysis and Machine Learning

Artitaya Homkrajae | GIA, Carlsbad

Although most pearl identification still relies on X-ray techniques, a combination of trace element chemistry and machine learning can provide a useful adjunct with a greater degree of confidence. This poster presents a study on known natural and cultured *Pinctada maxima* pearls employing laser ablation–inductively coupled plasma–mass spectroscopy paired with analysis using machine learning methods (figure 5).

Jewelry Verification Service

Najmeh Anjomani | GIA, Carlsbad

This poster provides an overview of GIA's Jewelry Verification Service and describes aspects of the service with examples. The service verifies the condition, measurements, metal type, and metal purity of a jewelry piece, along with the identity of any stones including the presence of treatments, and authenticates the brand, if applicable. Verification employs energy-dispersive X-ray fluorescence for the metals and Fourier-transform infrared and Raman spectroscopy for the stones. This service checks the description provided by the seller and offers surety for the buyer, benefiting everyone in the supply chain.

Metal Analysis for GIA Jewelry Services

Carlos Bautista | GIA, Carlsbad

This poster explains the use of X-ray fluorescence (XRF) testing to analyze and identify metals in jewelry pieces for GIA's laboratory services. It outlines the process, use of standards, testing procedures for jewelry items, and capabilities of the XRF devices used. Also described are some of the testing considerations involving multitone jewelry items, use of solder and repairs, and the presence of plating, all of which must be taken into account by the technician.

GIA HANDS-ON SESSIONS

Hands-on sessions afforded Converge attendees the opportunity to learn from GIA experts and work with samples from the Institute's extensive reference collection. All entries were written by GIA staff.

The Natural Diamond Story: Natural and Laboratory-Grown Diamond Differentiation

Dr. James Shigley (GIA, Carlsbad) presented a session focused on the incredible geologic story of natural diamond, reminding participants what a remarkable mineral diamond is (figure 1). He explained that the gem's origins provide jewelry professionals with memorable and relatable information they can use to educate consumers on the value of mined diamonds, to differentiate natural from laboratory-grown, and to address common misconceptions about abundance, mining practices, corruption, and human rights abuses. In this practical session, Dr. Shigley covered key aspects of natural diamonds' value and rarity, including their incredible geologic age and remarkable formation process, along with how and when they arrived at the surface through kimberlite eruptions. He explained how geologists search for viable diamond deposits and mining companies recover these diamonds, also providing an outline of the world's significant mines and their projected remaining production years. Also covered were the many positive micro and macro social benefits to communities involved in diamond mining, as well as environmental impact and sustainability. Dr. Shigley explained what is currently scientifically possible in terms of determining the geographic origin of a natural mined diamond—also covered by GIA's Dr. Michael Jollands in a speaker presentation—and outlined GIA origin services. Participants were able to handle natural and lab-grown rough and faceted gems and use their microscopes to examine interesting natural inclusions.

Beauty in Unexpected Places: The New Frontiers of Ruby and Sapphire

In this hands-on seminar, **Dr. Aaron Palke** (GIA, Carlsbad) and **Wim Vertriest** (GIA, Bangkok) provided an in-depth report on rubies and sapphires from lesser-known deposits including the United States (Montana), Tanzania, Kenya, Afghanistan, Sri Lanka, and Greenland (figure 2). They demonstrated practical tips for identifying corundum from these alternative deposits and gave context for understanding the place of these gems in the complex global colored stone trade. Participants were able to examine ruby and

Figure 1. Left: James Shigley presents on the unique story of natural diamond. Right: A kimberlite eruption plucked this 52.45 ct diamond octahedron from deep below the earth's surface, where it might have rested for billions of years. Photos by Emily Lane (left) and Robert Weldon; courtesy of the GIA Sir Ernest Oppenheimer Student collection (right).

Figure 2. Top: Wim Vertriest outlines key characteristics of gem corundum from less familiar localities in a session held during Converge 2025. Bottom: Attendees use their cell phones to capture images of intriguing inclusions. Photos by Emily Lane.

sapphire samples from the GIA colored stone reference collection representative of these newer localities and hear directly from the field gemologists who visited the areas and collected the gems.

(Un)Natural Beauty: Treatments in Ruby and Sapphire and Their Identification

It is increasingly rare to come across ruby and sapphire with beauty and appeal entirely due to natural processes. The majority of stones on the market have been treated to enhance their appearance. In this hands-on seminar, GIA's **Dr. Aaron Palke** and **Wim Vertriest** provided an in-depth orientation into the various artificial treatments for ruby and sapphire (figure 3). Using samples from GIA's colored stone reference collection, participants learned practical tips for identifying these treatments and gained an understanding of their value.

Figure 3. Aaron Palke helps orient a treated gemstone under the microscope for seminar attendees to view its diagnostic inclusions. Photo by Emily Lane.


Figure 4. Left: Nathan Renfro delivers practical hints and tips to seminar participants. Right: Attendees viewed inclusion scenes like these golden yellow rutile needles in rock crystal quartz. Photos by Emily Lane (left) and Nathan Renfro; field of view 7.61 mm (right).

Photomicrography of Gems

Inclusions in gemstones often captivate gemologists with their natural beauty. In this session, **Nathan Renfro** (GIA, Carlsbad) demonstrated that inclusions can also provide valuable information about gems, including what they are and whether they are treated, natural, or synthetic (figure 4). Renfro presented various lighting control techniques used to significantly enhance photomicrographs. He focused on a variety of interesting gemstone inclusions, encouraging participants to use their cell phones to practice some of the lighting techniques covered. Renfro explained that documenting observations with a photograph is a useful method of recording inclusions that is easily shared with others. Photomicrographs appeal to a broad audience, from those who are interested in the hidden beauty of the natural world to an appraiser who uses inclusions as a "fingerprint" to document the identity of a unique stone.

For more information, see Renfro N. (2015) Digital photomicrography for gemologists. *G&G*, Vol. 51, No. 2, pp. 144–159, http://dx.doi.org/10.5741/GEMS.51.2.144

Figure 5. Left: Al Gilbertson provides an introduction to jewelry forensics. Right: Attendees inferred manufacturing processes and likely provenances for jewelry pieces like this platinum and gold Edwardian brooch. Photos by Mimi Travis (left) and Robert Weldon; courtesy of Brian Davenport (right).


Introduction to Jewelry Forensics

While jewelry appraisers, those who take in jewelry for repair, and buyers of used jewelry go through a process to identify, analyze, and assess the quality and nature of a jewelry item, it is often not as comprehensive and systematic as they might wish. Many know only certain aspects of manufacturing and are only able to recognize a narrow range of specific characteristics. In this lecture and hands-on seminar, GIA Carlsbad's **David Etheridge** and **Al Gilbertson** guided participants through a systematic GIA framework to help them recognize and identify basic characteristics of key manufacturing processes (figure 5). They demonstrated the fundamentals of jewelry forensics, including identifying hand-fabricated, cast, and CAD/CAM-manufactured components, as well as cast-in-place gemstones.

Advanced Gemological Testing Workshops at GIA

Three sessions of an advanced gemological testing workshop were offered during the GIA Open House on September 7 as part of Converge 2025. Developed and led by **Dr. Tao Hsu** (GIA, Carlsbad), the two-hour workshop provided an overview of and hands-on experience with the six core advanced testing techniques commonly used in gemological laboratories: ultraviolet/visible/near-infrared, Fourier-transform infrared, Raman, and photoluminescence spectroscopy along with an X-ray fluorescence analyzer and a DiamondView. Together these techniques aid in the accurate identification of diamonds, colored stones, and pearls. The reliability and accessibility of these instruments make them viable tools for students. Some of these instruments are portable and could potentially be used in small businesses.

Each session opened with a lecture on the basic principles and major applications of the six techniques. Then students participated in hands-on activities in pairs. At each activity station, an instructor guided students through the testing process before they conducted their own analyses using select samples showing the main applications, strengths, and limitations of each instrument.

Many participants were GIA Graduate Gemologists with extensive trade experience (figure 6). The workshop helped refresh their knowledge and enhance their understanding of advanced gemological testing. Some participants noted that the workshop clarified questions about the advantages and limitations of these techniques.

Following the success of the workshop, GIA Education continues to develop this program to meet the demand for more in-depth gemology education.

Figure 6. Attendees of the first session of GIA's advanced gemological testing workshop held during Converge 2025, along with workshop developer Tao Hsu and six instructors from the Carlsbad education team. Photo by Russel Samson.

Figure 1. Faceted garnets (1.81–16.00 ct) along with rough fragments (largest piece is 12 g) from a new deposit in the Lao Cai province of northern Vietnam. Photo by Nuttapol Kitdee; courtesy of Precious Le Gems.

REGULAR FEATURES

COLORED STONES AND ORGANIC MATERIALS

New red garnet production from northern Vietnam. Since mid-2024, a newly discovered deposit in northern Vietnam has produced some fine red garnet. These stones are found in the rural Bao Yen district of the Lao Cai province, roughly 50 km northwest of the ruby-spinel mining district of Luc Yen. Artisanal miners dig for the garnet in river sediments and colluvial material at the base of hilly flanks. The rough stones are typically recovered as broken elongated fragments. Rough fragments can get very large, with pieces over 10 g routinely found. Euhedral garnet crystals have not been reported.

GIA recently studied a selection of rough and cut garnet from the new source (figure 1), loaned by Precious Le Gems. The color of the stones is typically a pure red, with a medium to dark tone. In rare cases, a slight purple tint can be observed. The stones were isotropic with a refractive index (RI) between 1.753 and 1.758. The specific gravity measured between 3.80 and 3.85, correlating

Figure 2. Left: Rutile needles and platelets are commonly observed in red garnet from northern Vietnam. Right: A well-formed, opaque metal sulfide crystal stands out due to its metallic luster. Photomicrographs by Suwasan Wongchacree; fields of view 4.80 mm (left) and 1.80 mm (right).

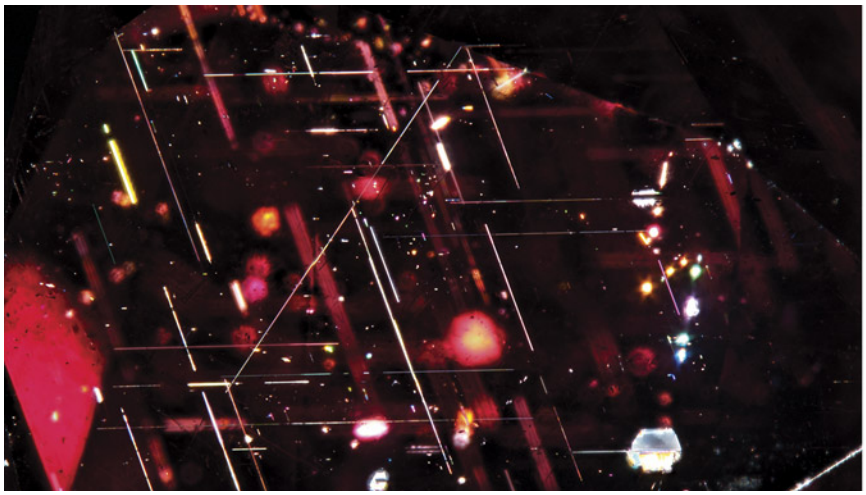

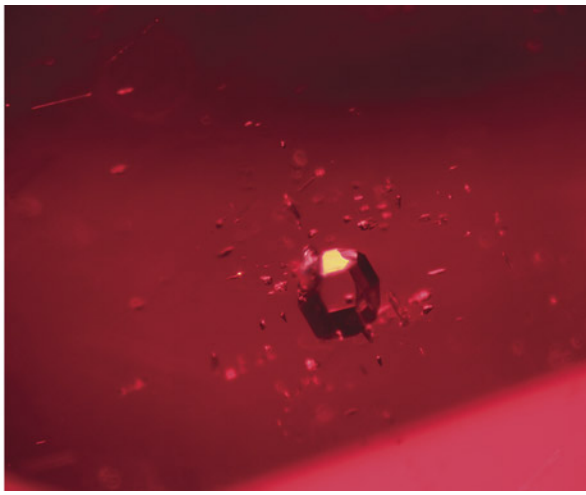

with the higher RI. A handheld spectroscope showed three strong bands in the green to yellow region of the spectrum around 505, 530, and 575 nm, with the 505 nm band being strongest and sharpest, and two more subtle lines in the blue region around 460–470 nm. These properties are typical for pyrope-almandine garnet. Chemical analysis revealed 50.0–52.7% pyrope and 34.1–37.5% almandine in the garnets, with a smaller component of grossular (11.0–12.5%) and spessartine (1.4–2.7%).

Most stones appeared eye-clean. When observed under high magnification, some stones showed an inclusion scene typical of red garnet (figure 2). The inclusions consisted of reflective needles and platelets. Crystal inclusions were limited to opaque sulfides and small translucent primary rutile, which were identified by Raman spectroscopy.

While northern Vietnam has only been explored for a few decades and has traditionally focused on spinel and corundum, this new discovery shows that there is a large potential for other gems as well.

Narint Jaisanit and Wim Vertriest
GIA, Bangkok

SYNTHETICS AND SIMULANTS

Fuchsite-bearing dolomite aggregate as a new jadeite imitation. Recently, a carved green snuff bottle was submitted as jadeite jade for identification at the Taiwan Union Lab of Gem Research (TULAB) (figure 3). The surface of the bottle displayed a white matrix with dense mottled green areas. A spot refractive index was approximately 1.68–1.69, which was noticeably higher than the typical range of values for jadeite jade. However, such results may occur if jadeite contains kosmochlor.

Under microscopic observation, the surface of the carving revealed a white matrix with green patches (figure 4).

Figure 3. A green snuff bottle (64.7 × 51.3 × 25.9 mm) submitted for identification as jadeite jade. Photo by Shu-Hong Lin.

Interestingly, these green patches appeared red when viewed through a Chelsea filter. To further identify the material, Raman spectroscopy (785 nm laser) was performed and

Figure 4. The surface of the snuff bottle shows a white matrix with green patches and black metallic minerals, most likely chromite. Photomicrograph by Kai-Yun Huang; field of view 2.75 mm.

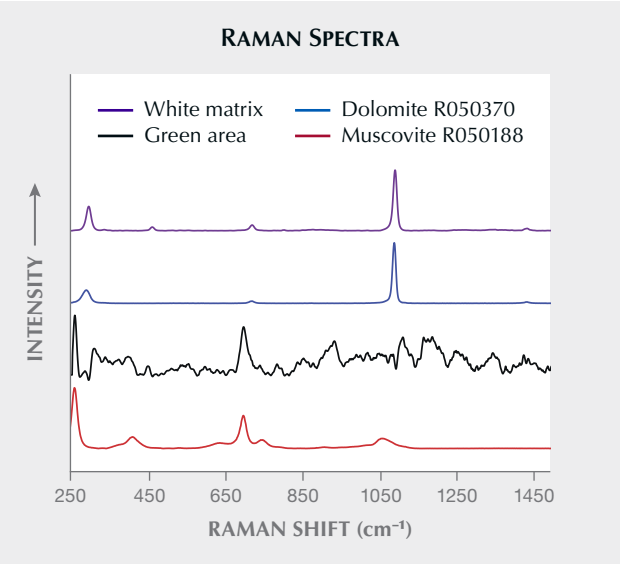

Figure 5. Comparisons of the Raman spectra from the green areas and white matrix of the tested object with spectra for dolomite and muscovite from the RRUFF database. Spectra are baseline corrected and normalized for comparison and offset vertically for clarity.

compared with the RRUFF database (B. Lafuente et al., 2015, https://rruff.info/about/downloads/HMC1-30.pdf). The results indicated that the white matrix was dolomite, while the dark green patches were muscovite (figure 5). With the assistance of energy-dispersive X-ray fluorescence (EDXRF) analysis, the green portions were confirmed to be fuchsite (chromium muscovite).

All testing indicated that the snuff bottle was composed of a dolomite aggregate with fuchsite. Although its appearance resembled jadeite jade, the bottle's refractive index and Chelsea filter reaction clearly distinguished it from jadeite jade. Raman spectroscopy and EDXRF were used as more precise methods to confirm the material, which appears to be a new jadeite simulant that has recently appeared on the market.

Tsung-Ying Yang, Kai-Yun Huang, Yu-Shan Chou, and Shu-Hong Lin
Taiwan Union Lab of Gem Research, Taipei

Reconstructed specimens and the rise of deceptive practices in Pakistan. Recent field observations in Pakistan have revealed that specimens circulating in local gem markets and near mine sites have increasingly been artificially assembled or altered. Local dealers and prospectors from the Hunza and Gilgit mining areas offered "Frankenstein" specimens, pieces assembled by gluing together fragments of crystals and host rock (figure 6). While adhesives can sometimes be seen under magnification, many joints are subtle enough to mislead buyers or tourists. Crystals such as aquamarine are often skillfully mounted onto matrices to imitate natural specimens, with some pieces further polished, dyed, or even oiled to enhance their appearance (figure 7). In certain cases, resins mixed with crushed marble or host rock are applied, making detection even more difficult. For example, in Peshawar's Namak Mandi gem market, a ruby reportedly from Jegdalek was identified as a synthetic crystal mounted on natural host rock. In addition to this deceptive practice of adhering specimens to host rock, broken specimens are also repaired with adhesives, often without disclosure. With time, the quality of assembly is improving, making detection more challenging.

The close proximity of these reconstructed specimens to the mines is a reminder that "from the mine" does not automatically guarantee authenticity. Collectors and gemologists should be aware that stones described as directly sourced may have undergone significant human intervention. Similar practices are common in neighboring regions, including Afghanistan.

Figure 6. Left: Marble-hosted ruby specimens (ruby crystals ranging from 0.6 to 1.0 cm in height) reportedly mined from Hunza and acquired from the nearby local market. The natural specimen components have been artificially assembled with a resin-like adhesive. Right: In some specimens, the adhesive is well camouflaged and difficult to detect (indicated by arrow), especially if oiled. Photos by Talha H. Bakht.

Figure 7. Left: A beryl specimen dyed with pigment clearly visible to the unaided eye. Right: The aquamarine are attached with glue to appear as a natural occurrence within this host rock. Photos by Talha H. Bakht.

Economic pressures play a major role in these trends. With average salaries in Pakistan ranging from 20,000 to 60,000 PKR per month (approximately US$70 to $212), many dealers and retailers offer inexpensive alternatives to natural gemstones. As a result, the domestic trade is dominated by simulants, imitations, and heavily treated stones. Dyed stones including lapis lazuli, nephrite jade, and emerald are widespread, as well as glass-filled sapphires, composite stones, and resin-treated turquoise. Irradiation is another common practice, particularly for beryl, tourmaline, and topaz. Large gemstone trading centers in Lahore, Karachi, Islamabad, and Peshawar (Namak Mandi) are particularly affected, making vigilance essential for anyone in the trade as these treatments are often undisclosed and may be unstable.

In another deceitful practice, problematic gemstones are often mixed into lots of natural stones. One 77 ct parcel of melee-sized red stones labeled as natural Jegdalek ruby, for instance, actually contained a mixture of natural unheated, heated, glass-filled, and synthetic ruby. Some dealers have even dotted natural jasper with blue dye to imitate the popular granite-like stone with distinctive blue spots found near K2 Mountain in Pakistan.

A general lack of understanding of gemstones in Pakistan, coupled with minimal regulation and a challenging economy, allows deceptive dealers to take advantage of unaware buyers, often presenting laboratory reports with misleading words such as "natural dyed emerald" or "natural glass-filled blue sapphire" or failing to disclose treatments. The word *natural* has been used incorrectly for such stones, which is a problem for local gem testing laboratories, although efforts are being made to revise the terminology applied to these types of materials. Similarly, terms such as "Shajri natural turquoise" have been applied to resin-composite mixtures intended to imitate the natural weblike structure of turquoise. Treatments are often left undisclosed, including the dyeing of natural opal and the oiling of natural emerald rough to hide fractures. Additionally, authentic reports have been reprinted and fraudulently attached to multiple stones in various markets such as Lahore.

Historically, Pakistani jewelers supplied royalty, from Nawabs to Maharajas, but many traditional techniques are fading in favor of faster, cheaper production. Many craftsmen are making jewelry with thinner or plated metal and/or including synthetic or imitation stones (figure 8), or closing their businesses, as the domestic trade cannot support the higher costs of gold and precious stones. For collectors, gemologists, and buyers, these trends underscore the importance of scrutiny, education, and caution when navigating Pakistan's complex gemstone market. Once a deal is done, it is very difficult to recover funds.

The increasing presence of glued reconstructed specimens near Pakistan's mining areas and all the above-stated practices underscore the need for vigilance in the field. Transparency in trade practices is essential for maintaining trust in the region's gem market. Unfortunately, many sellers fail to disclose such treatments, making it essential for buyers to exercise caution. Regardless of where the specimen is acquired and the price being asked, one should

Figure 8. Nearly all of the stones in these rings offered in markets throughout Pakistan are synthetics or simulants or have been enhanced. Photo by Talha H. Bakht.

suspect alterations unless proven otherwise. If the gemstone market in Pakistan is to gain worldwide recognition, more awareness and stricter regulations must be implemented. At the same time, many genuine and honest people remain in Pakistan's gem industry, and the actions of a few should not ruin the reputation for all.

Talha H. Bakht and M. Moeez Shah
Origin Gems
United Kingdom and Pakistan

ANNOUNCEMENTS

2026 Sinkankas Symposium: Gems and Minerals of Burma (Myanmar). The Twentieth Sinkankas Symposium will be held at GIA headquarters in Carlsbad on Saturday, April 25, 2026. This all-day educational event will feature presentations related to the science, history, and beauty of Burmese gems and minerals (figure 9). The symposium brings together 10 notable speakers: Tao Hsu, Richard Hughes, Bill Larson, Aaron Palke, Nathan Renfro, Stuart Robertson, Roland Schluessel, Laichen Sun, Rachelle Turnier, and Wim Vertriest. The lectures will be followed by a reception for attendees where they can tour the GIA Museum's exhibit, Temples & Treasures of Southern Asia. To register, go to www.sinkankassymposium.net.

Al Gilbertson receives Robert M. Shipley Award. Al Gilbertson is the 2025 recipient of the American Gem Society's (AGS) prestigious Robert M. Shipley Award, honoring his lifelong commitment to the trade and his contributions to understanding the influence of cut on the appearance of finished gemstones. Named for the founder of both GIA and AGS, the award was presented to Gilbertson (figure 10) on September 9 at Converge, an event combining GIA's gemological research and education with AGS's professional development and networking opportunities.

Figure 10. Al Gilbertson accepts the Robert M. Shipley Award at Converge in Carlsbad, California. Photo by Russel Samson.

Driven from an early age by a fascination with gems and minerals, Gilbertson was shaping cabochons at his parents' lapidary shop in the 1960s. When a short stint in the U.S. Air Force as a Russian linguist was interrupted by the untimely death of his father in 1974, he returned to the family business. Thus began a storied career in the jewelry trade as a colored stone cutter, appraiser, custom jewelry specialist, and period jewelry restorer. Gilbertson's inquiring mind and wide experience with gemstone cutting made him an invaluable research contributor on the appearance of gems and diamonds. After working on the team that established cut grade standards for AGS Laboratories, GIA recruited him as a researcher in 2000, where he helped invent the Institute's cut grading system for round brilliant diamonds. Today, Gilbertson is an integral part of the GIA team developing a cut grading system for fancy-shaped diamonds. He is the seventh GIA recipient to win the Shipley award.

Figure 9. The 2026 Sinkankas Symposium will explore the world of Burmese gems, including peridot (left) and ruby (right). Photos by Robert Weldon; courtesy of the Larson family.

Susan Jacques receives Richard T. Liddicoat Award for Distinguished Achievement. At a staff reception following the November board of governors meeting, GIA honored retiring president and CEO Susan Jacques with the Institute's highest honor—the Richard T. Liddicoat Award for Distinguished Achievement (figure 11). Current board chair Lisa Locklear and incoming GIA president and CEO Pritesh Patel presented the award to Jacques, praising her vision, integrity, compassion, and the lasting impact of her leadership on GIA.

Born in Zimbabwe to an Australian mother and a British father, Jacques' entrée into the industry came with a job as junior typist for the country's largest jewelry company. Noticing her boss taking GIA correspondence courses, she persuaded her parents to enroll her in GIA's in-residence graduate gemologist (GG) program at the Santa Monica, California, campus in 1980. For Jacques, gaining her GG had life-changing results, leading to a job at Borsheims in Omaha, Nebraska—one of the largest U.S. independent jewelers. Investor and philanthropist Warren Buffett's purchase of Borsheims in 1989 elevated the business and provided an opportunity for Jacques, culminating with Buffett offering her the position of CEO, which she held for 20 years. Jacques joined GIA's board in 1996 and became board chair in 2008 before her appointment as GIA's president in 2014. In addition to her GG diploma from GIA, she is a fellow of the Gemmological Association of Great Britain (Gem-A).

Established in 1994, there have only been 14 recipients of the Richard T. Liddicoat Award for Distinguished Achievement, including Tom Moses, executive vice president and chief laboratory and research officer; Alice Keller, editor-in-chief emerita of *Gems & Gemology*; Dona Mary Dirlam, librarian emerita; Kathryn Kimmel, GIA's first chief marketing officer (retired); John Koivula, analytical microscopist; and Dr. James Shigley, GIA's distinguished research fellow.

Figure 11. Susan Jacques accepts the Richard T. Liddicoat Award for Distinguished Achievement while incoming GIA president and CEO Pritesh Patel looks on. Photo by Russel Samson.

New edition of Tillander's *Diamond Cuts in Historic Jewellery 1381–1910.* First published in 1995, Herbert Tillander's classic work on the history of diamond cutting styles from the medieval period to the early twentieth century has been edited and updated by his daughter, jewelry scholar Ulla Tillander-Godenhielm (figure 12). This new edition includes additional scholarship and new photographs of Renaissance jewelry and famous diamonds. Herbert Tillander (1909–2006) was a legend in the Finnish jewelry industry, especially in the nomenclature and practice of diamond grading. Grandson of a jeweler to the Russian Imperial Court, Tillander devoted much of his life to the study of diamond cuts in historic jewelry collections.

Figure 12. A new edition of Herbert Tillander's book, updated by his daughter, Ulla Tillander-Godenhielm.

in the
spotlight

Temples and Treasures of Southern Asia
A GIA Museum Exhibit

Terri Ottaway, Rachelle Turnier, and Erin Hogarth | GIA, Carlsbad

Gems are universally admired for their exquisite beauty and alluring interaction with light. For geologists searching for clues about Earth's processes, gems are scientific treasures as much as visual ones. Rubies and sapphires are evidence of enormous heat and pressure deep underground; aquamarines are products of continental (tectonic) collisions. Inclusions in billion-year-old diamonds offer rare glimpses into Earth's inaccessible mantle.

GIA's museum team recently explored another dimension of gem appreciation: the bridges between human beings and higher powers. This exhibit in the Rotunda gallery at GIA in Carlsbad, California, showcases the extraordinary crystals and gems central to the cultures of southern Asia. In this region, gems symbolize connections to celestial bodies and the divine. As sacred talismans, they are seen to provide protection and wield powerful influence in every aspect of life.

Thus, when we admire a gem, we partake in a tradition almost as old as humanity. A single stone can embody beauty, wealth, Earth's history, and spiritual meaning all at once. This layering of significance gives gems their enduring power—and explains why, from ancient temples to modern museums, they continue to captivate us.

The following pages highlight some of the displays and items in the exhibit, which will be at GIA headquarters in Carlsbad until May 2026. All photos by Emily Lane. Exhibit case design by McKenzie Santimer, MCKmetal; exhibit graphics by Tom Kwolik, Ikon Ideas, Inc.

ACKNOWLEDGMENTS

Several lenders generously contributed gems, crystals, jewelry, and artifacts that made this exhibit possible. GIA sincerely thanks the Larson family, the Somewhere in the Rainbow collection, the Department of Mineral Sciences at the National Museum of Natural History, the Bindra family of B&B Fine Gems, and a private collector. We also appreciate donors who contributed pieces to the GIA Museum collection that were used in this exhibit: Mark Patterson, Sophie Leu, and Laura Ramsey (in memory of John Ramsey).

Sanctuary of Splendor. Temples and Treasures of Southern Asia invites visitors into GIA's peaceful Rotunda "temple." Accompanied by the sounds of singing bowls and sitar, the exhibit allows one to pause and appreciate the riches of more than 200 fine specimens from the region.

Sacred Stones, Eternal Purpose. The connection between temples, gems, and treasures reflects the view that beauty and spiritual purpose are deeply interlinked—that a gem is not just a stone, but a gift to the divine, a conduit of energy, and a testament to centuries of devotion.

Burmese jewelry from the sixth to eleventh centuries AD and shrine courtesy of the Larson family.

Moonlight in the Palm of Your Hand. Moonstone, a variety of feldspar, is cherished as a mystical gem. In Hindu tradition, it was linked to the moon god Chandra and believed to hold the moon's light within. Moonstone's ethereal glow made it popular in both royal adornment and religious offerings, symbolizing purity, serenity, and the divine feminine.

Moonstones from India, Sri Lanka, and Myanmar courtesy of the Larson family.

Aquamarine. Reminiscent of tranquil waters, Vietnamese aquamarine is notable for its darker blue hue, whereas Sri Lankan aquamarine is found in lighter blue shades.

Vietnamese aquamarine crystals courtesy of the Larson family. Specialty-cut Sri Lankan aquamarine faceted by Mark Gronlund; courtesy of the Somewhere in the Rainbow collection.

Enigmatic Energy. In Indian astrology, blue sapphire is associated with the planet Saturn (*Shani*) and regarded as one of the most powerful and potentially volatile gemstones. Saturn's energy relates to discipline, karma, and justice. Wearing a blue sapphire can bring great luck or disaster, depending on one's spiritual alignment. Buddhists connected the deep blue color with heaven and offered the gems to Buddha statues as a symbol of devotion.

Sapphire, diamond, and platinum brooch designed by Raymond Yard; courtesy of a private collector. Faceted Sri Lankan sapphires (1.10 to 16.41 ct) from the GIA Museum collection. Star sapphire rings and all sapphire crystals courtesy of the Larson family.

Bismarck Sapphire Necklace. One of the most iconic pieces in the Smithsonian's National Gem Collection is the Bismarck sapphire necklace. At its center is a stunning 98.57 ct deep blue sapphire from Myanmar. Designed by Cartier in 1935, this platinum necklace featuring more than 300 diamonds and accent sapphires was once owned by style icon and American socialite Countess Mona von Bismarck. The Burmese origin of the large sapphire was confirmed by the GIA laboratory.

Courtesy of the Department of Mineral Sciences, National Museum of Natural History; gift of Countess Mona von Bismarck.

Yellow Sapphire: Jupiter's Gem. Brilliant yellow sapphires from Sri Lanka—formerly known as Ceylon—are prized for their luminous colors, which range from soft lemon to vivid golden shades. Their color is caused by traces of iron in corundum's crystal structure. Sri Lanka's abundant gem-bearing gravels have supplied these treasured stones for centuries, earning the island the nickname "jewel box of the Indian Ocean." In Hinduism, planets are seen as powerful deities. Yellow sapphires, or *pukhraj* in Hindi, are linked to wisdom, prosperity, and the benevolent influence of the planet Jupiter.

"Sunrise of Ceylon," a 115.13 ct unheated yellow sapphire, courtesy of the Bindra Family, B&B Fine Gems, Los Angeles. Cultured pearl necklace featuring a 10.27 ct yellow sapphire surrounded by diamonds gift of the Greenfield family. "Intensity" yellow sapphire and diamond brooch gift of Mark Patterson.

Maw Sit-Sit. Maw sit-sit is a rare, vibrant green ornamental stone found only in northern Myanmar, made up of several minerals, including kosmochlor, chromium jadeite, and albite. Although maw sit-sit was first officially described in 1963, locals had been using it long before that, believing it to be a type of jade. As a result, maw sit-sit holds the same spiritual significance as jade.

Gecko carved by Patrick Dreher; all maw sit-sit pieces courtesy of the Larson family.

Valley of the Rubies. The world's most renowned and legendary source of rubies is the remote, mystical valley of Mogok in Myanmar. Rubies have been mined from the white marble host rock for centuries. This same ruby-bearing marble extends into Vietnam.

Rubies courtesy of the Larson family.

Ruby: The Fire Within. Rubies from Myanmar are revered for their intense "pigeon's blood" red color, symbolizing passion, strength, and protection. Spiritually, they were thought to contain "living fire," linking them to the life force and divine energy. This ruby and diamond necklace, the "Queen of Passion," exemplifies the very finest quality of Burmese rubies, none of which have been heated or enhanced. The 5 ct ruby in the center is an extraordinary size for this quality.

Courtesy of a private collector.

The Ultimate Trickster. Throughout history, spinel has been mistaken for ruby and sapphire and therefore afforded the same reverence, often used in royal regalia or as offerings in temples. Spinel's perfect octahedral crystals are called *anyon nat thwe*, Burmese for "polished by the spirits."

Tumbled spinel from Myanmar, Thailand, and Vietnam courtesy of the Somewhere in the Rainbow collection; faceted spinel from Myanmar and Sri Lanka courtesy of the Larson family and the GIA Museum collection.

The King Gem and Queen Gem. Mined from legendary alluvial deposits near Golconda, the only source of diamonds until the seventeenth century, Indian diamonds were revered as symbols of royal authority and were considered the "King Gem." Diamonds were believed to amplify spiritual power, making them treasures of both earthly and cosmic importance. Their rarity and mystical reputation elevated them well beyond mere material wealth.

Pearls were regarded as gifts from sea deities, especially in coastal and island communities in southern Myanmar, Vietnam, the Philippines, and Indonesia. For some, they represented spiritual wisdom and were considered the "Queen Gem." Rarer golden pearls were connected to the sun and were symbols of wealth, prestige, and divine blessing.

Golden pearls and strands courtesy of a private collector and the GIA Museum collection. Diamonds courtesy of H.K. International and the GIA Sir Ernest Oppenheimer Student collection.

Enlightenment. The name *padparadscha* is derived from the Sinhalese words for "lotus blossom." These pink-orange sapphires are admired for their auspicious coloring, like that of the setting sun. In Buddhist culture, the lotus and sunset are associated with enlightenment and spiritual awakening.

Padparadscha gems (5.05 to 9.05 ct) and 25.03 g crystal from GIA's Dr. Edward J. Gübelin collection and the GIA Museum collection.